

Plasmonic nanostructures for physical and biological applications

THÈSE N° 6562 (2015)

PRÉSENTÉE LE 3 MARS 2015

À LA FACULTÉ DES SCIENCES ET TECHNIQUES DE L'INGÉNIEUR
LABORATOIRE DE NANOPHOTONIQUE ET MÉTROLOGIE
PROGRAMME DOCTORAL EN PHOTONIQUE

ÉCOLE POLYTECHNIQUE FÉDÉRALE DE LAUSANNE

POUR L'OBTENTION DU GRADE DE DOCTEUR ÈS SCIENCES

PAR

Shourya DUTTA GUPTA

acceptée sur proposition du jury:

Prof. C. S. Brès, présidente du jury
Prof. O. Martin, Dr L. Juillerat-Jeanneret, directeurs de thèse
Prof. M. Käll, rapporteur
Prof. B. Reinhard, rapporteur
Prof. F. Stellacci, rapporteur



ÉCOLE POLYTECHNIQUE
FÉDÉRALE DE LAUSANNE

Suisse
2015

Our greatest weakness lies in giving up.
The most certain way to succeed is to try just one more time.
— Thomas A. Edison

To my grandparents and parents...

Acknowledgements

At this time, I would like to acknowledge and thank the people because of whom the work presented in this thesis was made possible.

Firstly, I would like to thank my supervisor Prof. Olivier Martin for giving me this opportunity to work in his lab for the last four and half years. The interactions that I had with you as well as observing you at the different official venues allowed me to learn a lot about various facets of research as well as develop some of the presentation skills necessary for propagating the results of the aforementioned research. I am extremely deeply thankful to you for all your guidance and support during my PhD.

Secondly, I would like to express my deep gratitude to my co-supervisor Dr. Lucienne Juillerat-Jeanneret for teaching and helping me develop my biology skills. The exposure into biology that I got by working in your lab at the CHUV was immensely helpful. Without your help I would not have been able to study the interdisciplinary research area involving nanoparticles and biology.

I am also very grateful to Prof. Camille Brès, Prof. Francesco Stellacci, Prof. Mikael Käll and Prof. Björn Reinhard for agreeing to be part of the thesis jury and for all your invaluable comments about the thesis.

In addition to my supervisors, I had the distinct pleasure of interacting with a lot of colleagues in the NAM lab and I would like to thank them for it: Christian - for helping and discussing with me whenever I had any questions not only about my work (especially the nanofabrication) but also about life in swiss in general, Guillaume - for introducing me to the fascinating area of surface chemistry and for all your assistance in adjusting to life in Lausanne, Andreas Kern - for introducing me to the SIE method, it was immensely useful for my thesis, Benjamin - for all the discussions that we had about Fano resonances, Andrea Lovera - for being an awesome office mate for most of my PhD duration and for all the scientific and non-scientific discussions that we had in the office, Arash - for all the fun with juggling and the various trips with you and Umlaut, Banafsheh - for the work on circular polarization as well as the philosophical discussions about life, Volodia - for helping me out immensely in the chemistry aspects of my work, Mohsen- for all the discussions that we had on perfect absorption, Jeremy - for all the discussion on second harmonic and for translating my abstract into French, Krishnan - for all the nice discussions we had in the evening about life and science and Thomas - thanks for the opportunity to delve into SERS with plasmonic structures. A big thank you to Beatrice, Cathy

Acknowledgements

and Pierette for all the help with the administrative details. To all the other people in the lab- Raziman, Xiaolong, Chen, Madasamy, Robert, Gabriel, Simon, Sergio, Nicolas and Kyuang-Yu for being great colleagues.

During my PhD, I also worked in Lucienne's lab at CHUV which enabled me to explore some facets of biology. During this time I received immense support from the people at CHUV some of whom would like to specifically acknowledge : Catherine - thank you very much for all your help in cell culture and showing me the protocols for various assays and Davide- for all the discussions that we had about the various experiments and for introducing me to the methodologies used in Biology. To all the other colleagues in CHUV : Blanka, Catherine, Frederick, and Francoise - thank you very much for all the help with the cell culture work. I would also like to thank Dr. Sandrine Gerber for allowing me to perform cell culture work in her lab during the last year of my PhD and for the discussions. I am also very grateful to the staff at the CMi for all their assistance and help with the nanofabrication and the BIOP staff for their help with the two photon imaging.

In addition to the people that I was introduced to in a scientific capacity, I also interacted with a lot of people socially especially the Indians at EPFL. It was a great pleasure to be part of YUVA and work for the various events which made me feel at home even in Lausanne.

Finally, I would like to thank my family, especially my parents - both my mother and father, for their constant support, encouragement and for motivating me continuously all through my PhD. Without their support during this time I would not be here at this stage presenting my thesis.

Lausanne, 31 January 2015

Shourya

Abstract

In the last few decades, plasmonic nanostructures have been studied and used vividly for numerous applications ranging from medicine and diagnostics to efficiency enhancement of solar cells. In line with this, the main focus of this thesis is to investigate the applicability of plasmonic nanostructures and develop new methodologies for improving their capabilities for certain specific physical and biological applications.

Biosensing is one of the areas which has benefited significantly from the plasmonic resonances supported by those nanostructures. Even though significant advances in sensing methods have been made, the detection of small molecules still remains a challenging task. The first part of the thesis investigates the possibility of exploiting coupling between the resonances of plasmonic nanostructures and absorbing molecules for sensing small biologically relevant species. Both the weak and strong coupling regimes between the plasmonic resonances and the absorption bands of molecules are studied.

Another principal application of plasmonic nanostructures lies in the field of medicine and diagnostics. The biocompatibility of plasmonic nanostructures is an important question that must be addressed for applications in this field. Furthermore, approaches which can improve or enhance the bio-compatibility properties of nanostructures are much sought after. It is now well known that the biocompatibility of plasmonic nanoparticles is closely associated with the coating of the molecules around the structure. A potential route for synthesis of plasmonic nanoparticles using human cells is studied in the second part of this thesis. The synthesized nanoparticles are shown to possess a rich protein coating, known as the protein corona. Preliminary experiments for understanding the uptake characteristics of the human cell synthesized nanoparticles are also performed.

The next application that is investigated is the detection of nanoparticles using plasmonic nanostructures, exploiting the coupling between two plasmonic resonances. This technique allows the detection of individual 30 nm particles. The data acquired from this method could, in future, be used to complement information obtained from the traditional nanoparticle analysis techniques.

On a different note, nonlinear optical processes can also be enhanced using the high near fields generated in plasmonic nanostructures. However, the conversion efficiency is strongly dependent on the modal properties of the nanostructures. For this reason, a technique for

Abstract

calculating the eigenmodes of a plasmonic nanoclusters is developed. The modal structure computed using the developed method is then used for analyzing and understanding second harmonic generation from the nanoparticle clusters.

It is well known that the maximum obtainable enhancement of an optical process via the use of plasmonic nanostructure is limited by the amount of energy that can be trapped in its near-field. The final part of this thesis studies and exploits different ways for developing plasmonic nanostructures which absorb all the incident energy at a given wavelength. When a nanostructure is illuminated with two incident beams simultaneously, it is possible to exploit the phenomenon of destructive interference to achieve perfect absorption. This is demonstrated both theoretically and experimentally. A single beam analog is also presented and the corresponding near field enhancement is validated using SERS signals from molecules.

Keywords: Optics, plasmon, surface plasmon, localized plasmon, near field thin film, gold nanoparticle, nanostructure, chemical synthesis, strong coupling, anti-crossing, weak coupling, Hemoglobin, Cytochrome *c*, surface enhanced Raman scattering, plasmonic trapping, human cells, biosynthesis, protein corona, peroxide, glutathione, reactive oxygen species, cell membrane, cancer, metastasis, hybridization, extraordinary optical transmission, nanohole arrays, nanoparticle detection, size analysis, eigenmodes, nanoparticle clusters, eigenwavelength, eigenfrequency, field distribution, Green's tensor, second harmonic generation, circular polarization, perfect absorption, coupled plasmons, long range surface plasmon, short range surface plasmon, composite, waveguide, crescent array, critical coupling, anomalous scattering.

Résumé

Durant la dernière décennie, les nanostructures plasmoniques ont été étudiées et utilisées pour des applications diverses et variées, allant des diagnostics médicaux aux cellules solaires. Cette thèse s'inscrit dans ce cadre, étudie la possibilité d'utiliser les nanostructures plasmoniques à des fins pratiques et discute le développement de nouvelles méthodes pour des applications spécifiques en physique et en biologie.

Le développement de biocapteurs est l'un des domaines qui a le plus profité des résonances de plasmon de surface dans les structures plasmoniques. Bien que des avancées significatives aient été faites, la détection de petites molécules avec cette approche reste une tâche difficile. La première partie de cette thèse se concentre sur la possibilité d'exploiter le couplage entre les résonances de plasmon de surface et des molécules absorbantes pour la détection de petites entités biologiques. Les régimes de couplage fort et faible sont étudiés en détails.

Une autre application importante rencontrée en plasmonique est le diagnostic médical. La compatibilité biologique des nanostructures plasmoniques est une question importante qui doit être posée pour le développement de telles applications. De plus, de nouvelles approches permettant d'augmenter leur biocompatibilité sont nécessaires. Il est bien connu que la biocompatibilité des nanoparticules métalliques dépend de la couche moléculaire les enrobant. Une voie possible pour la synthèse de nanoparticules en utilisant les cellules humaines est proposée et étudiée dans la deuxième partie de cette thèse. Les nanoparticules synthétisées de cette manière possèdent une couche protectrice riche en protéines. Des expériences préliminaires pour comprendre les caractéristiques de ces nanoparticules synthétisées par les cellules humaines ont été réalisées.

L'application étudiée ensuite est la détection de nanoparticules en utilisant des nanostructures plasmoniques et le couplage entre deux modes plasmoniques. Cette technique permet la détection de nanoparticules avec un diamètre de 30 nm. Les données collectées avec cette méthode permettront, dans le futur, d'obtenir des informations complémentaires à celles obtenues par les méthodes conventionnelles d'analyse.

Dans un autre registre, les processus optiques non linéaires peuvent être exaltés grâce au fort champ proche induit par les nanostructures plasmoniques. Cependant, cette exaltation dépend fortement des propriétés modales des nanostructures. Pour cette raison, une technique

numérique pour le calcul des modes propres d'une collection de nanoparticules a été développée. La structure modale calculée est utilisée pour analyser et comprendre la génération de seconde harmonique dans les nanoparticules métalliques.

Il est bien connu que l'exaltation maximale d'un processus optique par l'utilisation des structures plasmoniques est limitée par la quantité d'énergie qui peut être localisée dans le champ proche. La dernière partie de cette thèse étudie et exploite différentes approches pour le développement de nanostructures plasmoniques qui absorbent toute l'énergie incidente à une longueur d'onde donnée. Quand une nanostructure est éclairée simultanément par deux faisceaux lumineux, il est alors possible d'utiliser le phénomène d'interférence pour réaliser une absorption parfaite. Ceci est démontré à la fois expérimentalement et théoriquement. Une analogie utilisant un seul faisceau est aussi présentée et l'exaltation du champ proche est validée en utilisant le signal SERS provenant de molécules.

Mots clefs : optique, plasmon, plasmon de surface, plasmon localisé, champ proche, film fin, nanoparticule d'or, nanostructure, synthèse chimique, couplage fort, anti-crossing, couplage faible, hémoglobine, cytochrome *c*, diffusion Raman exaltée de surface, piégeage plasmonique, cellules humaines, biosynthèse, protéine corona, peroxyde, glutathion, oxygène, oxydation, Membrane cellulaire, cancer, métastases, hybridation, transmission optique extraordinaire, réseau de nano-ouvertures, détection de nanoparticules, analyse en taille, modes propres, agrégats de nanoparticules, longueur d'onde propre, fréquence propre, distribution du champ, tenseur de Green, génération de seconde harmonique, polarisation circulaire, absorption parfaite, plasmons couplés, surface plasmon propagatif, matériaux composites, guide d'onde, réseau de croissant, couplage critique, diffusion anormale.

Contents

Acknowledgements	v
Abstract (English/Français)	vii
List of figures	xiv
List of tables	xix
1 Introduction	1
2 Plasmon modified absorption of molecules	7
2.1 Introduction	7
2.2 Strong coupling between surface plasmons and absorbing bio-molecules . . .	9
2.2.1 Modeling the optical response of hemoglobin molecules	9
2.2.2 Modification of sensing characteristics due to strong coupling	11
2.3 Plasmon enhanced absorption of cytochrome <i>c</i>	17
2.3.1 Cytochrome <i>c</i> and its properties	17
2.3.2 Theoretical formulation	18
2.3.3 Experimental methods	20
2.3.4 Interaction of single gold nanoparticle and a cytochrome <i>c</i> molecule . .	22
2.3.5 Effect of a layer of Cyt <i>c</i> on a gold nanoparticle	26
2.3.6 SERS based confirmation of Cyt <i>c</i> on the synthesized gold nanoparticles	30
2.3.7 Detection of Cyt <i>c</i> using extinction measurements	34
2.4 Summary	37
3 Human cell assisted synthesis of gold nanoparticles	39
3.1 Introduction	39
3.2 Experimental protocols	40
3.2.1 Chemicals	40
3.2.2 Cell culture and gold nanoparticle synthesis	41
3.2.3 Extraction of intracellular and extracellular biosynthesized gold nanopar- ticles	41
3.2.4 Two photon imaging	41
3.2.5 TEM characterization	42
3.2.6 STEM characterization	42
	xi

3.2.7	Proteomic analysis	42
3.2.8	Intracellular thiol and ROS determination	43
3.2.9	Cell viability evaluation	44
3.2.10	Cell membrane permeability evaluation	44
3.3	Results and discussion	44
3.3.1	Conditions necessary for synthesis of unaggregated gold nanoparticles	44
3.3.2	Two photon characterization of cells incubated with HAuCl_4	47
3.3.3	TEM characterization of cells	47
3.3.4	Proteomic analysis of the protein corona	49
3.3.5	Cell viability evaluation after exposure to HAuCl_4	51
3.3.6	Effect of initial cell state on particle characteristics	52
3.3.7	Effect of redox state of the cell	54
3.4	Cell vicinity synthesis of gold nanoparticles	56
3.5	Uptake of biosynthesized nanoparticles by human cells: Preliminary results	58
3.5.1	Nanoparticle synthesis by various human cell lines	58
3.5.2	Experimental procedure for studying nanoparticle uptake by human cells	59
3.5.3	Two-photon microscopy of nanoparticle uptake	60
3.6	Summary	65
4	Coupling mediated detection of plasmonic nanoparticles	67
4.1	Introduction	67
4.2	Methods	68
4.2.1	Numerical calculations	68
4.2.2	Nano-fabrication	68
4.2.3	Optical measurements	70
4.3	Results and discussion	70
4.3.1	Effect of hole size	70
4.3.2	Spectrum modification due to nanoparticle coupling	73
4.3.3	Limitation of periodic simulations	77
4.3.4	Experimental measurement of particle size	81
4.3.5	Gold nanoshells: Identification of the core diameter	84
4.4	Summary	85
5	Eigenmodes of plasmonic nanoclusters and their effect on polarization conversion and second harmonic generation	87
5.1	Introduction	87
5.2	Theoretical formulation	89
5.2.1	Eigenmode calculation	90
5.2.2	Second harmonic (SH) calculation	91
5.3	Eigenmodes of nanoparticle clusters	92
5.3.1	Monomer	93
5.3.2	Symmetric dimer: Effect of particle size and gap	94
5.3.3	Effect of symmetry breaking in a nanoparticle trimer	96

5.4	Polarization changing nanoparticle cluster	100
5.5	Correlation between mode symmetry and second harmonic generation from nanoclusters	105
5.5.1	Symmetric dimer	105
5.5.2	Asymmetric dimers	112
5.5.3	Linear trimer	116
5.6	Summary	117
6	Perfect absorption of light by plasmonic structures	119
6.1	Introduction	119
6.2	Coherent perfect absorption mediated selective mode excitation	121
6.2.1	Simulation of gap plasmon waveguide structures	122
6.2.2	Fabrication of plasmon waveguide structures	123
6.2.3	Optical measurements of gap plasmon waveguide structures	123
6.2.4	Theoretical demonstration of CPA and SS	124
6.2.5	Experimental demonstration of CPA and SS using gap plasmons	128
6.3	Perfect absorption of light by a metal-dielectric composite slab	132
6.3.1	Simulating the optical response of metal-dielectric films	132
6.3.2	CPA using a metal-dielectric composite film	134
6.4	Probing near-field enhancement in single beam CPA structures	137
6.4.1	Numerical simulation of the critical coupling structure	137
6.4.2	Fabrication of the crescent array structures	137
6.4.3	Optical measurements	138
6.4.4	Critical coupling mediated SERS enhancement	138
6.5	Summary	144
7	Conclusions and future outlook	145
A	Abbreviations	149
B	Plasmon modified absorption of molecules: Additional data	151
B.1	Hemoglobin	151
B.2	Cytochrome <i>c</i>	151
B.3	Variation of differential absorption and scattering signals from a gold core-Cyt <i>c</i> particle as a function of the core size	152
C	Biological system assisted gold nanoparticle synthesis	155
C.1	Gold nanoparticle synthesis by cell culture media	155
C.2	Gold nanoparticle synthesis by human cells: Additional data	156
C.3	Time dependent modification of cell morphology on incubation in PBS	157
C.4	Complete list of proteins	157

Contents

D Nanoparticle sensing using metallic hole arrays	161
D.1 Spectral dependence on pairs of hole-particle size	161
D.2 Proof of hybridization of plasmon modes of particle and hole	161
D.3 Modulation of transmission and reflection intensities due to a gold nanoparticle in a symmetric hole array structure	162
E Eigenmode analysis of plasmonic clusters: Additional data	165
F Perfect absorption of light mediated by plasmon resonances	167
F.1 CPA mediated anomalous reflection from a corrugated metallic film	167
Bibliography	212
Curriculum Vitae	213

List of Figures

1.1 Schematic of the thesis aims.	6
2.1 Geometry used for strong coupling	10
2.2 Dielectric function of hemoglobin	11
2.3 Dispersion diagrams illustrating strong coupling	13
2.4 Wavelength modulated SPR	14
2.5 Angle modulated SPR	15
2.6 Redox state dependent optical absorption of Cyt <i>c</i>	18
2.7 Chemical synthesis of Cyt <i>c</i> coated gold nanoparticles	21
2.8 Scattering and absorption spectra of a AuNP-Cyt <i>c</i> system	22
2.9 Distance dependence of absorption enhancement of Cyt <i>c</i>	25
2.10 Differential scattering and absorption spectra for a gold-Cyt <i>c</i> system and an isolated Cyt <i>c</i> molecule	26
2.11 Effect of modification of gold core size on the scattering and absorption spectra	27
2.12 Differential scattering and absorption for two gold core sizes: 50 nm and 68 nm	29
2.13 Effect of Cyt <i>c</i> shell thickness on the optical spectra of Cyt <i>c</i> coated gold nanoparticles	30
2.14 Size histogram of Cyt <i>c</i> coated AuNPs	31
2.15 SERS spectra from aggregates of Cyt <i>c</i> coated gold nanoparticles	32
2.16 Analysis of SERS signal from Cyt <i>c</i> gold nanoparticle aggregates	33

List of Figures

2.17 Plasmonic trapping and SERS measurements on a single Cyt <i>c</i> coated gold nanoparticle	35
2.18 Detection of Cyt <i>c</i> by extinction measurements	36
3.1 Cell mediated biosynthesis of gold nanoparticles	45
3.2 Absorbance of extracellular medium on incubation with HAuCl ₄	46
3.3 Two photon visualization of intracellular gold nanoparticles	47
3.4 Two-photon Z-scan imaging	48
3.5 TEM characterization	50
3.6 Proteomic analysis	51
3.7 Cell viability after exposure to HAuCl ₄	51
3.8 Trypan blue exclusion test for cell viability after exposure to HAuCl ₄	52
3.9 Trypan blue exclusion test after exposure to ethanol and formaldehyde	52
3.10 Cell state dependent biosynthesis.	53
3.11 Modifying the intracellular redox state.	55
3.12 Color of the culture well on addition of HAuCl ₄ to cells cultured with DMEM (with HEPES)+10% FBS	56
3.13 TEM images of cells cultured with DMEM (with HEPES) +10% FBS and incubated with HAuCl ₄	57
3.14 Scheme for human cell assisted nanoparticle synthesis and uptake of nanoparticles	58
3.15 Size histograms of gold nanoparticles synthesized by various human cells	59
3.16 Uptake of human cell synthesized gold nanoparticles by A549 cells	61
3.17 Uptake of human cell synthesized gold nanoparticles by CaCO ₂ cells	62
3.18 Uptake of human cell synthesized gold nanoparticles by HCEC	63
3.19 Uptake of human cell synthesized gold nanoparticles by MDA-MB-231 cells	64
4.1 Schematic of the nanohole array used for nanoparticle detection	69
4.2 Fabrication of nanohole arrays	69

4.3	SEM images of the fabricated nanohole array	70
4.4	Schematic of the optical setup	71
4.5	Optical properties of nanohole arrays	72
4.6	Modification of the optical spectrum due to the presence of a nanoparticle . . .	74
4.7	Hybridization diagram.	75
4.8	Modification of the spectrum due to particle position	76
4.9	Detection limit for nanoparticle sensing	77
4.10	Particle filling of the hole array with nanoparticles	78
4.11	Optical spectra for different filling fractions of the hole array	80
4.12	Effect of number of holes in the array on the normalized transmission	81
4.13	Experimental detection of a single 30 nm particle	82
4.14	Histogram of differential signals	83
4.15	Determining the core size in the case of gold nanoshells	84
5.1	Eigenmode computation	89
5.2	Modes of a nanoparticle monomer	92
5.3	Modes of a symmetric nanoparticle dimer	94
5.4	Modes of a symmetric nanoparticle dimer: gap variation	96
5.5	Symmetry breaking in a nanoparticle trimer	97
5.6	Field distribution of a nanoparticle trimer	98
5.7	Coupling induced control over circular polarization generation by Abasahl <i>et al.</i> [1]100	
5.8	Circular polarization generation from a nanoparticle quadrumer	101
5.9	Eigenmodes of the polarization changing quadrumer	102
5.10	Coupling induced bifurcation of DOP	103
5.11	Intensity and phase conditions in under-coupled, critically coupled and over-coupled regimes	104
5.12	Energy diagram and field distributions for a symmetric nanoparticle dimer . .	106

List of Figures

5.13 SH generation from symmetric nanoparticle dimer	108
5.14 Schematic of a symmetric nanoparticle dimer along with illumination conditions	109
5.15 SH generation from symmetric nanoparticle dimer: propagation along dimer axis	110
5.16 Schematics and modes of asymmetric dimer	112
5.17 SH generation from asymmetric dimer with 20 and 30 nm particles	113
5.18 SH generation from asymmetric dimer with 20 and 40 nm particles	114
5.19 Schematic of linear trimer	115
5.20 Energy diagram and field distributions of a linear trimer	115
5.21 SH generation from a linear trimer	116
6.1 Comparison between reflectivity and field enhancement for a thin gold film . .	120
6.2 Gap plasmon waveguide structure	122
6.3 Optical setup for simultaneous dual plane wave incidence	124
6.4 Interchangeable CPA and SS at the long range and short range gap plasmons .	125
6.5 Field enhancement and suppression due to CPA and SS	126
6.6 CPA and SS at the short range plasmon resonance	127
6.7 Experimentally measured dispersion of gap plasmon waveguide structure . . .	128
6.8 Experimental demonstration of CPA and SS at the short range surface plasmon	129
6.9 Phase control of CPA and SS	130
6.10 Schematics of the CPA geometry using metal-dielectric composite film.	132
6.11 Dielectric function of metal-dielectric composite films	133
6.12 Dependence of CPA frequency on the volume fraction of metal in a composite film	134
6.13 Realization of CPA at multiple wavelengths using a composite film	135
6.14 Parametric study of CPA in a composite film	136
6.15 Critical coupling geometry	139
6.16 Effect of spacer thickness on critical coupling wavelength	140

6.17 Effect of nano-crescent gap on critical coupling	141
6.18 SERS intensity as a function of reflectivity and dynamic tunability of critical coupling	143
7.1 Future outlook	146
B.1 Real and imaginary parts of the dielectric constant of Cyt c	152
B.2 Gold core size for optimal differential signals	153
C.1 Biosynthesis control experiments	156
C.2 Particle size histograms.	158
C.3 PBS induced cell morphology modification	159
D.1 Transmission spectra for hole-particle pairs	161
D.2 Schematic of the system	162
D.3 Demonstration of hybridized modes in particle-hole system	163
D.4 Transmission and reflection spectra from various nanoparticle positions a symmetric hole array	164
E.1 Eigenmode computation using frequency as the eigenvalue	165
E.1 Schematic of the geometry	168
E.2 CPA at the long range surface plasmon	169
E.3 CPA at short range surface plasmon	170
E.4 Anomalous scattering of light	171

List of Tables

2.1	Extracted parameter values for 25 mM Hb.	10
2.2	Parameters of Eq. (2.6) corresponding 50 mM solution of reduced and oxidized Cyt <i>c</i>	19
2.3	Peaks extracted from the Raman spectra of Cyt <i>c</i> coated gold nanoparticles . . .	34
3.1	Qualitative assessment of uptake of cell synthesized gold nanoparticles by human cells.	65
3.2	Common metastasis sites of some cancers. Data taken from national cancer institute at the national institutes of health (http://goo.gl/CrttBq).	65
A.1	Table of frequently used abbreviations.	149
A.2	Table of frequently used chemicals and their abbreviations.	150
B.1	Parameters for the dielectric function of oxygenated Hemoglobin	151
B.2	Parameters for the dielectric function of deoxygenated Hemoglobin	151
B.3	Parameters for the dielectric function of reduced Cytochrome <i>c</i>	152
B.4	Parameters for the dielectric function of oxidized Cytochrome <i>c</i>	153

1 Introduction

Gold has fascinated mankind since the ancient times. Bulk gold, in the form of ornaments and jewelry, was often considered as a symbol of wealth and prosperity. In addition, evidence shows that nanosized gold was also used in some ancient relics. The Lycurgus cup is a prime example, where nanosized gold was used in order to create different visual effects based on how it was illuminated [2]. When the cup was illuminated from the outside it appeared green, whereas, when illuminated from the inside it appeared red. Certain stained glass windows in cathedrals also made use of nanogold for special visual effects [3]. However, it is not yet clear whether these effects were created knowingly. It was only in the late nineteenth century that Michael Faraday experimentally demonstrated the special optical properties of gold nanoparticle suspension (gold particles with dimensions ranging from 1 to 100 nm) [4]. He demonstrated that the size of the nanoparticles controlled the color of the resulting suspension. It was the seminal work of Gustav Mie in 1908 that allowed a clear understanding of this interesting optical phenomenon [5]. The color of the suspension is determined by the scattering and absorption characteristics of the gold nanoparticles, which in turn are governed by their size dependent resonances, nowadays well known as plasmon resonances.

Concurrent with these developments involving gold nanoparticles, Wood observed the presence of certain sharp anomalies when a corrugated gold film was illuminated with light [6]. These anomalies or resonances were later attributed to the excitation of plasmon resonances supported at the gold-dielectric interface. Plasmon resonances, supported by gold particles or thin films, are resonant coherent oscillations of electrons at the metal-dielectric interface [6–22]. This resonant oscillation of electrons in turn generates a strong electromagnetic field at the metal-dielectric interface. In case of a particle the electromagnetic field at resonance is confined to the particle and hence they are commonly known as localized surface plasmons [12–22]. In addition to the size dependence, the localized plasmon resonance also depends strongly on the shape, structure and the dielectric constant of the background [13, 19, 21, 22]. On the other hand, in planar structures, the electromagnetic field propagates along the metal-dielectric interface and is confined to the metal-dielectric interface. These are referred to as propagating surface plasmons or delocalized surface plas-

mons [6–9]. As in the case of a particle, the plasmon resonance can be tuned by controlling the various geometrical parameters and the dielectric constant of the background. However, for exciting propagating plasmons at metal-dielectric interfaces, special excitation geometries are required, which enables the matching of the momentum of the incident light to the momentum of the surface plasmon wave [6]. Furthermore, the properties of the plasmon resonance strongly depend on the metal used. At present gold and silver are the ideal choices in the visible region of the optical spectrum [23, 24]. Recently, aluminum plasmonics has also gained prominence because of the strong plasmons supported by aluminum in the UV region of the spectrum [25–27]. A great deal of activity has been directed towards developing materials based on semiconductors, metallic alloys, transparent conducting oxides, metal nitrides, silicides, germanides and 2D materials like graphene which show plasmonic properties and can be used as an alternative to the traditional noble metals [23, 24, 28].

A major advantage of localized and surface plasmons stems from the evanescent character of the field in the near vicinity leading to large local field enhancement [6–12]. The evanescent fields can be used to probe nano objects beyond the diffraction limit, while there have been innumerable examples of amplifying tiny effects by field enhancement. The field enhancement has been not only used for studying various fundamental effects but also for diverse applications. Some of the well investigated areas include fluorescence modification [29–47], surface enhanced Raman scattering (SERS) [48–73], enhancing nonlinear processes [11], photothermal therapy of cancer [74–78], targeted triggered drug delivery [79], imaging [79–86], plasmonic trapping [87–92] and sensing [13, 15–19, 21, 22, 93–115]. In particular, when a fluorescent molecule is placed near a structure supporting plasmon resonances, its fluorescence can either be enhanced or quenched [38]. In addition to the excitation enhancement, the plasmon resonances also open up new radiative and non-radiative channels for the molecules to relax which in turn modifies the lifetime. Both of these processes dictate the fluorescence enhancement and such systems, exhibiting enhanced fluorescence from molecules, have been used in many applications [38, 39, 41]. Analogous near field enhancement has also been used for strongly increasing the Raman signals arising from molecules [52, 53, 59, 62]. The enhancement in Raman scattering is proportional to $|\mathbf{E}_{ex}|^2 |\mathbf{E}_{em}|^2$, where subscripts *ex* and *em* refer to the excitation and emission processes, respectively. This fourth power dependence on the field in conjunction with high near fields generated by plasmonic nanostructures enables the detection of single molecules and bio-analytes at ultra low concentrations using SERS [55–57, 61, 66, 71–73, 116].

The other notable advantage is the tunability of the engineered plasmonic structures. Rapid advances in nanofabrication and chemical synthesis techniques open up new avenues to control the geometrical parameters of the plasmonic system leading to realization of complex plasmonic structures [58, 117–127]. For example, the resonance of a nanoshell can be tuned from 500 nm to 1000 nm depending on the core radius and shell thickness [75, 77, 128]. Besides, by varying the core-shell parameters it is also possible to tune the strength of scattering relative to the absorption of the nanoshell. Further control over the plasmon resonance is achieved by arranging multiple nanoparticles in certain patterns. In a multi-particle system

proximity of the nanoparticles allows the interaction and hybridization of the plasmon modes [120, 129–146]. The concept of a plasmonic ruler was demonstrated exploiting the coupling in a two particle system, where a strong correlation exists between the resonance wavelength and the gap between the particles [144]. Additionally, in a multi-mode plasmonic system, interference between the modes can be used for controlling the line width of the plasmon resonances. Fano resonances in plasmonic nano structures [147–163], characterized by their narrow asymmetric line shape, are a classic example which involves the interference of two or more plasmonic modes. Another interesting example of interference was the recently reported control of absorption [164, 165]. It was shown that a properly tuned structure under specific coherent illumination can absorb all the incident light, referred to as coherent perfect absorption (CPA) or anti lasing, since it mimics the time reversed operation of a laser. However, very few studies on the application of CPA to plasmonic structures exist as of now.

It should be noted that while plasmon resonances have a dramatic effect on the underlying physical phenomenon in the case of fluorescence and Raman scattering, they themselves are not affected significantly. A distinct situation occurs in cases where the molecules exhibit a strong absorption resonance [166–198]. Due to the coupling between the modes of the molecular and plasmonic systems, the resulting coupled system can show totally distinct optical properties. This is commonly referred to as the strong coupling regime. A coupled system corresponds to the periodic exchange of energy between the interacting modes, resulting in normal mode splittings (in case of degenerate modes). Examples of strong coupling regimes have been demonstrated using a variety of plasmonic systems. It also opens up new routes for tuning the optical and chemical properties of molecules and has been exploited for varied applications [183, 186, 189, 196, 197]. In this context, the effect of strong coupling of bio-molecules with plasmonic systems still remains of critical interest.

Let us now focus on biosensing which has been one of the major applications of plasmonics. Plasmonic biosensors based on both localized and propagating surface plasmons have been employed for detecting a host of analytes some of which include viruses, bacteria, proteins, amino acids and single strands of DNA [7, 9, 10, 13, 15–22, 93–105, 199–201]. A standard plasmonic biosensor detects changes in the refractive index in the vicinity of the sensor due to the presence of the analyte. The change in refractive index is associated with a concentration of the analyte using a predetermined calibration curve. Furthermore, the real time detection ability of these sensors allows the measurement of the binding rates and affinities of molecular analytes to substrates in addition to their concentration [13, 16, 19]. Note that in its basic configuration, plasmonic biosensors are not specific towards a given bioanalyte but rather measure any change in the refractive index [9, 16, 18]. The specificity of the plasmonic biosensors is ensured by using surfaces functionalized with molecules which specifically bind to the bioanalyte of interest. For example, for detecting the protein immunoglobulin G (IgG), the SPR sensor is prefunctionalized with the antibody for IgG, anti-IgG, which possess a high binding affinity with IgG [9, 10]. In addition to standard plasmonic sensors, colorimetric assays based on aggregation of gold nanoparticles in solution due to a particular analyte has also been studied extensively for low cost, rapid and low concentration detection of analytes [202–211].

The aggregation in these assays is generally caused by either the collapse of the stabilizing layer around the nanoparticle or due to a cross-linking molecule which binds two neighboring particles. Dithiol molecules, molecules with two thiol groups, can cause the cross-linking in a gold colloidal suspension and lead to aggregating due to high binding affinity of thiol towards gold [212]. Since, plasmonic detection of analytes is based on monitoring changes in the refractive index, direct detection of molecules with low molecular weight still remains a challenging task. For example, the refractive index of a 30% H_2O_2 solution is 1.35, which decreases on dilution in water (taken from <http://goo.gl/G80F6q>). Using a plasmonic sensor with a sensitivity of 500 nm/RIU and an instrument resolution of 0.1 nm, it is clear that only around 1 mM H_2O_2 can be detected. However, the concentration range of H_2O_2 found in biological systems, like human cells and algae, are orders of magnitude lower, in the range of few hundred nM or μM [213–216]. Therefore, alternative indirect sensing routes are necessary for the detection of molecules with low molecular weight. One approach towards answering this problem, is based on bioanalytes which introduce a significant change in the refractive index of the molecules on the surface, rather than the direct binding of the analyte to the molecules on the biosensor surface. It is this refractive index change of the functionalized layer that is finally detected by the sensor. In this context I study the feasibility of using plasmonic biosensors for detection of H_2O_2 and this is discussed in detail in Chapter 2.

Recently, plasmonic sensors which can detect analytes directly from a biological sample, like blood or saliva, or can be used for detecting analytes in or around biological entities, like cells, have been greatly desired. In both of these cases, the integration of a biosensor with an active biological system still remains a challenging task and of significant scientific importance. One of the main challenges involves understanding the interaction of the plasmonic probes, like nanoparticles, with the molecules, mainly proteins, present in the biological system. It should be noted here that the interaction of proteins with nanoparticles is not limited to plasmonic nanoparticles, but rather it is a generic phenomenon that occurs when any material comes in contact with a biological system. Recall that many nanoparticle suspensions are stabilized by attaching a charged capping agent to the nanoparticle surface during the synthesis step [217–225]. The presence of the charged capping molecule introduces a net surface charge to the nanoparticle. When these particles are exposed to a biological sample, the proteins present in the vicinity of the nanoparticle can bind to its surface via electrostatic interactions. This leads to the formation of a protein layer/shell around the nanoparticle, now known as the protein corona [226–248]. This protein corona shields the core of the nanoparticle from direct exposure to the surrounding environment. Additionally, most common biological pathways in cells used for recognition of materials are governed by the interaction of the molecules present on the material surface with the receptors available on the cell membrane. Thus, what the cell actually observes in many cases is the protein corona rather than the synthesized nanoparticles. Therefore, the protein corona plays a critical role in determining the interaction of nanoparticles with cells and also dictates the biocompatibility and toxicity properties of the nanoparticles. As mentioned previously, the protein corona is formed in part due to the electrostatic interactions between the proteins and the charged nanoparticles. Thus by

modifying the properties of a nanoparticle, like surface charge, material, capping molecule and size, it is possible to engineer the protein corona [228, 229, 233, 234, 236, 239, 241–243]. In addition to the dependence of the corona on the nanoparticle properties, the composition of the corona is also dependent on the proteins present in the solution. For example, consider a protein solution which consists of two different proteins, one at high concentration with a low binding affinity (say protein A) for the nanoparticle surface and a second protein at low concentration with a high binding affinity (say protein B). When nanoparticles are exposed to this protein solution, protein A rapidly binds to the nanoparticle surface in the initial stage of the incubation due to its high concentration forming the protein corona. However, for longer incubation times protein B displaces protein A due to its relatively higher binding affinity for the surface. Thus the composition of the protein corona is determined by the dynamic equilibrium between the proteins in the corona and the proteins available in the solution. Indeed the dynamic nature of the protein corona is one of its most fascinating features and has been demonstrated in various systems using techniques like mass spectroscopy, fluorescence correlation spectroscopy and plasmonic sensing [230, 235, 238, 244]. The initial protein corona, consisting mainly of high concentration proteins, is known as the ‘soft corona’, whereas the final corona, possessing proteins with high binding affinities, is referred to as the ‘hard corona’. Most of these studies presented here regarding the protein corona involve two distinct steps. The first step consists of the synthesis of the nanoparticles with the desired properties while the second involves the exposure of the nanoparticles to the protein solution and further analysis. A different approach where the synthesis of the nanoparticle and the formation of the corona occur simultaneously can also be used for creating particles with tailored protein coronas. One way of achieving this is via nanoparticle synthesis mediated by biological organisms like algae, human cells and bacteria [249–253]. Nanoparticles synthesized through this route possess an intrinsic protein corona characteristic of the organism used for the synthesis. However, synthesis of gold nanoparticles assisted by human cells is yet largely unexplored and it is an promising field of research [254]. Therefore, in Chapter 3 of this thesis I study the human cell assisted synthesis of gold nanoparticles and analyze the properties of the synthesized particles.

Having discussed briefly the general directions of plasmonics and few of its trends, I outline the scope of the current thesis (see Fig. 1.1 for a bird’s eye view):

Chapter 2 of this thesis is devoted towards understanding and using the interaction between molecular and plasmonic modes for enhanced biosensing. In the first section of this chapter we use the strong coupling to enhance the sensing capabilities of a SPE sensor. In the second part of this chapter, the interaction between localized plasmons and molecular modes of a bio molecule are probed.

Keeping in mind the importance of gold nanoparticles with enhanced biocompatibility for various applications, chapter 3 of this thesis is devoted towards studying and characterizing the properties of gold nanoparticles synthesized by human cells. Biosynthesized particles synthesized through this route are shown to be stable and their properties are dependent on the

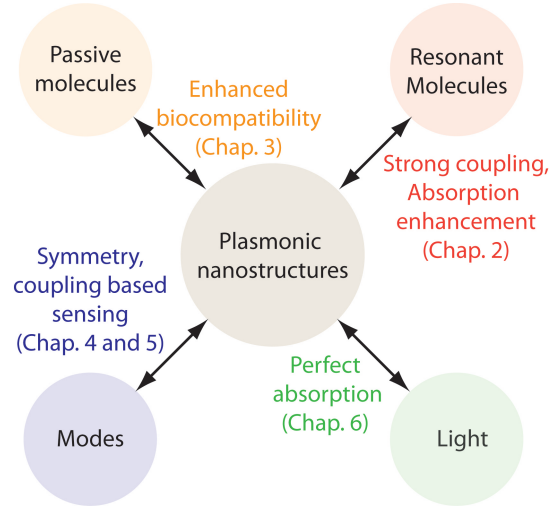


Figure 1.1: Schematic of the thesis aims.

characteristics of the cells used for fabrication. They are expected to be more biocompatible due to the protein corona associated with them during the synthesis step.

The fourth chapter of this thesis exploits plasmon hybridization for developing a novel tool for determination of plasmonic nanoparticle size. The advantages and disadvantages of using such a plasmonic sensing scheme over conventional particle measurement techniques is also discussed.

In the next chapter, I develop an eigen-mode analysis technique based on the Green's function approach and use it to study the effect of the modes of the plasmonic structure on the generated second harmonic signal.

In Chapter 6, I use both the localized and surface plasmons to demonstrate CPA in plasmonic structures. I show that all the incident energy can be absorbed by the structure. In the context of the coupled surface plasmons the incident light energy is shown to be transferred to one of the preselected modes. Finally, a one plane wave analogue of CPA is used to demonstrate that the perfect absorption by a plasmonic structure leads to a greater near field enhancement.

Finally, the main conclusions of the thesis along with future outlook of the work performed in this thesis are presented in Chapter 7.

2 Plasmon modified absorption of molecules

In this chapter, I study the influence of plasmonic nanostructures on the absorption spectra of molecules located in their vicinity. The first section deals with a system consisting of a thin silver film and a layer of hemoglobin molecules. Strong coupling between the surface plasmon resonance (SPR) and the absorption bands of hemoglobin is demonstrated and its effect on the SPR sensing characteristics is studied. In the second part of this chapter, I study the absorption enhancement of cytochrome c molecules placed close to a spherical gold nanoparticle. To validate the theoretical predictions, gold nanoparticles coated with cytochrome c are prepared using a single step synthesis approach. Optical measurements indeed show the signature of cytochrome c molecules albeit with different resonance wavelengths.

2.1 Introduction

Surface plasmon resonance (SPR) biosensors based on both propagating and localized surface plasmons have been extensively investigated and used for various applications. [6–14, 16–19, 79]. In general, SPR sensors detect the change in the refractive index of the surrounding dielectric medium due to the presence of a bio-analyte close to the interface supporting the plasmon resonance. Using standard plasmonic sensors, the presence of proteins and antibodies can be detected easily. However, the detection of smaller analytes such as oxygen, hydrogen peroxide and ascorbic acid still remains a challenging task using the traditional plasmonic sensors. Instead, indirect plasmonic sensors provide a better sensitivity in case of these small analytes [200]. Indirect plasmonic sensing is based on monitoring the change in the refractive index of a detection layer placed on the plasmonic sensor rather than the refractive index change due to the presence of the small analyte. The refractive index change of the detection layer is generally due to its reaction with the small bio-analyte. For example, hemoglobin is a prime candidate for facilitating the detection of oxygen, due to the high binding affinity of oxygen towards hemoglobin [255]. Oxygen binding to hemoglobin leads to drastic modification of its absorption bands, which in turn changes the refractive index of the hemoglobin layer.

Additionally, since the detection layer is placed close to the interface supporting plasmon resonance, the interaction of the absorption bands of the detection layer and the surface plasmon resonance exists. Broadly, two different regimes can be realized, namely, the strong and the weak coupling regimes [98, 99, 101, 104, 166, 167, 180–183, 191, 193]. In the strong coupling regime, the modes of the detection layer hybridize with the modes of the plasmonic structure to form new hybrid modes illustrating characteristics of both the individual systems [101, 104, 166, 167, 180–183, 191, 193, 195]. Anti-crossing or avoided boundary crossing in the dispersion diagram is a typical signature of strong coupling. In the first section of this chapter, I study the effect of strong coupling, between the absorption bands of hemoglobin and the surface plasmon resonance of a thin silver film, on the sensing characteristics of the plasmonic sensor. Note that even though past studies have reported an enhancement in the sensitivity if the antibody coating layer used for the detection of a specific antigen has an absorption band in the vicinity of the SPR resonance, the effect of strong coupling is not well known in this context [99, 101].

In addition to the use of strong coupling between the plasmon resonance and absorption bands of molecules for enhancing the performance of a sensor, it is also possible to work in the weak coupling regime [166–169]. For example, if one of the resonances is very weak as compared to the other, then strong coupling between the resonances does not occur. Rather, the response of this system can be explained via the use of perturbation models due to minimal change in the frequencies of the original resonances and is typically known as the weak coupling regime. However, the presence of the weak coupling enables one to transfer energy from one oscillator to the other. Therefore this allows the transferring of the energy from a highly excitable mode (for example the plasmon resonance) to a mode with low absorption cross section (for example the absorption band of a molecule) [166]. Note that such systems are always precursors for strong coupling regime and have been studied in various systems [166–169]. Weakly coupled plasmonic sensors attain even more significance for sensing molecules via indirect sensing means because of the sensitivity boost due to absorption enhancement. As mentioned previously, H_2O_2 is one small analyte of great importance in biological environment because H_2O_2 and other reactive oxygen species (ROS) are indicators of the oxidative stress level in the cells [213]. Oxidative stress in a cell is defined as the imbalance between the level of oxidants and anti-oxidants within the cell. Recently, Liu *et al.* showed that the absorption spectrum of free unbound cytochrome *c* (Cyt *c*) could be measured in the scattering spectrum of the gold nanoparticle (AuNP) when the distance between them was in the order of a few nanometers [256]. The explanation given was that the absorption of Cyt *c* was enhanced by the local field enhancement at the plasmon resonance and thus they named the phenomenon plasmon resonance energy transfer (PRET) [256, 257]. It should be noted that in the paper by Liu *et al.* the Cyt *c* was not bound to the surface of the AuNP, thus the distance between gold and Cyt *c* was not fixed, which is a critical parameter in any energy transfer process [256]. Recently, it was shown that the absorption spectrum of Cyt *c* could also be seen in the scattering spectrum of a dielectric medium that possessed no plasmonic resonances [258]. Thus it is not immediately clear what exactly is PRET and what

are the necessary conditions for having PRET. In the second part of this chapter, I study the modification of the absorption bands of Cyt *c* when it is conjugated to gold nanoparticles.

2.2 Strong coupling between surface plasmons and absorbing bio-molecules

In this section, I show that it is possible to achieve strong coupling between surface plasmons and the weak absorption bands of hemoglobin (Hb). Moreover, I demonstrate how the presence of strong coupling between hemoglobin and surface plasmon can enhance the sensitivity of a standard SPR sensor for both wavelength and angle modulation modes of operation. I address this issue by proposing a method of detection for oxygen exploiting the enhanced sensitivity of a SPR sensor provided by strong coupling between the surface plasmon and Hb absorption bands.

2.2.1 Modeling the optical response of hemoglobin molecules

Consider the system shown in Fig. 2.1. The layered structure consists of a 50 nm silver (Ag) film and a 100 nm hemoglobin (Hb) layer stacked on top of a SiO₂ slab ($\epsilon = 2.25$). The dielectric function of silver is modeled using the data given by Johnson and Christy [259]. The total concentration of Hb molecules in the Hb layer is kept fixed at 25 mM for all the simulations (Hb concentration in whole blood varies between 8 and 15 mM). I introduce a parameter f_r ($0 \leq f_r \leq 1$) that gives the fraction of Hb molecules that are in the oxygenated state, i.e. the Hb molecules that have O₂ bound to them. Therefore

$$f_r = \frac{n_{oxy}}{n_{oxy} + n_{deoxy}}, \quad (2.1)$$

where n_{oxy} and n_{deoxy} are the number of oxygenated and deoxygenated Hb molecules in the film, respectively. For example, $f_r = 1$ implies a completely oxygenated Hb layer whereas $f_r = 0$ implies a completely deoxygenated Hb layer. The dielectric function of Hb (for completely oxygenated or deoxygenated Hb) is modeled using the following empirical relation assuming a superposition of lorentzian responses at three distinct frequencies,

$$\epsilon_\alpha = \epsilon_w + \frac{v_{p1}^2}{v_{01}^2 - v^2 - i\gamma_{01}v} + \frac{v_{p2}^2}{v_{02}^2 - v^2 - i\gamma_{02}v} + \frac{v_{p3}^2}{v_{03}^2 - v^2 - i\gamma_{03}v}, \quad (2.2)$$

where α is *oxy* (Oxygenated Hb) or *deoxy* (Deoxygenated Hb), ϵ_w is the dielectric constant of water ($\epsilon_w = 1.7689$) and v is the frequency of the incident light. The parameters v_{0m} ($=c/\lambda_{0m}$;

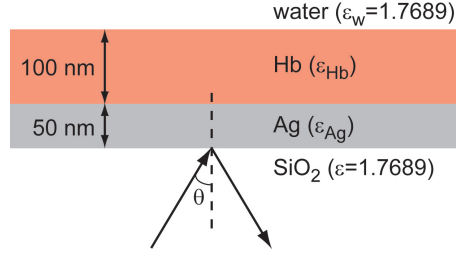


Figure 2.1: Geometry used for strong coupling.

	ν_{p1} (THz)	ν_{p2} (THz)	ν_{p3} (THz)	γ_{01} (THz)	γ_{02} (THz)	γ_{03} (THz)
OxyHb	23.5	15.8	87.0	32.5	15.0	39.0
DeoxyHb	35.5	3.0	64.5	66.0	10.0	20.0

Table 2.1: Extracted parameter values for 25 mM Hb.

c is the speed of light in vacuum), ν_{pm} and γ_{0m} (where $m = 1, 2, 3$) correspond to the position, strength and damping of the various resonances, respectively. For the case when the Hb film is partly oxygenated ($0 < f_r < 1$) I use a linear relation between ϵ_{oxy} and ϵ_{deoxy} to obtain the effective dielectric function of the Hb film:

$$\epsilon_{eff} = f_r \epsilon_{oxy} + (1 - f_r) \epsilon_{deoxy}, \quad (2.3)$$

The values of the parameters used in Eq. (2.2) are given in Table 2.1 for Hb concentration of 25 mM, they are obtained by comparing the absorption spectra obtained from Beer-Lambert law (using the experimental data of the absorption coefficient [255]) to the absorption spectra obtained using the transfer matrix formulation [260] with normally incident light for a 100 nm film of Hb suspended in water, i.e. both the incident and the emergence medium is taken to be water.

The resonances at λ_{01} and λ_{02} (λ_{03}) correspond to the Q-bands (Soret band) of the absorption spectra of Hb. Q-bands of the absorption spectra are of key interest here because they exhibit a large change as a function of the oxygenation state of the Hb layer, i.e. change in f_r . It should be noted that in case of deoxygenated Hb, the resonance at λ_{02} is very weak as compared to the resonance at λ_{01} ; whereas in case of oxygenated Hb the two resonances (at λ_{01} and λ_{02}) are of comparable strength. Figure 2.2 shows the real and imaginary parts of the dielectric function of both oxygenated and deoxygenated Hb films. The effect of the absorption peaks on the effective dielectric function diminishes from the resonances towards higher wavelengths λ . Above $\lambda = 800$ nm the difference between the imaginary parts of ϵ_{oxy} and ϵ_{deoxy} is negligibly small ($\leq 5.36 \cdot 10^{-4}$). In this regime i.e. when $\lambda \geq 800$ nm, there is a minimal contribution of the absorption bands of Hb towards the shift in the SPR peak caused by a change in f_r .

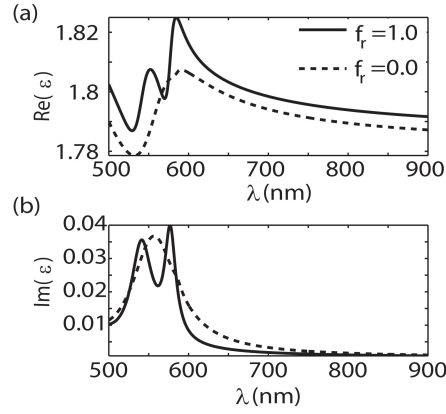


Figure 2.2: **Dielectric function of Hb.** (a) Real and (b) imaginary part of the dielectric function of oxygenated Hb (solid) and deoxygenated Hb (dashed).

One main advantage of using surface plasmons generated on thin metallic films is derived from their strong dispersion. As a consequence, the position of the resonance can be varied easily by changing the angle of incidence. This way one can spectrally overlap the SPR with the Hb absorption bands. Note that similar strong dispersive properties are absent in the localized plasmons of metal nanoparticles or metal nanocomposites. The locations of the Hb resonances are insensitive to the angle of incidence, while their comparative strengths can be controlled by concentration of Hb molecules in the Hb layer. The SPR location can be tuned by varying the angle of incidence resulting in strong coupling with the individual Hb modes for any value for f_r . In the next section I present numerical results demonstrating this strong coupling.

2.2.2 Modification of sensing characteristics due to strong coupling

Figure 2.3(a) shows the dispersion relation (plot of R vs. θ and λ) of a surface plasmon excited on a thin metal film (geometry is the same as shown in Fig. 2.1, except that the Hb layer is absent). All the calculations in this section are performed using the transfer matrix method [260]. Figure 2.3(b) and (c) show the dispersion diagram of oxygenated and deoxygenated Hb layers, respectively (geometry is same as shown in Fig. 2.1 except that the Ag layer is absent). In this case the absorption bands of Hb (both $f_r=0$ and $f_r = 1$) are seen to be non-dispersive, i.e. exhibit no angular dependence of the resonance positions. Furthermore, the absorption band in case of deoxygenated Hb is broader, compared to that of oxygenated Hb. By looking at the dispersion diagrams of the individual resonances, i.e. the surface plasmon resonance or the absorption bands of Hb (oxygenated or deoxygenated), it is clear that the individual systems do not possess an anti-crossing feature in their dispersion diagrams. Figure 2.3(d) and (e) shows the dispersion diagram of the complete system (Fig. 2.1) for the cases when $f_r=1$ and 0, respectively. When $f_r = 1$ the dispersion diagram shows the presence of two anti-crossings at the wavelengths of 546.0 and 577.0 nm, which correspond to the absorption bands of uncoupled oxygenated Hb. Similarly a single anti-crossing can be seen

at around $\lambda=556.0$ nm when $f_r = 0$, which corresponds to the absorption band of deoxygenated Hb. The presence of this kind of anti-crossings in the dispersion diagram is a clear indication of strong coupling between the surface plasmon and the absorption bands of oxygenated or deoxygenated Hb. The resonances of the strongly coupled system are very different from those of the uncoupled system. For example, the absorption bands of oxygenated or deoxygenated Hb shift due to coupling. Another effect of coupling is that the absorption bands which are generally weak can be enhanced so that their detection becomes easier. The anti-crossings are more prominent in case of oxygenated (Fig. 2.3(d)) compared to deoxygenated Hb (Fig. 2.3(e)) since the absorption bands in the former are sharper than in the latter. Another point of interest is that for a spectral region that is away from the anti-crossing region, i.e for $\lambda > 800.0$ nm, the two dispersion diagrams are very similar.

Now I demonstrate for both wavelength and angle modulated SPR sensors [7, 9, 10], that the shift of the resonance dips can be enhanced by working near the region of the strong coupling. Let us first consider a wavelength modulated SPR sensor, in which the angle of incidence is kept constant but the wavelength of incident light is changed so that reflectivity as a function of wavelength is measured. I compute the spectra at two different angles, $\theta_i = 72.9^\circ$ and 66° . When the angle of incidence is 72.9° the system is in the strong coupling regime, i.e. the surface plasmon mode and the absorption bands of Hb (oxygenated or deoxygenated) strongly couple, whereas when the angle of incidence is 66° the system is decoupled. Figure 4(a) shows the reflectivity as a function of wavelength for the two chosen angles for both $f_r = 0$ and 1. From the figure it can be seen that three, respectively two resonances are observed in the case of oxygenated, respectively deoxygenated Hb. I observe only two resonances in the case of deoxygenated layer even though it possesses three resonance dips (see Eq. (2.2)) since the resonance at $\lambda=586.0$ nm is very weak and does not show up in the reflection spectra of the coupled system. When the system is strongly coupled, i.e. the angle of incidence is 72.9° , it is seen that when f_r is changed from 1 to 0 the two resonances P1 (at 587.6 nm) and P2 (at 564.8 nm) converge to the resonance at 576.0 nm, whereas the resonance P3 moves from 541.7 nm to 546.4 nm. The position of the shoulder is given by the wavelength when $\partial^2 R / \partial \lambda^2$ is maximum in the vicinity of the shoulder. Considering the decoupled case, i.e. when the incident angle is 66° , the resonance peak P4 shifts from 842.0 nm to 836.0 nm when f_r changes from 1 to 0. Figure 4(b) gives the relative shifts of the resonances as a function of the oxygenation of the Hb layer, i.e. f_r varies from 0 to 1. The shift is measured by taking $f_r = 0$ as reference. From the figure it can be seen that the net shift (11.87 nm and 10.9 nm for P1 and P2 resonances) when the system is coupled is higher than when the system is decoupled (6.0 nm shift for P4 resonance). The peak P2 is followed from $f_r=0.2$ and not from $f_r=0$ because at very low values of f_r , distinguishing the resonances P1 and P2 becomes almost impossible. Also, rather than just looking at the shift of one resonance, the wavelength difference between two resonances, say P1 and P3, can also be used i.e.

$$\Delta\lambda = (\lambda_{p1} - \lambda_{p3}) - (\lambda_{p1}(f_r = 0) - \lambda_{p3}(f_r = 0)). \quad (2.4)$$

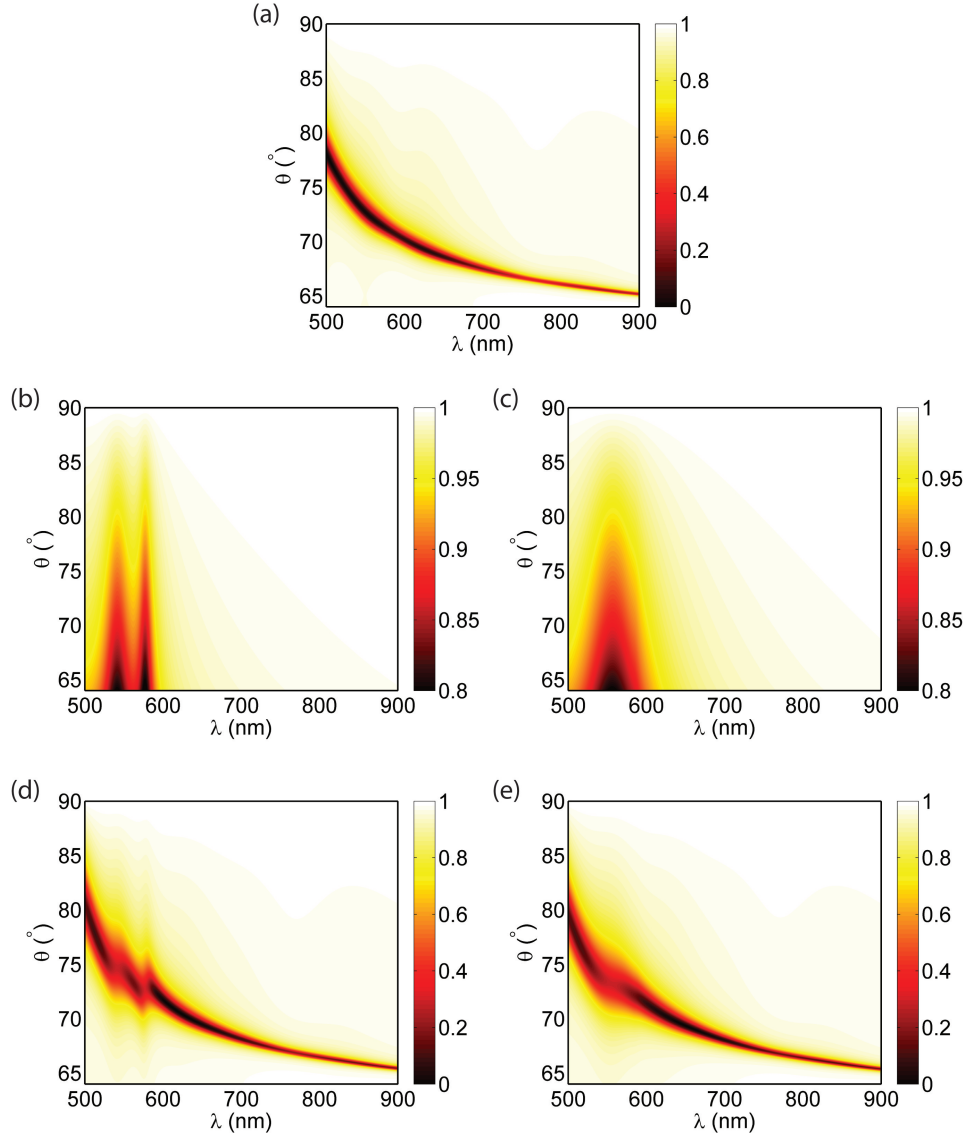


Figure 2.3: **Dispersion diagrams** Dispersion diagram of (a) a thin silver film placed on a SiO_2 substrate, (b) oxygenated Hb layer placed on top of SiO_2 substrate, (c) deoxygenated Hb layer placed on top of a SiO_2 substrate, (d) complete system (Fig. 1) when $f_r = 1.0$ and (e) complete system (Fig. 2.1) when $f_r = 0$.

Such a differential measurement appears to be even more sensitive, as visible in Fig. 2.4(b), where the P1-P3 data shows the strongest wavelength shift as a function of f_r .

An alternative way of determining the change in f_r can be by tracking the change in reflectivity of the resonance dips, as shown in Fig. 2.4(c). It is clear that if the change in the reflectivity is measured at the resonance P3 as a function of f_r , the change in reflectivity is much larger ($\Delta R = 0.16$) than in the decoupled case ($\Delta R = 0.0244$). Even when following the other two resonances i.e. P1 and P2; for $f_r > 0.3$ the change for these two resonances ($\Delta R = 0.114$ and

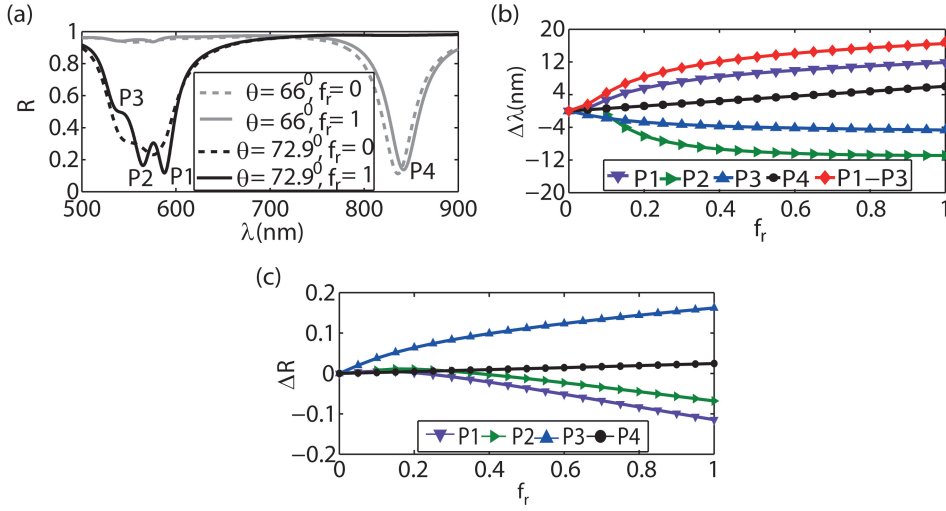


Figure 2.4: **Wavelength modulated SPR.** (a) Reflection spectra for two different angles of incidence; (b) Shift of the resonance peak as a function of oxygenation for both angles of incidence; (c) Change in reflectivity as a function of the fraction of oxygenation for both angles of incidence. The peaks traced in (b) and (c) are labeled in (a).

0.068 for P1 and P2, respectively) is greater than that of the uncoupled case ($\Delta R = 0.0244$).

Let us now study the effect of strong coupling on the angular shifts for another commonly used mode of operation for SPR sensors, namely angle modulation. In this mode of operation the incident wavelength is kept fixed (generally a laser source like He-Ne laser is used), whereas the angle of incidence is continuously varied. For computation, four different incident wavelengths are considered: 541.0, 556.0, 577.0 and 800.0 nm. The first two wavelengths correspond to the absorption Q-bands of oxygenated Hb, whereas the third wavelength corresponds to the absorption Q-band of deoxygenated Hb. The last wavelength is chosen such that the system is not strongly coupled at this wavelength. Figure 2.5(a)-(d) shows the reflection spectra as a function of angle of incidence for the four different wavelengths. It is seen that the resonances are broader for wavelengths of 541.0 nm (Fig. 2.5(a)), 556.0 nm (Fig. 2.5 (b)), 577.0 nm (Fig. 2.5 (c)), compared to 800.0 nm (Fig. 2.5 (d)). Figure 2.5(e) shows the angular shift of the resonance as a function of the oxygenation of the Hb film, i.e. when f_r is varied from 0 to 1. From the figure it is apparent that when the wavelength is near the anti-crossing region a larger angular shift ($\Delta\theta = 0.787^\circ$, 0.666° and 0.139° for wavelengths of 541.0 nm, 556.0 nm and 577.0 nm, respectively) is observed compared to the case when the chosen wavelength is away from the anti-crossing region (the shift is 0.073° only for $\lambda = 800$ nm (inset of Fig. 2.5(d))). It can be seen that when strong coupling is present in the system, the angular shift is at least enhanced by a factor of two and, if the optimal incident wavelength is chosen, the enhancement factor can reach 10 times compared to the decoupled case. As in the case of wavelength modulation, the change of reflectivity at the resonance dip can also be used to obtain an estimate of f_r . This is shown in Fig. 2.5(f), which reports the reflectivity change of the resonance as a function of f_r for the different incident wavelengths. It can be seen that the reflectivity change of the

2.2. Strong coupling between surface plasmons and absorbing bio-molecules

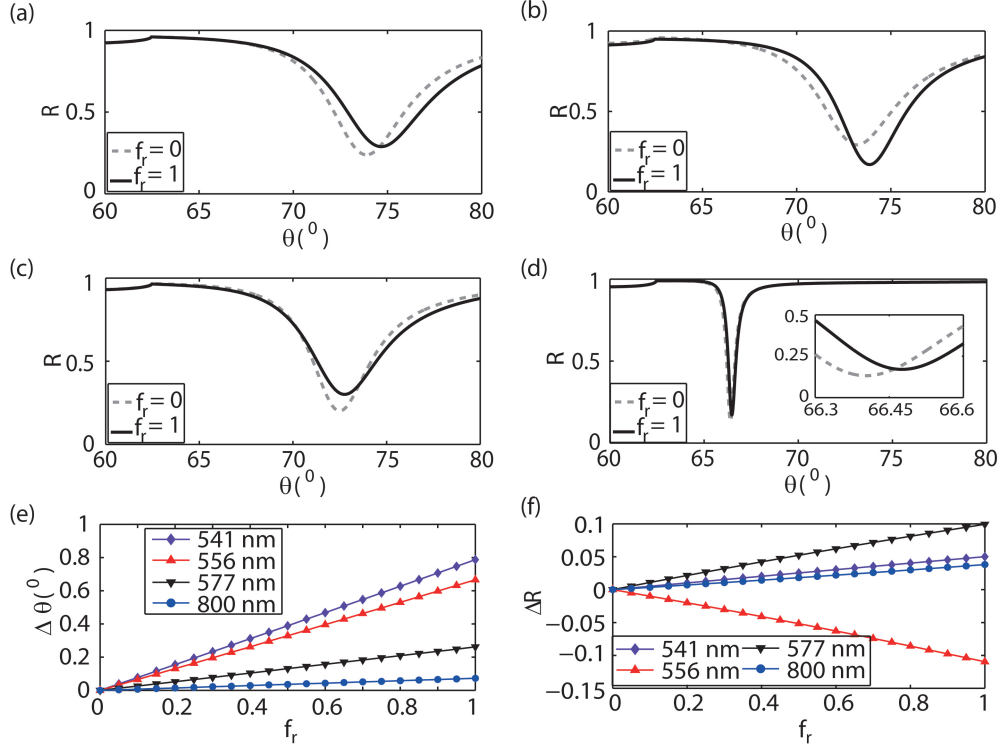


Figure 2.5: **Angle modulated SPR** Reflectivity from the layered structure for four different wavelengths (a) 546 nm, (b) 556 nm, (c) 577 nm, (d) 800 nm. (e) Angular shift as a function of oxygenation of the Hb layer for the four wavelengths; (f) Change in reflectivity as a function of the fraction of oxygenation.

resonance is enhanced by the presence of strong coupling. In that case, the reflectivity change of the resonance dip is 0.050, 0.110 and .099 for incident wavelengths of 541.0 nm, 556.0 nm and 577.0 nm, respectively; whereas for $\lambda = 800.0$ nm the change is only 0.038 when f_r is varied from 0 to 1.

By measuring the wavelength shift or the angular shift of the resonance dip, the change in the fraction f_r or Δf_r can be obtained. Thus the change in concentration of Hb molecules which have oxygen (O_2) bound to them can be inferred from the value of Δf_r . Let us carry out a brief discussion on the concentration of O_2 that can be detected easily using both the coupled and the decoupled systems. If Δf_r is being measured through wavelength shift or angular shift of the resonance dip, then the resolution of the instrument determines the lowest possible detectable concentration of O_2 . Since, 1 mole of Hb molecules can bind to four moles O_2 molecules, the minimum resolvable concentration of O_2 ($C_{O_2,min}$) is

$$C_{O_2,min} = 4(\Delta f_r)_{min}C, \quad (2.5)$$

where $(\Delta f_r)_{\min}$ is the minimum change in the fraction f_r than can be resolved from the shift of the resonance dip and C is the total concentration of Hb molecules ($C = 25$ mM). First consider a wavelength modulated SPR sensor with a wavelength resolution of 0.2 nm. In this system for a wavelength shift of 0.2 nm to occur f_r changes by 0.01 (following resonance P3, Fig. 2.4(b)) and 0.035 (following resonance P4, Fig. 2.4(b)) for the coupled and the decoupled case respectively (note that the initial value of f_r is 0). When the system is strongly coupled, i.e. the incident angle is 72.9° , then the value of $C_{O_2, \min}$ is 1.0 mM whereas when the system is not strongly coupled, i.e. the incident angle is 66° , then the value of $C_{O_2, \min}$ is 3.5 mM. The minimum detectable amount in the presence of strong coupling is four times lower than the decoupled case. Now consider the case of an angle modulated SPR sensor having an angular resolution of 0.0010. A angular shift of 0.001° is caused when f_r changes by 0.00125 ($\lambda = 541.0$ nm, Fig. 2.5(e)) and 0.0140° ($\lambda = 800.0$ nm, Fig. 5(e)) for the coupled and the decoupled case respectively (note that the initial f_r value is 0). When the system is strongly coupled, i.e. the incident wavelength is 541.0 nm, then the value of $C_{O_2, \min}$ is 0.125 mM whereas when the system is not strongly coupled, i.e. the incident wavelength is 800 nm, then the value of $C_{O_2, \min}$ is 1.4 mM. In this case the minimum detectable amount in the presence of strong coupling is almost 10 times smaller than in the decoupled case. It should also be mentioned here that Hb is allosteric and the affinity of O_2 towards Hb progressively with its oxygenation fraction [261]. This allosteric nature of Hb can affect the reaction kinetics of oxygenation and this must be taken into account when studying the kinetics using the studied strongly coupled plasmonic sensor.

2.3 Plasmon enhanced absorption of cytochrome *c*

In this section, I study the enhancement in the absorption of cytochrome *c* (Cyt *c*) molecules placed in the vicinity of a gold nanoparticle (AuNP). Two different theoretical approaches are used to explore this phenomenon. First, the absorption modification of Cyt *c* is studied using a Green's tensor technique. Second, generalized Mie theory is used to better mimic the experimental conditions and the dependence of the absorption enhancement on various system parameters is studied. The characteristic signatures of absorption modification are clearly illustrated using the theoretical analyses. To experimentally study this phenomenon, a single step synthesis of AuNP coated with Cyt *c* is developed and the synthesized particles are characterized using various techniques. The feasibility of using these nanoparticles for sensing hydrogen peroxide (H₂O₂) and ascorbic acid (AA) is also discussed.

2.3.1 Cytochrome *c* and its properties

Cytochrome *c* is a small hemoprotein with a molecular weight of 12 kDa and an approximate size of 3.4 nm [262]. Cyt *c* contains a heme porphyrin ring at its core surrounded by a polypeptide shell. It is associated with the inner membrane of the mitochondria in most plant and animal cells [263, 264]. Although, Cyt *c* extracted from various organisms differ in the composition of the polypeptide shell, all of them possess identical porphyrin rings. Its primary function is associated with the electron transport chain and it transports electrons by the oxidation and reduction of the iron ion (Fe²⁺ or Fe³⁺) present in the porphyrin ring [264].

Recently, researchers showed that Cyt *c* is also associated with the apoptosis pathway in cells [264]. In general, under normal physiological conditions Cyt *c* is not present in the cytosol of the cell. However on induction of apoptosis, Cyt *c* is released from the inner mitochondrial membrane into the cytosol and its presence in the cytosol disrupts normal physiological behavior.

The absorption spectrum of Cyt *c* is similar to the spectrum of hemoglobin and shows two distinct absorption states [263]. In Cyt *c* the two absorption states are associated with the reduced and oxidized state of the iron ion, contrasting from hemoglobin where the two states occur due to the presence and absence of oxygen. A typical absorption spectrum of reduced (Fe²⁺) and oxidized (Fe³⁺) Cyt *c* is shown in Fig. 2.6(b). The peak observed near 400 nm for both cases correspond to the Soret band whereas the peaks close to 550 nm are the Q-bands (520 nm and 550 nm for reduced Cyt *c* and 530 nm for oxidized Cyt *c*). Even though the Soret bands of Cyt *c* exhibit higher net absorption as compared to the Q bands, the change is more drastic in case of the Q-bands between the two states. Reducing agents like ascorbic acid (AA) convert oxidized Cyt *c* into reduced Cyt *c* and oxidizing agents like hydrogen peroxide (H₂O₂) transform reduced Cyt *c* to the oxidized state (see Fig. 2.6(a)). Figure 2.6(c) shows the time trace of absorption of Cyt *c* solution at 550 nm after the addition of ascorbic acid and H₂O₂. Prior to the addition of AA, the absorption remains constant and it starts increasing on the addition of AA. The absorption reaches a plateau at 750 s indicating that all the Cyt *c* available

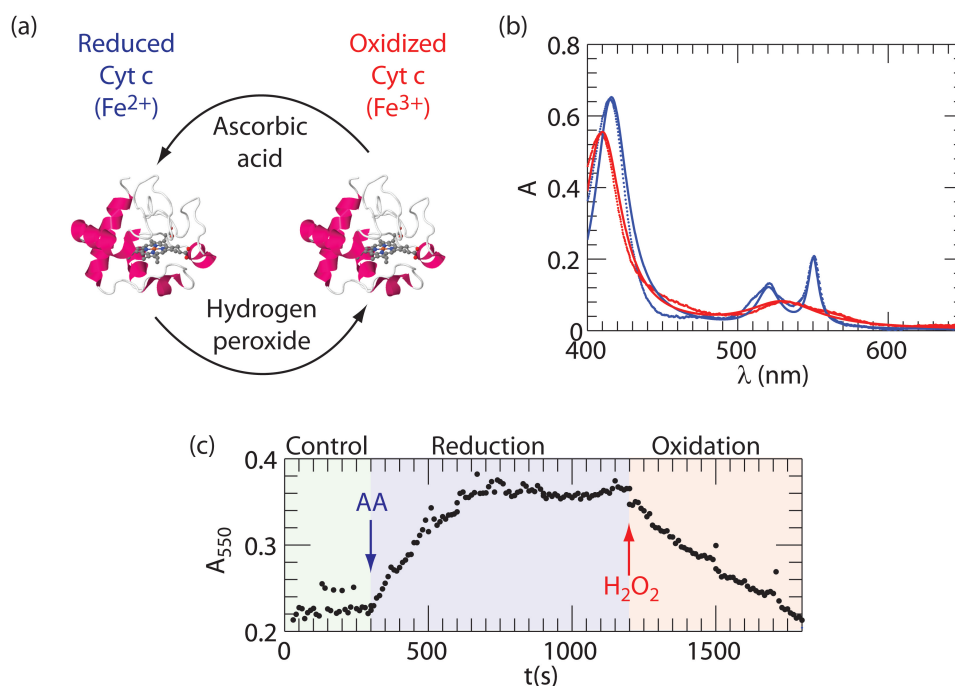


Figure 2.6: **Redox state dependent optical absorption of Cyt *c*.** (a) Schematic diagram illustrating the change of state of Cyt *c* by hydrogen peroxide and ascorbic acid. (b) Experimentally measured (dots) and theoretically calculated absorption spectra of 400 μM Cyt *c* solution in the reduced (blue) and oxidized (red) states. The thickness of the Cyt *c* solution is 80 μm . (c) Time trace of the absorption at 550 nm for a 40 μM solution of Cyt *c* showing reduction and oxidation on the addition of 1 μL AA (added at 300 s; $C = 2 \cdot 10^{-4}$ g/mL) and 2 μL H₂O₂ (added at 1200 s; $C = 270$ μM), respectively.

has been reduced. Subsequently, after the addition of H₂O₂, which converts the reduced Cyt *c* back into the oxidized form, a decrease in the absorption at 550 nm is observed. The reversibility in the absorption spectra between the reduced and the oxidized states by reaction with H₂O₂ makes it an ideal candidate for detection of species like H₂O₂ and other oxidative species using optical interrogation [258]. Furthermore, this kind of optical sensor can also be used for detection of other species via coupling to the requisite enzyme. For example, glucose can be detected by addition of the enzyme glucose oxidase to the Cyt *c* solution [265]. Glucose oxidase converts glucose to D-glucono- δ -lactone and in the process generates H₂O₂, which can then be detected using the optical spectrum of Cyt *c*.

2.3.2 Theoretical formulation

Dielectric constant of Cyt *c*

In the previous section, I briefly explained the main features of the electronic absorption spectra of Cyt *c*. To theoretically analyze the response of Cyt *c* in the vicinity of a AuNP it is necessary to obtain the dielectric function mimicking the response of Cyt *c*. It should be

mentioned here that the concept of dielectric constant is generally applied to macroscopic materials but it can still lead to a semi-quantitative idea of the enhancement factors in the case of isolated molecules or few thousands of molecules.

$$\epsilon_\alpha = \epsilon_w + \frac{\nu_{p1}^2}{\nu_{01}^2 - \nu^2 - i\gamma_{01}\nu} + \frac{\nu_{p2}^2}{\nu_{02}^2 - \nu^2 - i\gamma_{02}\nu} + \frac{\nu_{p3}^2}{\nu_{03}^2 - \nu^2 - i\gamma_{03}\nu}, \quad (2.6)$$

where α is either *red* or *oxi* which stands for reduced or oxidized Cyt *c*. ν_{pq} , ν_{0q} , and γ_{0q} ($q = 1, 2, 3$) are the resonance strength, frequency and width, respectively. The dielectric function of Cyt *c* is modeled using the sum of three lorentzians as given by Eq. (2.6). The first resonance corresponds to the Soret band whereas the other two correspond to the Q-bands of Cyt *c* [263]. The various parameters are extracted as follows. The absorption spectra for a given thickness and concentration of Cyt *c* layer is matched with the theoretically calculated absorption using the transfer matrix formalism [260]. Such a matching allows for the extraction of the various parameters of the dielectric constant. Table 2.2 shows the parameters extracted for 50 mM oxidized and reduced Cyt *c*. As an example, Fig. 2.6(b) shows both the theoretically calculated and experimentally measured absorption spectra for both oxidized and reduced Cyt *c*. It is found that only the oscillator strengths depend on the concentration and all the other parameters are independent of the concentration of Cyt *c* (parameters corresponding to the other concentrations are presented in the appendix B.2). Physically this signifies minimal molecule-molecule interaction in the concentration range of interest.

State	ν_{p1} (THz)	ν_{p2} (THz)	ν_{p3} (THz)	γ_{01} (THz)	γ_{02} (THz)	γ_{03} (THz)
Reduced	12.2	14.1	57.5	8	20	35
Oxidized	20.5	-	58.75	60	-	45

Table 2.2: Parameters of Eq. (2.6) corresponding 50 mM solution of reduced and oxidized Cyt *c*.

Green's tensor approach

The response of a system composed to a single AuNP and a Cyt *c* molecule is investigated using the Green's tensor approach [266]. Both the molecule and the nanoparticle are modeled classically and each is assumed to be represented by a single dipole. Briefly, the electric field at a given dipole due to the incident field and all the other dipoles present in the system can be expressed as,

$$\mathbf{E}_i = \mathbf{E}_i^0 + \sum_{j=1, j \neq i}^n \mathbf{G}_{ij} \cdot k_0^2 \Delta \epsilon_j V_j \mathbf{E}_j + \mathbf{M}_i \cdot \Delta \epsilon_i k_0^2 \mathbf{E}_i - \mathbf{L}_i \cdot \frac{\Delta \epsilon_i}{\epsilon_B} \mathbf{E}_i, \quad (2.7)$$

Chapter 2. Plasmon modified absorption of molecules

where \mathbf{G}_{ij} is the background Green's tensor at the dipole i due to the dipole j , \mathbf{M}_i is the self induced field of dipole i , \mathbf{L}_i is the depolarization term, $\Delta\epsilon_j (= \epsilon_j - \epsilon_B)$ is the dielectric constant contrast, k_0 is the wave vector in free space and ϵ_B is the dielectric constant of the background. The dielectric function of gold is modeled using Johnson and Christy data [259]. For Cyt c , I use the dielectric function described by Eq. (2.6) with the parameters corresponding to 50 mM Cyt c solution. Furthermore, the diameter of Cyt c is fixed to be 3.4 nm which corresponds closely to its physical diameter [262]. The concentration of 50 mM is chosen since it assigns one molecule of Cyt c to the requisite volume, sphere with a diameter of 3.4 nm. This set of equations can be solved self-consistently and the total electric field at each dipole computed. The electric fields at all other observation points is computed by

$$\mathbf{E}_o = \mathbf{E}_o^0 + \sum_{1 \leq j \leq n} \mathbf{G}_{oj} V_j k_0^2 \Delta\epsilon_j \cdot \mathbf{E}_j, \quad (2.8)$$

where the subscript o stands for the observation point. The scattering cross section (C_{sca}) are computed by integrating the field intensities at observation points on a sphere with a radius of 10 μm [267]. The absorption spectra (C_{abs}) are calculated using ohmic losses [267]. It should be noted that while scattering can only be computed for the whole system, no such restriction is present in case of absorption.

Mie theory for coated spheres

Generalized Mie theory is used for computing the response of Cyt c coated AuNPs [268]. The use of generalized Mie theory allows us to better mimic the realistic system where the gold particles are coated with a layer of Cyt c . As in the previous section, the dielectric function of Cyt c computed using Eq. (2.6) with 50 mM equivalent concentration and Johnson and Christy data is used for gold in all the simulations [259].

2.3.3 Experimental methods

Chemicals

Auric chloride ($\text{HAuCl}_4 \cdot 3\text{H}_2\text{O}$), ascorbic acid (AA), mercapto propanoic acid (MPA), hydrogen peroxide (H_2O_2), 4-(2-hydroxyethyl)-1-piperazineethanesulfonic acid (HEPES), bovine heart Cyt c and microperoxidase 11 (MP11) are purchased from Sigma-Aldrich. Phosphate buffer saline pH 7.2 (PBS) is acquired from Gibco®Life Technologies.

Chemical synthesis of cytochrome c coated nanoparticles

Two different approaches are used for the synthesis of Cyt c coated AuNPs. The first approach is based on replacing the citrate molecules used for stabilizing the pre-synthesized AuNPs with Cyt c molecules in solution. However, due to the opposite polarity of AuNPs (negatively charged) and Cyt c (positively charged at pH 7.2), this process of ligand exchange induced

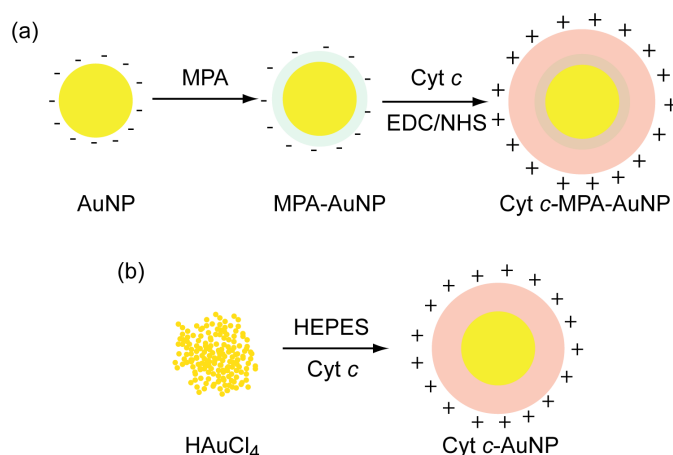


Figure 2.7: **Chemical synthesis of Cyt *c* coated gold nanoparticles.** (a) Synthesis via ligand exchange of Cyt *c* molecules to pre-synthesized citrate stabilized nanoparticles. (b) Single step synthesis of Cyt *c* AuNPs using HEPES as a reducing agent and Cyt *c* as a capping agent.

aggregation of nanoparticles and stable colloidal particles could not be synthesized.

In the second approach, a single step synthesis of AuNPs stabilized by Cyt *c* is performed. Briefly, 5 μ L of 0.1 M H₂AuCl₄ is added to 1 mL of PBS (pH 7.2) and the solution vortexed for 10 s. Next, 5 μ L of 1 M HEPES and a given volume (5 μ L, 10 μ L or 20 μ L) of 400 μ M Cyt *c* are added sequentially. The mixture is then vortexed again for 5 s and incubated at room temperature for 1 h to facilitate nanoparticle synthesis. The color of the solution turns from pale yellow (before the addition of HEPES and Cyt *c*) to dark red (1 h after the addition of HEPES and Cyt *c*). In this chemical synthesis HEPES acts as the reducer and Cyt *c* as the capping agent [269, 270]. To verify that HEPES does not act as the capping agent, I performed analogous experiments without adding Cyt *c*. All the syntheses carried out in the absence of Cyt *c* resulted in the formation of aggregated particles signified by the typical bluish black color. Even though direct single step synthesis of Cyt *c* has not been reported, synthesis where peptide sequences act as capping agents are quite well known and studied [270]. Furthermore, the particles synthesized in the absence of Cyt *c* sedimented rapidly within 1 h. After 1 h, the nanoparticle suspension is centrifuged twice at 2000 rpm to remove any large aggregates. Next, the supernatant is centrifuged twice at 10000 rpm for 1 h to collect the nanoparticles. The nanoparticle pellet is re-suspended in PBS (pH 7.2) after each centrifugation step. The centrifuged nanoparticle solution is stored at 4°C.

STEM characterization

The core diameter of the synthesized nanoparticles is analyzed using STEM (FEI Nova 600 Nanolab, dualbeam). The samples for observation are prepared by drop casting 30 μ L of the as-prepared nanoparticles on formvar coated TEM grids. Acquired STEM images are analyzed using the software ImageJ (v. 1.44p). Particle size histogram for each sample is created by

measuring the size of 100-150 particles from the STEM images.

Optical measurements

The extinction spectrum of the synthesized AuNPs is analyzed using a home built extinction setup. The sample placed on a inverted microscope (Olympus IX 71) is illuminated with a halogen light source and the transmitted light collected using a 20X objective (0.3 NA) and analyzed using a spectrometer (Horiba Triax 550). The raw experimental data is normalized with respect to the lamp to obtain the normalized transmission.

SERS signals are measured using an inverted microscope coupled to a He-Ne laser ($\lambda = 633$ nm) using an oil immersion objective (Olympus 60X, 1.4 NA) and further details of the setup are presented by Lovera [271]. The scattered light is collected using the same objective and analyzed using a air cooled spectrometer (Andor Shamrock). Laser powers between 1 and 5 mW are used in all the experiments and the focus spot of the laser has an area of around $40 \mu\text{m}^2$.

2.3.4 Interaction of single gold nanoparticle and a cytochrome *c* molecule

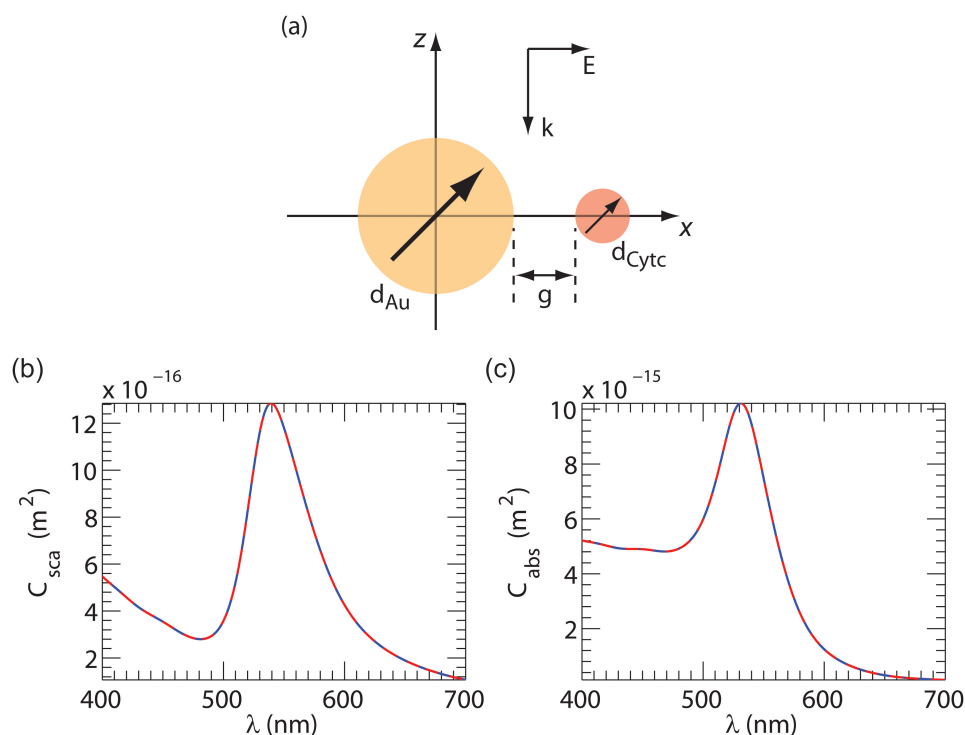


Figure 2.8: **Scattering and absorption spectra of a AuNP-Cyt *c* system.** (a) Schematic of a AuNP-Cyt *c* system with the various critical geometrical parameters. (b) Scattering and (c) absorption spectra of the Cyt *c* - AuNP system for reduced (blue) and oxidized (red) Cyt *c*. The gold nanoparticle and Cyt *c* size are fixed at 50 nm and 3.4 nm, respectively.

Let us consider a system composed of a single AuNP and a Cyt *c* molecule separated by a gap, g , as shown in Fig. 2.8(a). Let this system be illuminated by a plane wave propagating in the $-z$ direction and polarized along x axis. This illumination condition is chosen to facilitate the strongest overlap of the optical near-field of AuNP at the plasmon resonance wavelength with the molecular dipole [18, 166]. The scattering and absorption spectra of the AuNP-reduced Cyt *c* (rCyt *c*-AuNP) and AuNP-oxidized Cyt *c* (oCyt *c*-AuNP) systems for $g = 0$ nm are shown in Fig. 2.8(b) and (c), respectively. In these simulations, the size of the gold nanoparticle is fixed at 50 nm. The peak observed at around 530 nm in the spectra corresponds to the excitation of the plasmon resonance of the AuNP [272]. Note that a small shift exists between the absorption resonance wavelength ($\lambda_{peak} = 530$ nm) and the scattering resonance wavelength ($\lambda_{peak} = 540$ nm). This shift occurs due to the finite damping of the plasmon resonance and has been studied previously [273, 274]. However, no visible difference is observed between the two systems (rCyt *c*-AuNP and oCyt *c*-AuNP) especially close to either the *Q*-band wavelength or the Soret band wavelengths of Cyt *c*. The absence of visible modulation in the spectra of AuNP due to a single Cyt *c* clearly indicates the low dipole strength of Cyt *c*. Recall that past studies have shown that even the presence of single atom/molecule close to an optical resonator, with high Q , can strongly modify the resonance features of the resonator [275]. In our system, the inherent low Q of the plasmonic resonance as well as the low oscillator strength of the molecule prevents us from seeing a noticeable effect in a single molecule-resonator system.

Therefore, as a first step towards studying the absorption enhancement of Cyt *c*, I monitored the absorption of the Cyt *c* molecule as opposed to the total absorption of the system. Additionally, one of the parameters that has a strong effect on any absorption enhancement or energy transfer process is the separation distance, in this case g , between the acceptor and the donor [276–278]. Figure 2.9(a) shows the absorption of a reduced Cyt *c* molecule in the rCyt *c*-AuNP for gaps between 0 and 40 nm. As the gap between the AuNP and Cyt *c* molecule is reduced, a strong increase in the absorption is observed. In particular, when the molecule is placed directly on the surface of the AuNP, i.e. $g = 0$ nm, the absorption of reduced Cyt *c* is enhanced by a factor of almost 30 (at $\lambda = 550$ nm). Another interesting observation is that the enhancement is spectrally non-uniform. The enhancement factors for the other relevant wavelengths are 7.7 (at 416 nm) and 22 (at 520 nm). Furthermore, for a separation distance smaller than 6 nm, the *Q*-band at 550 nm exhibits higher absorption than the Soret band at 416 nm, as shown in Fig. 2.9(b). The highest enhancement is seen for the band at 550 nm due to its spectral vicinity to the near-field resonance of the gold particle. Analogously, in case of an oxidized Cyt *c* molecule placed close to a AuNP, a similar absorption enhancement is seen (Fig. 2.9(c) and (d)). The absorption enhancement factors for the *Q*-band and the Soret bands are 33.5 (at $\lambda = 530$ nm) and 7.6 ($\lambda = 410$ nm).

The spectral non-uniformity in the enhancement arises because of the Lorentzian line shape of the plasmon resonance. More specifically, the enhancement in the absorption occurs because of the high near-field around the AuNP at the plasmon resonance. The near-field spectrum exhibits a line shape similar to the scattering spectrum in this particular case. Furthermore,

the near-field decays rapidly as the distance between the observation point and the AuNP surface is increased. In a similar trend, the absorption at the Q-bands also falls rapidly as the gap, g , is increased (Fig. 2.9(b) and (d)). Such spectrally dependent enhancements as well as distance based reduction in enhancement have also been reported in fluorescent systems previously [38, 40, 279]. However, in contrast to our case where the maximum enhancement occurs for $g = 0$ nm, in fluorescence the maximum enhancement is observed for a finite non-zero value of g [280]. It is also evident from Fig. 2.9(c) that the peak position of the Q-band of oxidized Cyt c in oCyt c -AuNP is spectrally shifted by nearly 10 nm as compared with the absorption band of an isolated oxidized Cyt c molecule (Q-band is at 530 nm). This possibly also occurs due to the Lorentzian line shape of the plasmon resonance and such shifts are more evident in case of resonances with higher damping [274]. On a different note, it is also seen that the absorption of the Cyt c molecule is 3 orders of magnitude lower than the absorption of the whole system (Fig. 2.8 (c) and Fig. 2.9(a)), making it clear why the signature of a single molecule is not seen in the spectrum of the complete system.

Even though it is clear that an enhancement in the absorption of Cyt c does indeed occur, it is not feasible to measure the absorption of just the Cyt c molecule in the Cyt c -AuNP system. In order to circumvent this limitation, I make use of the differential signal exploiting the fact that the plasmon resonance does not show a significant change between rCyt c -AuNP and oCyt c -AuNP systems. I define the differential scattering and absorption as follows:

$$\Delta C_{sca} = C_{sca}(f_r = 1) - C_{sca}(f_r = 0), \quad (2.9)$$

and

$$\Delta C_{abs} = C_{abs}(f_r = 1) - C_{abs}(f_r = 0), \quad (2.10)$$

where $f_r = 1$ and $f_r = 0$ correspond to rCyt c -AuNP and oCyt c -AuNP systems, respectively. Note that C_{abs} and C_{sca} are the absorption and scattering of the complete system. Figure 2.10 shows the differential scattering and absorption spectra for gaps of 0 and 1000 nm. It is clear that for $g = 0$ nm, the differential scattering and absorption signals near the Q-bands are enhanced by a factor of nearly 1000 and 20 around $\lambda = 550$ nm, respectively. Considering the differential scattering spectra first, I see that for a very large gap, $g = 1000$ nm, the signal close to the Q-bands (500-600 nm) mimics the real part of the dielectric function of Cyt c (see appendix B.2). However for $g = 0$ nm, the spectral profile changes and a prominent dip close to 550 nm is observed. The modification close to the Soret band is not as drastic. Comparing the modulation of the ΔC_{sca} signal in the Q-band spectra region for the two cases ($g = 0$ nm and $g = 1000$ nm) an enhancement of $3.5 \cdot 10^3$ is observed. The Soret band on the other hand exhibits an enhancement of $1.8 \cdot 10^3$. On the other hand, the differential absorption spectrum for a large separation ($g = 1000$ nm) shows a line shape which is nearly the sum of two Lorentzians close to the Q-bands. However, on decreasing the distance, the

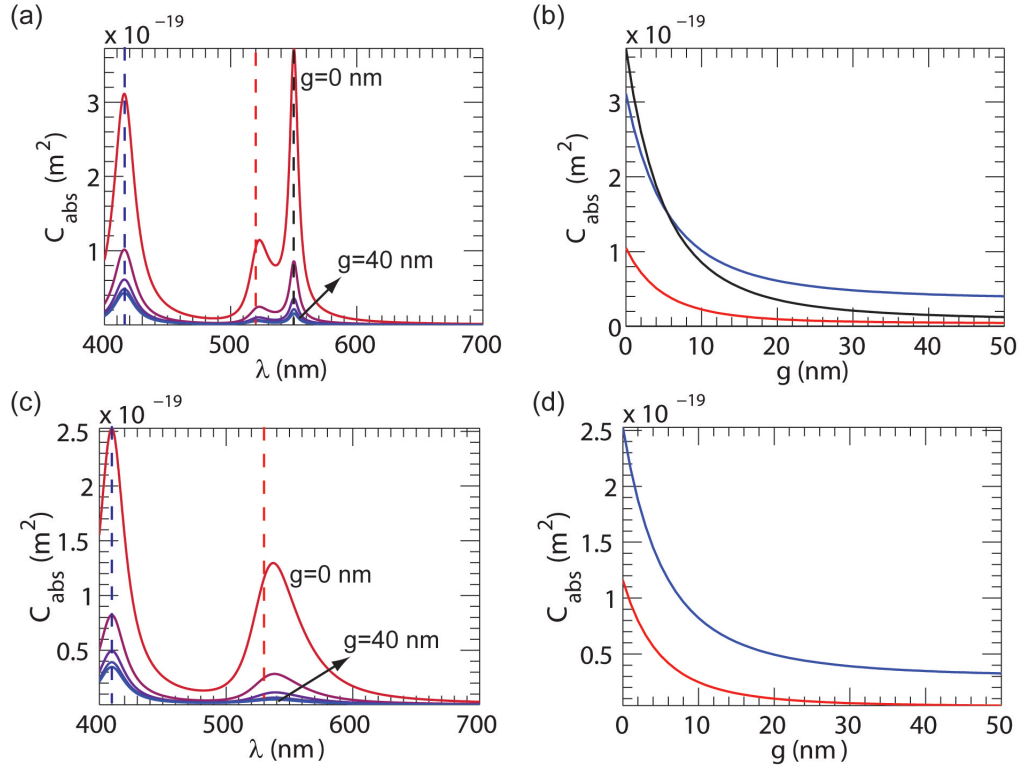


Figure 2.9: **Distance dependence of absorption enhancement of Cyt *c*.** Absorption spectra of (a) reduced and (c) oxidized Cyt *c* for various separation distances between the gold nanoparticle and Cyt *c* molecule. The trace of the absorption intensity of the Cyt *c* molecule at the Soret and Q-bands of (b) reduced and (d) oxidized Cyt *c* as a function of distance. The gold nanoparticle and Cyt *c* size is fixed at 50 nm and 3.4 nm, respectively. The Q-bands of isolated reduced Cyt *c* are at 520 nm and 550 nm (red and black lines in (b); wavelengths indicated by red and black dashed lines in (a)). The Q-band of isolated oxidized Cyt *c* is at 530 nm (red line in (d); wavelength indicated by a red dashed line in (c)). The Soret bands of reduced and oxidized Cyt *c* are at 416 nm and 410 nm, respectively (blue lines in (b) and (d); blue dashed lines in (a) and (c)).

differential absorption spectrum gains a distinct asymmetric line shape near the Q-bands due to the selective spectral enhancement in both the oxidized and reduced states of Cyt *c*. The asymmetry in the differential signal is further accentuated by the spectral shift of Q-band of oxidized Cyt *c* at small separation distances. For a gap of 0 nm, the Q-band at 550 nm shows a stronger modulation as compared to the Soret band, similar to the behavior observed earlier. This trend reverses itself for larger separations, i.e. $g=1000$ nm, where the Soret band is dominant. The relative enhancements in the modulation of the differential absorption signal close to the Q-band and the Soret band are 40.5 and 5.7, respectively.

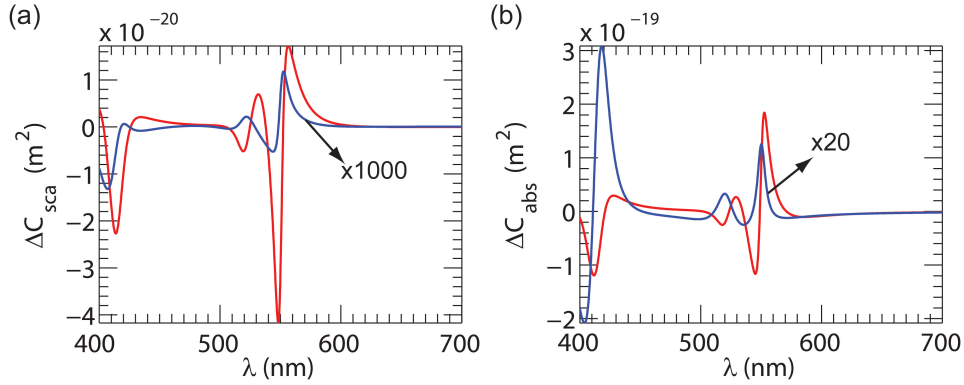


Figure 2.10: **Differential scattering and absorption spectra for a gold-Cyt *c* system and an isolated Cyt *c* molecule.** (a) The differential scattering and (b) differential absorption spectrum for a Cyt *c*-AuNP system (red, $g=0$ nm) and for a single Cyt *c* molecule (blue). The gold nanoparticle size and Cyt *c* molecule size are fixed at 50 nm and 3.4 nm, respectively.

2.3.5 Effect of a layer of Cyt *c* on a gold nanoparticle

In the previous section, I investigated a system composed of a single gold nanoparticle and a Cyt *c* molecule. However, realization and experimental measurements on such systems are very difficult and often impractical from the point of view of applications. What is more feasible is a system made up of a Cyt *c* coated gold nanoparticle. Similar structures albeit with other molecules have been studied extensively in the past few decades [166, 167, 281]. Due to the spherical symmetry of this system, generalized Mie theory is an ideal candidate for investigating its optical characteristics [268]. The structure is placed in water ($\epsilon_B = 1.7689$) and illuminated with a plane wave and the various optical properties are analyzed as a function of the relevant parameters. The main geometrical parameters are the gold core size (d_{Au}) and the Cyt *c* shell thickness ($t_{Cyt c}$). Recall that a monolayer of Cyt *c* has a thickness of 3.4 nm [262].

Figure 2.11(a) and (b) shows the color maps of normalized scattering and absorption as a function of wavelength and gold core size, d_{Au} , for a rCyt *c*-AuNP system (the Cyt *c* is in the reduced state). The reduced state of Cyt *c* is chosen since it exhibits the highest absorption amongst the two oxidation states. Normalized spectrum is used to track the change in the peak position as well as check whether the presence of the Cyt *c* shell shows up in the spectra of the complete system. As expected, a red shift is seen for the resonance wavelengths of both the scattering and absorption spectra on increasing the particle size. However, even in this case a strong modulation in the absorption or scattering spectra is not visible.

Again I employ the differential scattering and absorption, defined by Eq. (2.9) and Eq. (2.10), to study the absorption and scattering enhancement. The differential spectra as a function of gold core size are depicted in Fig. 2.11(c) and (d). In case of differential scattering and absorption signals an optimal size for the maximum modulation is seen. In case of the differential scattering the optimum is at 106 nm (shown in the appendix Sec. B.3) whereas for the differential absorption the optimal diameter is 68 nm. For core diameters larger than this

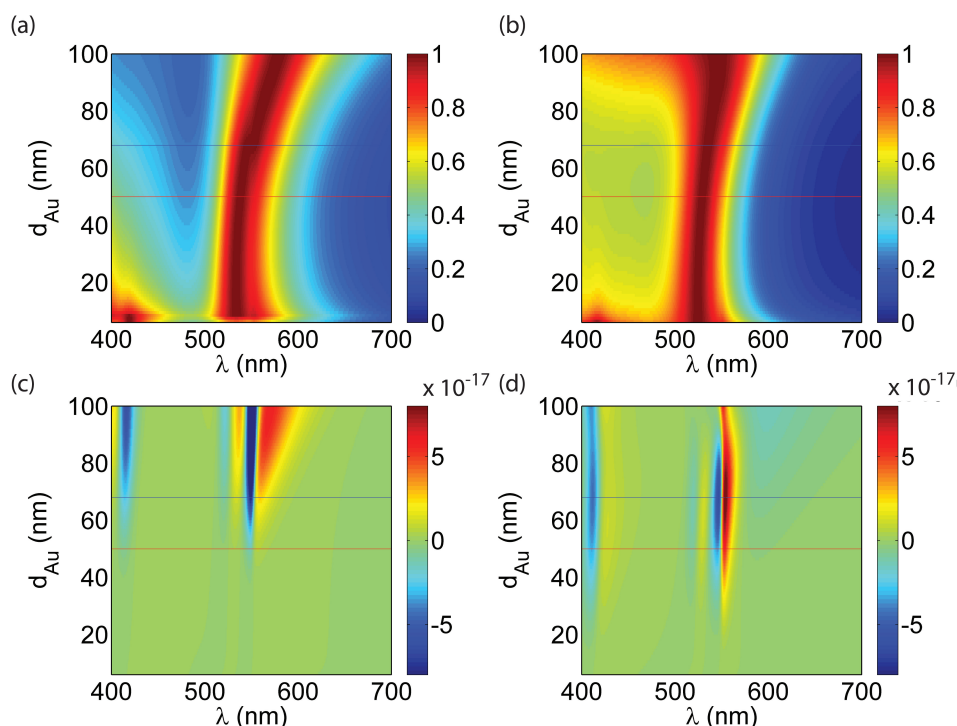


Figure 2.11: **Effect of modification of gold core size on the scattering and absorption spectra.** (a) Normalized scattering, (b) normalized absorption, (c) differential scattering and (d) differential absorption spectra of Cyt *c* coated gold nanoparticle for different values of the gold core size. For calculating the normalized scattering and absorption spectra, the Cyt *c* layer is taken to be in a fully reduced state. The thickness of the Cyt *c* layer is fixed at 3.4 nm. The red and blue lines indicate the core sizes of 50 nm and 68 nm, respectively.

value, the differential absorption reduces. The optimal values of the radius exist because of the intrinsic nature of resonant enhancement. For example, the resonant enhancement is governed by both the spectral overlap between the two oscillators as well as the resonance strength of each. In our case, as the size of the gold core is increased the dipolar plasmon resonance of the core-shell particle red shifts. For a gold core of 10 nm, the plasmon resonance in scattering is located at around 525 nm, which shifts to 550 nm on increasing the size to 68 nm. Further increase in size red shifts the plasmon resonance further. Therefore, an optimal size exists for the best match between the plasmon resonance and the Cyt *c* absorption band. If the size is increased further, a case exists in which the higher order quadrupolar mode can spectrally overlap with the absorption bands of Cyt *c*. Even in this case an optimal size corresponding to the maximum differential modulation can be determined (shown in the Appendix B.3). Another point that is evident is the shift in the optimal values of the radius for obtaining the maximum differential absorption and scattering signals. This is probably due to the intrinsic redshift of the near field of the plasmon resonance as compared to its far field response [274]. It must be mentioned here that as the size of the nanoparticle is increased, the number of Cyt *c* molecules coating the surface also increases. However, since this increase

is monotonic with the size, the differential spectra (absorption or scattering) normalized to the number of molecules show a behavior similar to the one seen in Fig. 2.11 (c) and (d). I have retained the non normalized spectra as this is what is obtained from experimental measurements.

Let us now consider two specific cases: $d_{Au} = 50$ nm (same as in Sec. 2.3.4) and $d_{Au} = 68$ nm (showing the maximum differential absorption signal). Figure 2.12 shows the various spectra for both of these cases. The scattering and absorption spectra for rCyt *c*-AuNP and oCyt *c*-AuNP systems do not show significant differences. However, a small modulation (dip) close to 550 nm is visible in the spectrum of rCyt *c*-AuNP with $d_{Au} = 68$ nm. Since absorption is additive, i.e. the absorption of the total system is the sum of the absorption of the individual components, no such modulation (dip) is seen. Thus, in case of absorption it is expected that the presence of the absorption layer should show up as a peak. Note that this current work is very similar to the work presented earlier by the group of L. Lee [256,257], where they studied a similar system of Cyt *c* placed close to gold nanoparticles. However, unlike their work where a very strong modulation in the scattering spectrum was observed, the modulation observed in our system is very small. This could possibly be due to the differences in the number of Cyt *c* molecules close to the AuNP. Another point is that, the small modulation (dip) in the scattering spectrum of the gold particle is very similar to those observed in case of surface enhanced infrared absorption (SEIRA), where the infrared absorption bands show up as modulations in the infrared spectrum of the plasmonic antenna [282].

Figure 2.12 (c) and (d) shows the differential scattering and absorption spectra for the two cases. As shown previously in case of a single molecule, the differential scattering signal shows a prominent dip close to 550 nm. The differential absorption spectra on the other hand exhibits an asymmetric line shape centered around 550 nm. In case of the differential scattering spectrum for the gold core size of 68 nm, enhancements of $2.8 \cdot 10^4$ and $3.61 \cdot 10^3$ are observed in the modulation of the spectra close to the *Q*-band and the Soret band, respectively. The enhancements are computed with respect to the differential scattering signal from a hollow core ($\epsilon_B = 1.768$)-Cyt *c* shell particle. In a similar manner, enhancements of 9.9 and 1.03 are seen in case of the differential absorption signal close to the *Q*-bands and the Soret band, respectively, for a 68 nm gold core-shell system. Note that a certain discrepancy exists between the enhancements calculated using the Cyt *c* coated nanoparticle and the system of a single Cyt *c* molecule close to a gold nanoparticle. One of the reasons could be the non-inclusion of higher order modes in the latter, which in principle can play a strong role in governing field enhancements [40, 51, 57]. Another possible reason is the averaging effect that naturally occurs when one considers a layer of Cyt *c* around a AuNP as opposed to a single Cyt *c* molecule. For example, in Sec. 2.3.4, I placed the Cyt *c* at the location which exhibited maximum field enhancement. If the molecules are placed along the *y* axis (as opposed to their placement on *x* axis as in Sec. 2.3.4), lower enhancements are observed due to lower near fields along this axis around the AuNP [19, 283]. Another point that is clear from this analysis is that higher enhancements factors are always observed in case of the differential scattering signal as compared to the differential absorption signal. However, it is still not clear why this is

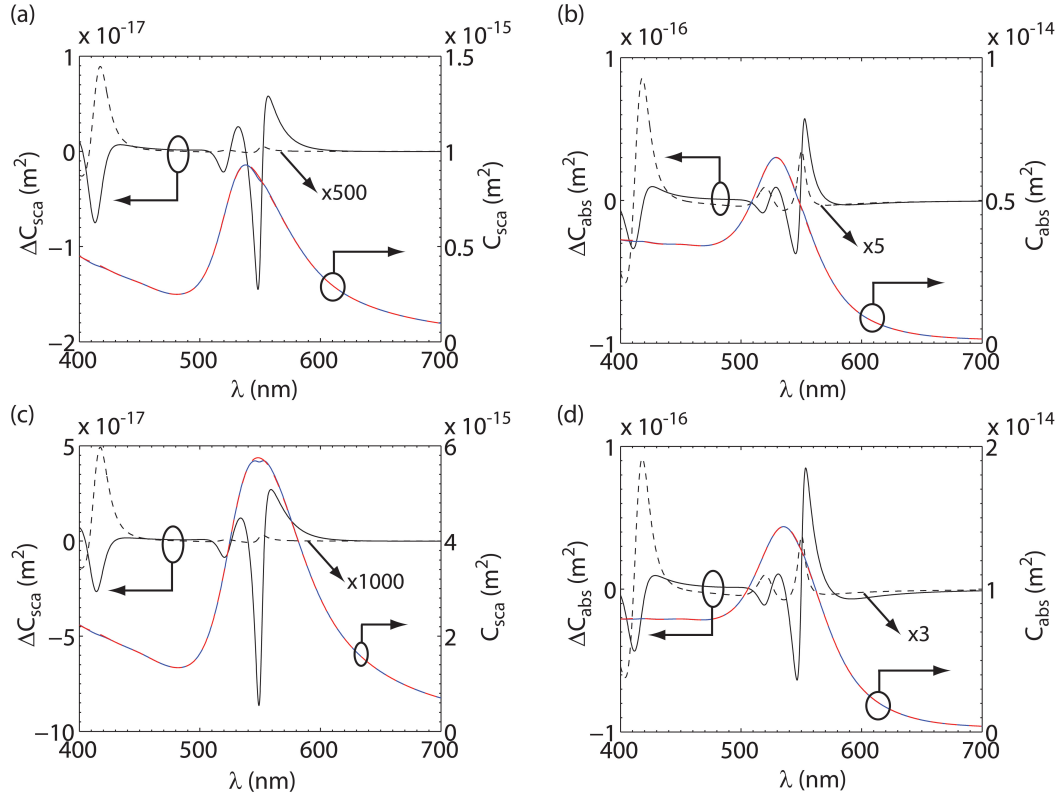


Figure 2.12: **Differential scattering and absorption for two gold core sizes: 50 nm and 68 nm.** (a) and (c) Differential scattering spectrum (black solid curve) for gold core sizes of 50 nm and 68 nm, respectively. The dashed black curves in (a) and (c) show the differential scattering spectrum for a hollow core-Cyt *c* particle with core diameters of 50 nm and 68 nm, respectively. The total scattering cross section for the two sizes, 50 nm (a) and 68 nm (c), in the reduced (blue curve) and oxidized state (red) curve are also shown. (b) and (d) Differential absorption spectrum (black solid curve) for gold core sizes of 50 nm and 68 nm, respectively. The dashed black curves in (b) and (d) show the differential absorption spectrum for a hollow core-Cyt *c* particle with core diameters of 50 nm and 68 nm, respectively. The total absorption cross section for the two sizes, 50 nm (b) and 68 nm (d), in the reduced (blue curve) and oxidized (red) states are also shown. The thickness of the Cyt *c* layer is fixed at 3.4 nm for all simulations.

so and has to be investigated further.

Let us now consider the effect of modifying the Cyt *c* shell thickness, $t_{Cyt c}$. For this analysis, I keep the diameter of the gold core fixed at 68 nm. Figure 2.13(a) and (b) shows the scattering and absorption spectra for different values of the shell thickness for the case of reduced Cyt *c* shell. The maximum shell thickness, 68 nm, corresponds to nearly 20 layers of Cyt *c* molecules. As the shell thickness is increased, the Soret band close to 416 nm becomes more prominent. Secondly, the dip associated with the Q-band (at 550 nm) in the scattering spectrum also deepens on increasing the shell thickness. In contrast, a shoulder is seen to appear in the absorption spectra close to 550 nm for large values of shell thickness ($t_{Cyt c} > 40$ nm). However,

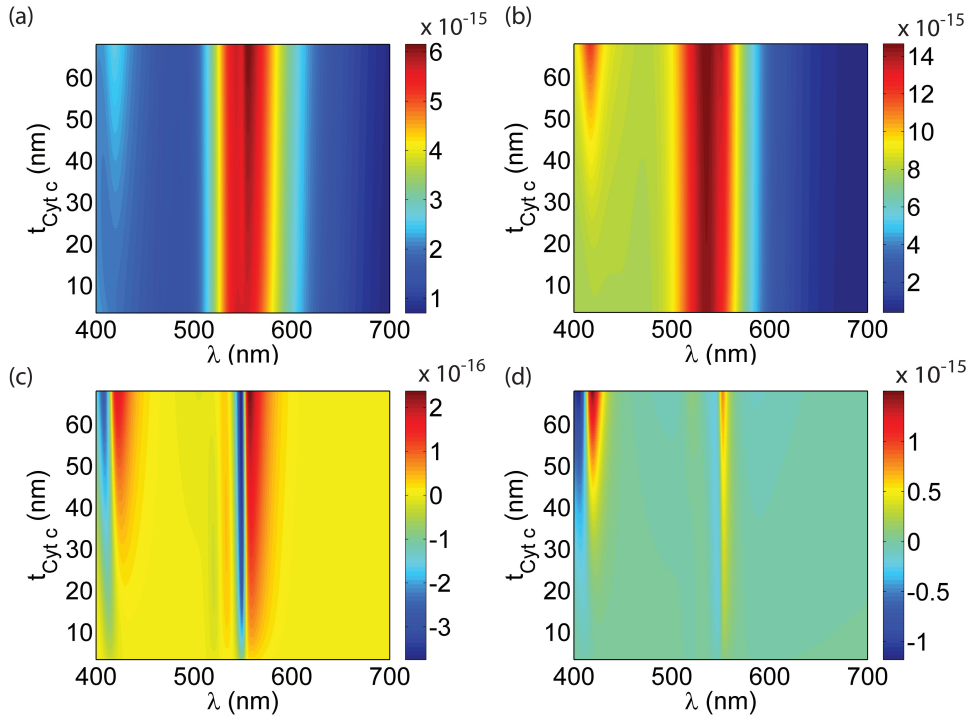


Figure 2.13: **Effect of Cyt *c* shell thickness on the optical spectra of Cyt *c* coated gold nanoparticles.** Color map of (a) scattering, (b) absorption, (c) differential scattering and (d) differential absorption as a function of wavelength and Cyt *c* shell thickness, $t_{Cyt\ c}$. Scattering and absorption in (a) and (b) are computed assuming Cyt *c* shell to be in a completely reduced state. The size of the gold core is fixed at 68 nm.

it is the differential scattering and absorption spectra that show the most prominent changes as a function of shell thickness, Fig. 2.13(c) and (d). For small shell thicknesses, the differential signals (both scattering and absorption) close to the Q-bands is higher than the signal near the Soret band. However, as the shell thickness is increased, this trend reverses, i.e. the differential signal close to the Soret band becomes higher than the signal near the Q-bands. This clearly shows that as the shell thickness is increased, the Cyt *c* molecules on the outer surface of the shell exhibit properties similar to that of isolated Cyt *c* molecules. This is because, as the distance between the gold surface and the Cyt *c* molecules on the outer layer is increased due to increase in $t_{Cyt\ c}$, the molecules feel progressively lower effects of the plasmonic near-field due to its rapid decaying nature [19, 22, 283]. Therefore, even though the modulation in the scattering signal might appear more prominent, not all the molecules are necessarily enhanced via the plasmon resonance by the same factor .

2.3.6 SERS based confirmation of Cyt *c* on the synthesized gold nanoparticles

To experimentally validate the theoretical findings presented earlier, I synthesized gold nanoparticles coated with Cyt *c* using the protocol presented in Sec. 2.3.3. Figure 2.14 shows a size

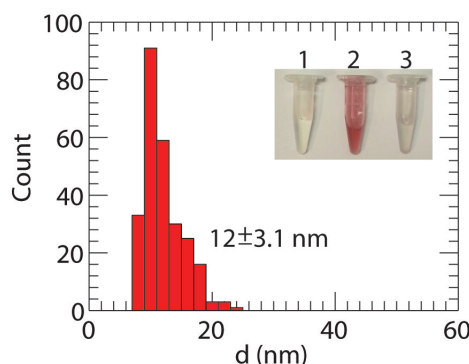


Figure 2.14: Particle size histogram of the synthesized Cyt *c* coated gold nanoparticles. The inset shows the eppendorfs with (1) 5 μL of 0.01 M HAuCl_4 dissolved in 1 mL PBS, (2) Cyt *c*-coated AuNP solution and (3) reaction product of the synthesis in absence of Cyt *c*.

histogram of the Cyt *c*-AuNP solution synthesized using this method. The particles exhibit a mean size of 12 nm. However, prior to the measurements of absorption enhancement due to excitation of plasmon resonance, it is necessary to confirm the presence of Cyt *c* on the AuNP. For this purpose, I employed SERS for detecting the presence of the Cyt *c* molecules on the particles [50, 51, 53–57, 59]. Two different samples are used for acquiring the SERS signals of molecules from the nanoparticle sample: (a) Using nanoparticle aggregates and (b) plasmonic trapping of single gold nanoparticles and subsequent SERS analysis of the trapped particles. In the first approach, the nanoparticle solution is allowed to aggregate via drying on a glass cover slip (thickness 150 μm). The exact protocol is as follows: 30 μL of the nanoparticle solution is drop cast on the cover slip and allowed to dry under ambient conditions. After 1 h, the sample is gently washed with PBS to remove the particles still in suspension and 30 μL of fresh PBS is added to the sample. The SERS from the aggregates is then measured. In the second approach, a single nanoparticle is trapped using a resonant optical nano-antenna [92, 271]. Following the trapping event, SERS originating from the coated nanoparticles are recorded.

SERS spectra acquired at various times is shown in Fig. 2.15(a). SERS spectra at two different times can exhibit quite different spectral features, as shown in Fig. 2.15(c). For example, the spectrum acquired at $t = 225$ s shows a prominent peak at 1595 cm^{-1} . However, this peak is not present in the spectrum acquired at $t = 483$ s. Similar observations can be made about the other SERS peaks. Additionally, the time trace at a fixed wavenumber also shows a similar fluctuating of the SERS intensity, Fig. 2.15(b). Therefore, a statistical analysis route must be used for extracting the Raman peaks from the data. Here, I use the analysis method developed by Margueritat *et al.* [284] to extract the necessary data. First, the Mandel Q-parameter defined as,

$$Q = -1 + \frac{\sigma_v^2}{\langle A_v \rangle}, \quad (2.11)$$

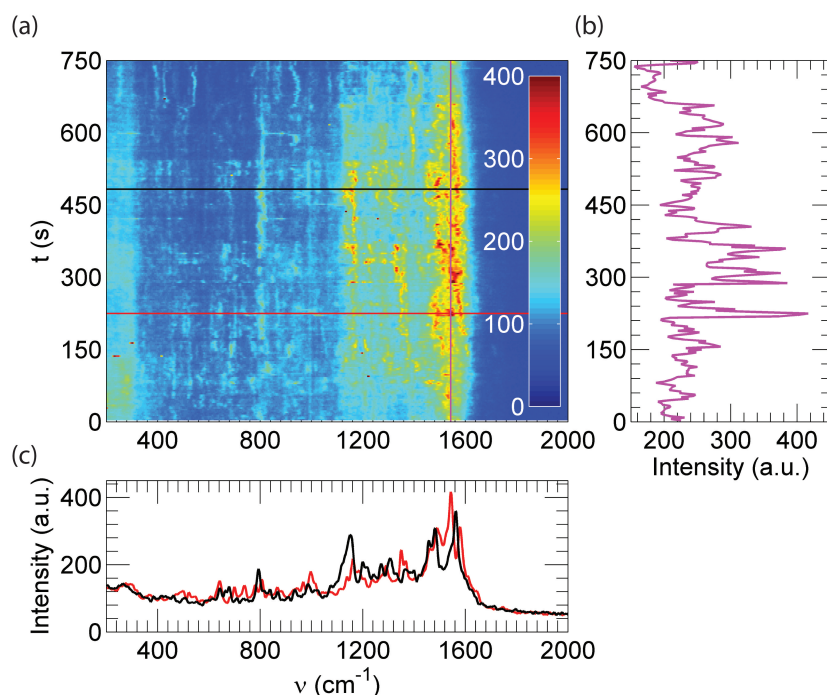


Figure 2.15: **SERS spectra from aggregates of Cyt *c* coated gold nanoparticles.** (a) SERS signal as a function of wavenumber ν and time t from nanoparticle aggregates. (b) Time trace of the SERS intensity at 1543 cm^{-1} . (c) SERS spectra from the aggregate at two different times (red - 225 s and black - 483 s). Laser power of 2 mW is used and each spectrum acquired using 3s integration time.

where σ_ν and $\langle A_\nu \rangle$ are the standard deviation and the arithmetic mean of the Raman intensity, respectively, calculated at the wavenumber ν . Note that the Mandel parameters shows the statistical fluctuations in the SERS intensity for a given wavenumber. Figure 2.16(a) shows the Mandel parameter for various wavenumbers calculated for the SERS intensities measured from the aggregate sample. It is clear that the peaks in the range of 1000 cm^{-1} show the highest value of Q parameter, indicating that the highest fluctuations occurs here. Even though from the Q parameter it is clear that multiple peaks can be identified, what is still unclear is the number of times a particular peak appears in the Raman spectrum during the whole experiment. To determine this, a histogram of the peaks is generated and analyzed, Fig. 2.16(b). The peaks extracted from these two analyses are presented in Table 2.3 and compared with the known Raman peaks of Cyt *c* and HEPES (chemicals used for nanoparticle synthesis). Seventeen peaks in total could be assigned to the Raman spectrum of Cyt *c*. Additionally, 13 other peaks are seen to match with the known Raman spectrum of HEPES.

As a further proof for the presence of Cyt *c* on the a single AuNP SERS signals from single trapped particles is also measured. These single particle trapping and SERS measurements were performed by Andrea Lovera, a colleague in the lab. Briefly, plasmonic nano-antennas (two gold rods (50 nm) separated by a small gap (20 nm)) are fabricated and used for the

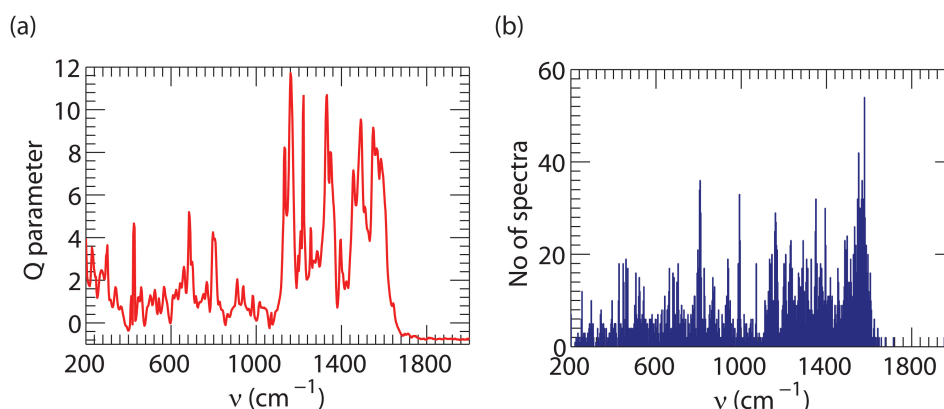


Figure 2.16: **Analysis of SERS signal from Cyt *c* gold nanoparticle aggregates.** (a) Mandel Q parameter as a function of wavenumber ν computed from the SERS intensities measured from nanoparticle aggregates. (b) Histogram of the peaks extracted from the SERS measurements. 250 spectra are used for computing the histogram and the Mandel Q parameter.

trapping experiment (schematic shown in Fig. 2.17(a)). The nano-antennas are illuminated with a laser ($\lambda = 633 \text{ nm}$) to trap the gold nanoparticles (mean size 12 nm) and subsequently measure the SERS signal [271]. Note that unlike the aggregates where the hot-spot for the SERS enhancement occurs due to the uncontrolled aggregation, in this case the hot-spot for the SERS enhancement is located between the trapped particle and the antenna walls. Furthermore, since the antennas are not functionalized with molecules, the SERS signals observed arise mainly from the molecules present on the AuNP. Figure 2.17(a) shows the SERS spectrum obtained at different times. It should be noted that the sample layer is used for trapping and SERS measurements. Initially the laser is off ($t < 10 \text{ s}$) and no SERS signal is seen. At $t = 10 \text{ s}$ the laser is switched on at low power ($P = 0.2 \text{ mW}$) a broad background is seen in the SERS spectrum, which does not fluctuate with time. However, at $t = 70 \text{ s}$ the laser power is increased to 2 mW. Subsequently at $t = 90 \text{ s}$, strong peaks in the spectrum are observed, which indicates that a trapping event has occurred. At $t = 125 \text{ s}$, laser is switched off and the signal again drops to zero. Turning on the laser again to an identical power at $t = 150 \text{ s}$ shows a broad background but the lack of any prominent peaks. This clearly shows that during the experiment, a nanoparticle is trapped, as indicated by the SERS signal, and then subsequently released. Let us now analyze the time during which the nanoparticle is trapped. Fluctuations of the SERS intensity can be seen on comparing the SERS spectra at various time points or the SERS intensity at a given wavenumber (Fig. 2.17(c) and (d)). It should be noted that in addition to the fluctuations that occur because of the motion of the molecules in solution, as in the case of aggregates, in the trapping geometry the particles can also move in the gap, which incorporates added complexity in the analysis. Therefore, even in this case, I use both the Mandel parameter and the peak histogram to study the SERS peaks. The peaks identified via this method are also presented in Table 2.3. Again, multiple peaks from both Cyt *c* and HEPES can be identified, confirming the presence of Cyt *c* on the gold nanoparticles. Note that some of the peaks extracted from the SERS measurement could not be matched with

ν (cm ⁻¹)	Molecule	Agg.	Trap	ν (cm ⁻¹)	Molecule	Agg.	Trap
425	H	x		447		x	x
460	H	x		490		x	x
502		x	x	524	C	x	x
542		x		567	C/H	x	x
609		x		624		x	
642	C	x	x	660	C	x	
684		x		700	C	x	x
717	H	x		767		x	x
803	C	x	x	826	H	x	
864		x		910	H	x	x
940	H	x	x	985	C	x	x
1017	C	x		1071		x	x
1091	C	x	x	1133	C	x	
1161	C/H	x	x	1197		x	x
1208	C	x	x	1222	H	x	x
1255	H	x	x	1272	H	x	x
1285		x		1332		x	x
1351	C	x		1362	C	x	
1397	C	x	x	1424	H	x	
1456	H	x		1490		x	x
1512		x		1525		x	x
1549	C	x	x	1567		x	x
1585	C	x	x	1622		x	x
1643	C	x	x				

Table 2.3: **Peaks extracted from the Raman spectra of Cyt *c* coated gold nanoparticles.** Peak positions of the Raman peaks extracted from the SERS measurements of the nanoparticle aggregate sample (Agg.) and via the trapping method (Trap). The table also compares the Raman peaks extracted in this work with that of Cyt *c* (labeled : C, taken from [285,286]) and HEPES (labeled : H, taken from <http://goo.gl/kcduzC>).

either the Raman peaks of Cyt *c* or HEPES. One possible origin of these peaks could be the molecules present in the PBS buffer.

2.3.7 Detection of Cyt *c* using extinction measurements

Let us now consider the extinction response of the synthesized gold nanoparticle solution. Recall that extinction (=1-transmission) is defined as the sum of scattering and absorption as per the optical theorem [268]. Figure 2.18(a) shows a representative experimentally obtained transmission spectra of the Cyt *c* coated particles both in the reduced state (blue curve) and in the oxidized state (red curve). The nanoparticle samples are prepared by adding 30 μ L of the as-prepared particles to a 374 well plate. 30 μ L of PBS is also added to make the total

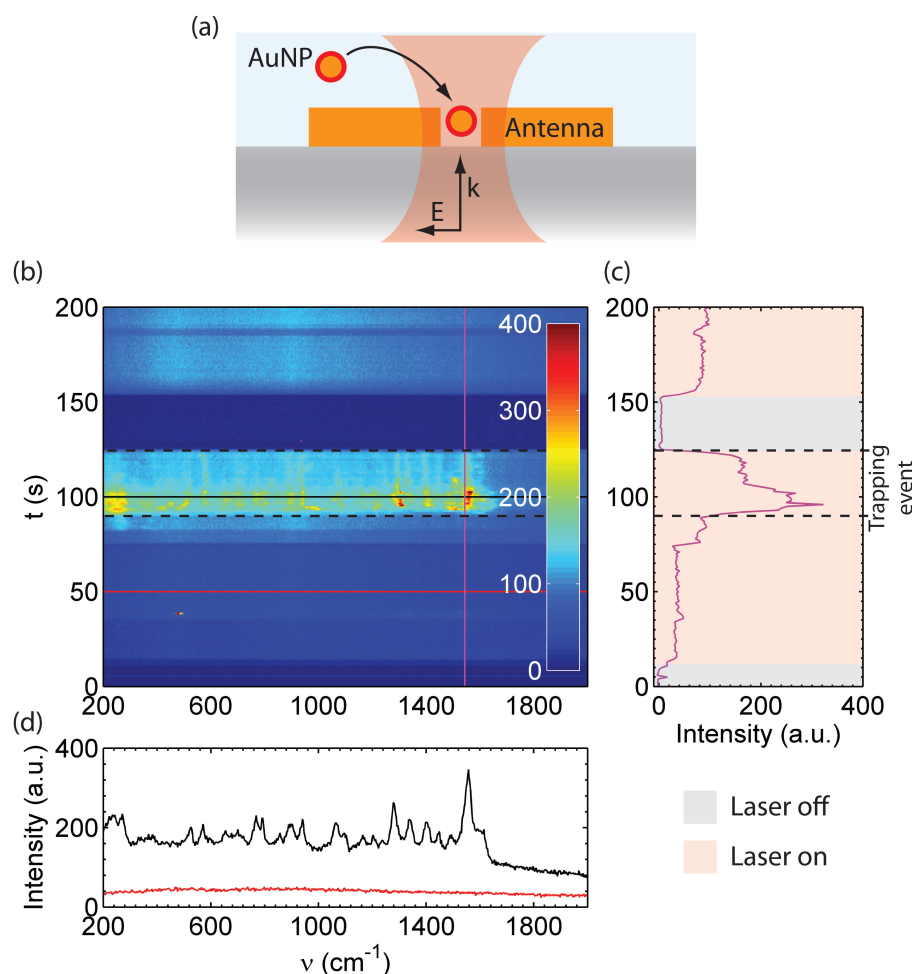


Figure 2.17: **Plasmonic trapping and SERS measurements on a single gold nanoparticle.** (a) Schematic of the trapping geometry and the laser excitation. (b) SERS signal as a function of wavenumber ν and time t from nanoparticle aggregates. (c) Time trace of the SERS intensity at 1543 cm^{-1} . (d) SERS spectra from the aggregate at two different times (red - 50 s and black - 100 s).

volume $60\text{ }\mu\text{L}$. The reduction and oxidation of the as-synthesized particles is carried out by the addition of either $10\text{ }\mu\text{L}$ of ascorbic acid ($2 \cdot 10^{-5}\text{ g/mL}$) or $10\text{ }\mu\text{L}$ of hydrogen peroxide ($8 \cdot 10^{-5}\text{ M}$) to each of the wells, respectively. The broad dip observed at 520 nm corresponds to the plasmon resonance of the gold nanoparticle. Additionally, two smaller features are observed at around 560 nm and 596 nm , respectively. Note that these two dips occur only in the transmission spectrum of the particles treated with AA, i.e. corresponds to particles coated with reduced Cyt *c*. It is well known that for small particles (gold core size smaller than 20 nm), the contribution of absorption is higher than that of scattering in total extinction spectrum. Because of the small size of the gold nanoparticles in our case the transmission spectrum exhibits more predominantly the features of absorption. Hence, an additive behavior is seen for the absorption bands of Cyt *c*, i.e. the transmission is lower for the reduced Cyt *c* particles

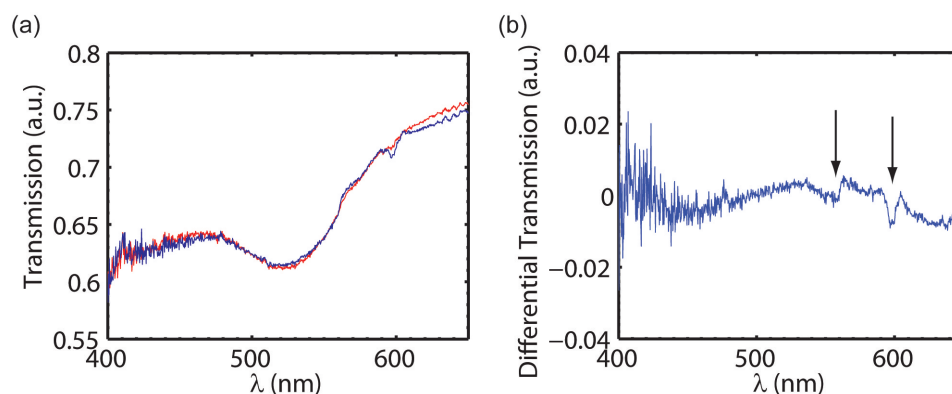


Figure 2.18: **Detection of Cyt *c* by extinction measurements.** (a) Transmission spectra of oxidized (red) and reduced (blue) Cyt *c* coated gold nanoparticles. (b) Differential transmission spectrum between the reduced and oxidized Cyt *c* coated gold nanoparticles.

as compared to the oxidized Cyt *c* particles close to 600 nm (Fig. 2.18(a)). Figure 2.18(b) shows the differential transmission spectra between the reduced and oxidized Cyt *c* coated gold particles, i.e., particles treated with AA and H_2O_2 . The differential transmission spectrum clearly reveals the presence of the two dips. As mentioned previously these peaks are located at a different wavelengths (560 and 596 nm) as compared to the resonances of native Cyt *c* (520 and 550 nm) [263]. No other major changes occur to the extinction spectrum of the sample on the addition of either AA or H_2O_2 . This is similar to the theoretical results obtained in Sec. 2.3.5 where a small modulation is also observed on changing the state of the Cyt *c* molecules. Again, the modulations observed in this study are still much smaller than the ones reported by the group of Lee [256, 257]. One possible reason for the shift in the absorption peaks of the Cyt *c* molecule present on the gold nanoparticles as compared to native Cyt *c* could be due to the interaction of the heme porphyrin ring with the gold surface. Such interactions between gold nanoparticles and resonant molecules have been shown to modify the absorption characteristics of the molecules [40]. However, this is unlikely since only small shifts are expected via this mechanism. Another possible reason could be related to the origin of absorption in the porphyrin rings. In general porphyrin rings exhibit 4 different *Q*-bands [287]. The relative spectral strengths of the various *Q*-bands is governed by the metallic ion in the porphyrin ring as well as its surrounding. It is possible that the chemical route used here for synthesis of Cyt *c* coated gold nanoparticles could somehow alter the surrounding of the propyirin ring and hence result in such a spectral modification, i.e., the *Q*-bands close to 575 nm and 600 nm are seen rather than the ones close to 520 nm and 550 nm. However, more detailed experiments have to be carried out to understand the origin of this change in the spectrum of Cyt *c* attached to gold nanoparticles. It is clear that the extinction spectrum of gold nanoparticles incubated with either AA shows a small modulation that is absent in case of gold nanoparticles treated with H_2O_2 . However, the modulation in the signal is very small and a significant number of acquisitions is necessary to acquire such a modulation. Fifty averages are necessary for obtaining modulation shown in Fig. 2.18(b). The absorption enhancement must be increased significantly before this system can be employed for sensing

of either H_2O_2 or AA. Some potential ways for enhancing the absorption further and making this system suitable for biosensing applications are discussed in Sec. 7.

2.4 Summary

In conclusion, in the first part of this chapter I have shown that strong coupling between a surface plasmon resonance and the absorption bands of metallo-proteins such as Hb is feasible. Furthermore it has been demonstrated that this strong coupling can be exploited to enhance the sensitivity of a conventional SPR sensor. Numerical simulations based on transfer matrix approach show that for a wavelength modulated sensor the resonance shift is enhanced by a factor of 3, whereas in case of angle modulated sensor the resonance shift can be enhanced by a factor of 10. Finally this sensitivity enhancement can be exploited for oxygen sensing.

In the second part of this chapter, I studied the modification of absorption of cytochrome *c* molecules placed in the vicinity of a gold nanoparticle. Theoretical calculations based on Green's tensor approach and generalized Mie theory are used to demonstrate theoretically the absorption enhancement of Cyt *c* molecules by the plasmon resonance of a gold nanoparticle. It is shown that even though an enhancement in the absorption does occur, this effect is small as compared to the spectra of the complete system. I also tried to investigate this enhancement experimentally by synthesizing gold nanoparticles coated with Cyt *c*. The presence of Cyt *c* on the gold nanoparticles is confirmed by SERS measurements. However, extinction measurements showed the presence of small modulations, at 560 nm and 596 nm, present in the spectrum of gold nanoparticles treated with AA. However, these modulations are shifted with respect to the absorption bands of native Cyt *c* molecules. Furthermore, even in the measured spectrum, the redox state dependent modulation is small making it unsuitable for use directly as a sensor of either H_2O_2 or AA. Additional enhancements to the absorption of Cyt *c* via different means could potentially lead to development of biosensors for detection of H_2O_2 or AA.

3 Human cell assisted synthesis of gold nanoparticles

In this chapter, human cell assisted synthesis of gold nanoparticle is studied. The synthesized nanoparticles are found in the intracellular as well as the extracellular regions of the cell. It is shown that the size of the synthesized nanoparticles can be tuned by modifying the concentration of the gold salt. Furthermore, proteomic analysis of the corona reveals the presence of a large number of proteins associated with various organelles in the cell. Finally, it is shown that the initial intracellular redox state can modify the size of the synthesized nanoparticles. Preliminary nanoparticle uptake experiments are also carried out to evaluate the specificity of the synthesized particles.

3.1 Introduction

Over the last decade, gold nanoparticles and their derivatives have found numerous applications in biology and medicine. The successful utilization of propagating surface plasmons for sensing has prompted the utilization of localized plasmon resonances in nanoparticles to acquire spatial information as well [13, 17, 19, 22, 79]. Furthermore, nanoparticles have been used in optical tagging [200, 288, 289], sensing [13, 17, 19, 22, 79, 290], SERS spectroscopy [53, 59], photothermal treatment of cancer [75, 77, 78] and drug delivery [218]. These numerous applications have prompted the development of various recipes for the synthesis of gold nanoparticles, with the aim of controlling their size, shape, polydispersity and surface functionalization [219, 221–225, 247, 248, 291–295]. Most recipes involve the reduction of chloroauric acid (HAuCl_4) to metallic gold using reducers like sodium citrate, sodium borohydride and ascorbic acid in the presence of capping agents to prevent aggregation [58, 296–302]. Alternative techniques for the synthesis of inorganic nanoparticles via biosynthesis routes have gained popularity in the last decade, primarily due to the enhanced biocompatibility provided by biological proteins and other molecules acting as surfactants [249–253, 303]. In the biosynthesis approach, bio-organisms such as bacteria, algae and others play the role of chemical reactors, providing the required reducing and capping agents resulting in the synthesis of stable nanoparticles. Inorganic particles of different materials such as Au, Au-Ag, CdS, Ag and TiO_2 , as well as particles of different morphologies have been synthesized using

these techniques [249–253, 303].

Recently, Anshup *et al.* used various human cell lines, cancerous and non-cancerous, to demonstrate intracellular gold nanoparticle synthesis over a period of 96 hours [254]. In that study, differences observed between the absorption spectra of nanoparticles synthesized by cancerous and non-cancerous cell lines were attributed to their different cellular metabolisms. Furthermore, it was hypothesized that the reducers responsible for converting Au^{3+} into Au^0 were different proteins present inside the cells. Later, Shamsaie *et al.* used intracellularly grown gold nanoparticles for SERS measurements in single cell [304]. Even though gold nanoparticle synthesis by human cells has been reported by these authors, the exact effect of the initial cell state is not yet clear.

In the present chapter, I demonstrate that human endothelial cells can synthesize gold nanoparticles of various sizes from HAuCl_4 . To elucidate the intracellular nature of the biosynthesis process two-photon and electron microscopy are used. Proteomic analysis performed on the protein corona of the biosynthesized nanoparticles reveals the presence of numerous proteins originating from various cellular organelles on both the intracellular and extracellular particles. In the final section of the paper, I show that the intracellular biosynthesis process is strongly dependent on the redox state of the cells prior to HAuCl_4 addition. The dependence of the particle size on the redox state is demonstrated by inducing stress in cells using two different stress-inducing agents, namely, N-acetyl cysteine (NAC) and buthionine-(S,R)-sulfoxime (BSO). Preliminary experiments on the uptake of human cell synthesized nanoparticles by other human cells are also performed.

3.2 Experimental protocols

3.2.1 Chemicals

Chloroauric acid ($\text{HAuCl}_4 \cdot 3\text{H}_2\text{O}$), Triton X-100, glutaraldehyde, paraformaldehyde (PFA), N-acetyl cysteine (NAC), buthionine-(S,R)-sulfoxime (BSO), Durcupan (epoxy resin), Cacodylate buffer, potassium ferrocyanide, uranyl acetate, lead citrate, iodoacetamide, NaCl, glycerol, NP40, CHAPS, EDTA, vanadate, NaF, Tris-HCl and CdCl_2 were purchased from Sigma-Aldrich and utilized without further purification. 5/6-Carboxy-2,7-dichloro-dihydro-fluorescein (Carboxy – H_2DCFDA) is purchased from Invitrogen, 5,5'-dithiobis-(2-nitrobenzoic acid) (DTNB, Ellman's reagent) and urea from Fluka Chemie AG. Osmium tetroxide is purchased from Electron Microscopy Sciences (EMS). Acetonitrile is obtained from Biosolve Chemie. Dithioerythritol (DTE) and CaCl_2 were purchased from Merck. ProteaseMax Surfactant and trypsin were bought from Promega. Premixed WST-1 is purchased from Clontech. Dulbecco's modified Eagle's medium (DMEM), Phosphate buffered saline (PBS), Hank's balanced salt solution (HBSS)s (with MgCl_2 and CaCl_2), 4% Trypan blue solution (in PBS 1X) and Tryple express are purchased from Gibco Life Technologies.

3.2.2 Cell culture and gold nanoparticle synthesis

Human cerebral endothelial cells (HCEC) (a kind gift from D. Stanimirovic, Ottawa, Canada) are cultured in DMEM 4.5 g/l glucose, without phenol red, supplemented with 10% heat-inactivated FBS and antibiotics (all from Gibco Life Technologies). The cells are initially seeded in 48-wells plates at a concentration of $5 \cdot 10^4$ cells/well in a 48 well plate (Costar, Corning, USA), then grown for 24 h at 37°C and 5% CO₂. For the experiments studying nanoparticle biosynthesis by live cells, semi-confluent (80%) HCEC are washed twice with PBS and then exposed to HAuCl₄ dissolved in PBS for 96 h. Cells not exposed to HAuCl₄ but treated under the same conditions are used as controls. To study the effects of membrane permeability, the cells are treated with either 50% ethanol for 5 min or with 4% formaldehyde for 15 min, prior to washing twice with PBS and the addition of HAuCl₄ dissolved in PBS for 96 h. To study the effects of modifying the redox state of the cells, the cells are pre-cultured for 6 h with NAC or BSO prior to the addition of HAuCl₄ dissolved in PBS for 96 h.

3.2.3 Extraction of intracellular and extracellular biosynthesized gold nanoparticles

The intracellular gold nanoparticles are extracted from cells after washing the cells with PBS and freezing for 24 h at -20°C. Then, 110 µL of extraction buffer (137 mM NaCl, 10% v/v glycerol, 1% v/v NP40, 1% w/v CHAPS, 2 mM EDTA, 20 mM Tris-HCl, 2 mM vanadate, 50 mM NaF, pH 7.2) is added to each well and the culture plate is gently shaken for 10 min. The cells are then scraped using a cell scraper and transferred to Eppendorf tubes. Freeze-thawing using liquid nitrogen is performed thrice to lyse the cell membrane and extract the intracellular particles. The Eppendorf tubes are then centrifuged at 1000 rpm to pellet cell debris, which are then discarded. The supernatants after removal of cell debris are then centrifuged at 8000 rpm (5724 g) for 30 min at 25°C to pellet the intracellular nanoparticles and the pellet is resuspended in 375 µL PBS. This step is repeated twice. To recover the biosynthesized nanoparticles found extracellularly, the cell-conditioned medium is centrifuged at 1000 rpm for 5 min to remove large materials, the pellet is discarded and the supernatant is centrifuged at 8000 rpm to pellet the nanoparticles. The pellet is suspended in 375 µL PBS. These steps are repeated twice.

3.2.4 Two photon imaging

After exposing HCEC to 0.5 mM HAuCl₄ in PBS for 96 h, the cells are washed twice with PBS prior to fixation with 4% formaldehyde for 30 min at 37°C. Cells not exposed to HAuCl₄ are used as controls. The samples are then imaged using a two-photon microscope (Leica SP5 multi-photon microscope). Two emission bands at $\lambda = 430 - 470$ nm (second harmonic generation signal, SHG) and at $\lambda = 480 - 750$ nm (two photon photo luminescence signal, TPPL) are simultaneously monitored for a fixed excitation wavelength at $\lambda_{ex} = 900$ nm.

3.2.5 TEM characterization

The cells are exposed for 96 h to 0 mM, 0.2 mM or 0.5 mM HAuCl_4 , then fixed for 1.5 h in 2% paraformaldehyde-2.5% glutaraldehyde in 0.1 M phosphate buffer pH 7.4. Adherent cells are washed three times with 0.1 M cacodylate buffer pH 7.4 at 4°C. The samples are postfixed using 1% osmium tetroxide and 1.5% potassium ferrocyanide in cacodylate buffer at room temperature for 40 min. Then, the solution is replaced with 1% osmium tetroxide in cacodylate buffer for 40 min. The cells are then washed twice using distilled water for 5 min, dehydrated using a graded alcohol series (50%, 70%, 90%, 95%, 100% alcohol), immersed in a 1:1 solution of absolute ethanol and Durcupan for 30 min and subsequently in 100% Durcupan for 1 h, followed by a 2 h incubation in fresh Durcupan, and embedded by overnight heating at 65°C. Using ultramicrotome 50 nm thick sections are cut and placed on nickel grids. The samples are washed 3 times in double distilled water. Then the grids are blotted on both sides with 2% uranyl acetate under standard conditions for 10 min and subsequently rinsed with double distilled water. The grids are immediately floated on droplets of lead citrate (Reynold's stain) in a carbon dioxide-free chamber for 5 min. The grids are again washed 2 times in double distilled water and dried. The dried grids are analyzed using a transmission electron microscope (FEI Tecnai Spirit transmission electron microscope operating at 80 KeV).

3.2.6 STEM characterization

The core size of the biosynthesized gold nanoparticles is analyzed by scanning transmission electron microscope (STEM). Thirty μL of the biosynthesized gold nanoparticle suspension is drop-cast on formvar coated TEM grids (Plano GmbH) and left to dry under ambient conditions. The nanoparticles on the grids are then imaged using the STEM detector in an SEM (FEI Nova 600 Nanolab). The size histogram is obtained by measuring the size of 100-150 particles using the analysis software ImageJ 1.44p. To determine the size distribution of the nanoparticles in solution, localized plasmon resonance of the nanoparticles is also recorded. One hundred μL of the nanoparticle suspensions are transferred to a 374-well plate (Nunc, Thermo scientific, USA) and the extinction spectra measured using an inverted microscope (Olympus IX 71) coupled with a spectrometer (Jobin Yvon Triax 550).

3.2.7 Proteomic analysis

Proteomic analysis of the nanoparticle corona is performed on suspensions of biosynthesized particles found both in the intracellular as well as extracellular regions of the cell. Gold salt concentration of 0.5 mM is used for the synthesis of particles required for proteomic analysis. The pelleted gold nanoparticles (after nanoparticle extraction) are suspended in 1 mL of 4 M urea in 10% acetonitrile. ProteaseMax surfactant is added at a final concentration of 0.05% and the pH is adjusted to 8.0 with Tris-HCl. Reduction of the protein disulfides is performed by the addition of 10 mM dithioerythritol (DTE, final concentration) for 1 h at 36°C. The pH of the solution is again adjusted to 8.0 and thiol alkylation is performed by the addition of 40 mM

iodoacetamide (final concentration) for 45 min at 36°C. The alkylation reaction is quenched by the addition of excess DTE and the samples are diluted 5 times with 20 mM Tris-HCl pH 8.0. Then, 10 mM CaCl₂ (final concentration) and trypsin is added to obtain a final protein/trypsin ratio of ~ 50/1. Proteolytic digestion is performed overnight at 37°C. The reaction is stopped by acidification to pH 2 prior to sample desalting through a C18 Sepak cartridge (Waters Corp.). The resulting concentrated peptides are dried by Speed-Vac and suspended in LC-MS initial conditions buffer (2% acetonitrile/0.1% formic acid/98% water). For mass spectrometry analysis the suspended samples are injected first into a capture column (Magic C18; 3 μ m-200 Å; 2 cm x 100 μ m), then separated over a 200 min gradient starting from 100% solvent A (2% acetonitrile/ 0.1% formic acid) to 90% solvent B (100% acetonitrile/0.1% formic acid) on a capillary column (Magic C18; 3 μ m- 100 Å; 15 cm x 75 μ m ID) at 250 nL/min. Mass spectrometric detection is performed on an LTQ-Orbitrap XL (Thermo Scientific) using Data Dependent Acquisition mode with dynamic exclusion. For each MS scan, the ten most intense detected ions are fragmented and then excluded for the following 30 seconds. Experimentally generated data are submitted to protein database search through Proteome Discoverer 1.1 and Mascot 2.3 search engines under the Uniprot Human Protein database (March 2012 version 1.2 including its reversed format). Scaffold 3 Viewer is used to finally compile the results.

3.2.8 Intracellular thiol and ROS determination

Cellular thiol levels are estimated by measuring the reaction of free thiol groups with DTNB. After exposure to NAC or BSO at the indicated concentration, the cells are washed with PBS twice and lysed using 0.1% Triton 100X in PBS. Ninety μ L of the lysate is added to 90 μ L of 5 mM DTNB in PBS and the absorbance of the resulting solution is measured at $\lambda = 405$ nm using a multiwell plate reader (Synergy HT reader from BioTek). The cellular thiol levels in treated cells is provided as the percentage change of the absorbance as compared to non-treated cells. The experiments are performed in triplicates and repeated twice.

The cellular ROS levels are measured by monitoring the fluorescence increase following the generation of H₂DCFDA from carboxy – H₂DCFDA. The cells are exposed to NAC or BSO at the indicated concentration, washed twice with PBS and 250 μ L of 20 μ M carboxy – H₂DCFDA dissolved in complete culture medium (without phenol red) is added to each well. After 30 min incubation the cells are washed with PBS twice and 250 μ L of fresh complete culture medium, DMEM+10% FBS (without phenol red), is added to each well. The fluorescence at $\lambda_{ex}/\lambda_{em} = 485/580$ nm is measured every 20 min in a thermostated multiwell-plate reader fluorescence reader (Synergy HT reader from BioTek) over a period of 1 h. The change in the level of intracellular ROS in exposed cells is given by the percentage change of the sample fluorescence compared to the control unexposed cells.

Means and standard deviations (SD) are calculated for all the data. Data are compared using a homoscedastic, two-tailed distributed Student's t-test. Details about comparisons are specified in the caption of each figure. Significance is expressed as: * $p < 0.05$; ** $p < 0.01$; *** p

< 0.001.

3.2.9 Cell viability evaluation

Following exposure to HAuCl_4 , the cell viability is evaluated using the WST-1 assay. HCEC are exposed for 1 h to increasing concentrations of HAuCl_4 in PBS and the cells layers are washed twice with PBS. Then, 20 μL of the WST-1 solution is added to the culture wells and the cells are incubated for a further 30 min at 37°C . One hundred μL of the supernatant from each well is transferred to a 96 well plate (Costar, Corning, USA) and the absorbance is measured at $\lambda = 405 \text{ nm}$ in a multiwell plate reader (Synergy HT reader from BioTek). The cell viability of treated cells is given by the percentage change of the absorbance compared to the viability of non-treated cells. The experiments are performed in triplicates and repeated twice. Means and standard deviations (SD) are calculated. Data are compared using a homoscedastic, two-tailed distributed Student's t-test. Details about comparisons are specified in the caption of each figure. Significance is expressed as: * $p < 0.05$.

3.2.10 Cell membrane permeability evaluation

The cell membrane permeability is evaluated using the trypan blue exclusion test. After exposing the cells to the required chemicals, each culture well is washed twice with PBS and incubated with 375 μL of 4% trypan blue solution for 5 min. The trypan blue solution is then discarded and the wells are again washed twice with PBS. In the final step, 375 μL of PBS is added to each well. The stained cells are then imaged using an upright microscope (Leica DIC microscope).

3.3 Results and discussion

3.3.1 Conditions necessary for synthesis of unaggregated gold nanoparticles

First, the conditions necessary for cell-assisted synthesis of gold nanoparticles are determined. Gold nanoparticle synthesis is observed on exposing the human cerebral endothelial cells (HCEC) to HAuCl_4 for 96 h using the experimental procedure sketched in Fig. 3.1(a). The color of the extracellular medium progressively changed from light yellow, characteristic of gold salt solution, to reddish pink indicating the presence of gold nanoparticles (insets in Fig. 3.1(c)). Figure 3.2 shows the absorbance at $\lambda = 450 \text{ nm}$, which provides a quantitative measurement for the amount of gold present at different times in the solution [272]. A clear increase in the absorbance is observed due to the higher concentration of gold nanoparticles. Therefore, an incubation time of 96 h is used in all the experiments presented henceforth. In addition to the change in color of the extracellular medium, the adherent HCEC themselves also develop a strong coloration, from pink (at low HAuCl_4 concentrations) to a purplish-black color (at high HAuCl_4 concentrations). This clearly indicates the presence of gold nanoparticles both in the

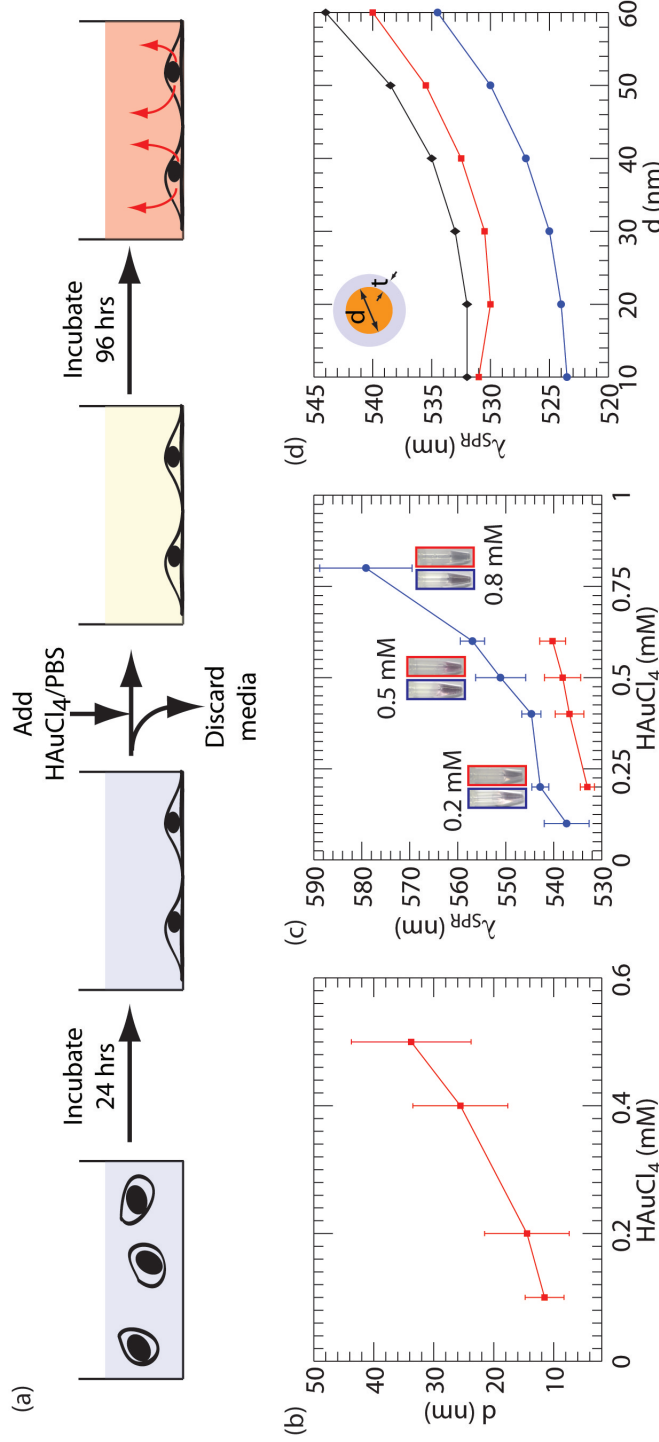


Figure 3.1: **Cell mediated biosynthesis of gold nanoparticles.** (a) Schematic of the protocol used for particle synthesis. (b) Size of extracellular particles as a function of HAuCl₄ concentration. (c) Variation of λ_{SPR} for intracellular and extracellular nanoparticles extracted from extinction measurements for different HAuCl₄ concentrations. Insets show the color of the colloidal solution of extracellular (red) and intracellular particles (black), 10 nm (purple) and 20 nm (green). The refractive index of the shell is fixed at 1.5.

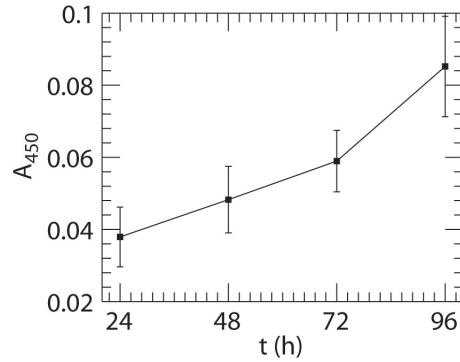


Figure 3.2: Absorbance of the extracellular medium of cells exposed to 0.5 mM HAuCl₄ measured at $\lambda = 450$ nm as a function of time.

intracellular and extracellular spaces.

Gold nanoparticles found in the extracellular (extracellular nanoparticles) and intracellular (intracellular nanoparticles) locations of the cells are recovered and characterized. The gold core size measured using scanning transmission electron microscopy (STEM) of the extracellular nanoparticles (Figure 3.1(b)) showed a progressive increase with the concentration of HAuCl₄, varying from 10 to 32 nm for a concentration increasing from 0.1 mM to 0.5 mM. Similar variations of the particle size as a function of HAuCl₄ concentration have been reported for other nanoparticle synthesis recipes [296, 299]. A similar evaluation of the core size for intracellular nanoparticles using STEM is not possible due to the inefficiency of the extraction procedure. Hence, the plasmon resonance wavelength, which depends on the nanoparticles size [272], is used instead to provide a qualitative picture of the intracellular particles sizes. Figure 3.1(d) indicates that resonance wavelength is very sensitive to the particle diameter both for a gold particle without or with a dielectric shell; the presence of the shell shifting the plasmon resonance further to longer wavelengths. Figure 3.1(c) shows the plasmon resonance wavelengths measured for both the intracellular and extracellular nanoparticles for different HAuCl₄ concentrations. The plasmon resonance wavelength, λ_{SPR} , of the intracellular particles is red shifted as compared to the extracellular particles for all the HAuCl₄ concentrations studied here. This difference could be due to the difference in the gold core size of the nanoparticle and/or the presence of different protein shells, the so-called protein corona, around the particles. Indeed, Figure 3.1(d), indicates that in both cases the plasmon resonance is shifted to a longer wavelength. For HAuCl₄ concentrations above 0.6 mM too few particles are present in the extracellular medium and it is not possible to characterize them. However, for this high concentration the plasmon resonance of the intracellular particles is strongly shifted, indicating large particles, which possibly could not get externalized. In the absence of cells, HAuCl₄ dissolved in PBS and added to culture wells did not result in the synthesis of gold nanoparticles. Therefore, the HCEC are necessary for the formation of gold nanoparticles, and these particles are found both extracellularly and intracellularly.

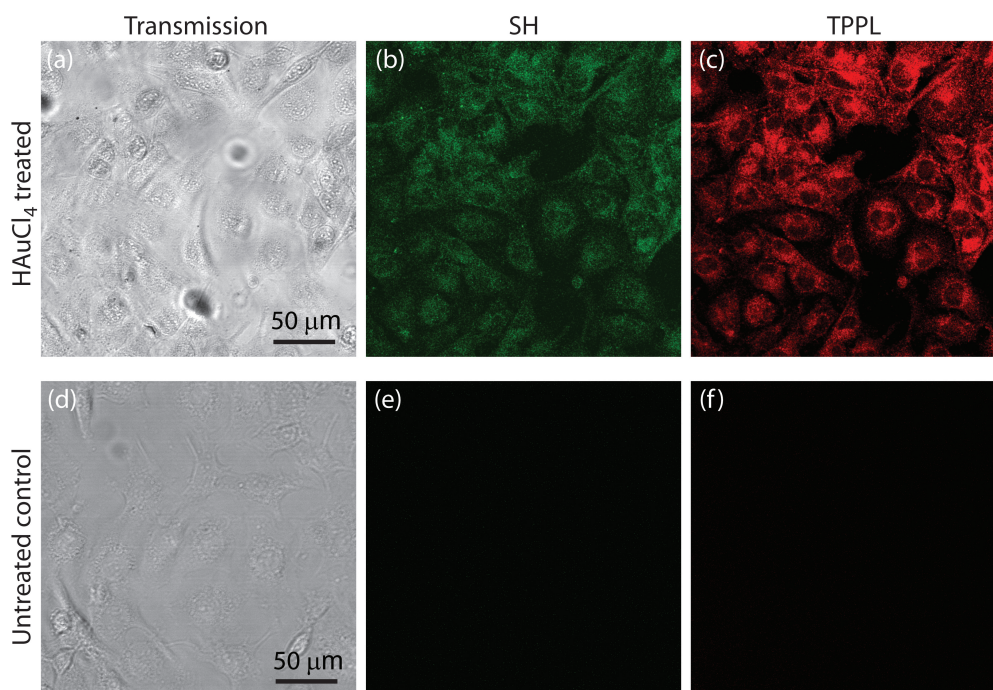


Figure 3.3: **Two photon visualization of intracellular gold nanoparticles.** (a,b,c) Bright field, channel 1 (430-470 nm) and channel 2 (470-750 nm) of two photon imaging of cells with nanoparticles ($\text{HAuCl}_4 = 0.5 \text{ mM}$, incubated for 96 h). (d,e,f) Bright field, channel 1 (430-470 nm) and channel 2 (470-750 nm) of two photon imaging ($\lambda_{ex} = 900 \text{ nm}$) of cells not treated with HAuCl_4 .

3.3.2 Two photon characterization of cells incubated with HAuCl_4

Two-photon microscopy is performed on HAuCl_4 exposed and non-exposed cells (control) to study the intracellular localization of nanoparticles. This imaging technique provides direct visualization of the gold nanoparticles [305]. In cells treated with 0.5 mM HAuCl_4 for 96 h, a second harmonic (SH) and a two-photon photoluminescence signal (TPPL) are demonstrated, originating mainly from gold nanoparticles present in the cytoplasm (Fig. 3.3(a)-(c)). These SH or TPPL signals are absent in cells not exposed to HAuCl_4 and imaged under identical conditions (Fig. 3.3(d)-(f)). Furthermore, two-photon photoluminescence images recorded at various heights (Z -scan) clearly demonstrate that the nanoparticles are localized throughout the cytoplasm of all cells (Fig. 3.4).

3.3.3 TEM characterization of cells

To prove that biosynthesized gold nanoparticles are found intracellularly and to determine the cell organelles where they can be detected, transmission electron microscopy (TEM) images of ultrathin sections of cells treated with gold salt are obtained (Fig. 3.5). Nanoparticles can be clearly identified in TEM micrographs at different magnifications for cells exposed to two

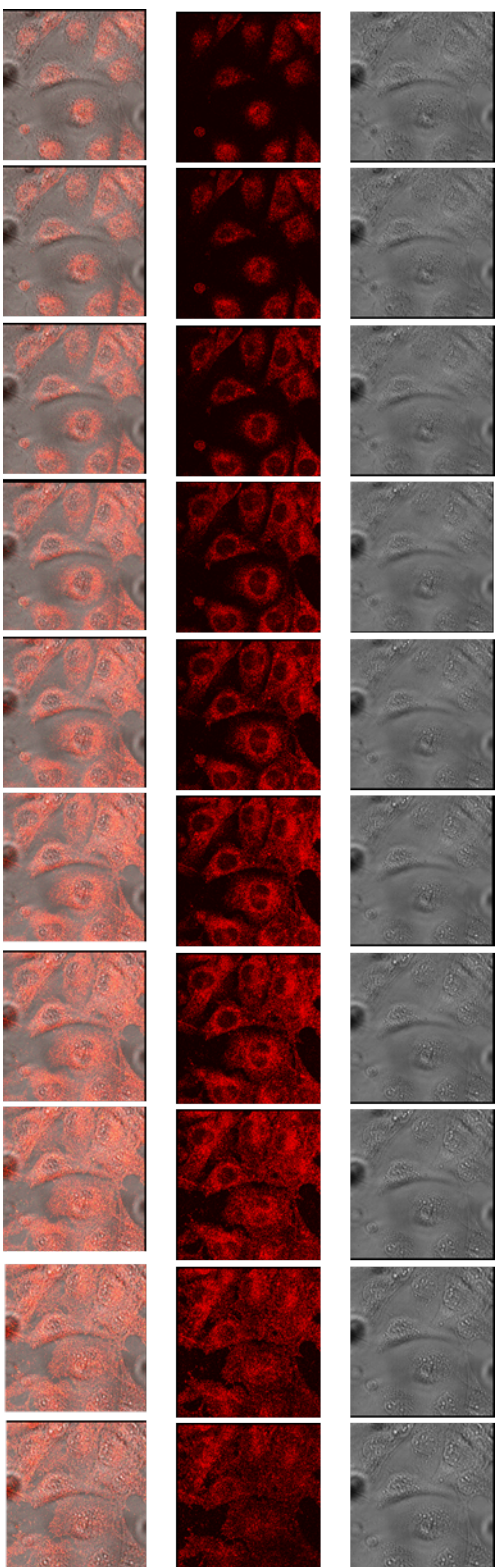


Figure 3.4: **Two-photon Z-scan imaging.** Z-scan of cells treated with 0.5 mM HAuCl₄ performed using a two photon microscope ($\lambda_{ex}=900$ nm). Top row shows the bright field images, middle row show the TPP signal (470-750 nm) and bottom row shows the two overlaid signals. The z position varies by 0.8 μ m between consecutive images.

different HAuCl_4 concentrations (Fig. 3.5(a)-(f)), while unexposed cells did not exhibit any such particles (Fig. 3.5(g)-(i)). The density of the nanoparticles is higher in cells exposed to the higher concentration of HAuCl_4 . No significant nanoparticle aggregation is observed for both concentrations. Low magnification images clearly show that no major changes occur in the cell membrane of the HAuCl_4 exposed cells as compared to the unexposed cells (compare Fig. 3.5(a), (d) and (g)). It should be noted that although the cell membrane remained intact, high magnification images indicated that intracellular organelles are progressively degraded with increasing concentration of HAuCl_4 . The degradation of cellular organelle integrity also correlates with the loss of cell viability following exposure to gold salts and during the synthesis of gold nanoparticles as shown subsequently. The different behavior of the HAuCl_4 towards the cell membrane (not disrupted on exposure to HAuCl_4) as compared to the organelle membranes could possibly be due to the differences in their composition.

3.3.4 Proteomic analysis of the protein corona

It is quite remarkable that the biosynthesized nanoparticles produced using HCEC are stable under ambient conditions and do not aggregate with time. The stability of the nanoparticles arises from the presence of a corona, including the protein corona, which is formed when any nanoparticle interacts with a biological environment [229, 231, 235, 238, 246–248, 306–310]. Moreover, it is this protein corona that determines the interaction of the nanoparticle with its environment. The protein corona is analyzed using mass spectroscopy for both intracellular and extracellular HCEC-synthesized gold nanoparticles (Fig. 3.6). About 1800 and 1300 proteins could be identified from the protein corona on the intracellular and extracellular particles, respectively. The link to the complete list of identified proteins is presented in Appendix C.4. To ascertain that the proteins identified via the proteomic analysis originated from cell synthesized nanoparticles, the following control sample is used. HCEC are pretreated with 50% ethanol for 5 min prior to incubation in PBS without HAuCl_4 for 96 h and then the PBS containing the diffused proteins is analyzed. About 350 proteins are identified for the control sample. Note that 5 min incubation with ethanol is not sufficient for removal of the intracellular proteins via diffusion, which requires significantly longer incubation times [311]. A Venn diagram depicting the proteins common and unique to each extracellular and intracellular samples (Fig. 3.6(a)) shows an overlap of the proteins found on the intracellular and extracellular gold nanoparticles. In addition to the proteins common to both nanoparticles, a large number of proteins (greater than 1000 for intracellular and 500 for extracellular nanoparticles) are unique to intracellular or extracellular nanoparticles. Further comparison based on the cellular origin of the proteins did not demonstrate a preferential organelle of synthesis (Fig. 3.6(b)). This is probably due to the disruption of the organelle membranes which occurs when the cells are incubated with HAuCl_4 , as illustrated by the TEM images (Fig. 3.5(a)-(f)). Thus, HCEC-synthesized gold nanoparticles possess a rich protein corona with a large number of common and unique proteins on both the intracellular and extracellular nanoparticles which stabilize the nanoparticles in biological media.

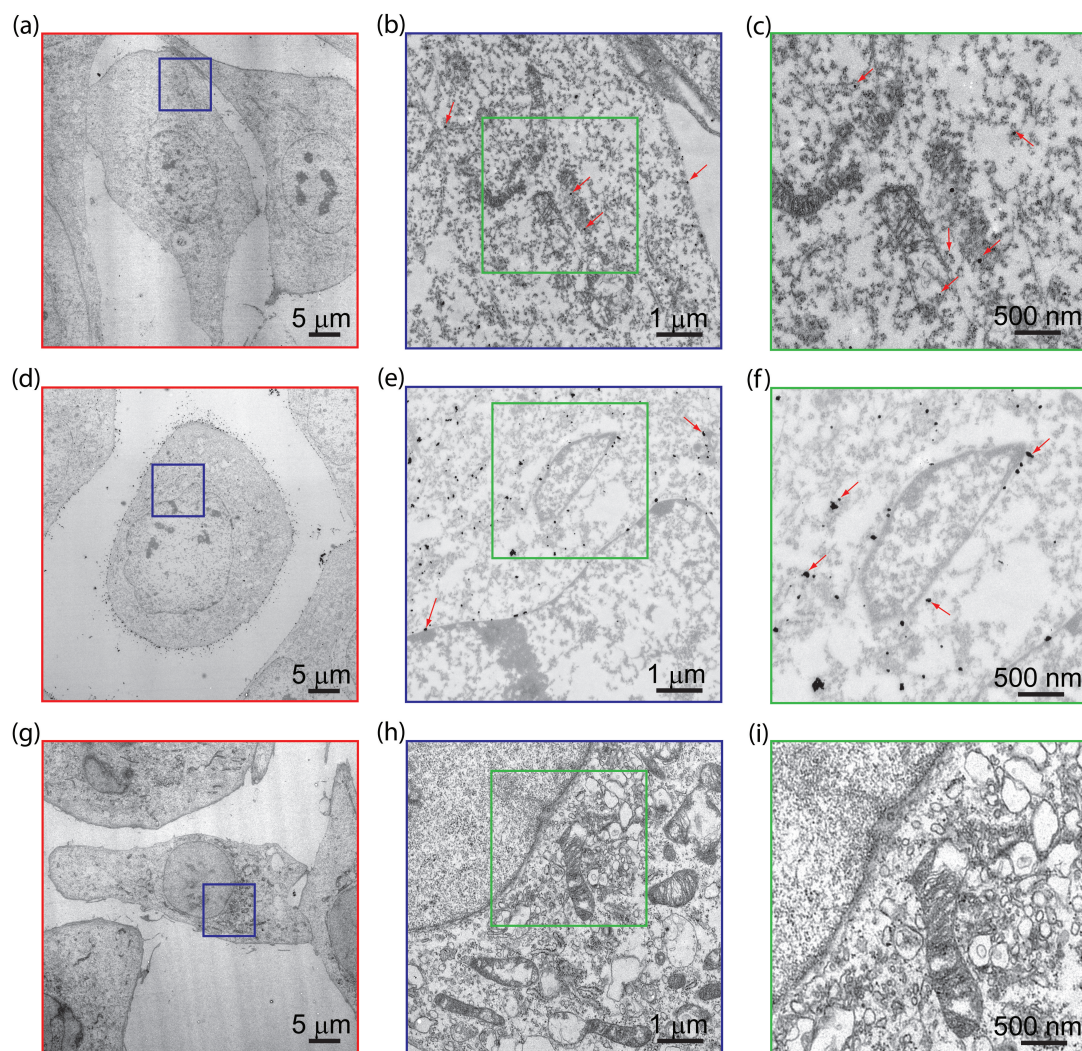


Figure 3.5: **TEM characterization.** (a,b,c) TEM images of cells treated with 0.2 mM HAuCl₄ for 96 hours. (d,e,f) TEM images of cells treated with 0.5 mM HAuCl₄ for 96 hours. (g,h,i) TEM images of untreated cells. Red arrows indicate some nanoparticles.

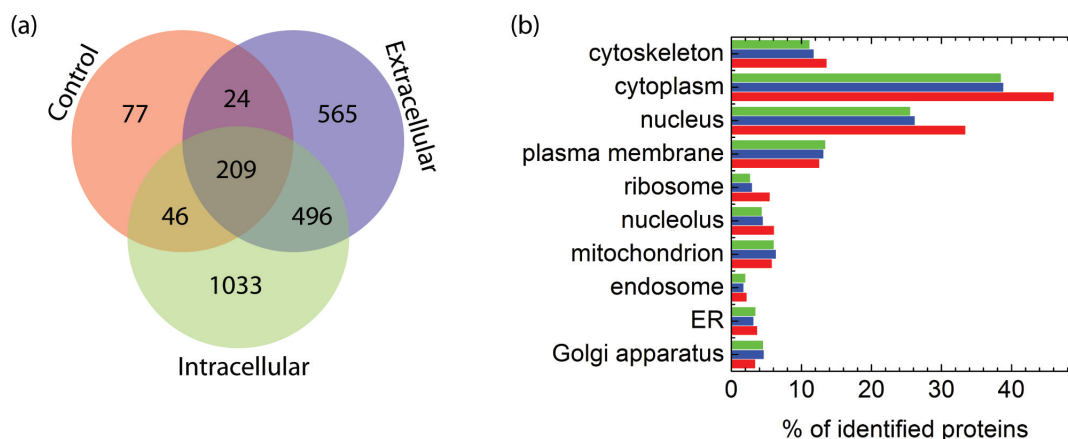


Figure 3.6: **Proteomic analysis.** (a) Unique and common proteins identified from proteomic analysis between control, extracellular and intracellular nanoparticles. (b) Origin of the identified proteins from various cellular organelles.

3.3.5 Cell viability evaluation after exposure to HAuCl_4

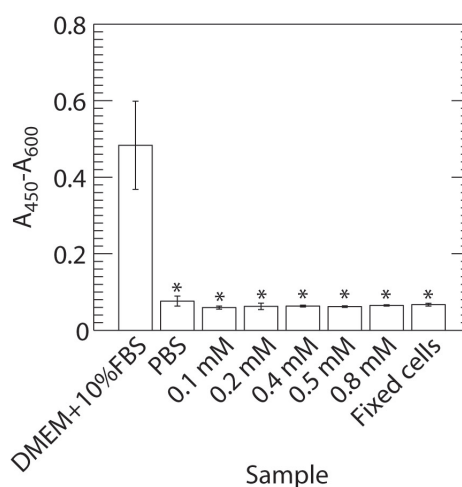


Figure 3.7: **Cell viability after exposure to HAuCl_4 .** Viability of cells after treatment with HAuCl_4 for 1 hour evaluated using WST-1. Statistical significance is calculated with respect to the control sample (cells cultured in DMEM+10%FBS) and expressed as: * $p < 0.05$.

The viability of the cells after exposure to HAuCl_4 is also assessed quantitatively and qualitatively using WST-1 and trypan blue exclusion tests. Figure 3.7 clearly shows that the cells are not viable even after 1 h exposure to various concentrations of HAuCl_4 . Additionally, trypan blue exclusion test results (Fig. 3.8) elucidate that the cells get stained on exposure to trypan blue, indicating that the cell membrane is permeable to the dye. Even though the cells die rapidly after exposure to HAuCl_4 , in less than 1h, the cellular morphology remains intact and no major differences are observed from the optical images (Fig. 3.3 (a)-(c)).

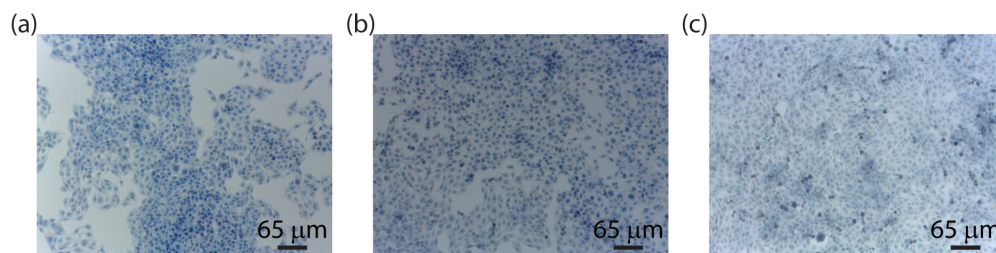


Figure 3.8: **Trypan blue test for cell viability after exposure to HAuCl₄.** Trypan blue stained images of cells exposed to (a) 0.1 mM, (b) 0.2 mM cells and (c) 0.5 mM HAuCl₄ for 1 h. Note that the cells are stained with the Trypan blue solution after the 1 h exposure step.

3.3.6 Effect of initial cell state on particle characteristics

As evidenced from the TEM images the cell membrane does not get structurally affected on incubation of the cells with HAuCl₄. For this reason, the influence of the cell membrane permeability at the start of exposure to gold salt, on the characteristics of the synthesized nanoparticles is assessed (Fig. 3.10). To modify the cell membrane permeability, cells are either untreated or pretreated with 50% ethanol or with 4% formaldehyde prior to the addition of HAuCl₄ (Scheme of the experimental design Fig. 3.10(a)). The pretreatment of cells with ethanol or formaldehyde leads to different modes of cell fixation [312]. The cell membrane permeability is significantly affected by these pretreatments as qualitatively indicated by trypan blue exclusion, which is excluded by cells with a non-permeabilized membrane (Fig. 3.9). Trypan blue staining is maximal after ethanol treatment, low after formaldehyde treatment and absent in untreated cells. This indicates that larger pores are created in the cell membrane of cells treated with ethanol as compared to cells treated with formaldehyde. The extracellular nanoparticles synthesized by cells pretreated with ethanol or formaldehyde exhibited different core sizes as compared to untreated cells. The smallest core size is observed in the case of formaldehyde-treated cells (Fig. 3.10 (b)). However, in all the three cases, the size of the extracellular nanoparticles increased with increasing HAuCl₄ concentrations and the plasmon resonance wavelength λ_{SPR} of the nanoparticles red shifted in agreement with the gold core size (Fig. 3.10(c)). Using absorbance at $\lambda = 450$ nm (away from the plasmon resonance [272])

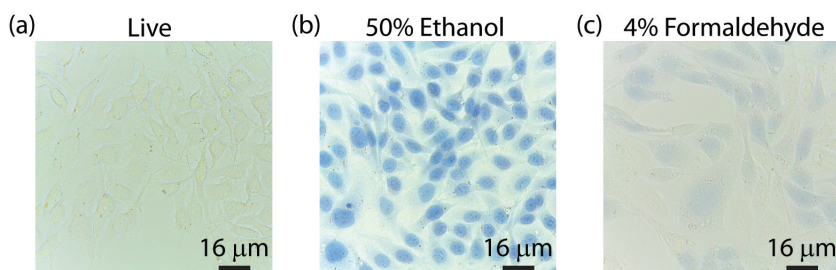


Figure 3.9: **Trypan blue exclusion test after exposure to ethanol and formaldehyde.** Image of (a) Untreated cells, (b) 50% ethanol fixed cells and (c) 4% formaldehyde fixed cells after treatment with Trypan blue stain (5 min).

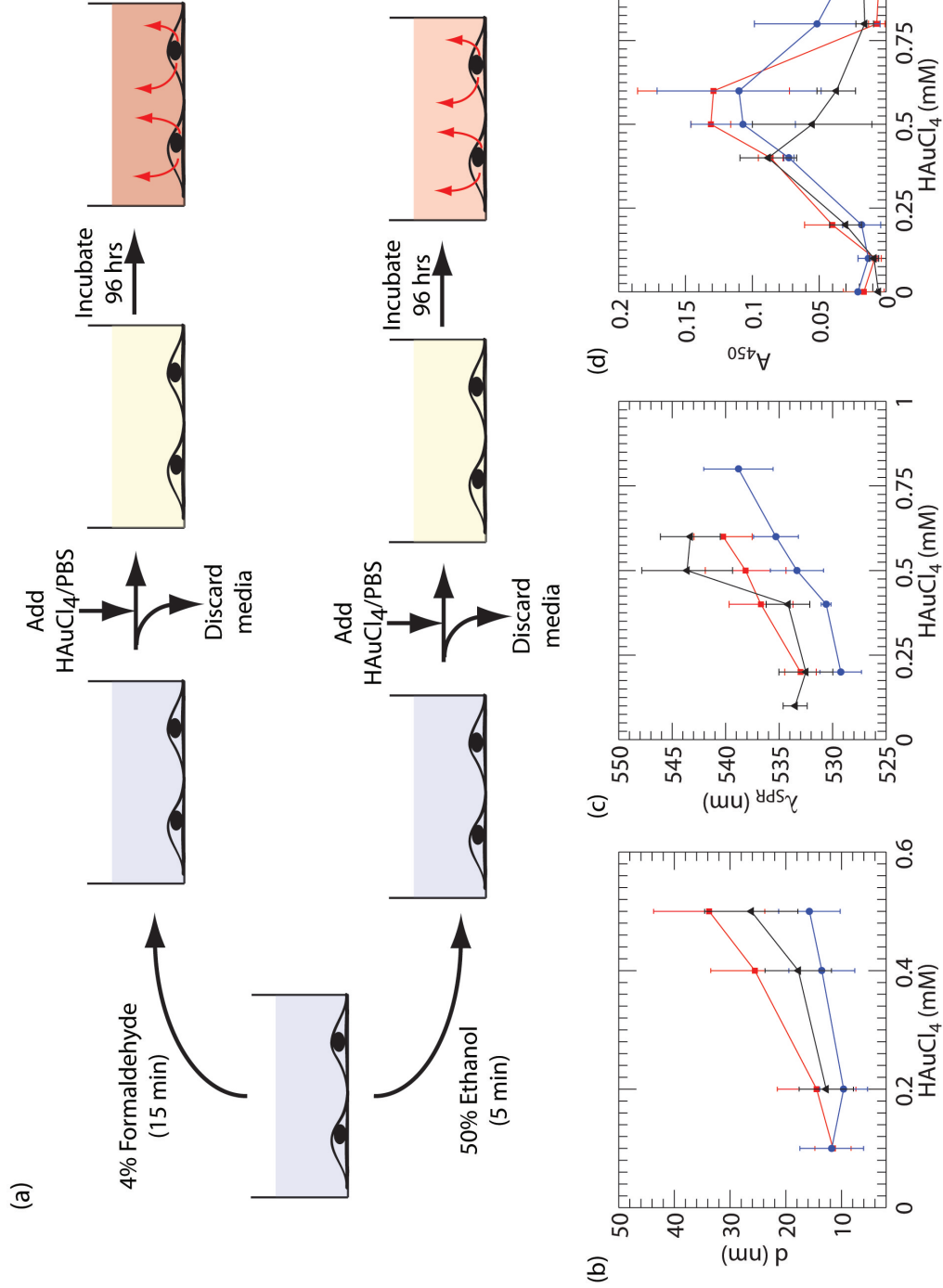


Figure 3.10: **Cell state dependent biosynthesis.** (a) Schematic of the protocol used for studying the effect of initial cell state on biosynthesis. (b) Extracellular particle size measured from STEM images when synthesized using live cells (red), cells fixed with 4% formaldehyde (blue) and cells fixed with 50% ethanol (black). (c) Wavelength of the localized plasmon resonance of the synthesized particles for the three cases. (d) Absorbance at 450 nm for the three cases.

to quantify the density of the nanoparticles in the extracellular medium, I observe that for these three treatments absorbance increased with increasing HAuCl_4 concentration up to 0.6 mM (Fig. 3.10 (d)), then decreased with further increasing HAuCl_4 concentration. The color of cells containing intracellular nanoparticles, as observed under an optical microscope (not shown), progressively increased with the HAuCl_4 concentration. I hypothesize that only nanoparticles below a certain size can be excreted into the extracellular space whereas larger nanoparticles formed at higher HAuCl_4 concentrations remain trapped within the cells, with a size threshold dependent on the porosity characteristics of the cell membrane and passive diffusion.

3.3.7 Effect of redox state of the cell

It has been shown previously that HCEC exposed to iron oxide, silica and titanium dioxide nanoparticles respond to their uptake by generation of oxidative stress [313, 314]. In line with this, the effect of the redox state of the cells, prior to their exposure to HAuCl_4 , on the size and optical characteristics of the biosynthesized gold nanoparticles is still not clear (Fig. 3.11). To modify the intracellular redox state, the cells are exposed either to N-acetyl cysteine (NAC), which increases the cellular thiols creating a more reducing environment, or to the glutathione (GSH)-depleting agent buthionine-(S,R)-sulfoxime (BSO) which increases the intracellular peroxides, inducing an oxidative cell stress [315–320]. Glutathione (GSH) is one of the main antioxidant in cells [317, 318, 321], and can also bind to gold nanoparticles via its thiol group. The scheme of the experiment is shown in Fig. 3.11(a). Upon NAC exposure, as expected the cellular thiol level progressively increased as a function of NAC concentration, however, increasing NAC concentration first increased, then induced a decrease in the level of intracellular peroxides (Fig. 3.11(b) and (c), black curves). The core size of the extracellular nanoparticles synthesized by the cells decreased from 30 nm to 23 nm when the cells are treated with up to 20 mM NAC, (Fig. 3.11(d), black curve). When the cells are pretreated with BSO, the cellular thiol levels remained constant while the level of intracellular ROS increased (Fig. 3.11(b) and (c), red curves) While the core size of the extracellular nanoparticles synthesized by HCEC pretreated with low (0.5 mM) BSO increased from 30 to 42 nm, this size decreased to 34 nm for high BSO (20 mM) concentrations. One of the possible reasons for this modification of the nanoparticle size, could be the direct modification of the intracellular oxidants and anti-oxidants by pre-treatment of cells with NAC or BSO, which participate in the cell mediated synthesis of gold nanoparticles. On a different note it is well known that induction of oxidative stress in cells leads to the modification of the relative levels of intracellular proteins. This change in the levels of various proteins can also influence the size of the synthesized nanoparticles. Therefore I have demonstrated that the size of the gold nanoparticles synthesized by the HCEC is dependent on the oxidative/reducing state of the cells at the time of their exposure to the gold salt.

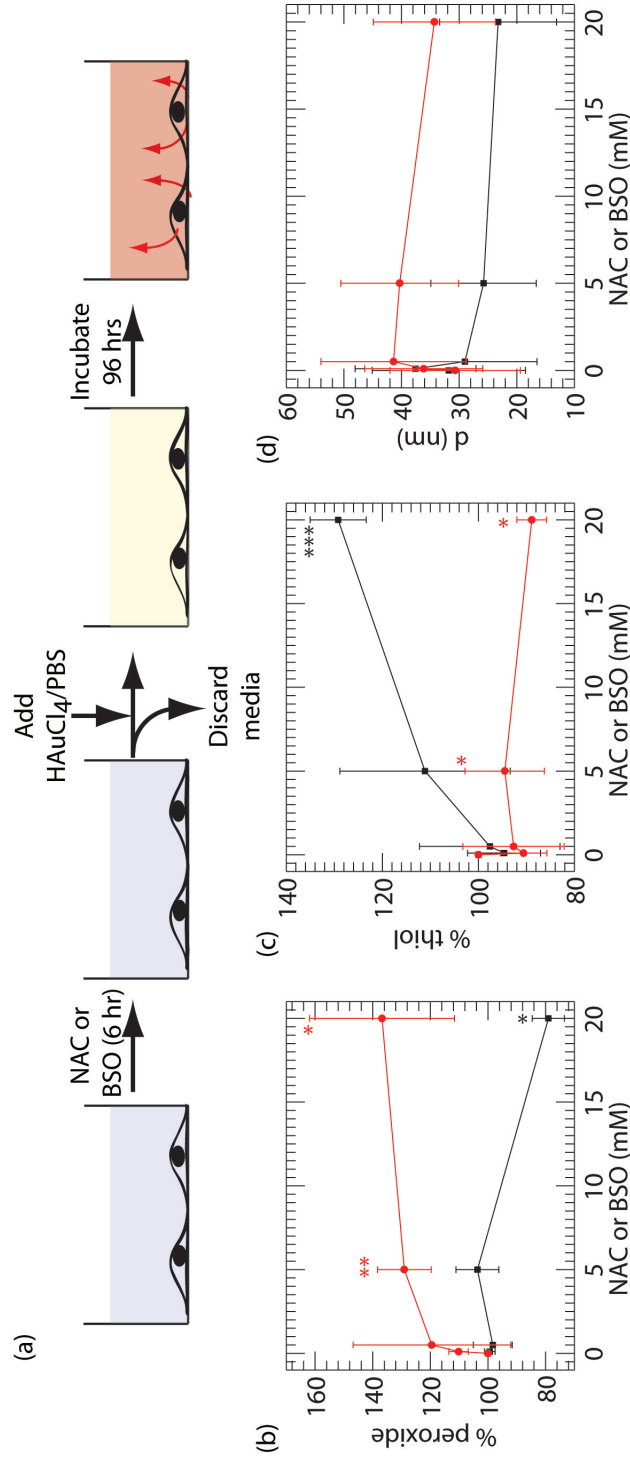


Figure 3.11: **Modifying the intracellular redox state.** (a) Schematic of the protocol used. (b) Variation in the amount of intracellular peroxide due to treatment with NAC (black) or BSO (red). (c) Change in the intracellular concentration of thiol due to NAC or BSO treatment. Statistical significance was calculated with respect to the control samples and expressed as: * $p < 0.05$; ** $p < 0.01$; *** $p < 0.001$. Black and red stars correspond to NAC or BSO treatment. (d) Modification of extracellular particle size due to treatment of the cells with NAC or BSO prior to addition of HAuCl₄. The size is measured using STEM.

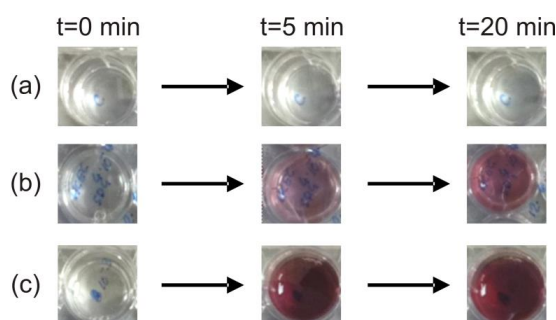


Figure 3.12: **Color of the culture well on addition of HAuCl₄ to HCEC cultured with DMEM (with HEPES)+10% FBS.** Color of the cell culture wells at different times after the addition of (a) no HAuCl₄, (b) 0.2 mM HAuCl₄ and (c) 0.5 mM HAuCl₄.

3.4 Cell vicinity synthesis of gold nanoparticles

In the previous sections, human cell mediated gold nanoparticle synthesis is demonstrated. This synthesis is made feasible by the presence of various reducing as well as capping agents, predominantly proteins, in the cell. However, during the course of this study, I found that some of the chemicals used during standard cell culture protocols can also facilitate the synthesis of gold nanoparticles. Amongst them, glucose and HEPES are the chemicals which are present at high concentration in cell culture media and can synthesize gold nanoparticles [269, 322]. In case of glucose containing medium, nanoparticle synthesis is observed within 12-24 h after the addition of gold salt (shown in Appendix C.1). Whereas if medium supplemented with HEPES is used, then nanoparticle synthesis is observed within <30 min after the addition of gold salt. For example, Fig. 3.12 shows the color of the extracellular medium at various times after the addition of HAuCl₄ to the cells. The main distinction in this protocol is the following: DMEM (supplemented with HEPES) +10% FBS is used as the culture medium and no washing step is introduced between the removal of the cell culture medium and addition of HAuCl₄ salt dissolved in PBS. The absence of the washing step plays a crucial role and around 20 μ L of medium is still left over after the discarding step. It is this remaining medium that facilitates the formation of the nanoparticles in such a short time duration (<30 min). Note that analogous experiments performed in the absence of cells also lead to the formation of nanoparticles over a period of <30 min. However, the addition of identical concentrations of HAuCl₄ to complete undiluted DMEM (supplemented with HEPES) +10% FBS (without dilution in PBS) did not lead to particle synthesis. Furthermore, the use of DMEM medium without HEPES also did not lead to the generation of the nanoparticles using both the protocols presented here with 30 min. This clearly shows that the HEPES is the chemical that facilitates nanoparticle synthesis.

A few interesting observations can be made here. First, even though the synthesis process occurs due to the presence of residual medium and over a short duration, nanoparticles can be found in the intracellular organelles (Fig. 3.13 (a)-(d)). A significant distinction of this case as compared to cell mediated synthesis, which occurs over a period of 96 h, is the presence of the intact organelles (Compared Fig. 3.13 (b)-(d) and Fig. 3.13 (f)-(h)). Second, the proteomic

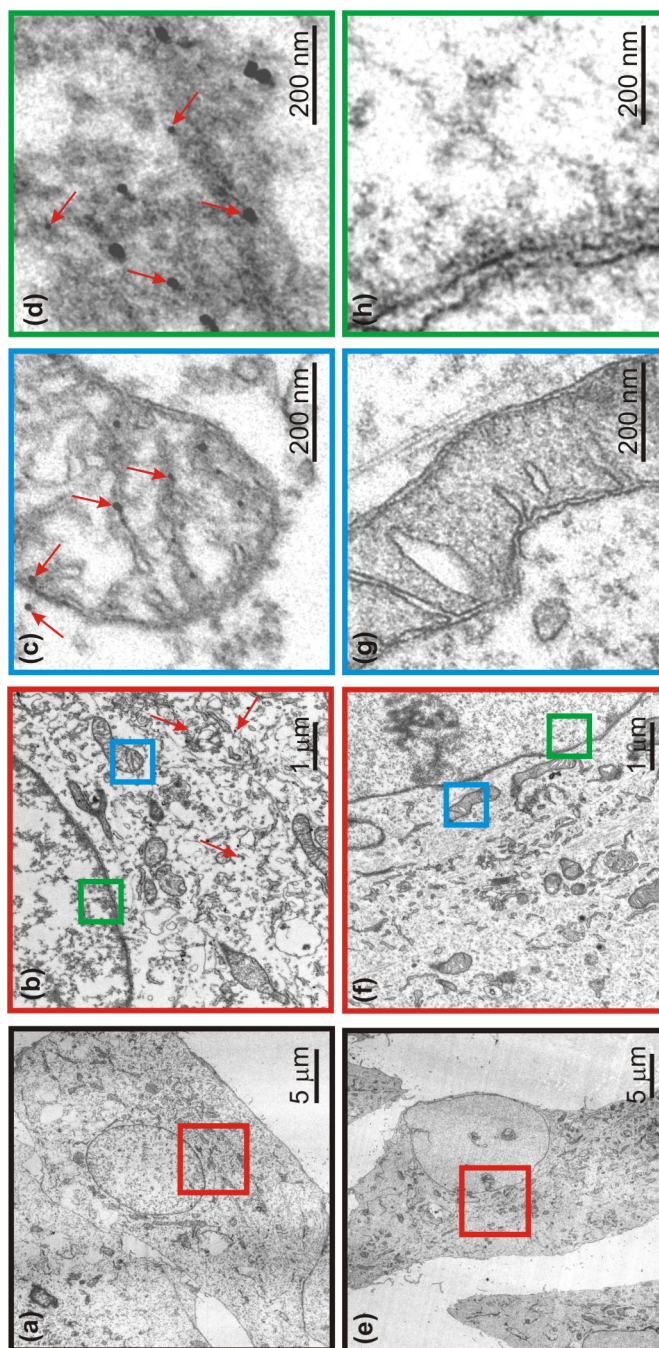


Figure 3.13: TEM images of cells cultured with DMEM (with HEPES) + 10% FBS and incubated with HAuCl_4 . TEM images of (a)-(d) cells treated with 0.5 mM HAuCl_4 for 20 min prior to fixation and (e)-(f) cells not treated with HAuCl_4 (control experiment). (b) and (f) Enlarged images of the red square marked in (a) and (e), respectively. (c) and (d) Magnified portions of (b), represented by blue and green borders, respectively. (g) and (h) Enlarged areas represented by blue and green squares in (f). Arrows in (b), (c) and (d) indicate the location of some selected nanoparticles.

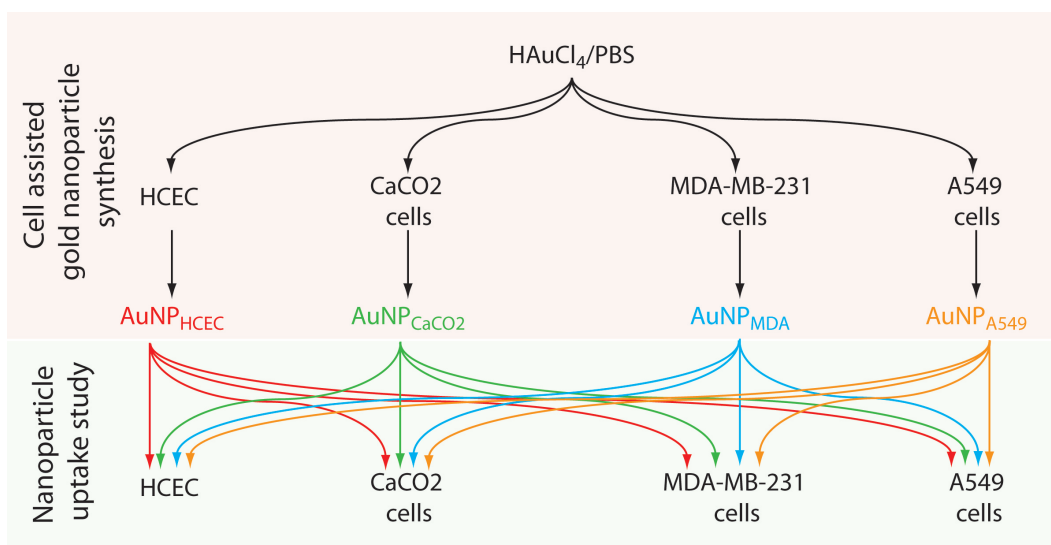


Figure 3.14: A scheme showing the two distinct steps involved in this experiment. In the first step nanoparticles are synthesized using four different human cell lines. In the second step, the uptake of the synthesized particles by human cells is investigated.

analysis of the nanoparticles showed that a smaller number of proteins, 92 in total, could be identified on these particles. Even among this small number of proteins, some of the identified proteins are not found in the extracellular space of the cells and are absent from the control sample (the link to the complete list of identified proteins is presented in Appendix C.4). This indicates that some of the proteins present within the cell are released during the synthesis procedure and are then attached to the nanoparticle. A second possibility that exists is that the nanoparticles are first internalized, coated with the proteins and then released using natural cell mechanisms. However, this is unlikely as the cells rapidly die when exposed to HAuCl_4 concentrations above 0.1 mM, which is the minimum concentration used in this study. Therefore, this extracellular synthesis of gold nanoparticles with the simultaneous capping of the particles with cell specific proteins could also lead to an alternative route for designing specific cell compatible nanoparticles.

3.5 Uptake of biosynthesized nanoparticles by human cells: Preliminary results

3.5.1 Nanoparticle synthesis by various human cell lines

Four different human cell lines originating from various organs are used in this study. They are A549 (Lung cancer cells), MDA-MB-231 (Breast cancer cells), HCEC (Brain endothelial cells) and CaCO_2 (Colon cancer cells). The cell mediated synthesis protocol for all the cells is identical and outlined in Sec. 3.2.2. A gold salt concentration of 0.5 mM is used for the synthesis of gold nanoparticles by all the different cell lines. Only the extracellular particles

3.5. Uptake of biosynthesized nanoparticles by human cells: Preliminary results

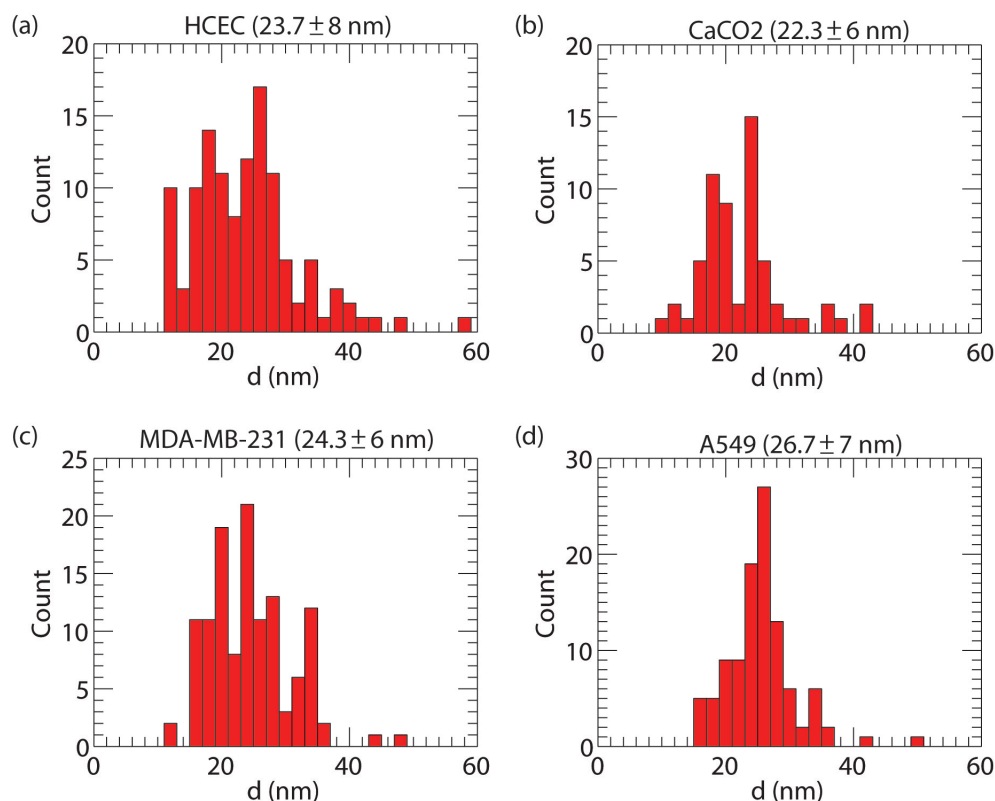


Figure 3.15: **Size histograms of gold nanoparticles synthesized by various human cells.** Histograms of particle size synthesized by (a) HCEC, (b) CaCO₂ cells, (c) MDA-MB-231 cells and (d) A549 cells. The mean and SD of the size are also indicated.

are used for the uptake studies. Furthermore, the size of the nanoparticles synthesized by the various cell lines is measured using STEM analysis (details presented in Sec. 3.2.6). In total four sets of nanoparticle solutions, each synthesized using one of the cell lines, is used subsequently in the uptake experiments (Fig. 3.14). The size histograms of the synthesized gold nanoparticles by various cells are shown in Fig. 3.15. The mean size of gold nanoparticles synthesized by various cell lines is very similar which reduces the complexity in the analysis of the results of the nanoparticle uptake experiment. This is because it is well known that the uptake of nanoparticles by human cells is also strongly dependent on their size [217, 323–328].

3.5.2 Experimental procedure for studying nanoparticle uptake by human cells

All the cells are cultured in DMEM (without HEPES) 4.5 g/l glucose supplemented with 10% FBS (all from Gibco Life Technologies). The cells are seeded at a density of 1×10^5 cells/mL in a 12 well plate (Costar) (1.5 mL per well). Post-seeding the cells are incubated for 24 h at 37°C and 5%CO₂. The cells are washed twice with PBS (pH 7.2) and 1.0 mL HBSS (with MgCl₂ and CaCl₂) is added to each of the culture wells. Then 100 μ L of the synthesized nanoparticle suspension is added to each well and the cells are incubated for a further 6 h at 37°C and

5%CO₂. After this, the cells are washed twice with PBS and fixed using 4% formaldehyde for 15 min. In case of the uptake experiments, a total of 16 combinations of nanoparticle-cell exists as shown in Fig. 3.14. Furthermore, control samples are also cultured in parallel using the same protocol as detailed above, with the difference that no nanoparticle solution is added after the addition of 1 mL of HBSS (with MgCl₂ and CaCl₂) .

3.5.3 Two-photon microscopy of nanoparticle uptake

Two photon imaging is used for visualizing the internalized gold nanoparticles. Three different channels are acquired simultaneously: Transmission, channel 1 ($\lambda = 600 - 700$ nm) and channel 2 ($\lambda = 430 - 470$ nm). The excitation wavelength is fixed at 900 nm and identical laser powers are used for the acquisition of all the images. Channel 1 and channel 2 correspond to the two-photon photoluminescence (TPPL) and the second harmonic generation (SHG) signals arising from the gold nanoparticles, respectively. Figure 3.16 shows the images of A549 cells incubated with and without the cell synthesized gold nanoparticles. As compared to the control cells, the cells incubated with AuNP showed a higher TPPL and SHG signal. Furthermore, the maximum signal is observed in case of A549 cells incubated with AuNP_{CaCO₂}. Similarly, particle uptake experiments with CaCO₂ cells show that the cells incubated with particles exhibit higher signals as compared to control cells (Fig. 3.17). A small signal is visible in the TPPL channel, which is probably due to cross-talk with the auto-fluorescence signal arising from the fixative, formaldehyde. In case of CaCO₂, the maximum signals are obtained when the cells are incubated with AuNP_{HCEC} and AuNP_{MDA} (Fig. 3.17). In the case of uptake by HCEC, the maximum signal is seen for AuNP_{CaCO₂} and AuNP_{MDA} incubation (Fig. 3.18). Finally, the uptake experiment using MDA-MB-231 cells show that the maximum uptake occurs when the cells are incubated with AuNP_{A549} and AuNP_{MDA}. A qualitative assessment of the nanoparticle uptake determined from the TPPL and SHG signals is presented in Table 3.1. It is clear that significant variations exist in the uptake properties of these cell synthesized nanoparticles. One possible reason for such a difference in uptake could arise from the differences in the protein corona around the nanoparticles. A interesting point that must be noted here is that, the order of nanoparticle uptake shows some similarity with the commonly known metastatic sites of common cancers (see Table 3.2). For example, colon cancer often metastasizes to the lung. From the uptake experiments, I also observe that particles generated using CaCO₂ cells are taken up at the highest amounts by A549 cells (lung cancer). Similar observations can also be made for particles synthesized by A549 cells, as they are taken up more readily by MDA-MB-231 cells. These preliminary investigation into the uptake properties of the cell synthesized nanoparticles show interesting results, especially with respect to cancer metastasis. Also, the apparent amount of AuNPs internalized correspond to the known absorptive properties of the cells in the organ of origin : Colon >lung >breast or brain endothelial cells [329]. However, quantitative analysis of particle uptake has to be carried out for conclusively proving the analogy presented here.

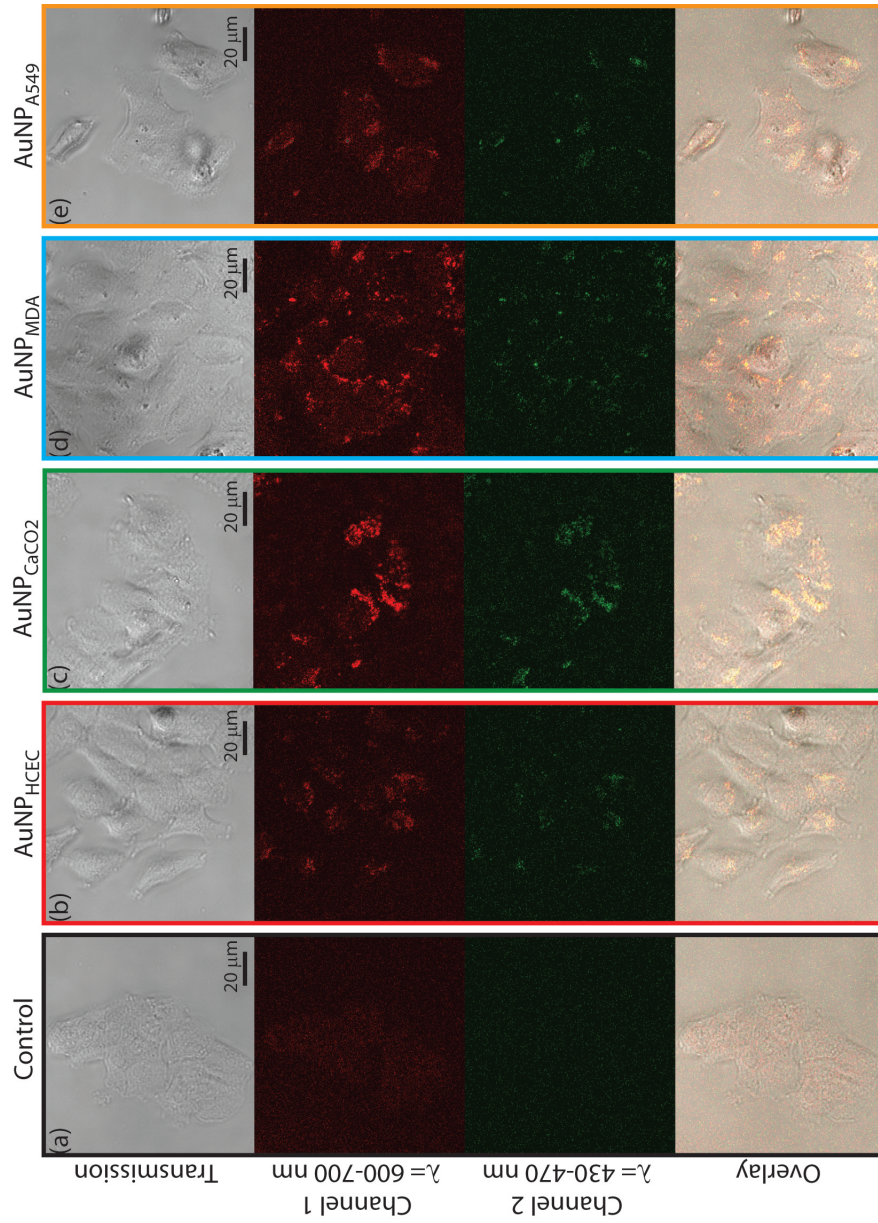


Figure 3.16: **Uptake of human cell synthesized gold nanoparticles by A549 cells.** Optical images of A549 cells incubated (a) without nanoparticles, (b) with AuNP_{HCEC}, (c) with AuNP_{CaCO₂}, (d) with AuNP_{MDA} and with (e) AuNP_{A549}. The vertical panels in each subfigure corresponds to Transmission, Channel 1 ($\lambda = 600 - 700$ nm), Channel 2 ($\lambda = 430 - 470$ nm) and the overlay of all the channels, respectively. The excitation wavelength is 900 nm.

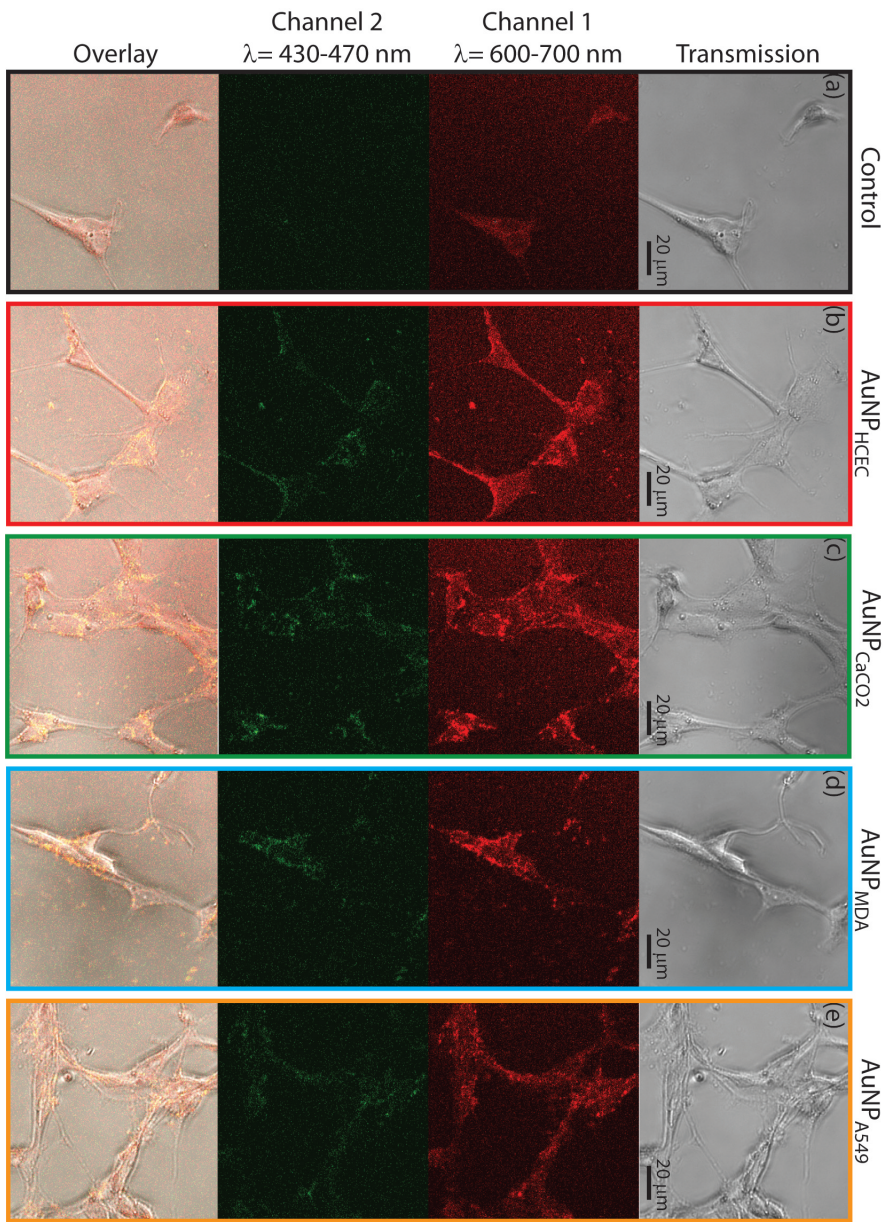


Figure 3.17: **Uptake of human cell synthesized gold nanoparticles by CaCO₂ cells.** Optical images of CaCO₂ cells incubated (a) without nanoparticles, (b) with AuNP_{HCEC}, (c) with AuNP_{CaCO₂}, (d) with AuNP_{MDA} and (e) with AuNP_{A549}. The vertical panels in each subfigure corresponds to Transmission, Channel 1 (λ = 600 – 700 nm), Channel 2 (λ = 430 – 470 nm) and the overlay of all the channels, respectively. The excitation wavelength is 900 nm.

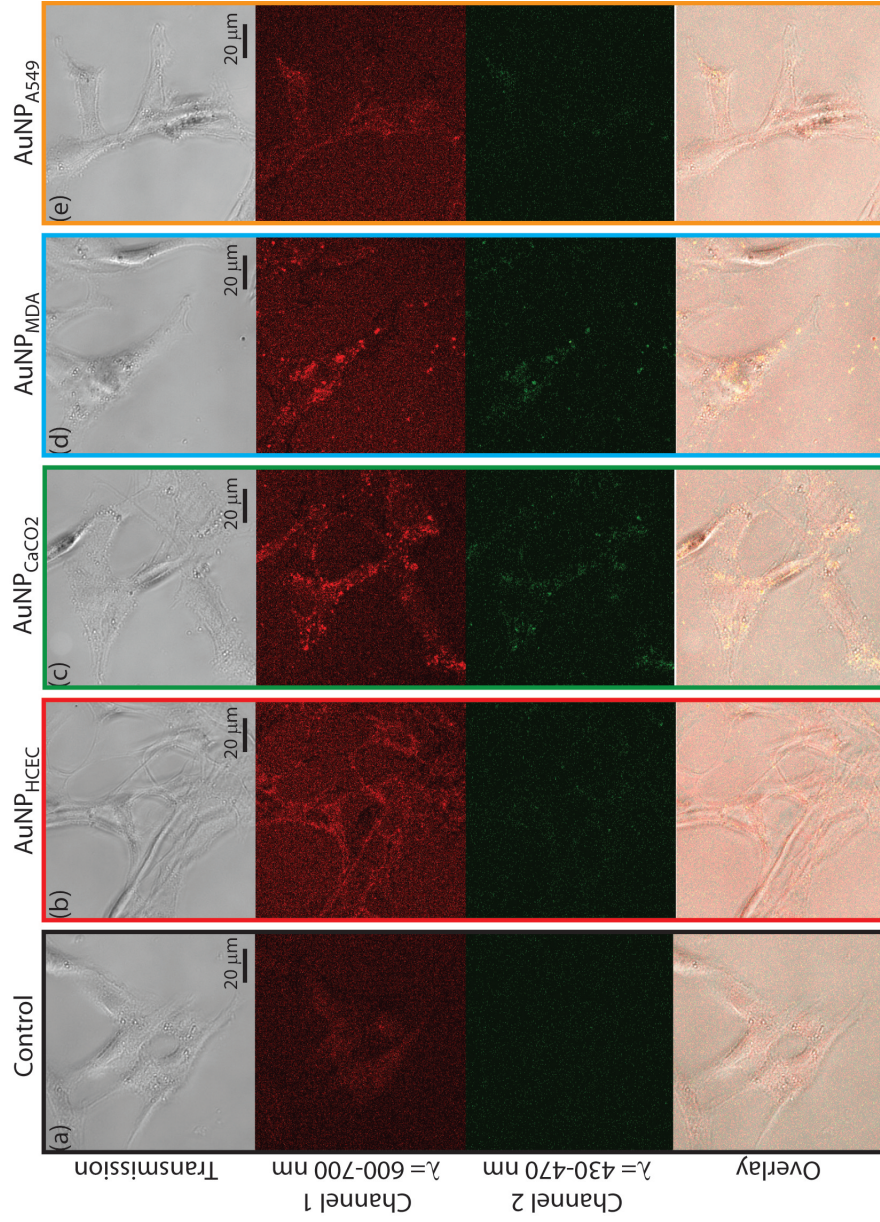


Figure 3.18: Uptake of human cell synthesized gold nanoparticles by HCEC cells. Optical images of HCEC cells. (a) without nanoparticles, (b) with $\text{AuNP}_{\text{HCEC}}$, (c) with $\text{AuNP}_{\text{CaCO}_2}$, (d) with AuNP_{MDA} and (e) with $\text{AuNP}_{\text{A549}}$. The vertical panels in each subfigure corresponds to Transmission, Channel 1 ($\lambda = 600 - 700$ nm), Channel 2 ($\lambda = 430 - 470$ nm) and the overlay of all the channels, respectively. The excitation wavelength is 900 nm.

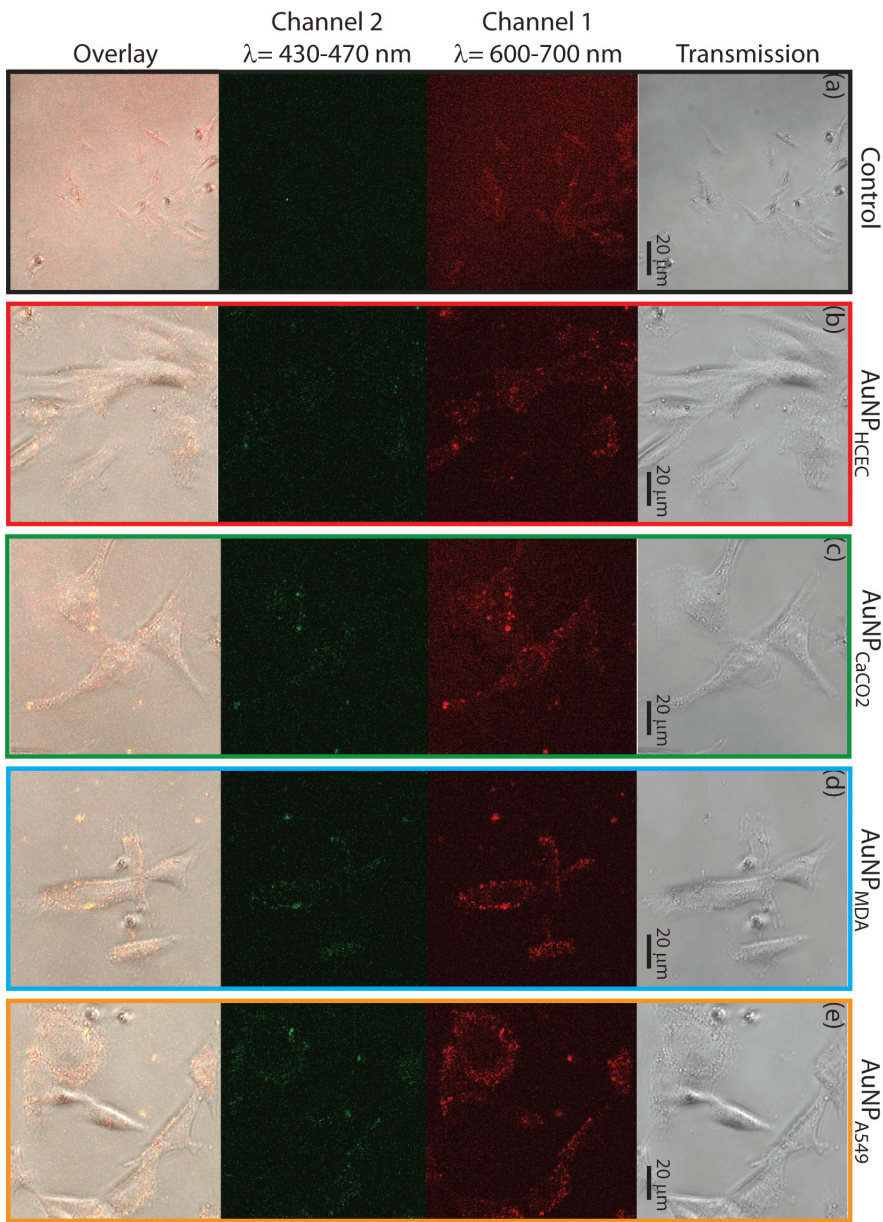


Figure 3.19: **Uptake of human cell synthesized gold nanoparticles by MDA-MB-231 cells.** Optical images of MDA-MB-231 cells incubated (a) without nanoparticles, (b) with AuNP_{HCEC}, (c) with AuNP_{CaCO₂}, (d) with AuNP_{MDA} and (e) with AuNP_{A549}. The vertical panels in each subfigure corresponds to Transmission, Channel 1 ($\lambda = 600 - 700$ nm), Channel 2 ($\lambda = 430 - 470$ nm) and the overlay of all the channel, respectively. The excitation wavelength is 900 nm.

Cell Line	Order of nanoparticle uptake
A549	AuNP _{CaCO2} >AuNP _{MDA} >AuNP _{A549} >AuNP _{HCEC} >Control
CaCO2	AuNP _{CaCO2} ~ AuNP _{MDA} ~ AuNP _{HCEC} >AuNP _{A549} >Control
HCEC	AuNP _{CaCO2} >AuNP _{MDA} >AuNP _{HCEC} >AuNP _{A549} >Control
MDA-MB-231	AuNP _{A549} >AuNP _{MDA} >AuNP _{CaCO2} ~ AuNP _{HCEC} >Control

Table 3.1: Qualitative assessment of uptake of cell synthesized gold nanoparticles by human cells.

Cancer	Common metastasis sites
Lung	Adrenal gland, bone, brain, liver, other lung
Breast	Bone, brain, liver, lung
Colon	Liver, lung, peritoneum

Table 3.2: Common metastasis sites of some cancers. Data taken from national cancer institute at the national institutes of health (<http://goo.gl/CrttBq>).

3.6 Summary

In conclusion, I have studied intracellular biosynthesis of gold nanoparticles by human endothelial cells using HAuCl₄ as a precursor. The size of the generated gold nanoparticles is shown to be strongly dependent on the initial gold salt concentration and cell state prior to gold salt addition. For example, on increasing the initial HAuCl₄ concentration the nanoparticles tend to become progressively larger. Initial cell state is modified by treatment of cells with ethanol and formaldehyde prior to addition of gold salt. Nanoparticles in the range of 5-50 nm could be produced dependent on the pretreatment, with formaldehyde treated cells giving the smallest particles. Two-photon and electron microscopic investigations have clearly shown the intracellular localization of the nanoparticles. TEM further illustrates that, HAuCl₄ treatment leads to organelle dissolution in a concentration dependent manner but not cell membrane dissolution. The synthesized nanoparticles are found to be extremely robust against aggregation, thanks to a rich protein corona. The composition of this corona is analyzed by mass spectrometry, revealing the presence of proteins originating from the different intracellular organelles and the cytosol. Experiments performed with NAC and BSO showed that the nanoparticle size can vary from 23 to 42 nm depending on the intracellular redox state, i.e. the balance between the levels of anti-oxidants and oxidants. My experiments clearly demonstrate that the initial cell state is critical and paramount for understanding the biosynthesis in human cells.

Preliminary experiments of the uptake of cell synthesized gold nanoparticles by other human

Chapter 3. Human cell assisted synthesis of gold nanoparticles

cells show interesting results. Some similarities can be seen between the uptake of these cell synthesized nanoparticles with the commonly known metastasis sites of common cancers. However, quantitative analysis of the uptake is necessary to obtain definite answers to this link.

4 Coupling mediated detection of plasmonic nanoparticles

Hybridization of plasmonic resonances has been exploited for various applications. In this chapter, the technique based on hybridization of plasmonic resonances is extended to detect single gold nanoparticles. Nanohole arrays with subwavelength dimensions are experimentally realized and used for the detection of 30 nm gold nanoparticles. An extension of this technique for determination of the core size of gold nanoshells is also shown.

4.1 Introduction

Hybridization of plasmonic modes has been exploited significantly for tuning the properties of plasmonic structures [1, 120, 122, 271, 283, 330–341]. Among all the applications exploiting plasmon hybridization, the best known are 2D and 3D plasmon rulers, which are based on the coupling between two or more plasmonic particles [131, 144, 337, 342, 343]. Specifically in a 2D plasmon ruler, the gap between the two nanoparticles is correlated with the resonance wavelength of the structure. Therefore, by measuring the resonance wavelength, it is possible to extract information on the gap with nanometric precision [82–86, 113, 114, 144, 343–345]. Recently, a nonlinear analog of 3D plasmonic rulers was presented which used the anisotropy in SH scattering for detecting changes in the position of the nanorods [337]. Non-resonant approaches for detection of nanoparticles have also been studied extensively [88–90, 92, 271]. For example, Zhang *et al.* used gold nano-antennas for the selective trapping and detection of single 10 nm particles [92]. The presence of the particle induced a small shift in the resonance wavelength of the nano-antenna and was used as a marker for the nanoparticle. However, note that in this study the resonance wavelength of the antenna was significantly different from the resonance wavelength of the particle being detected. Furthermore, the particles needed to be trapped in the nano-antenna gap for obtaining an accurate measure of the particle's properties. Alternative approaches have used double hole structures made in a metallic film for trapping and detection of nanoparticles [346–348]. Although these methods are extremely sensitive, they require the trapping of the nanoparticle in the plasmonic trap before the properties of the particles can be determined. Therefore, a technique that can detect and characterize nanoparticles without employing plasmonic trapping has significant potential. This is the

main focus of this chapter, i.e. to develop a technique based on plasmonics for detection of nanoparticles in a non-trapping geometry. In particular, extraordinary transmission of light (EOT) through plasmonic nano-hole arrays is used for detecting nanoparticles [110, 349–355].

Recall that EOT of light occurs due to excitation of either localized or propagating plasmons in a periodic nanohole array. In particular, nanohole arrays with periods smaller than the wavelength, exhibit EOT only via the excitation of localized surface plasmons of the individual holes [352]. Since the demonstration of EOT in 1998, nanohole arrays of various geometries have been used for diverse applications [110, 356–368]. For example, Eftekhari *et al.* showed that nanohole arrays fabricated on gold films on free standing SiN membranes could be used as nanochannels for studying fluid flow at the nanoscale [360]. They also demonstrated that the flow-through approach provided better sensitivities as compared to flow-over approach for traditional plasmon based biosensors. On a different note, the technique developed here can also be used for size analysis of a nanoparticle suspension. In principle, the data obtained with this method would complement the data acquired from other commonly used techniques for particle size analysis like TEM, SEM, DLS and ultracentrifugation [58, 219, 220, 272, 297, 369–371].

4.2 Methods

4.2.1 Numerical calculations

Numerical simulations performed using the periodic surface integral approach are used to study the effect of different geometrical parameters on the optical response of structures, Fig. 4.1 [372]. The geometry and mesh of the structure are defined using COMSOL multiphysics (version 4.1), with the maximum size of the triangle fixed at 10 nm in all the simulations. This ensures the convergence of the numerical simulation to the desired accuracy. The dielectric function of gold is modeled using the data of Johnson and Christy [259]. The dielectric function of Si₃N₄ and water are taken to be 4 and 1.7689, respectively. The structures are illuminated using a plane wave propagating in the $-z$ or z direction (normal incidence) and polarized along the x axis. The reflection and transmission intensities are then computed by calculating the time averaged Poynting vector at points on a plane ($|z| = 10 \mu\text{m}$) in the far field.

4.2.2 Nano-fabrication

The nanohole arrays in a gold film deposited on silicon nitride membranes (Fig. 4.1) are fabricated using the procedure shown in Fig. 4.2. The first step involves the fabrication of free standing Si_xN_y ($x \sim 3$ and $y \sim 4$) membranes. To make the membranes, a single photolithography step followed by an etching step are used to define the membrane boundaries on a Si wafer coated with a 100 nm thick Si₃N₄ on both sides. This is followed by an anisotropic etching step using 23% KOH. Etching using KOH ensures that the process is self limiting and the final boundaries of the membrane are formed using the $\langle 111 \rangle$ plane of crystalline silicon.

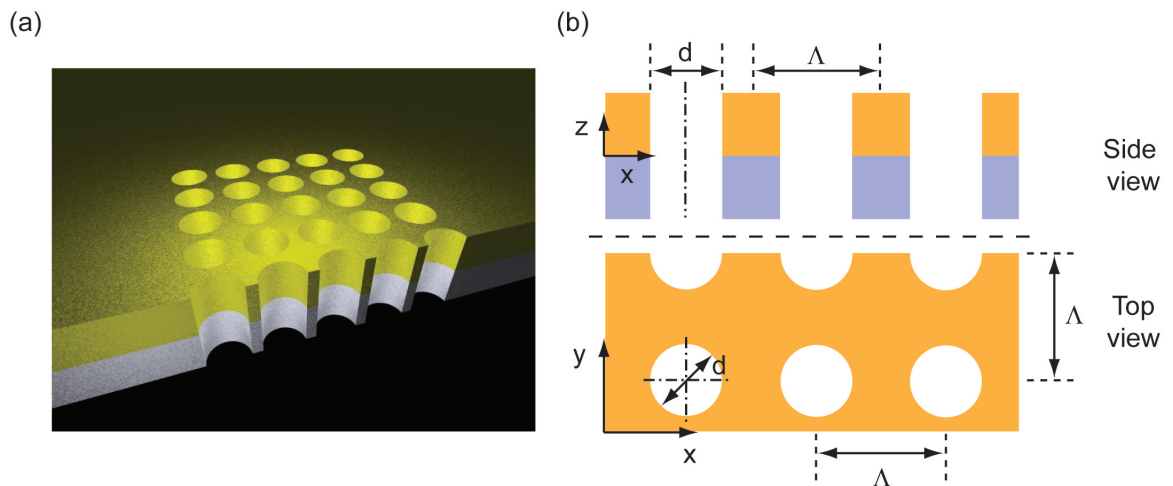


Figure 4.1: **Schematic of the nanohole array used for nanoparticle detection.** (a) 3D visualization of the structure used for particle sensing. (b) Cross-sectional views of the structure under study defining the various relevant parameters.

The Si_3N_4 membranes are coated with 100 nm Au and 60 nm Cr protection layer prior to focused ion beam (FIB) milling. In the last step the Cr layer is etched using chrome etch. SEM images prior to Cr etch and after Cr etch are shown in Fig. 4.3.

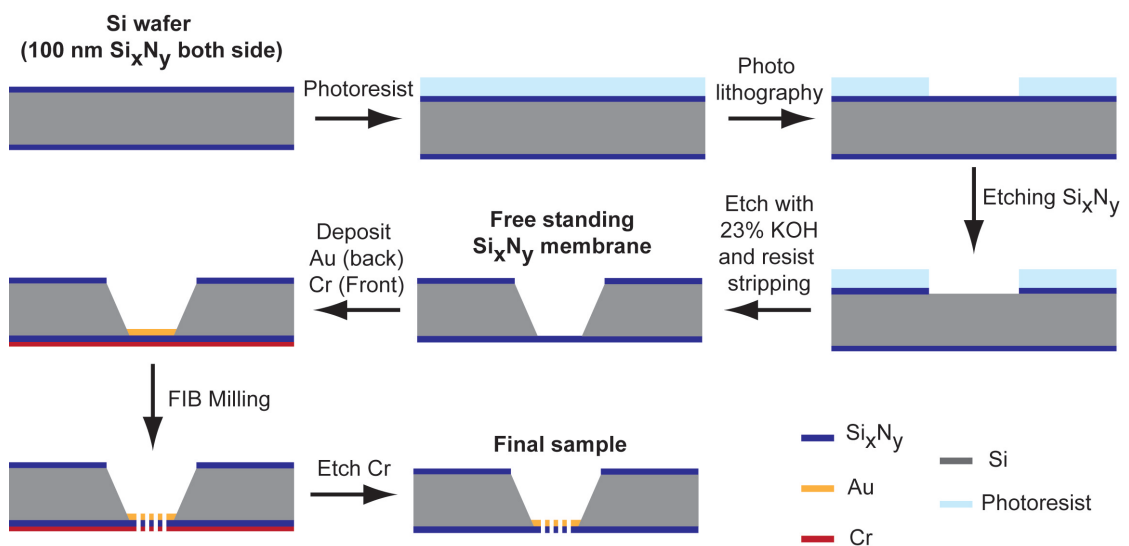


Figure 4.2: **Fabrication of nanohole arrays.** Schematic showing the various steps for fabricating the free standing metal hole array.

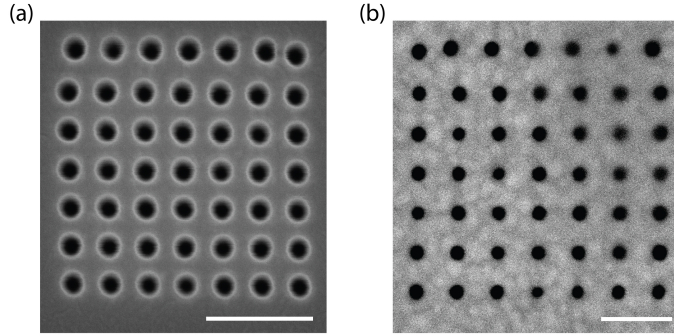


Figure 4.3: **SEM images of the fabricated nanohole array.** SEM images of hole arrays in a metallic film (a) before Cr etch (from the Si_xN_y side) and (b) after Cr etch (from the Au side). Scale bars in (a) and (b) indicate 300 nm and 200 nm, respectively.

4.2.3 Optical measurements

The transmission and reflection spectra of the hole arrays are measured using a home built optical step which contains an inverted microscope (Olympus IX 71) coupled to a spectrometer (Horiba Triax 550). In transmission measurements (schematically shown in Fig. 4.4(a)), the sample is illuminated from the top using normal incident polarized light and the transmitted light is collected using a 60X objective (Olympus 60X NA 0.7). The collected light is then analyzed using the spectrometer. The transmitted intensity is normalized with the directly transmitted light (without the sample) to get the normalized transmission intensity of the sample. In reflection measurements (schematically shown in Fig. 4.4(b)), the sample is illuminated using the 60X objective and the reflected light collected using the same objective. The incident angles are in the range of 0° to 10° , which is due to the large NA of the objective. The collected reflected light is then analyzed using the spectrometer. The raw reflected intensity from the sample is normalized to the reflected intensity measured from a silver mirror to get the reflectivity of the sample. In case of both the transmission and reflection measurements, a limited range of pixels corresponding to the sample are integrated to get the intensity from the sample.

4.3 Results and discussion

4.3.1 Effect of hole size

Consider a hole array made in a 100 nm gold film placed on top of a Si_3N_4 membrane with $\Lambda = 100$ nm, as shown in Fig. 4.1. The background medium for all the subsequent simulations and measurements is taken to be water. The transmission and reflection from such a structure for different hole sizes due to normally incident light is shown in Fig. 4.5. The periodicity

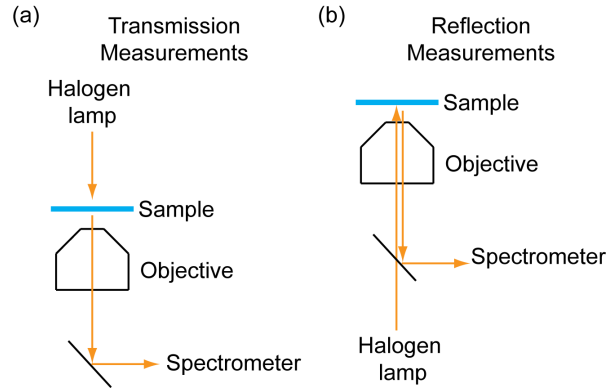


Figure 4.4: Schematic showing the optical setup used for (a) transmission and (b) reflection measurements.

is fixed at 100 nm to ensure that no periodicity related resonances, i.e. grating orders, are present in the wavelength range of interest. The simulated transmission spectra, Fig. 4.5(a), exhibits two peaks for a given hole size. For a 50 nm hole, the resonance wavelengths are observed at 525 nm and 570 nm whereas for a 70 nm hole the peaks are located at 535 nm and 580 nm. Three different contributions must be considered to understand the resonance features observed in the simulated transmission spectrum. First, the intrinsic properties of a gold film leads to a peak in transmission close to 500 nm. Second, a contribution from the plasmon resonance corresponding to the hole at the top interface (gold-water interface). Finally, a third contribution from the plasmon resonance of the hole at the gold-Si₃N₄. Note that the resonance wavelength of the hole at the bottom interface is red-shifted as compared to the hole at the top interface. This is due to the presence of Si₃N₄ near the bottom interface. However, it is difficult to explicitly attribute a certain weight for each of these contributions to the final spectrum. To understand further this system, I plot the electric field intensity as well as the real part of the normal component of the electric field on a xy -plane at $\lambda = 540$ nm for an array with hole size of 50 nm, Fig. 4.5(e) and (f). The electric field intensity shows that the field is localized around the periphery of the nanohole, showing a typical signature of localized plasmon. Similar field distributions have been reported earlier for nanohole arrays [352, 354, 361]. Furthermore, Fig. 4.5(f) depicting the real part of the z component of electric field shows that the resonance exhibits a dipolar nature. The field distribution on a cross section plane, also provides additional proof of the excitation of localized plasmons of the nanoholes near the top interface (Fig. 4.5(g)). On the other hand, the simulated reflection spectra for both the hole sizes do not show any noticeable dips, Fig. 4.5(b). The broad feature observed is analogous to the reflectivity profile from a bare gold film. However, as the hole size is increased the reflectivity at any given wavelength reduces. Figure 4.5(c) and (d) show the measured transmission and reflection intensities from the fabricated nanohole arrays. Also shown in Fig. 4.5(c) is the transmission through a 100 nm thick gold layer placed on top of Si₃N₄ membrane. It is clear that an increase in transmission is seen for the 50 nm hole arrays as compared to the bare film. Furthermore, transmission through the 70 nm hole

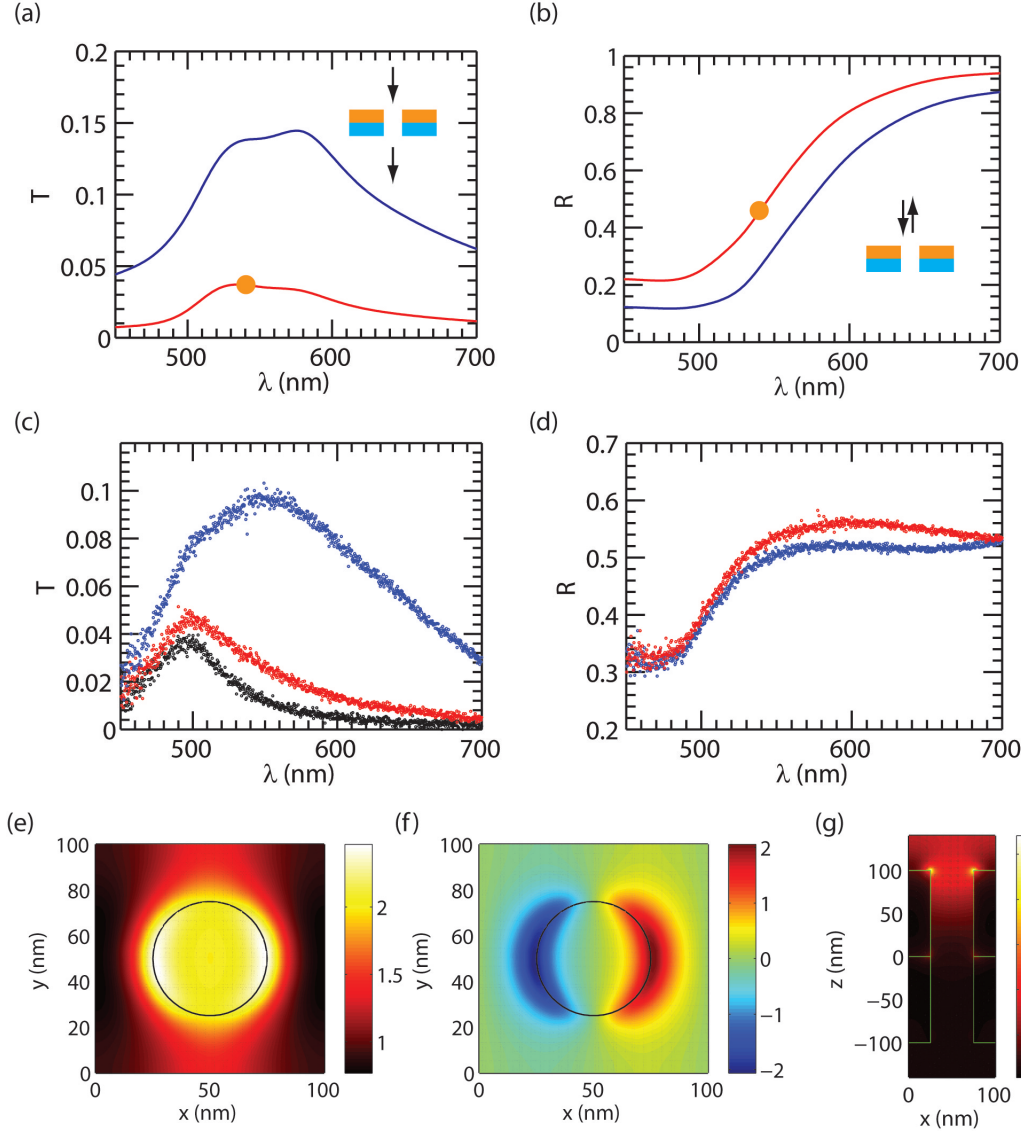


Figure 4.5: Optical properties of nanohole arrays. (a) and (c) Simulated and measured transmission spectra from the hole arrays with 50 nm (red) and 70 nm (blue) holes. The black curve in (c) shows the transmission through a 100 nm thick gold layer placed on a Si_3N_4 layer. (c) and (d) Simulated and measured reflection spectra from the hole arrays with 50 nm (red) and 70 nm (blue) holes. The direction of illumination and collection is indicated in the inset of the figure (a) and (b). All the fabricated hole arrays had 7x7 holes. Simulated plot of the (e) electric field magnitude and (f) real part of E_z on a xy -plane 5 nm above the top gold surface at $\lambda = 540$ nm. (g) Electric field magnitude on a xz -plane ($y=0$ nm).

array is higher than the transmission through the 50 nm hole array. A prominent peak close to 550 nm is also seen in case of the 70 nm holes. Two main reasons exist for increase in transmission through the nanohole arrays. First, as the hole size is increased for a given period, the volume of metal reduces, hence reducing the absorption and reflection, in turn

increasing the transmission. This is evidenced by the increase in transmission close to 500 nm, which is due to the intrinsic absorption of gold. Second, as the hole size is increased, the strength of the plasmon resonance supported by the hole increases, hence the resonant light transmission mediated by the localized plasmon is also enhanced. In case of reflection, the 70 nm hole array demonstrates a lower reflectivity as compared to the 50 nm hole array, as in the case of simulations (Fig. 4.5(d)). Note that even though the experimental measurements and simulations do not exactly match, the basic features seen via the simulations are also exhibited in the measured spectra. The differences in the experiments and the simulations could be due to the non-perfect shape of the fabricated hole array. Note that this difference between the simulation (performed assuming an hole array with infinite holes) could also be due to the limited number of holes in the fabricated sample (7x7 hole array in this particular case). Another possible origin of this discrepancy could be the difference of the dielectric constant of gold at the nanoscale as compared to that of bulk gold [373].

A point that must be mentioned here is that the transmission spectrum of the structure on incidence from the top or the bottom is the same. However, in case of reflection this does not hold true, i.e., the reflection of the structure from illuminated from the bottom shows a spectrum that differs from the spectrum for top illumination. This is so because the light is predominantly reflected from the first medium with high value of the dielectric constant and does not penetrate the material significantly. In our case, reflection measurements with top illumination, excite the localized plasmons at the gold-water interface. Whereas, for illumination from the bottom the localized plasmon at the gold-Si₃N₄ is probed.

4.3.2 Spectrum modification due to nanoparticle coupling

Let us now study the effect of including a particle in the hole. Figure 4.6 (a) and (b) shows the change in the transmission and reflection spectrum of an 50 nm hole array in the presence of a particles. The particles are placed at the center of the hole at $z = 100$ nm. Figure 4.6(a) shows that the presence of a particle in the transmission spectrum shows up as a peak, whereas, in reflection spectra a prominent dip is produced. Furthermore, the peak position of the resonance strongly red-shifts as the particle size is increased. For a particle of 40 nm, the resonance shifts by nearly 100 nm as compared to the resonance of an empty hole array. However, in case of reflection, it is difficult to measure such a shift as the resonance peak for a bare hole array is not visible in the spectrum. Even, comparing the cases of a 20 nm and 40 nm particles, a strong red-shift of nearly 80 nm is observed. It should be noted that while the resonances in both reflection and transmission spectra show a strong red-shift because of the nanoparticle, the modulation in the intensities in the two cases is very different. In case of transmission the intensity gets modified by 3-5% due to the particle, whereas in reflection a modulation of nearly 90% can be obtained (40 nm particles in 50 nm holes).

Figure 4.6 also shows the near field plots in the presence of particles. In all the cases, the fields are localized between the nanoparticles and the walls of the holes. Also, the fields in

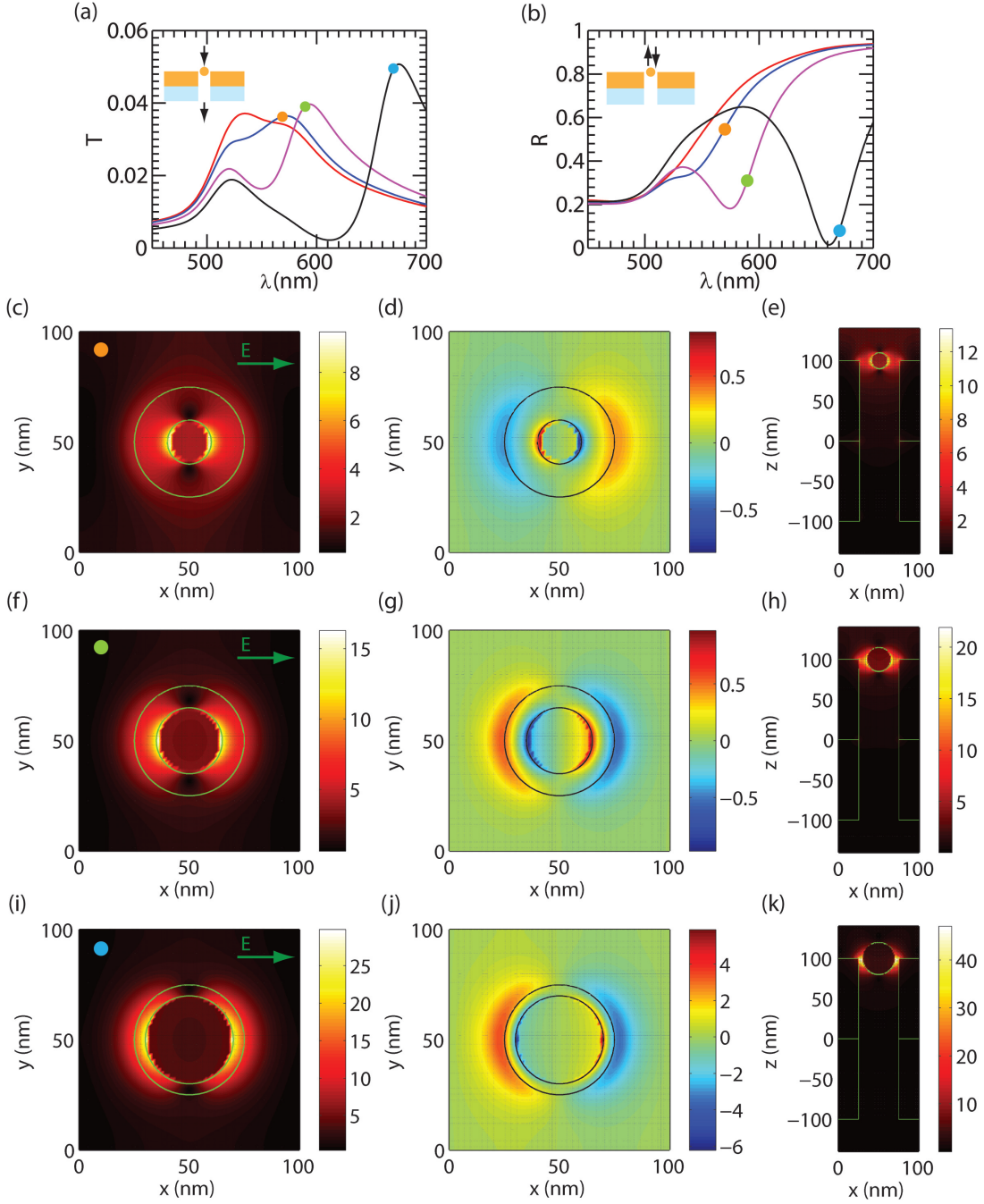


Figure 4.6: Modification of the optical spectrum due to the presence of a nanoparticle. (a) Transmission and (b) reflection spectra of the structure ($d=50$ nm, $\Lambda=100$ nm) without nanoparticle (red), with 20 nm AuNP (blue) with 30 nm AuNP (magenta) and with 40 nm AuNP (black). ((c), (f) and (i)) Total electric field magnitude and ((d), (g) and (j)) show the real part of E_z on a xy plane 5 nm above the top gold interface at $\lambda = 570$ nm, $\lambda = 590$ nm and $\lambda = 670$ nm, respectively. The incident polarization is indicated using a green arrow. The black lines show the boundaries of the particle and cylinder in the $z=0$ nm plane. (e), (h) and (k) Total electric field magnitude on a xz plane ($y=50$ nm) for $\lambda = 570$ nm, $\lambda = 590$ nm and $\lambda = 670$ nm, respectively. The dots in (a) and (b) show the wavelengths at which the fields are computed.

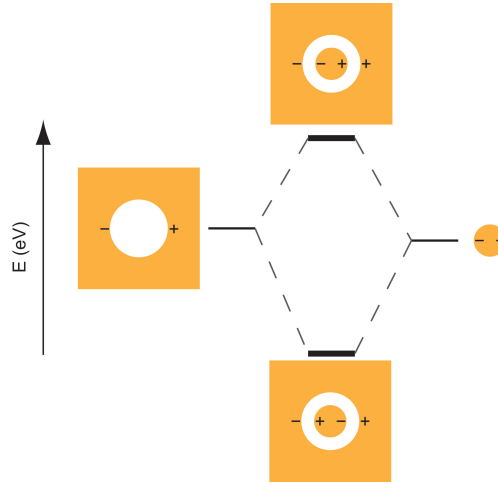


Figure 4.7: Hybridization diagram.

the presence of a nanoparticle are enhanced as compared to the fields present in an empty hole (see Fig. 4.5(e)). The electric field magnitude can be enhanced from 5.5, for an empty hole, to 45, for the case when a 40 nm particle is placed in the hole. Additional proof of the localized nature of the resonance can be seen from the cross-sectional field plots, which show that the field remains constrained between the particle and the hole. It is also evident that as the particle size is increased, the field confinement improves as the effective gap between the particle and the hole decreases. However, the charge distributions, Fig. 4.6(d), (g) and (i), show that the dipole orientations in the particle and the hole show identical distribution and are not dependent on the size of the nanoparticle. In all the cases, the dipole of the nanoparticle is aligned opposite to the dipole of the nanohole.

The drastic red-shift of the plasmon resonance can be explained using the hybridization model proposed by Prodan *et al.* [128]. The plasmon mode of the hole (close to 530 nm) hybridizes with the plasmon mode of the particle (close to 540 nm), due to spectral and spatial overlap and leads to the formation of two new modes, schematically shown in Fig. 4.7. However, in all the cases shown in Fig. 4.6 only the low energy (high wavelength) mode is observed. The low energy mode is characterized by the hole and particle exhibiting opposing dipole moments. The higher energy mode is not seen as it is strongly damped due to the interband transitions of gold close to 500 nm. Further proof of hybridization is given in the appendix D.2, where I show that both modes can be identified if the particle-hole system is placed in a high index background.

Now let us consider the effect of a 30 nm particle as its z position is modified. Figure 4.8(a) shows the transmission spectra for the various z positions of the particle. The structure is illuminated from the top and $z = 0$ nm corresponds to the gold-Si₃N₄ interface. As the particle approaches the hole, the transmission resonance of the hole red-shifts and the maximum short is observed when the particle is located at $z=100$ nm. As the particle is moved further in the hole, a blue shift in the resonance is seen. This occurs because of reduction in the

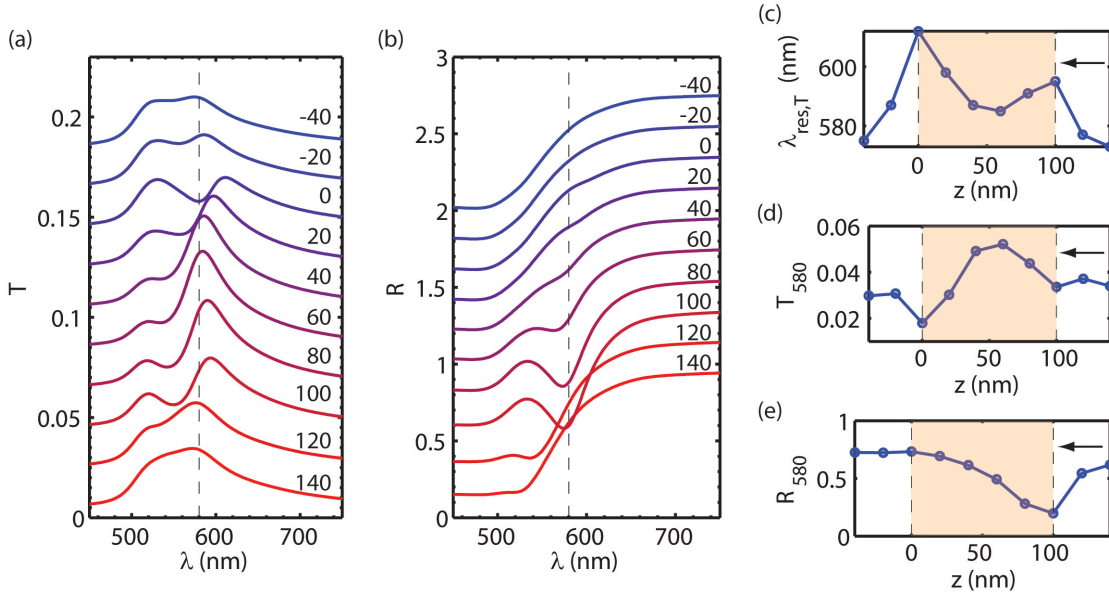


Figure 4.8: Modification of the spectrum due to particle position. (a) Transmission and (b) reflection spectra for various z positions of the particle. The transmission and reflection spectra are shifted by 0.02 and 0.2 respectively for clarity. $z=0$ indicates gold- Si_3N_4 interface and $z=100$ indicates the gold-water interface. (c) Transmission resonance wavelength, (d) transmission intensity at 580 nm and (e) Reflection intensity at 580 nm as a function of the z position of the particle. The illumination direction is indicated by the black arrow.

coupling between the plasmon of hole at the top interface and the particle plasmon. However, as the particle starts approaching the Si_3N_4 , a second red-shift is seen. This occurs due to the increased coupling between the particle plasmon and the plasmon of the hole at the gold- Si_3N_4 interface. Finally, as the particle leaves the gold film, i.e. $z < 0 \text{ nm}$, the resonance again exhibits a blue shift. The resonance positions extracted from the spectra for various particle positions are presented in Fig. 4.8(c). The shifts due to the particle, as explained previously, become amply clear from this figure. Therefore, the particle position in the nanohole can be inferred from its transmission spectrum. Additionally, it is also possible to monitor the transmission intensity at a given wavelength to obtain the z -position of the particle, as shown in Fig. 4.8(d). The transmission intensity as a function of z position also exhibits a behavior that is similar to that of the resonance wavelength.

The reflection spectra also exhibit a strong dependence on the particle position, as shown in Fig. 4.8(b). However, reflection and transmission spectra get modified differently due to the change in particle position. As the particle approaches the hole, a strong modulation is seen in the reflection spectra. The maximum modulation is seen when the particle is located at $z=0 \text{ nm}$. As the particle goes through the hole, the signal keeps decreasing progressively. The same is evident from the trace of reflection intensity at 580 nm as a function of z position, Fig. 4.8(e).

To study the detection limit of the nanohole arrays for particle sensing, I studied the effect

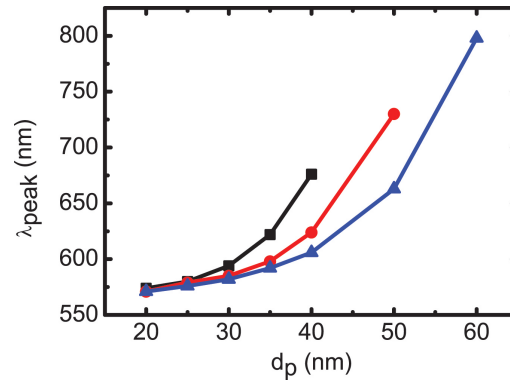


Figure 4.9: **Detection limit for nanoparticle sensing.** Peak wavelength (λ_{peak}) extracted from transmission spectra as a function of gold particle size (d_p) for hole diameters of 50 nm (black), 60 nm (red) and 70 nm (blue). The particles are placed at the center of the hole on a $z=100$ nm plane and the structure is illuminated with a plane wave propagating in the $-z$ direction and polarized along x axis.

of various particle size-hole size combinations. Figure 4.9 shows the peak positions of the transmission spectrum due to the presence of particles in hole arrays with different sizes. By varying the hole size from 50 nm to 70 nm, the dynamic range as well as the limit of detection can be controlled. For example, using a 50 nm hole array allows the detection of particles in the size range of 20 to 40 nm. However, if 70 nm hole arrays are used instead, particle sizes in the range of 20 nm to 60 nm can be analyzed. Although, the dynamic range can be increased by increasing the hole size, this is at the cost of loss of sensitivity for detection of smaller particles. Therefore, an appropriate choice of the nanohole array is necessary for the best sensing capabilities. This method can be extended to detect particles with even smaller sizes by correspondingly reducing the hole diameters.

4.3.3 Limitation of periodic simulations

As mentioned previously, periodic SIE is used for computing the optical response of the nanohole array structures. This simulation routine places the constraint that only two extreme cases can be considered: either all the holes are empty (without particles) or completely filled (with particles). However, in an experiment such a situation is highly unlikely and spectral modification due to partial filling of the hole array must be considered. However, full numerical simulations of such systems, with only some holes filled, are difficult and beyond the scope of the numerical tools available. To predict the response of a system with partial filling of the holes, two approaches are used. The first is based on using periodic SIE with a larger unit cell while the second is based on the linear combination of the two extreme cases.

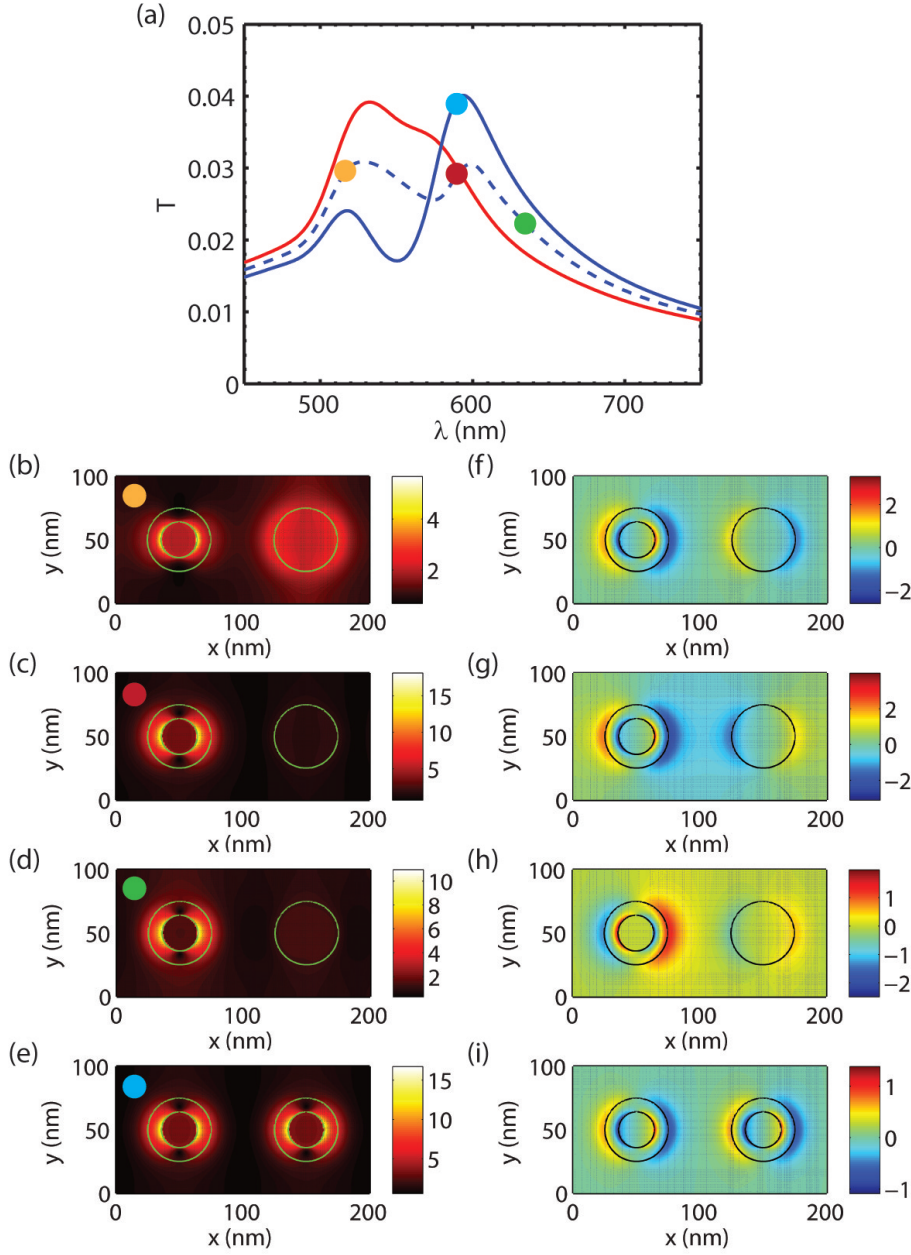


Figure 4.10: **Particle filling of the hole array with nanoparticles.** (a) Simulated transmission spectra of a hole array taking two holes as the unit cell for the case when no holes contain particle (red), a single hole contains a particle (dashed blue) and both holes contains a particle (solid blue). The dots indicate the wavelengths at which the electric fields are computed. (b)-(d) Total electric field magnitude and (f)-(h) real part of E_z for the case when a single hole is filled at $\lambda = 530$ nm, $\lambda = 590$ nm and $\lambda = 640$ nm, respectively. (e) Total electric field magnitude and (i) real part of E_z for the case when both the holes are filled at $\lambda = 590$ nm. The particles are always placed symmetrically on the $z=100$ nm plane and the fields are computed on a plane with $z=105$ nm. The structure is illuminated with a plane wave propagating in the $-z$ direction and polarized along x .

Supercell based numerical simulations

Consider a hole array with $d = 50$ nm and $\Lambda = 100$ nm as studied earlier. However, for simulating this structure using periodic SIE, I choose two holes as the unit cell in contrast to the single hole unit cell considered previously. Additionally, I choose these two holes of the unit cell to be along the x axis giving an effective period of 200 nm in the x direction and 100 nm in the y direction. Using these simulation parameters it is possible to investigate three distinct cases: either both the holes are empty, only one of the holes is filled and both the holes are filled with gold nanoparticles. These three cases correspond to filling fraction, f , equal to 0, 0.5 and 1, respectively. The transmission spectra for the various cases are shown in Fig. 4.10(a). As the filling fraction is increased, the peak at around 600 nm becomes more prominent whereas the peak at around 530 nm is diminished. Furthermore, the spectra corresponding to $f=1$, corresponds closely with the spectra computed considering a hole as the unit cell (Fig. 4.6).

The electric field magnitude as well as the real part of E_z ($Re\{E_z\}$) are for the different cases are also plotted in Fig. 4.10. For $f=0.5$, it is seen that the empty hole has the maximum field magnitude around $\lambda = 530$ nm (Fig. 4.10(b)) whereas the hole with the particle at around $\lambda = 590$ nm (Fig. 4.10(c)). Note that the maximum field magnitude for the empty hole occurs at identical wavelengths even in the case when $f=0$, i.e. all the hole are empty. This clearly shows that the presence of a particle in one of the holes does not modify the near field features of the neighboring hole in the array. The plots of $Re\{E_z\}$ also supplement this conclusion. $Re\{E_z\}$ indicates the orientation of the dipoles in the structure and the dipole orientation flip when one traverses across a resonance. For example, if the dipole moment is oriented along the $+x$ direction for wavelengths smaller than the resonance wavelength, then it will be oriented along $-x$ for wavelengths greater than the resonance wavelength. For the empty hole $Re\{E_z\}$ flips sign for wavelength between 530 nm and 590 nm (Fig. 4.10(f) and (g)), whereas for the filled hole flips for a wavelength between 590 nm and 640 nm (Fig. 4.10(g) and (h)). This again validates the fact the two holes do not couple strongly. This is because the distance between the two hole ensures that lower order grating modes are not excited which prevents coupling of the holes via propagating surface plasmons. Also, the separation between the holes is sufficiently large so that near field coupling is also minimized. For $f=1$, the field gets maximized around $\lambda = 590$ nm and this is identical to the maximum field magnitude observed for the hole filled with a particle in the case of $f=0.5$ (Fig. 4.10(c) and (e)). In the case when both the holes are filled, $Re\{E_z\}$ shows that both the hole show identical features as expected (Fig. 4.10(i)).

Linear combination approximation

I also use the linear combination of the two extreme cases, i.e. completely filled holes and totally empty holes, for estimating the response of a system with partial filling. For example, if $S_{f=1}$ and $S_{f=0}$ correspond to the spectra of a hole array with all the holes filled ($f=1$) and

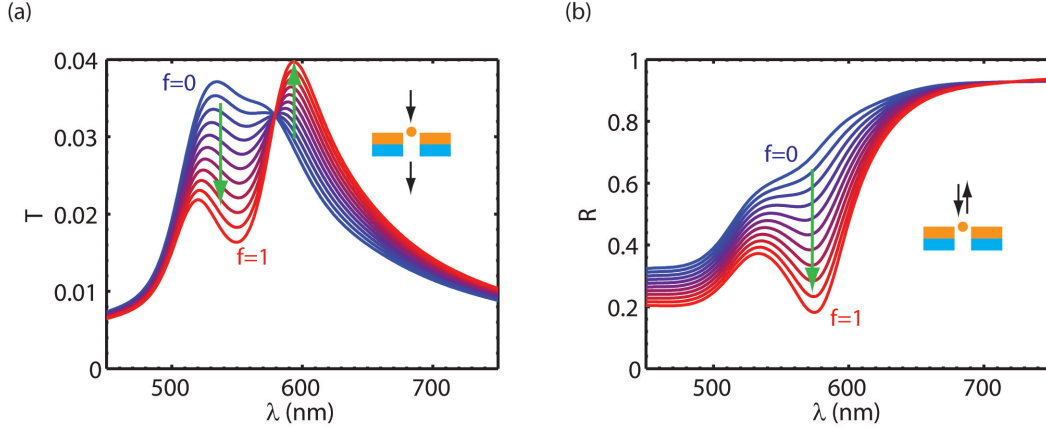


Figure 4.11: **Optical spectra for different filling fractions of the hole array.** (a) Transmission and (b) reflection spectra computed using the linear approximation approach for different filling fractions (blue - $f=0$ and red - $f=1$) of 30 nm gold particles in a 50 nm hole array. The particles are placed symmetrically on $z=100$ nm plane. The illumination and collection directions are shown in the inset of the figure.

empty ($f=0$), respectively, then the response of a partially filled hole array is given by

$$S_f = f S_{f=1} + (1 - f) S_{f=0}. \quad (4.1)$$

Note that this relation holds true for both reflection and transmission spectra. Figure 4.11(a) and (b) shows the results for the case of a 50 nm hole array with $\Lambda = 100$ nm and 30 nm gold particles. A single hole was taken as the unit cell in the simulations ($\Lambda_x = 100$ nm and $\Lambda_y = 100$ nm). In case of the transmission spectra, the peak at around 590 nm becomes more prominent as f is increased whereas the peak at 530 nm diminishes. This is similar to the results obtained in the case of partial filling shown in the previous section. In contrast, the dip in the reflection spectra at around 590 nm gets more pronounced as the f is increased. Additionally, the reflectivity at all wavelengths decreases on increasing the filling fraction, f .

Effect of number of holes in the array

The SIE simulations performed for computing the response of the hole array structures incorporate periodic boundary conditions. Physically this corresponds to the response of an hole array with infinite number of holes. However, experimentally only a finite sized array can be fabricated. To study this samples with differing number of holes (5x5, 7x7 and 15x7 holes) are fabricated. The transmission measurements of the structures are shown in Fig. 4.12. It is seen that as the number of holes in the array is increased, the transmission intensity increases. However, the line shape of the transmission spectrum is not strongly affected by the number of holes. Additionally, even a 5x5 hole array shows noticeable difference in transmission as

compared to a bare gold film. However, as differential signals rather than absolute transmission intensities are employed for the detection of nanoparticles, the number of holes should not have a limiting effect on the measurements.

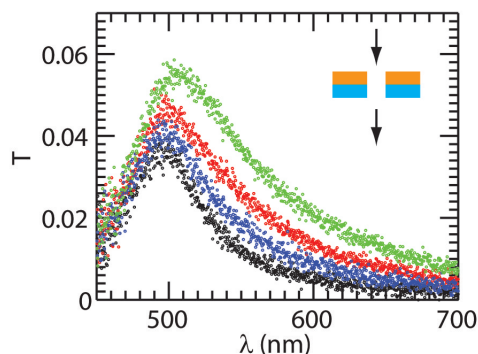


Figure 4.12: **Effect of number of holes in the array on the normalized transmission.** Measured transmission spectra for 50 nm hole arrays with 5x5 holes (blue), 7x7 holes (red) and 15x7 holes (green). The black curve shows the transmission through a bare 100 nm thick gold film. The illumination and collection directions are indicated by the black arrows in the inset.

4.3.4 Experimental measurement of particle size

The motivation for developing this technique was to characterize the particle biosynthesized by human cells described in Chapter 3. Unfortunately, the large protein corona surrounding these particles did not let them pass through the aperture and - in spite of numerous trials - I was not able to record the corresponding signal. Here I report on experiments based on commercial citrate stabilized gold nanoparticles, for which the experiments are conclusive.

The experimental detection of nanoparticles using the hole array structure is presented in this section. Figure 4.13(a) shows the schematic of the sample chamber used in the experiment. Two chambers are created with the help of O-rings (1 mm thickness) on the top and bottom of the silicon wafer with the hole arrays. The top chamber is filled with 30 nm AuNP suspension (purchased from BBI international). During the nanoparticle experiment 30 μL of the stock concentration of the nanoparticles ($2 \cdot 10^{11}$ particles per mL) is added to fill the top chamber. The chamber is sealed by placing a thin cover-slip on top of the O-rings. The bottom chamber is filled with 30 μL of Milli-Q water (resistivity of 1 M Ω -cm) and close with the help of another cover-slip. In case of control experiments the top chamber is also filled with 30 μL of water. The sample is illuminated from the bottom (Si_3N_4 side) and the reflected light analyzed using a spectrometer (see Sec. 4.2.3 for further details). The main motivation for using reflection is that the signal progressively increases as the particle traverses the hole, therefore allows us to infer the position of the nanoparticle. Secondly, due to the high reflection intensity, the integration time can be lowered significantly as compared to identical transmission measurements. This allows us to obtain better temporal resolutions in these measurements. However, note that this is a limitation of the current experimental setup and not that of the physical system.

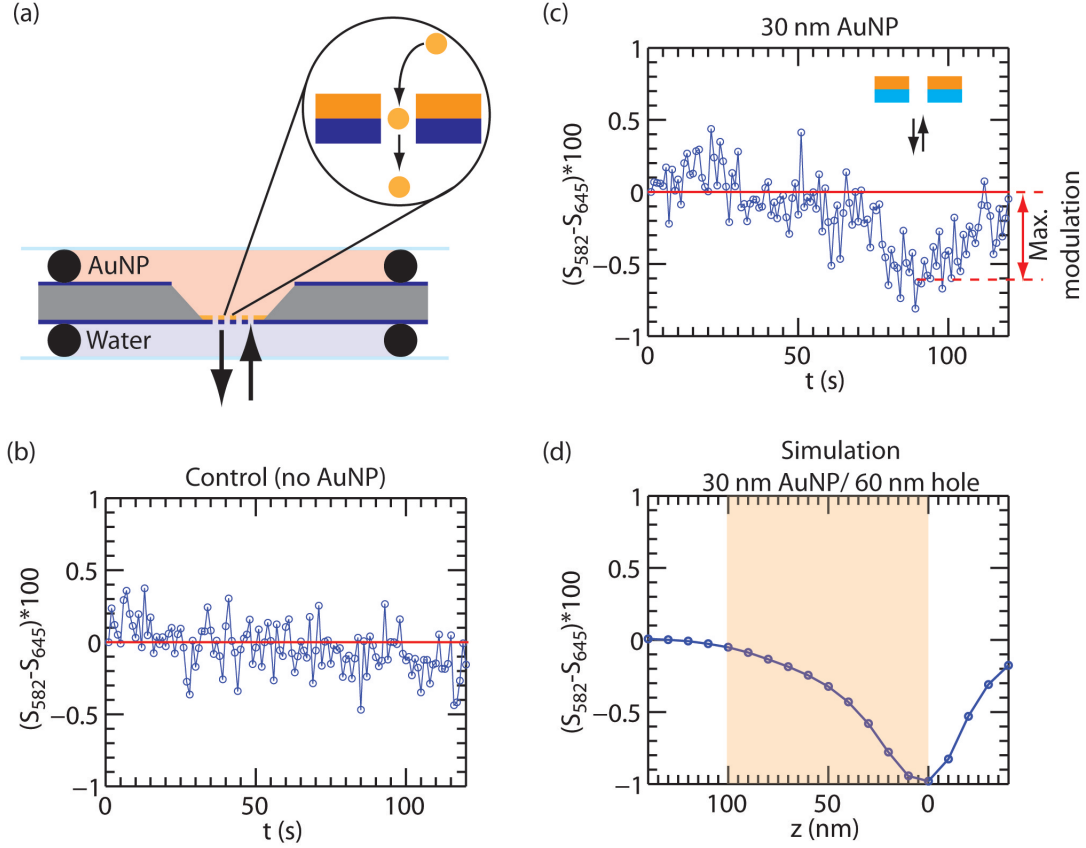


Figure 4.13: **Experimental detection of a single 30 nm particle.** (a) Schematic of the sample used for nanoparticle detection experiment. The top chamber is filled with 30 nm AuNP solution and the bottom chamber is filled with water. (b) The difference of the normalized differential reflectivity, $S_{582}(t) - S_{645}(t)$, as a function of time for the control experiment. In the control experiment, the AuNP solution in the top chamber is replaced with water. (c) The difference of the normalized differential reflectivity, $S_{582}(t) - S_{645}(t)$, as a function of time for the particle detection. 30 nm AuNP solution at stock concentration is filled in the top chamber. The inset shows the illumination and collection direction. (d) Simulated normalized differential reflectivity as a function of particle position in the nanohole. $z=0$ nm and $z=100$ nm correspond to the gold- Si_3N_4 and gold-water interface, respectively.

As shown before, the spectral modification due to a single particle can be small and hence I employ the normalized differential reflectivity defined as

$$S(\lambda, t) = \frac{R(\lambda, t) - R_{\lambda, f=0}}{R_{\lambda, f=0}} \quad (4.2)$$

for determining the particle presence. In this equation $R(\lambda, t)$ is the reflectivity at a wavelength λ measured at a time t and $R_{\lambda, f=0}$ is the reflectivity at a wavelength λ for the same hole array

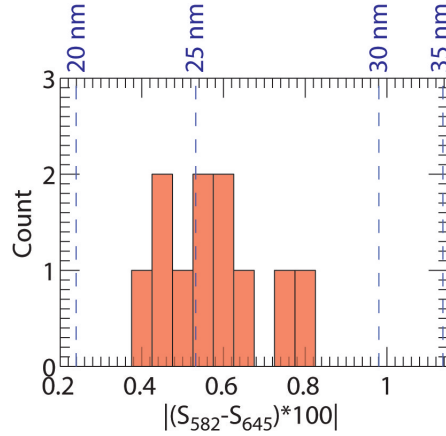


Figure 4.14: **Histogram of differential signals.** Histogram showing the maximum of the relative differential signals, $S_{582} - S_{645}$, measured from a 60 nm hole array structure with 30 nm AuNP. The dashed lines indicate the expected signals for different particle sizes computed using SIE simulations coupled with the linear combination method.

in water (in the absence of any nanoparticles).

All the experiments are performed using a 60 nm hole array with a period of 100 nm. The array has 7x7 holes in total. The acquisition time for each spectra is 2 ms and the time delay between successive measurements is 1 s. Figure 4.13(b) shows the time dependent normalized differential signal ($S_{582}(t) - S_{645}(t)$) for the case when both the top and the bottom chambers are filled with water. In this case, no significant modulation of this signal is seen. However, when the top chamber is filled with the 30 nm particle solution, modulations in the temporal signal can be observed, Fig. 4.13(c). Note that initially the signal is close to zero (at $t=0$ s) and then it reduces to -0.7 at $t=60$ s. Again for longer times the signal approaches 0 again (at $t=120$ s). This dip in the temporal signal is a typical signature of the presence of a nanoparticle in the nanohole array. To substantiate that the dip is a signature of the gold nanoparticle, simulations using periodic SIE are performed. Furthermore, I use the linear combination approach, detailed in Sec. 4.3.3, for estimating the signal due to filling just 1 hole with a particle in a 49 hole array. Figure 4.13(d) shows the differential signal ($S_{582} - S_{645}$) as a function of particle position computed using the simulations assuming only 1 out of the 49 holes are filled with a particle. Note that $z \leq 0$ nm corresponds to the Si_3N_4 membrane. As the particle traverses the hole (from $z=140$ nm to $z=-40$ nm) the normalized differential signal progressively becomes more negative till $z=0$ nm. After this, the signal again shows an increase and approaches 0 for $z=-40$ nm. Notice that the line shape obtained from the simulations is similar to the one acquired experimentally, Fig. 4.13(b). However, only some of the measurements performed exhibit the modulation corresponding to the presence of the nanoparticle. This is because the particle enters the hole via diffusion, which is not very efficient. Figure 4.14 shows the histogram of the maximum modulation (double sided red arrow Fig. 4.13(c)) observed in multiple sets of experiments for the same hole array and particle size. Also shown in the histogram are the simulated values of the maximum modulation for

various particle sizes (20, 25, 30 and 35 nm) with a 60 nm hole array. The histogram shows that the signals measured correspond to particles in the size range of 20-30 nm with the mean close to 25 nm. This shows a good match with the expected mean size of 30 nm. However, further optimization of the experimental apparatus as well as data analysis is necessary to achieve a better quantitative size histogram.

4.3.5 Gold nanoshells: Identification of the core diameter

Gold nanoshells, with a dielectric core and gold shell, have been extensively used for the photothermal therapy of cancer [77,374]. Like in the case of other plasmonic structures, the resonance of gold nanoshells can be tuned by controlling the core-shell diameter ratio [148, 375,376]. Therefore, for the same size of the shell (outer diameter), the core diameter can be changed to control the resonance wavelength [375]. As in the case of solid spherical particles, prior to their use the synthesized gold nanoshells must be characterized for confirming both their inner and outer diameters. Most of the light scattering techniques only provide information about the outer diameter and are unable to provide information about the internal structure of the particle. Therefore, in most of the past studies involving gold nanoshells the properties of the core were confirmed by the use of electron microscopy [77,374]. In contrast to these techniques which are insensitive to the plasmon resonance, the technique developed here for detection of nanoparticles is inherently based on the coupling between the resonance of the particle with that of the hole. Therefore, I theoretically demonstrate that it is possible to infer the diameter of a core-shell particle via this method. Figure 4.15 shows the calculated transmission spectra from the hole arrays due to the presence of the gold nanoshell (gold shell and dielectric core) with varying core size. The outer diameter of the shell is kept fixed at 30 nm and the dielectric constant of the core is taken to be 1.7689 (water). It is clear that

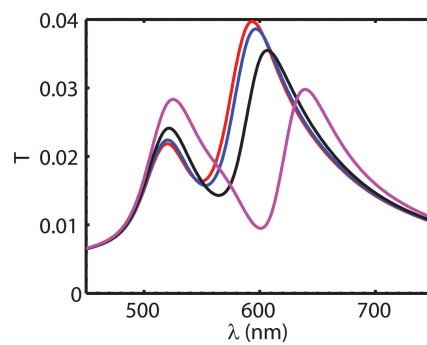


Figure 4.15: **Determining the core size in the case of gold nanoshells.** Transmission spectra of 50 nm hole array with hollow gold nanoshells (dielectric constant of core is 1.7689) with varying inner diameters : 10 nm (blue), 15 nm (black) and 20 nm (magenta). The spectrum due to the presence of a solid 30 nm gold particle is shown in red. The outer diameter is kept fixed at 30 nm and the particle placed at the top gold interface ($z=100$ nm). The structure is illuminated with a plane wave propagating in the $-z$ direction and polarized along x axis.

as the core diameter is increased, the peak wavelength of the transmission also red-shifts. For a core diameter of 10 nm the resonance is located at 590 nm which shifts to 640 nm for a core diameter of 20 nm. This behavior occurs due to the red-shift of the resonance of gold shell, which finally shifts the resonances of the coupled system. Therefore, by measuring the resonance wavelengths, it is in principle possible to infer the core diameter in case of a gold nanoshells if the outer diameter is known.

4.4 Summary

In this chapter, a technique for the detection of gold nanoparticles using nanohole arrays in the size range of 20 nm to 60 nm is studied. The detection is based on the hybridization of the plasmon resonance of the particle with that of the hole. Using numerical tools, I have studied the detection limits for particle size as well as the effect of geometrical parameters on the particle sensing characteristics. It is shown that the reflection spectrum from the hole arrays can be used for inferring the vertical position of the nanoparticle in the holes. Experimental demonstration of the proposed technique is also presented, whereby a single 30 nm particle is detected using the hole arrays. Finally, an extension of this method for determining the core size of gold nanoshells is also demonstrated theoretically.

5 Eigenmodes of plasmonic nanoclusters and their effect on polarization conversion and second harmonic generation

Many practical applications, which use plasmonic structures, involve the interaction of multiple plasmonic modes for optimized performance. Additionally, assemblies of plasmonic nanoparticles possess exotic properties which strongly depend on the modes supported by the structure. In this chapter, I extend the Green's tensor formalism to compute the eigenmodes of an assembly of plasmonic nanoparticles. Using the developed technique, I investigate the modes of a nanoparticle monomer, dimer, trimer and quadrumer. The influence of various geometrical parameters and symmetry breaking on the eigenmodes of the assemblies is studied in detail, as well as the illumination conditions required to excite specific eigenmodes. In the second part of this chapter, I study the effect of modes on polarization conversion and second harmonic generation from such clusters. Specifically, it is shown that the second harmonic intensity and pattern strongly correlate with the plasmonic modes located at the second harmonic wavelength.

5.1 Introduction

Metallic nanostructures supporting plasmon resonances have been used in various applications such as SERS [52, 53, 65, 116, 377], bio-sensing [1, 13, 16, 378], plasmonic trapping [87, 88, 92], and fluorescence enhancement [38, 43, 44, 379–381]. In addition to these applications, plasmonic resonances have also been exploited for enhancing non-linear signals like second harmonic generation [382–385], third harmonic generation [386, 387] and four-waves mixing [388] and have been used in applications such as nonlinear optical sensing [337, 389], nonlinear optical characterization [390–392], and nonlinear imaging [393, 394]. This high non-linear signal enhancement arises because of the high near field generated at the plasmon resonance. Optimization of a plasmonic structure for a particular application is made easier via the use of various computational tools. A large number of numerical techniques available like FEM [395–397], Green's tensor approach [266, 398, 399], discrete dipole approximation

(DDA) [400, 401], boundary elements method (BEM) [402–405], and surface integral equation (SIE) [267, 372, 406] compute the linear optical response of the structure due to an incident excitation. In cases involving nonlinear processes numerical methods computing the non-linear response are also used in conjunction with linear solvers [407–413].

In many situations, it is also beneficial or even necessary to determine the eigenmodes of the plasmonic system. However, only a rather limited number of numerical techniques that compute the eigenmodes of a plasmonic system are available [414–422]. For example, an electrostatic eigenmode solver based on the boundary integral equation was used to show that the near field of the plasmonic structures could be expressed as the linear superposition of the eigenmodes [422]. The knowledge of the modes and its relevance to near field provided a simple method for the identification of hot spots necessary for plasmon enhanced spectroscopies. This approach can be extended a step further to control and localize hot spots in plasmonic aggregates through the knowledge of underlying plasmonic modal structure [423]. In contrast to techniques that compute the eigenmodes of a plasmonic structure by full numerical calculations, it is also possible to exploit symmetry properties by using group theory to study the interaction of an external electric field with the localized plasmon modes of the structure as shown by Zhang *et al.* [420]. With this approach, they showed that the selection rules for a vector field are different as compared to the selection rules for a scalar field. The knowledge of eigenmodes of a plasmonic system can also be exploited for increasing the accuracy and speed of a numerical technique [424]. However, it should be noted that the discretization of the structure necessary for computing the eigenmodes of the plasmonic structure using numerical techniques, even within the electrostatic limit, makes the solvers time consuming and memory intensive [128, 331, 421, 422]. Furthermore, many of these techniques require initial guess values of the modes for accurate computation. On the other hand for simple structures it is possible to exploit the symmetry of the structure to compute the modes using dielectric constant as the eigenvalue of the system [420, 425, 426]. Even though eigenvalue analysis in the electrostatic approximation is easier and faster, the absence of retardation in the computation limits its applicability.

In this chapter, I extend the Green's tensor approach to compute the eigenmodes of a plasmonic structure composed of small nanoparticles. Our computation is fully vectorial and takes into account the retardation present between the nanoparticles. The developed technique is then used to analyze the eigenmodes of a nanoparticle monomer, dimer, trimer and quadrumer. Even though linear near field of plasmonic structures have been studied in terms of their modes, very few studies exist that correlate the modes with the generated non-linear signal. While the nonlinear optical response of complex nanoclusters can be numerically evaluated [405, 427–429], the role played by each individual plasmon mode is difficult to assess unless coupled with eigenmode analysis [430]. Hence, it is difficult to obtain a description of the nonlinear response of a plasmonic cluster in terms of its underlying modal structure, which is important for optimizing its nonlinear response [162, 431]. I will therefore also extend the developed formalism to for understanding second harmonic generation.

5.2 Theoretical formulation

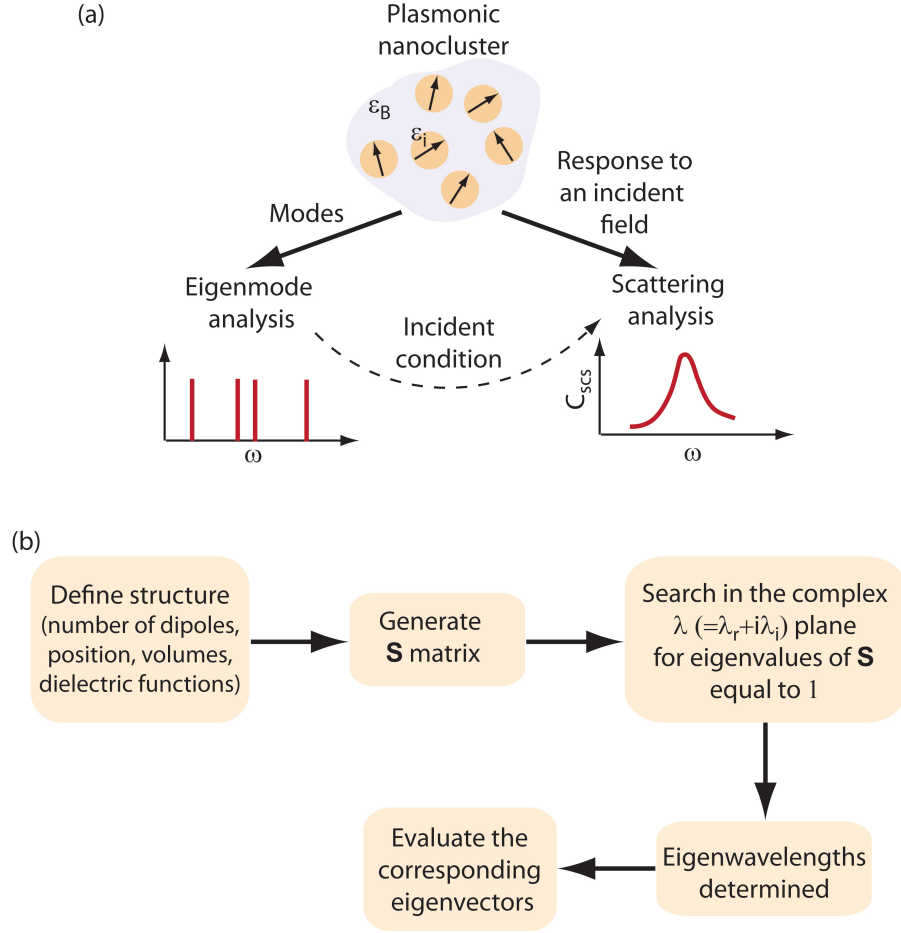


Figure 5.1: **Eigenmode computation.** (a) Schematic showing two distinct computational methodologies. (b) Schematic illustrating the principle steps involved in the computation of the eigenwavelengths.

In general, two distinct approaches exist for understanding the optical response of plasmonic nanoclusters, schematically shown in Fig. 5.1(a). The first approach involves the computation of the response due to a particular incident condition and is often termed as the scattering analysis. This analysis can be used to calculate the scattering and absorption spectra as well as the near field intensity. An alternative way of visualizing the response involves determination of the eigenmodes of the system which are independent of incident conditions. Additionally, once the modes of a plasmonic cluster are known, the optical response of the system due to any incident condition can be computed easily. However the inverse problem, i.e. the determination of the modes from scattering analysis, is quite difficult and in most cases not all the modes can be extracted. This is because for most incidence conditions only a few modes are excited at most. For example, in case of plasmonic clusters only those modes that exhibit a net non-zero dipole moment can be excited using plane wave illumination.

5.2.1 Eigenmode calculation

Consider a system of n nanoparticles placed in a background medium with dielectric constant ϵ_B . In systems where the particle size is significantly smaller than the wavelength of light, each nanoparticle can be represented by a single dipole with a finite polarizability [398]. In this chapter, I assume that each nanoparticle is represented by a single dipole with an arbitrary orientation. The response of this generalized n nanoparticle system can be calculated using the Green's tensor technique [266], where the field at each particle i is given by

$$\mathbf{E}_i = \mathbf{E}_i^0 + \sum_{j=1, j \neq i}^n \mathbf{G}_{ij} \cdot k_0^2 \Delta\epsilon_j V_j \mathbf{E}_j + \mathbf{M}_i \cdot \Delta\epsilon_i k_0^2 \mathbf{E}_i - \mathbf{L}_i \cdot \frac{\Delta\epsilon_i}{\epsilon_B} \mathbf{E}_i, \quad (5.1)$$

where \mathbf{G}_{ij} is the background Green's tensor, k_0 is the vacuum wavenumber, $\Delta\epsilon_i (= \epsilon_i - \epsilon_B)$ is the dielectric constant contrast, \mathbf{L}_i is the depolarization term, \mathbf{M}_i is the self term, \mathbf{E}_i^0 is the incident field at dipole i , and V_i is the volume of the particle. In this equation the interaction between two interacting particles, i and j , is given by the tensor \mathbf{G}_{ij} which depends on k_0 . Since a single dipole is assigned to a single nanoparticle, the self consistent fields computed using Eq. (5.1) also correspond to the dipole moments of the corresponding particles. This set of equations can be recast into the matrix form,

$$(\mathbf{I} - \mathbf{S}) \cdot \mathbf{E} = \mathbf{E}^0, \quad (5.2)$$

where \mathbf{I} is the identity matrix, \mathbf{S} is the matrix that defines the system, \mathbf{E}^0 and \mathbf{E} are vectors corresponding to the incident fields and self-consistent electric fields at the dipoles, respectively.

The matrix \mathbf{S} depends on the dielectric constant of the nanoparticle and we use the Drude model given by

$$\epsilon = \epsilon_\infty - \frac{\omega_p^2}{\omega^2 + i\gamma\omega}, \quad (5.3)$$

with $\epsilon_\infty = 9.5$, $\omega_p = 1.36 \cdot 10^{16}$ rad/s and $\gamma = 1.05 \cdot 10^{14}$ rad/s [375] for computation of the modes in Sec. 5.3.1, 5.3.2 and 5.3.3. These Drude parameters match well the experimentally measured dielectric function of gold in the 600 – 900 nm wavelength range. For rest of the calculations (Sec. 5.4 and 5.5) the modified Drude model proposed by Etchegoin *et al.* [432], which incorporates the interband transitions of gold is used. Note that the different terms of the matrix \mathbf{S} also depend on the wavelength of light, because of the non-electrostatic nature of the current formalism. However, it must be pointed out that a direct relation exists between the dielectric function and the wavelength, and frequency, as given by the Drude model. For eigenmode computation of the system, I further enforce the condition that the incident field is zero. Therefore, Eq. (5.2) reduces to

$$(\mathbf{I} - \mathbf{S}) \cdot \mathbf{E} = \mathbf{0}. \quad (5.4)$$

The eigenmodes of this system can be determined by locating the parameters at which \mathbf{E} is

non-zero. Let $\xi(\lambda)$ be the eigenvalue of the matrix \mathbf{S} at a given wavelength λ . It is evident that for $\xi(\lambda) = 1$, non-zero \mathbf{E} are possible. The corresponding wavelengths are the eigenwavelengths of the system. In plasmonics, \mathbf{S} is a complex matrix and the equation $\xi(\lambda) = 1$ is not satisfied for purely real λ . Therefore, in order to solve Eq. (5.4) a complex wavelength, $\lambda = \lambda_r + i\lambda_i$, must be assumed. Corresponding to this complex eigenwavelength, the complex eigenfrequency can be calculated using $\omega = 2\pi c/\lambda$, where c is the speed of light in vacuum. A schematic of the various critical steps involved in the computation of the eigenmodes is shown in Fig. 5.1. Such complex eigenwavelengths or eigenfrequencies are also found in other physical systems like damped harmonic oscillators [433], and RLC circuits [434]. The real and imaginary parts of the eigenwavelength of a mode correspond to the resonance position and half-width of the resonance, respectively [433]. The eigenvector of the matrix \mathbf{S} at the eigenwavelength provides the electric field distribution for the given mode. Fig. 5.1(b) shows a flow diagram indicating the critical steps of the eigenmode analysis.

5.2.2 Second harmonic (SH) calculation

The SHG computations presented in this chapter have been performed using the SIE method reported in Ref. [405]. Note that this method has been recently extended to periodic nanostructures [336]. The SIE method for SHG is only briefly described here and the reader is referred to previous publications for the numerical implementation details [336, 405]. The linear surface currents, which are expanded on Rao-Wilton-Glisson (RWG) basis functions [406, 435], are used for the evaluation of the fundamental electric fields just below the gold surfaces and then used for the calculation of the surface SH polarization. Only the component $\chi_{S,\perp\perp\perp}$ of the surface tensor, where \perp denotes the component normal to the surface, is considered since recent experiments indicate that this term dominates the surface response of metallic nanoparticles [436]. Note that other contributions to the SH signal, namely the component $\chi_{S,\parallel\parallel\perp}$ of the surface tensor (where \parallel denotes the component tangential to the surface), as well as bulk contribution, are theoretically allowed but these contributions weakly contribute to the total SH response [436, 437]. Furthermore, the present work is focused on the role played by the plasmon eigenmodes in the SHG enhancement from nanoparticle assemblies and the following discussion is valid whatever the nonlinear sources. In the present case, only the normal component of the nonlinear polarization does not vanish which can be written as

$$P_{\perp}(\mathbf{r}, 2\omega) = \chi_{S,\perp\perp\perp} \mathbf{E}_{\perp}(\mathbf{r}, \omega) \mathbf{E}_{\perp}(\mathbf{r}, \omega). \quad (5.5)$$

The SH surface currents are obtained solving the SIE formulation taking into account the nonlinear polarization and enforcing the boundary conditions at the nanostructure surfaces [438]. Like the linear surface currents, the SH surface currents are expanded on RWG basis functions. The expanding coefficients are found by applying the method of moments with Galerkin's testing [406]. A Poggio-Miller-Chang-Harrington-Wu formulation is used to ensure

accurate solutions even at resonant conditions [266,437]. The SH electric field is then deduced from the SH surface currents using a singularity subtraction method for the evaluation of the Green's functions [406]. The surface of the plasmonic nanostructures is discretized with a triangular mesh with typical side of 2 nm.

5.3 Eigenmodes of nanoparticle clusters

In this section, I first study the modes of a single nanoparticle as a function of the system parameters and show that the eigenmodes computed using the current formalism converge

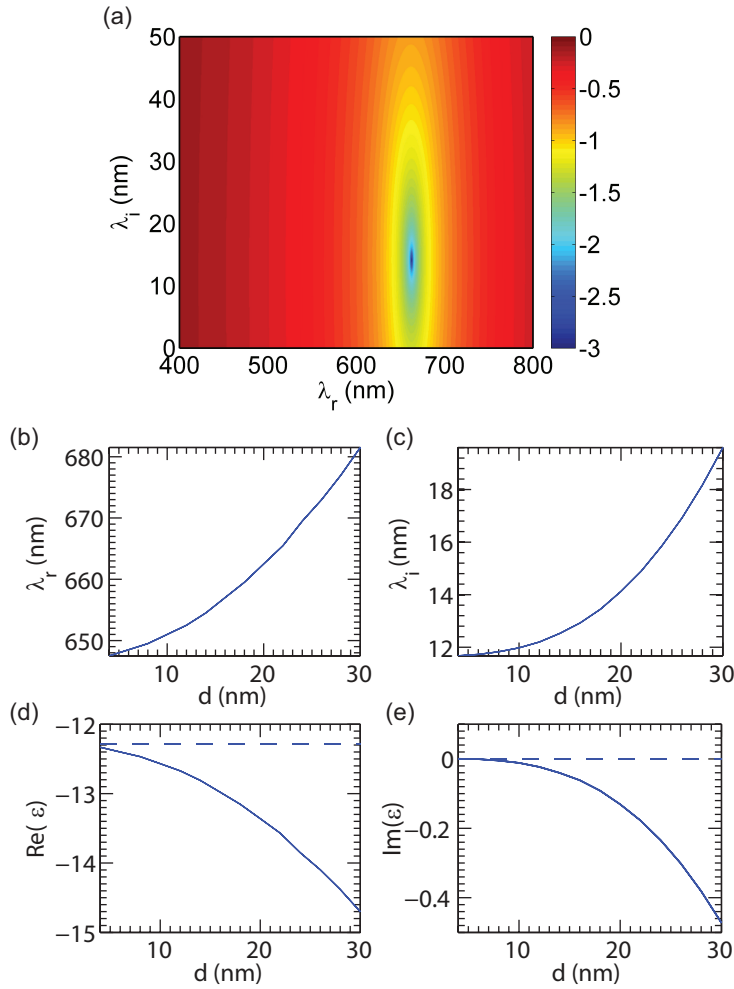


Figure 5.2: **Modes of a nanoparticle monomer.** (a) $\log_{10}|\xi - 1|$ plotted as a function of the real and imaginary parts of wavelength, λ , for a 20 nm gold particle. (b) Real and (c) imaginary parts of the eigenwavelength for a single nanoparticle as a function of the particle size d . (d) Real and (e) imaginary parts of the dielectric constant of gold at the corresponding eigenwavelength as a function of the size d . The dashed lines in (d) and (e) indicate the plasmon resonance in the electrostatic limit. The dielectric constant of the background is fixed at 6.145.

to the well known quasi-static limit in plasmonics for small particles. Next, the modes of a symmetric nanoparticle dimer are computed and their dependence on the system parameters investigated. The effect of symmetry breaking in a trimer is illustrated via eigenmode analysis subsequently. Finally, I study a nanoparticle quadrumer which can control the polarization of the scattered light from the eigenmodes perspective.

5.3.1 Monomer

Consider a single gold nanoparticle embedded in a medium with $\epsilon_B = 6.145$. The refractive index of the background corresponds to the refractive index of TiO_2 [439]. For this system $\log_{10}|\xi - 1|$ as a function of λ_r and λ_i is shown in Fig. 5.2(a). It is clearly seen that $\xi = 1$ is satisfied for $\lambda = 662 + 14i$. Furthermore, at this wavelength the matrix \mathbf{S} has an eigenvalue 1 with multiplicity three, i.e. this eigenvalue is triply degenerate. Furthermore, the dipole moments corresponding to these triply degenerate eigenmodes are oriented along the x , y and z directions. The degeneracy arises because all the axes are identical. Figure 5.2(b) and (c) show the variation of λ_r and λ_i as a function of particle size. As the particle size is increased from 4 nm to 30 nm, λ_r increases from 647 nm to 681 nm. Concurrently, the imaginary part of the eigenwavelength also shows a progressive increase as a function of the particle size. This increase in both the real and imaginary parts of the eigenwavelength as a function of size is due to the higher retardation effects for larger particles. Note that the retardation effects are taken into account by the presence of $k_0 R$ (R is the nanoparticle radius) terms in the expressions for \mathbf{G}_{ij} and \mathbf{M}_i . In this chapter the wavelength is taken as the eigenvalue because of its widespread use in most plasmonic studies. As detailed in Appendix E, identical results are obtained if frequency is used as the eigenvalue. As mentioned previously, it is also possible to compute the dielectric constant corresponding to the eigenwavelength using the Drude model. This is useful since dielectric constant is the preferred eigenvalue in most eigenmode analyses performed in the electrostatic limit [128, 375, 402]; hence, I plot the real ($\text{Re}(\epsilon)$) and imaginary ($\text{Im}(\epsilon)$) parts of the dielectric constant of gold at the eigenwavelengths (Fig. 5.2(d) and (e)). Both $\text{Re}(\epsilon)$ and $\text{Im}(\epsilon)$ decrease on increasing the size of the particle. Furthermore, ϵ approaches the well known quasi-static limit $\epsilon = -2\epsilon_B$ in the case of 4 nm particles. Let us now consider the imaginary part of the dielectric constant at the eigenwavelength. Recall that the quasi-static limit arises when the denominator of the polarizability, which is proportional to $|(\epsilon - \epsilon_B)|/|(\epsilon + 2\epsilon_B)|$, is zero. Unlike the case of non-lossy systems where the denominator is zero at $\epsilon = -2\epsilon_B$, in our system the denominator can be made equal to zero at the eigenvalue ϵ if we assume an effective complex dielectric constant of the background given by $\epsilon_B^{eff} (= \epsilon_{B,r}^{eff} + i\epsilon_{B,i}^{eff})$. Additionally, since $\text{Im}(\epsilon)$ is less than 0 in this particular system, $\epsilon_{B,i}^{eff}$ has to be positive. Therefore, at the eigenwavelength the system behaves as if the background had finite losses. The progressive decrease in $\text{Im}(\epsilon)$ and its negative sign on increasing the size indicates the increase of damping, both intrinsic and radiative, in the system.

5.3.2 Symmetric dimer: Effect of particle size and gap

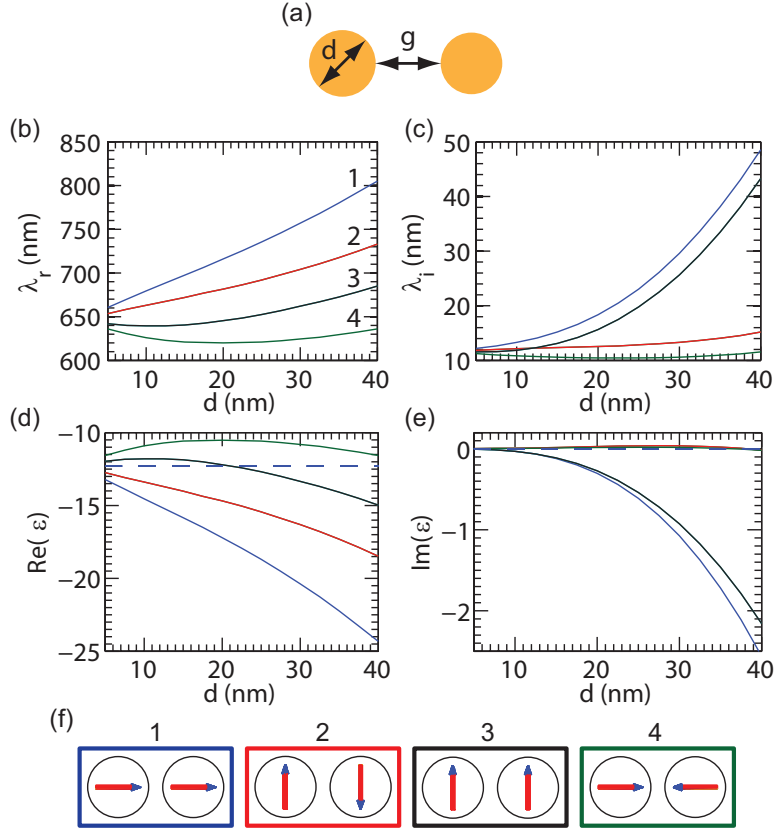


Figure 5.3: **Modes of a symmetric nanoparticle dimer.** (a) Schematic of the nanoparticle dimer. (b) Real and (c) imaginary part of the eigenwavelengths as a function of particle size d . (d) Real and (e) imaginary parts of the dielectric constant of gold at the eigenwavelength. (f) Dipoles orientations in the particles for the four distinct eigenmodes depicted in (b). The direction of the arrow indicates the dipole orientation with the blue head pointing towards the negative charge. Other parameters are $g = 4$ nm and $\epsilon_B = 6.145$.

Consider a nanoparticle dimer as shown in Fig. 5.3(a) in which two gold nanoparticles, each with diameter d , are separated by a gap g . Figure 5.3(b) and (c) show the computed λ_r and λ_i of this system for various particle sizes with the gap fixed at 4 nm. For any given particle size, four distinct modes can be identified [333, 440]. As the particle size is increased, the wavelength λ_r of modes 1 and 2 shows a progressive increase. In the case of modes 3 and 4, λ_r first shows a blueshift for $d < 15$ nm and then a redshift for larger values of d . The wider spectral separation of the eigenmodes for larger particle sizes clearly indicates the increase in the coupling between the particles due to greater field overlap. The imaginary part of the eigenwavelength, however, shows a totally different character. In the case of modes 1 and 3, a progressive increase is seen whereas for modes 2 and 4 it does not change significantly. These differences can be understood by studying the dipole orientations for the four modes, as shown in Fig. 5.3(f). These dipole orientations were obtained using the eigenvector of the matrix \mathbf{S} at the corresponding eigenvalues and it must be mentioned here that the dipole

orientations for the modes are independent of the nanoparticle size. In the case of modes 1 and 4, the dipole moment of the particles align along the axis joining the two dipoles, whereas for modes 2 and 3 the dipoles are oriented perpendicular to the axis [333, 440]. Additionally, in modes 1 and 3 the dipoles of the two particles are parallel whereas in modes 2 and 4 they are anti-parallel. Due to the symmetry about the axis joining the two particles, modes 2 and 3 are doubly degenerate. The net zero dipole moment for modes 2 and 4 prevents them from being excited using plane wave excitation and these modes are referred to as '*dark modes*' [333, 440]. This is because the light scattered by the first particle will destructively interfere with the light scattered by the second particle. On the other hand, modes 1 and 3 exhibit a net dipole moment which allows them to interact with the far field and are commonly known as '*bright modes*'. In contrast to modes 2 and 4, where destructive interference occurs, for modes 1 and 3 the particles scatter light in phase and we observe constructive interference. The imaginary part of the eigenwavelength, which corresponds to the half-width of the plasmon resonance, contains contributions from intrinsic damping (mainly caused by ohmic losses for gold) and radiative damping (due to the radiation of light into the far field). Since, modes 1 and 3 are radiative, they exhibit a much higher value of λ_i as compared to modes 2 and 4 for large particle sizes ($d > 15$ nm). This is further substantiated by the fact that as the particle size is reduced, thereby reducing the radiative damping, the values of λ_i for the modes become similar.

Figure 5.3(d) and (e) shows $\text{Re}(\epsilon)$ and $\text{Im}(\epsilon)$ at the various eigenwavelengths as a function of the particle size. $\text{Re}(\epsilon)$ and $\text{Im}(\epsilon)$ show trends analogous to that of λ_r and λ_i , respectively. The $\text{Im}(\epsilon)$ for modes 1 and 3, the bright modes, progressively becomes more negative as the particle size is increased. On the other hand for modes 2 and 4, the $\text{Im}(\epsilon)$ is positive and close to zero for all the particle sizes. For modes 3 and 4 the intrinsic damping for a given particle size is similar due to the proximity of their eigenwavelengths. However, the total damping for the two modes as shown by the value of λ_i are very different. This difference is due to the presence of radiative damping in the case of mode 3, which significantly increases the value of λ_i for larger particles as compared to mode 4. As explained in the case of a single nanoparticle, the imaginary part of the dielectric constant at the eigenwavelength can be understood as the effective background possessing a finite loss if $\text{Im}(\epsilon) < 0$. Applying a similar argument, I see that only in the case of modes 1 and 3, the dielectric constant possess a negative value of $\text{Im}(\epsilon)$ and correspondingly the background acts as a lossy medium which can extract light from these two modes at the eigenwavelengths. However, the positive $\text{Im}(\epsilon)$ for modes 2 and 4 shows that for these two modes, the effective background acts like a gain medium and therefore cannot act as a sink for light.

I now study the effect of varying the gap size in the case of a dimer made up of 20 nm particles. Figure 5.4 shows the eigenwavelengths and the corresponding epsilon as a function of the inter particle gap. First, the splitting between the various modes, i.e. λ_r and $\text{Re}(\epsilon)$, decreases on increasing the gap because of reduced coupling. For gaps close to 60 nm, the λ_r and $\text{Re}(\epsilon)$ approach the values of an isolated 20 nm particle. As mentioned previously, modes 1 and 3 exhibit a negative value of $\text{Im}(\epsilon)$ for all values of the gap. However, $\text{Im}(\epsilon)$ of modes 2 and 4

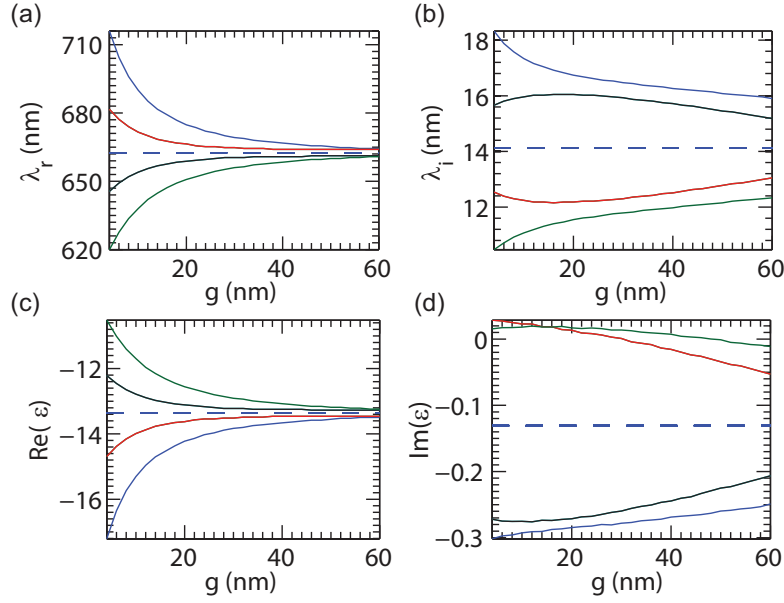


Figure 5.4: **Modes of a symmetric nanoparticle dimer: gap variation.** (a) Real and (b) imaginary parts of the eigenwavelength for a nanoparticle dimer as a function of the gap g . (c) Real and (d) imaginary parts of the dielectric constant of gold at the corresponding eigenwavelength as a function of the gap g . Other parameters are $d=20$ nm and $\epsilon_B = 6.145$. The dashed lines show the value of the corresponding parameter for a single 20 nm particle.

crosses zero at 30 nm and 48 nm gap, respectively. This means that beyond these gap values the modes start radiating due to retardation effects. Consequently the background starts acting like a lossy medium.

5.3.3 Effect of symmetry breaking in a nanoparticle trimer

Let us now consider a nanoparticle trimer made up of 20 nm particles as shown in Fig. 5.5(a). In case of an equilateral structure ($\Delta x = 0$ nm) the gap between the particles is 4 nm. Figures 5.5(b)-(d) show the variation of λ_r as a function of the displacement Δx of the top particle (P1) in the horizontal direction. As expected at most 9 modes are seen for a given Δx [441]. The colored dots in Fig. 5.5 depict the excitation strengths of the various modes on illumination with a polarized plane wave. For example, Fig. 5.5(b) shows the excitation strength of the modes due to a plane wave propagating in z direction and polarized along x axis. The excitation strengths are computed by the summation of the overlap of the incident field with the field of a given mode. The summation is performed over all the dipoles in the system. Similarly, Fig. 5.5(c) and (d) show the excitation strength for plane waves propagating along z and x direction, respectively, and polarized along y and z , respectively. As Δx is increased from 0 nm to 12 nm, the spectral splitting between the modes (in-plane or out of plane modes) increases due to increased coupling. Maximum coupling is observed around $\Delta x = 12$ nm when the structure closely resembles a right angled trimer. This is because for $\Delta x = 12$ nm

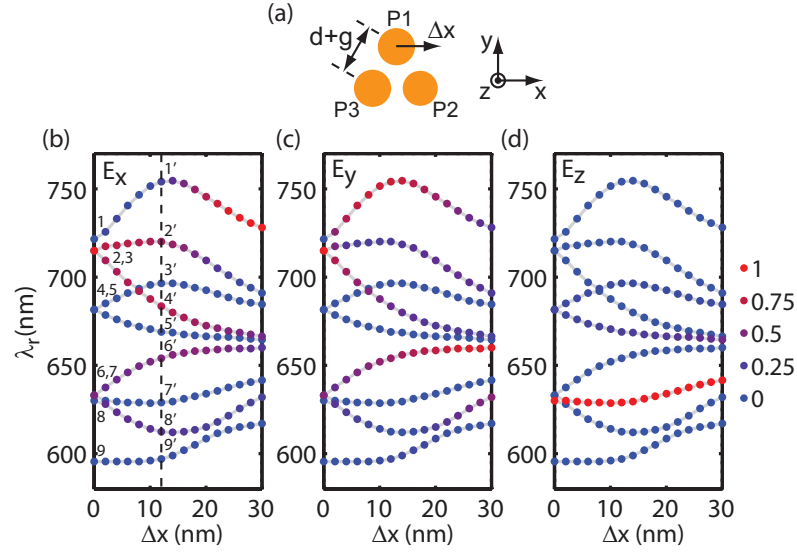


Figure 5.5: **Symmetry breaking in a nanoparticle trimer.** (a) Schematic of the nanoparticle trimer. (b) Real part of the eigenwavelength and the corresponding excitation strengths as a function of the displacement Δx . The incident condition is a plane wave propagating in the z direction and polarized along x axis. (c) Real part of eigenwavelength and the corresponding excitation strengths as a function of the displacement Δx . The incident condition is a plane wave propagating in the z direction and polarized along the y axis. (d) Real part of eigenwavelength and the corresponding excitation strengths as a function of displacement, Δx . The incident condition is a plane wave propagating in the x direction and polarized along the z axis. Other parameters are $d = 20$ nm, $g = 4$ nm and $\epsilon_B = 6.145$.

the separation between the particles P1 and P2 is minimized resulting in a greater field overlap. On further increasing Δx the splitting between the modes reduces as the separation between particles P1 and P3 becomes larger. In addition to the spectral splitting, the excitation strengths are also strongly dependent on Δx . For example, the excitation strength of the mode at the highest wavelength (mode 1) progressively increases on increasing Δx in the case of x polarized plane wave. On the contrary, for y polarized plane wave excitation, this mode is best excited at $\Delta x = 12$ nm.

To better understand the behavior of this system I correlate the excitation strengths of the various modes with their dipole distributions. The field distributions of the modes of an equilateral trimer, $\Delta x = 0$ nm, are shown in Fig. 5.6(a). This system has 6 modes with the dipoles oriented in the plane of the structure (modes 1, 2, 3, 6, 7 and 9), whereas for 3 modes the dipoles are oriented perpendicular to the plane of the structure (modes 4, 5 and 8). Furthermore, due to symmetry of the structure it has 3 pairs of doubly degenerate modes (modes (2,3), (4,5) and (6,7)). Clearly, modes 1, 4, 5 and 9 have a zero net dipole moment and cannot be excited using plane wave excitation. This is also evident from Fig. 5.5(b)-(d) whereby the excitation strength of these modes is zero regardless of the light polarization. On the other hand modes 2, 3, 6 and 7 possess a net dipole moment in the xy plane and can be excited

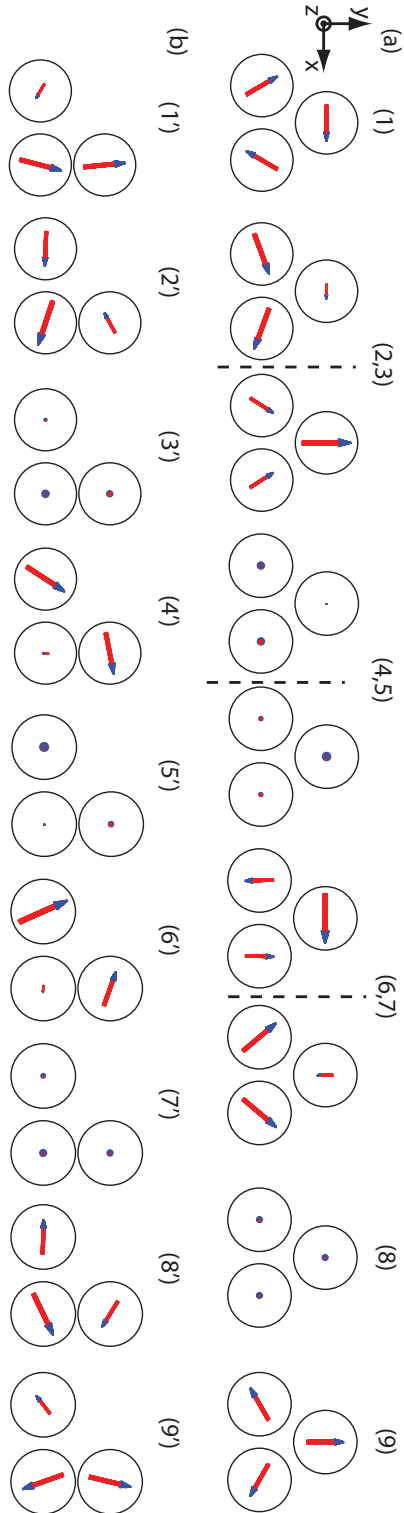


Figure 5.6: **Field distribution of a nanoparticle trimer.** (a) Field distribution of the various eigenmodes of an equilateral trimer ($\Delta x = 0$ nm). Degenerate eigenmodes have been clubbed together for clarity. The number of the modes is also shown in Fig. 5.5(b) for clarity. (b) Field distribution of the various eigenmodes of a trimer ($\Delta x = 12$ nm). The numbers of the modes is also shown in Fig. 5.5(b) for clarity. The direction of the arrow indicates the electric field orientation with the blue head pointing towards the negative charge. A solid blue circle indicates the electric field pointing in the $+z$ direction and a hollow blue circle with a red dot indicates the electric field pointing in the $-z$ direction.

using either x or y polarized plane wave. Mode 8 however exhibits a net dipole moment along the z direction and can only be excited using a plane wave polarized along z direction. Note that modes 2, 3, 6 and 7 can not be excited with a z polarized plane wave and are thus '*dark modes*' for this given polarization. This is also depicted in Fig. 5.5(d) where these modes exhibit a zero excitation strength. Analogously, since mode 8 can not be excited using either x or y polarized plane wave, it acts like a '*dark mode*' for these polarizations and shows a zero excitation strength (Fig. 5.5(b) and (c)).

As the particle P1 is displaced in the x direction, the symmetry of the structure breaks and consequently I observe that the degeneracy of the modes, present in case of the equilateral structure, is lifted. As mentioned previously the spectral separation between the in-plane modes (1, 2, 3, 6, 7 and 9) and out of plane modes (4, 5 and 8) increases for $\Delta x < 12$ nm and then decreases. For example, the mode 2 and 3 (for $\Delta x = 0$ nm) splits into two modes (leading to modes 2' and 4' for a structure with $\Delta x = 12$ nm). Each of these split modes show different excitation strengths for different values of Δx . For an x polarized plane wave, both the split modes show comparable excitation strengths for $\Delta x < 12$ nm, but for larger values of Δx mode 4' is excited more efficiently (Fig. 5.5(b) and Fig. 5.6(b)). This is because in case of mode 2' as the particle P1 is displaced, its dipole moment along x axis progressively increases. In addition, the dipole of particle P1 is aligned opposite to the dipoles of particle P2 and P3, which reduces the net dipole moment and lowers the excitation strength of the mode. In case of mode 4' the dipoles of particles P1 and P3 are predominantly excited and they are always in phase considering the x axis, therefore this mode exhibits larger excitation strengths even for larger values of Δx (Fig. 5.5(b) and Fig. 5.6(b)). In contrast for y polarized light mode 4' demonstrates a higher excitation strength as compared to mode 2' for $\Delta x < 12$ nm (Fig. 5.5(c)). Larger values of Δx lead to comparable excitation strength of mode 2' and 4'. This behavior can again be traced back to the field distributions. Mode 2' shows a near zero dipole moment along the y direction and consequently a near zero excitation strength (Fig. 5.6(b)). Similar mode splittings are also observed in case of modes (4,5) and modes (6,7) of the equilateral structure on displacement of particle P1. Figure 5.6(b) shows the field distributions for a particular symmetry broken nanoparticle trimer with $\Delta x = 12$ nm which manifests maximal coupling in the system. In this case, none of the modes are degenerate and the system has 9 distinct modes. In this case, all the in-plane modes 1', 2', 4', 6', 8' and 9' show a non zero dipole moment along both x and y axis and a non-zero excitation strength (Fig. 5.5(b) and (c)). These modes can thus be excited using a plane wave with polarization in the plane of the structure. On the other hand, the out of plane modes, modes 3', 5' and 7', show a net non zero dipole moment along z axis and thus can be excited using z polarized plane wave. However, even in this case, the in-plane modes are '*dark modes*' for a z polarized plane wave and out of plane modes are '*dark modes*' for x or y polarized plane waves.

5.4 Polarization changing nanoparticle cluster

Plasmonic structures which can control and modify the polarization of incident light have found significant prominence in the past years [442–450]. Recently, such polarization control was demonstrated at a single structure level exploiting the coupling between two radiative dipolar modes [1]. When this structure is illuminated with a x -polarized incident plane wave, the scattered far-field exhibits a certain ellipticity which is closely associated with the coupling in the structure. Figure 5.7 shows the structure as well as its response due to a normally incident x -polarized plane wave. The degree of polarization (DOP), α , is defined as

$$\alpha = \frac{|C_{\text{right}}| - |C_{\text{left}}|}{|C_{\text{right}}| + |C_{\text{left}}|}, \quad (5.6)$$

where C_{left} and C_{right} are the coefficients of the electric field decomposition into the two-orthogonal left- and right-handed circular polarization, respectively. In case of a symmetric structure, where $d = c = 25$ nm, no polarization change is observed for the scattered light. However, as the perturbation is increased the value of α increases and is equal to 1 for $d = 17$ nm, i.e., the scattered light is circularly polarized.

In this section, I study the modal behavior of a nanoparticle cluster which exhibits similar properties for the scattered light. I combine the results of the modal behavior with the results of the scattering problem to understand the generation of circular polarization using such structures. Figure 5.8(a) shows the schematic diagram of the structure under consideration which is composed of four identical 20 nm gold nanoparticles. For a normally incident x -polarized plane wave the scattering cross section and the DOP as a function of wavelength and

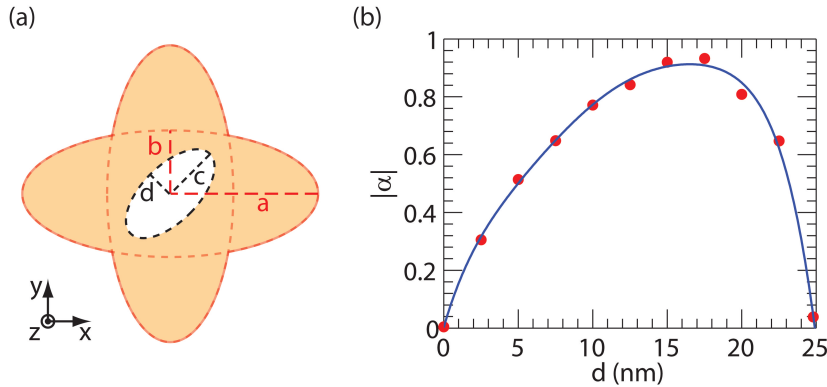


Figure 5.7: **Coupling induced control over circular polarization generation.** (a) Schematic of the structure used for circular polarization generation by Abasahl *et al.* [1]. (b) DOP as a function of minor axis of the elliptical perturbation, d . The other parameters were: $a = 60$ nm, $b = 20$ nm, $c = 25$ nm and $\epsilon_B = 1$. The structure was illuminated with a plane wave propagating in the z direction and polarized along the x -axis. The $(0, 0, 50)\mu\text{m}$ point was used for calculating the DOP.

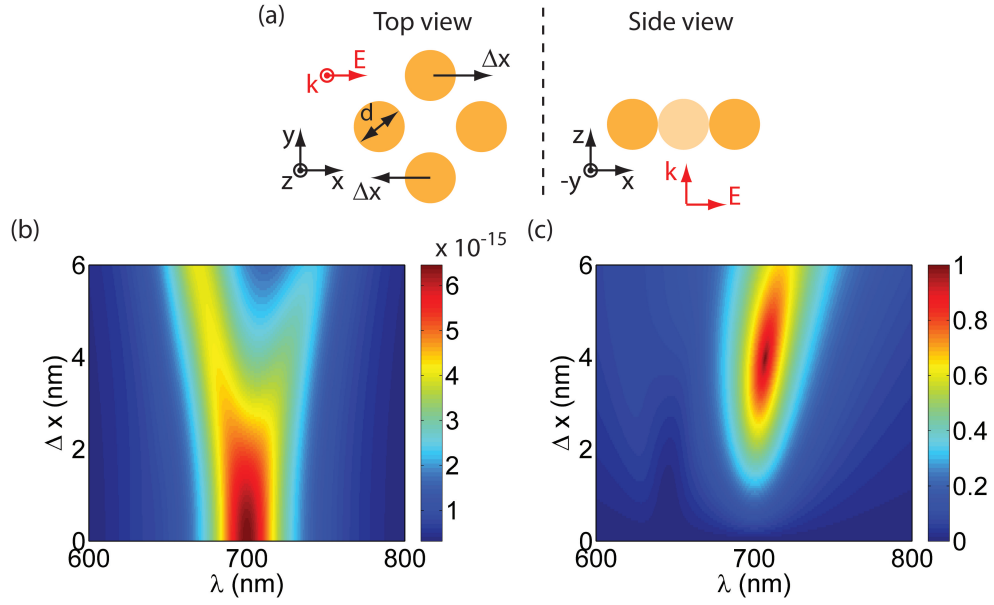


Figure 5.8: **Circular polarization generation from a nanoparticle quadrumer.** (a) Schematic of the nanoparticle quadrumer. (b) Scattering cross-section (m^2) and (c) degree of circular polarization (DOP) as a function of λ and displacement, Δx . The parameters were: $d = 20$ nm, $g = 4$ nm at $\Delta x = 0$ nm and $\epsilon_B = 6.145$. The structure is illuminated with a plane wave propagating in the $+z$ direction and polarized along x -axis. The DOP is computed at an observation point $(0, 0, 50) \mu\text{m}$.

displacement, Δx , is shown in Fig. 5.8(b) and (c), respectively. For $\Delta x = 0$ nm the scattering spectrum shows a single peak at 700 nm. On increasing the Δx , this peak splits into two resonances with the spectral separation being proportional to the displacement. As the symmetry of the structure is broken, α progressively increases and attains a value of 1 for $\Delta x = 3.95$ nm at $\lambda = 700$ nm. Further increase in Δx leads to lowering of the DOP at this wavelength. This behavior is analogous to the results presented by Abasahl *et al.* [1].

The energy levels, corresponding to the real part of the eigenwavelength, of the quadrumer with $\Delta x = 0$ nm and $\Delta x = 3.95$ nm are shown in Fig. 5.9(a) and (c). 12 modes are observed in each of these cases. For $\Delta x = 0$ nm, the particles are placed on the corners of a square and 3 pairs of modes are doubly degenerate (2 pair in-plane and 1 pair out-of-plane). I only consider the in-plane modes, since in the scattering problem the incidence condition is restricted to a normally incident plane wave with in-plane polarization. Furthermore, only two modes among the in-plane modes show a net non-zero dipole moment (modes labeled 1 and 2). These two modes are degenerate and exhibit net dipole moments orthogonal to each other. In case of the perturbed system, $\Delta x = 3.95$ nm, all the degeneracies are broken and 12 distinct modes are visible. Again, I depict the modes with a large dipole moment in the energy diagram (red and green levels). The field distributions corresponding to these two modes are shown in Fig. 5.9(d), which illustrates that the two modes support nearly orthogonal dipoles (relative angle $\sim 89.5^\circ$) albeit at different wavelengths. From this, it is clear that even

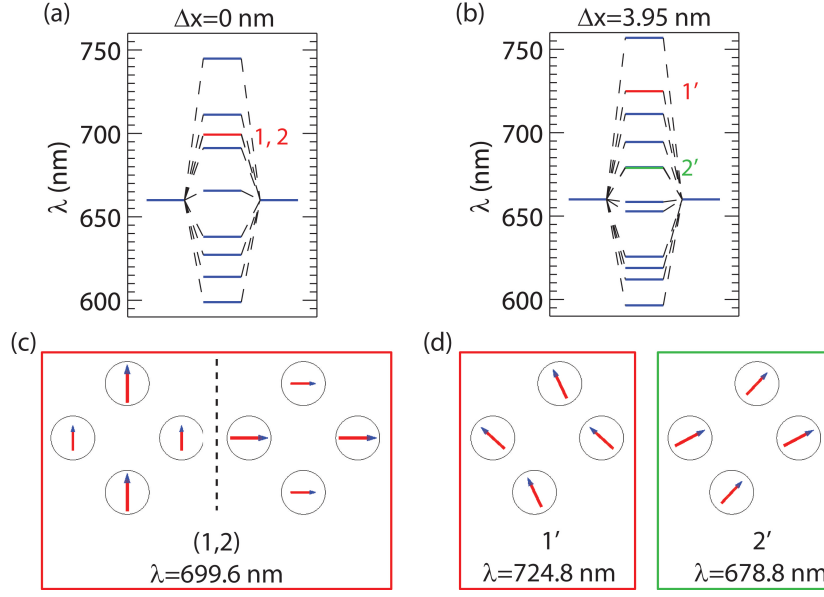


Figure 5.9: **Eigenmodes of the polarization changing quadramer.** (a) and (b) Energy diagrams and (c) and (d) Field orientations for the quadramer with $\Delta x = 0$ nm and $\Delta x = 3.95$ nm, respectively. The red and the green levels in the figures show the modes involved in generation of circular polarization. The size of the particles is 20 nm and gap for $\Delta x = 0$ nm is 4 nm.

the structures that generate circular polarization do not exhibit modes which are significantly non-orthogonal from a spatial point of view. However the question still pertains about why the coupling controls the polarization state of scattered light. Recall that for generating circular polarization two conditions must be satisfied simultaneously, namely the amplitudes of the two orthogonal dipoles must be equal and the phase difference between the two dipoles at that wavelength must be equal to $\pi/2$ [1]. Another point that must be mentioned here is that polarization control is intrinsically dependent on the incident conditions and represents a scattering problem.

As the coupling in the system is increased (Δx is increased), the spectral separation between the two resonances increases. Furthermore, it is well known that a phase change of π occurs across each excitable mode [155]. Therefore, for wavelengths in between the two resonances, a finite non-zero phase difference is accumulated which depends on the wavelength. Such phase differences are also responsible for the occurrence of Fano resonances in plasmonic structures exhibiting two bright modes [155]. In an analogous manner, the phase difference necessary for circular polarization generation can be acquired by spectral separation of the modes. Figure 5.10 shows the wavelength at which the maximum α is observed for a given Δx . This particular curve is calculated by scanning the parameter space of λ and ϕ , the polarization angle, for the maximum value of α . The size of the each point in the figure corresponds to the maximum value of α and the color of the dot represents the incidence polarization required for its excitation. Also shown in the figure are the two modes responsible for polarization conversion, presented as green and red triangles. Note that even though the

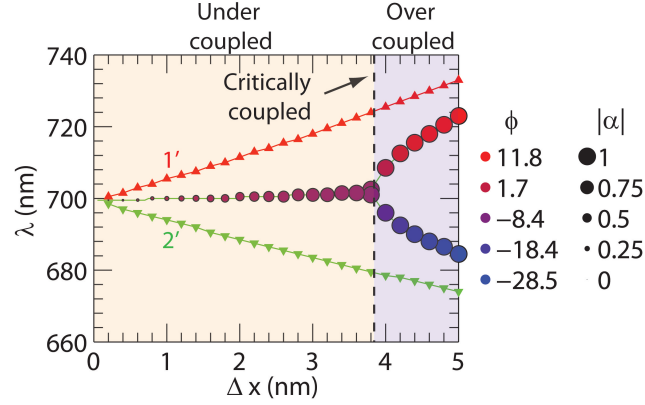


Figure 5.10: **Coupling induced bifurcation of DOP.** Wavelength corresponding to the maximum degree of polarization as a function of displacement, Δx due to incidence of a plane wave with a polarization angle ϕ . The size of the circular dots represents the DOP and the color of the dots represent the incident polarization necessary for achieving the maximal DOP. The triangles (green and red) show the real part of the eigenwavelengths of the two interacting modes as a function of Δx .

condition on the incidence polarization angle is relaxed, the excitation plane wave is still normally incident. The freedom of choosing the incidence polarization angle gives us the freedom of finding multiple wavelengths at which the amplitude condition is satisfied. This is because the incidence polarization angle ϕ only changes the relative excitation strengths of the two concerned modes. The variation of α as a function of Δx in this figure can be separated into three distinct regions:

1. Under coupled - maximum value of α is smaller than 1 regardless of ϕ and λ .
2. Critically coupled - maximum value of $\alpha \sim 1$ for a single pair of λ and ϕ .
3. Over coupled - $\alpha = 1$ for two pairs of λ and ϕ .

Let us now consider each domain separately by plotting the resonances corresponding to each of the concerned modes (Fig. 5.11). The resonances are plotted by using the intensity of a complex lorentzian curve defined with the resonance wavelength equal to the real part of the eigenwavelength and the damping given by the imaginary part of the eigenwavelength. In the undercoupled regime, even though the amplitude of the two oscillating dipoles can be matched for multiple ϕ (blue curve in Fig. 5.11(a)), the spectral separation between the two resonances is not sufficient to provide the $\pi/2$ phase difference necessary for $\alpha = 1$, as shown in Fig. 5.11(b). Note that even though the amplitudes of the two modes can be matched at multiple wavelengths, each such matching occurs for a different ϕ . As the coupling is increased further, the phase difference between the two dipoles attains the value of $\pi/2$ exactly at one wavelength (Fig. 5.11(d)). Simultaneously, the incidence $\phi = 0$ allows for matching of amplitudes of the two oscillating dipoles at the considered wavelength, as shown in Fig. 5.11(c).

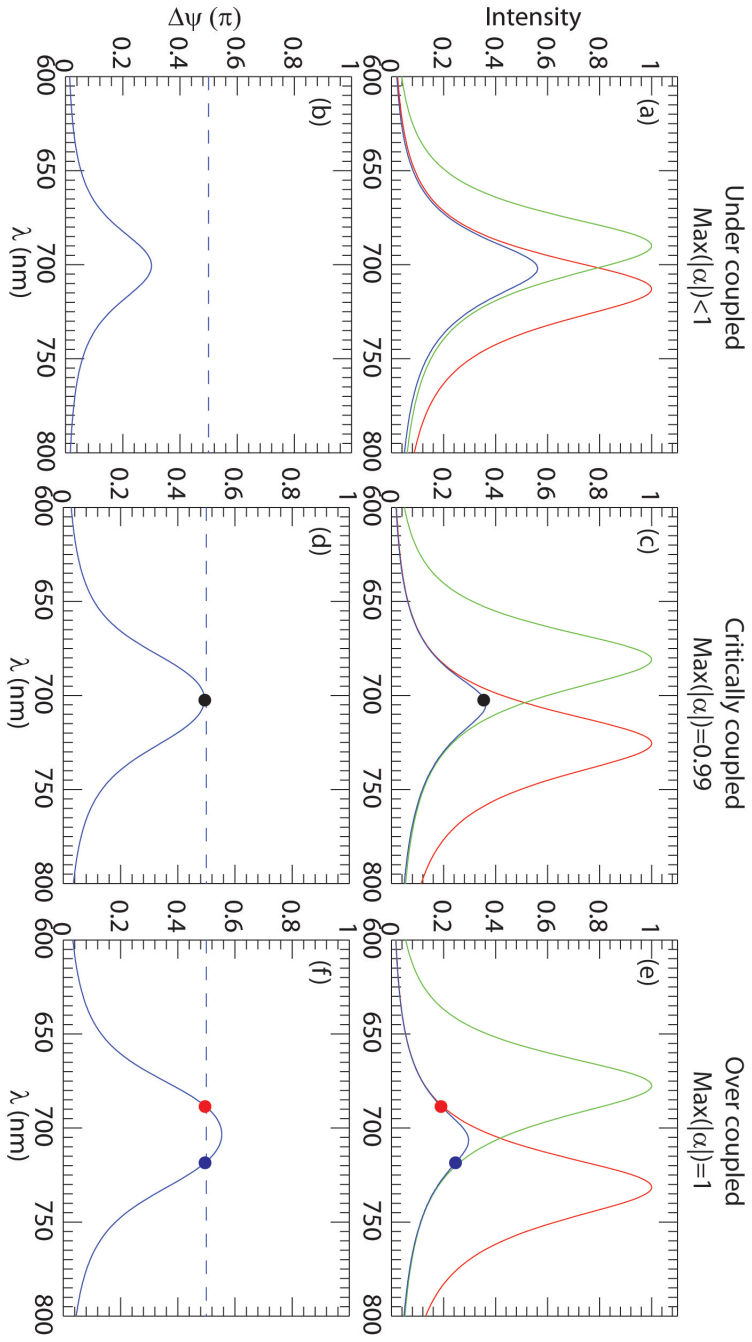


Figure 5.1.1: **Intensity and phase conditions in under-coupled, critically coupled and over-coupled regimes.** (a), (c) and (e) Intensity of the two modes ($1'$ and $2'$ responsible for circular polarization generation for the under-coupled ($\Delta x = 2$ nm), critically coupled ($\Delta x = 3.85$ nm) and over-coupled ($\Delta x = 4.6$ nm) case, respectively. The blue lines show the points at which the intensities of the two modes can be matched. Note that the incident polarization is not fixed for different points on the blue curves. (b), (d) and (f) Phase difference ($\Delta\psi$) between the two modes in the three coupling regimes.

5.5. Correlation between mode symmetry and second harmonic generation from nanoclusters

Therefore, $\alpha \sim 1$ at exactly one pair of λ and ϕ and this is defined as the critically coupled regime. When the coupling is increased further, the phase difference attains the value $\pi/2$ at two distinct wavelengths (Fig. 5.11(f)). Corresponding to each of these two wavelengths, polarization angles can be determined such that the amplitudes of the two oscillating dipoles are also matched, Fig. 5.11(e) (blue and red dots). Therefore, in the overcoupled regime it is possible to achieve $\alpha = 1$ for two distinct pairs of λ and ϕ . This is also clearly evident from Fig. 5.10 where a bifurcation in the curve depicting the maximum α is observed.

5.5 Correlation between mode symmetry and second harmonic generation from nanoclusters

In this section, the SHG from coupled metallic nanoparticles is investigated by linking the two methods described above: the ab-initio method for the determination of the eigenmode and the SIE method for complete electromagnetic computations. Our approach is as follows. The eigenmodes are first characterized i.e. their resonant wavelengths and their symmetry properties are determined. In order to understand the role played by the different modes in the nonlinear response of the nanoparticle clusters, the exact computations of the SHG are then analyzed using the information provided by the eigenmode analysis. Dispersive gold dielectric constants used for the SIE computation are obtained from experimental data of Johnson and Christy [66]. All the SIE and eigenmode computations are performed for nanoparticle clusters embedded in a high refractive index background ($\epsilon_m = 6.145$ corresponding to TiO_2) in order to shift the surface plasmon resonances away from the interband transition of gold ($\lambda \sim 500$ nm). Symmetric and asymmetric dimers are discussed first (section 5.5.1 and 5.5.2); the case of linear trimers is then investigated in section 5.5.3.

5.5.1 Symmetric dimer

Let us first consider a dimer of two identical gold nanoparticles with 20 nm diameters. The spacing between the nanoparticles is 4 nm, Fig. 5.12(a). The real part of the eigenwavelength of the mode of each individual nanoparticle occurs at $\lambda_m = 660$ nm. Figure 5.12(b) shows the resonant wavelengths for the different eigenmodes arising from the hybridization between the dipolar modes sustained by the individual nanoparticles. The arrows indicate the orientation of the dipolar moment in each nanoparticle. The total number of eigenmodes is 6, corresponding to 4 resonant wavelengths since some modes are doubly degenerate ($\lambda_m = 678$ nm and 645 nm). The degenerate modes have identical dipole moments but the dipoles are aligned along either the y -axis or the z -axis. As mentioned previously, the eigenmode with the longest resonant wavelength ($\lambda_m = 711$ nm) corresponds to the coupling between two aligned dipole moments pointing in the same direction. On the contrary, the eigenmode with the shortest resonant wavelength ($\lambda_m = 622$ nm) corresponds to the coupling between two aligned dipole moments pointing in opposite directions. The two other modes correspond to the symmetric and antisymmetric coupling between the dipoles but with the dipoles oriented perpendicular

to the axis joining both nanoparticles and parallel to the symmetry plane shown in Fig. 5.12(a). As a consequence, the symmetry properties are different for each mode. The SIE method permits computing the SH electromagnetic fields and the comparison with the eigenmode calculations is straightforward when calculating the distribution of the electric field associated with each mode. For this reason, the modes are sorted by considering the symmetry of their electric field. The real part of the x -component of the electric field evaluated with the ab-initio method for the four eigenmodes is shown in Fig. 5.12(c-f). The x -component corresponds to the vector component normal to the plane shown in Fig. 5.12(a). The eigenmodes fall into two categories depending on the symmetry of the electric field with respect to the symmetry

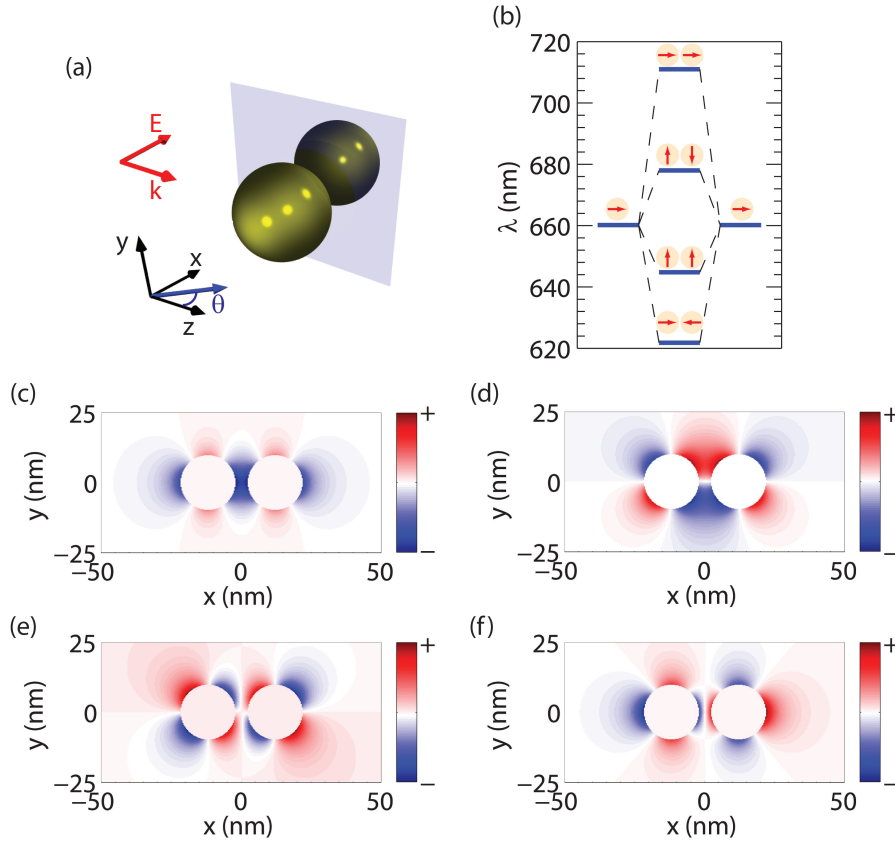


Figure 5.12: Energy diagram and field distributions for a symmetric nanoparticle dimer. (a) The symmetric gold nanodimers studied in this work. The nanoparticle diameter is 20 nm and the spacing is 4 nm. The blue plane corresponds to the plane discussed in the main text ($x = 0$). This plane is alternatively a symmetry or antisymmetry plane for the electromagnetic field (see the discussion in the main text). The excitation condition used for the SIE computations is also shown. The scattering angle θ is defined relatively to the z -axis. (b) Diagram describing the resonant wavelength of the eigenmodes arising from the coupling between the dipolar modes of two 20 nm gold nanoparticles with a nanogap of 4 nm. The arrows indicate the orientation of the dipolar moments for the corresponding eigenmodes. (c-f) Normalized real part of the x -component of the electric field evaluated for the eigenmode with a resonant wavelength of (c) $\lambda = 711$ nm, (d) $\lambda = 678$ nm, (e) $\lambda = 645$ nm, and (f) $\lambda = 622$ nm.

5.5. Correlation between mode symmetry and second harmonic generation from nanoclusters

plane shown in Fig. 5.12(a). The two modes with the longest resonant wavelength ($\lambda_m = 711$ nm and 678 nm) are defined as antisymmetric modes since the plane shown in Fig. 5.12 is an antisymmetry plane (similar to a perfect electric conductor [451]) for these modes, Fig. 5.12(c) and (d). The two modes with the shortest resonant wavelength are defined as symmetric modes, Fig. 5.12(e) and (f). Indeed, the normal component of the electric field associated with these modes vanishes in the plane $x = 0$ indicating that this plane is a symmetry plane (similar to a perfect magnetic conductor [451]) for these mode.

To investigate the link between the eigenmodes supported by a plasmonic nanostructure and its SH response, let us first consider the excitation of the symmetric nanodimer by an incoming planewave. SIE computations have been performed with an incident planewave polarized along the x -axis and propagating along the z -axis. The incident wavelength is $\lambda = 1244$ nm. The near-field distributions of the intensity and the real part of the x -component of the electric field are shown in Fig. 5.13(a) and (c), respectively. It is obvious that these distributions correspond to that of the mode with a resonant wavelength equal to $\lambda_m = 711$ nm demonstrating that this mode is excited in this case, compare Fig. 5.13(c) with Fig. 5.12(c). Obviously, the incident wavelength used in the SIE calculation ($\lambda = 1244$ nm) does not match the resonance wavelength of the $\lambda_m = 711$ nm mode; still, only this mode fulfills the symmetry selection rules imposed by both the cluster geometry and the incident beam properties. Hence, this excitation scheme corresponds to off-resonant excitation, which is of course weaker than in the resonant case (let us recall that the excitation of a Lorentzian mode does not require an exact match between the excitation wavelength and the resonance wavelength, although the excitation is strongest in that, on-resonant, case) [268]. The near-field distribution in Fig. 5.13(a) is mainly characterized by a significant enhancement of the electric field in the nanogap, where it reaches 30 times the illumination intensity. The intensity enhancement evolves from 25 for an incident wavelength $\lambda = 1422$ nm to 36 for an incident wavelength $\lambda = 1150$ nm. This hotspot is induced by charges with opposite signs standing on each side of the nanogap and is characteristic of the linear response of metallic nanoantennas [452].

Now we turn our attention to the SHG from this nanodimer. Figure 5.13 shows the SH near-field intensity (panel (b)) as well as the real part of the x - (panel (d)) and y -components (panel (f)) of the SH electric field computed with the SIE. It is obvious that these distributions differ from the ones obtained for the fundamental wave. For instance, the SH field is not enhanced in the nanogap as is the case for the fundamental field [453]. Contrary to the fundamental electric field which is driven by an incident planewave, the SH electric field is driven by the nonlinear polarization sources located at the nanoparticle surfaces. The nonlinear polarization can be expressed as [407]:

$$P_{\perp}(\mathbf{r}, 2\omega) = \chi_{S, \perp \perp \perp} \hat{r}(\hat{r} \cdot \mathbf{E}(\mathbf{r}, \omega))^2, \forall \mathbf{r} \in S \quad (5.7)$$

where $\mathbf{E}(\mathbf{r})$ is the fundamental electric field evaluated in the metallic nanoparticle, just below

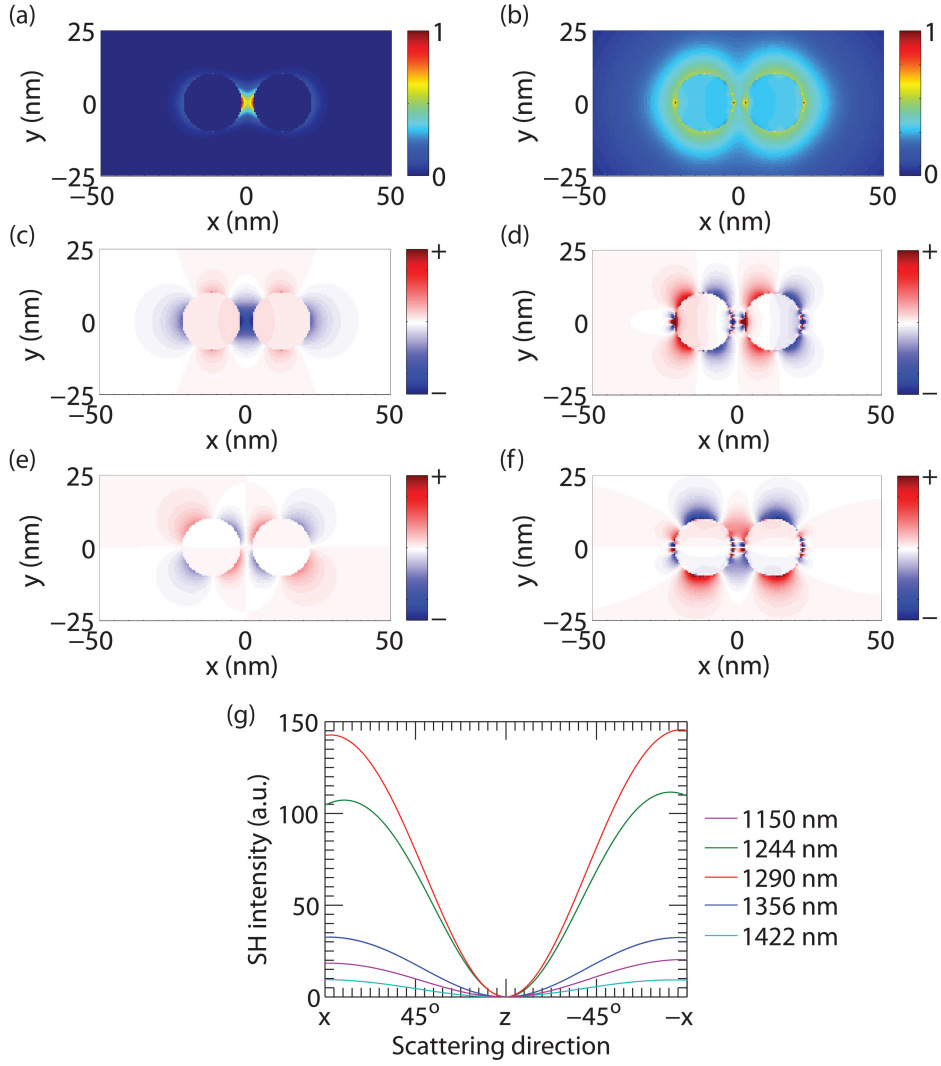


Figure 5.13: **SH generation from symmetric nanoparticle dimer.** Near-field distribution of (a) the fundamental and (b) the SH intensities close to a nanodimer composed of two 20 nm gold nanoparticles. The spacing between the two nanoparticles is 4 nm. The incident wavelength is $\lambda = 1244$ nm. Real part of the x -component for (c) the fundamental and (d) the SH electric fields, as well as the real part of the y -component for (e) the fundamental and (f) the SH electric fields. (g) Scattered SH intensity as a function of the scattering direction θ (Fig. 5.12) computed for different incident wavelengths increasing from $\lambda = 1150$ nm to 1422 nm.

the surface S , and \hat{r} is the outward vector normal to the surface. The following relations are deduced from the properties of the near-field at the fundamental wavelength, see Fig. 5.13(c) and Fig. 5.13(e), and the expression of the nonlinear polarization, Eq. (5.7):

$$P_x(\mathbf{r}_1, 2\omega) = -P_x(\mathbf{r}_2, 2\omega), \quad (5.8)$$

5.5. Correlation between mode symmetry and second harmonic generation from nanoclusters

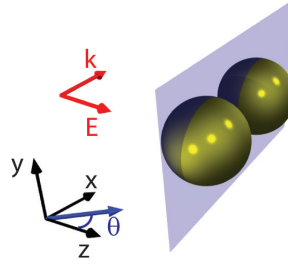


Figure 5.14: **Schematic of nanoparticle dimer along with illumination conditions.** The symmetric gold nanodimers studied in this work. The nanoparticle diameter is 20 nm and the spacing is 4 nm. The blue plane corresponds to the plane discussed in the main text ($z = 0$). Contrary to Fig. 5.13, an incident planewave propagating along the x -axis and polarized along the z -axis is considered. The scattering angle θ is defined relatively to the z -axis.

$$P_{y,z}(\mathbf{r}_1, 2\omega) = P_{y,z}(\mathbf{r}_2, 2\omega), \quad (5.9)$$

where $\mathbf{r}_1 = (x, y, z)$ and $\mathbf{r}_2 = (-x, y, z)$ are linked by a mirror symmetry relation. Note that these relations can be directly deduced from the cluster geometry and the incident wave properties. Since the nonlinear polarization is the physical origin of the SH electric field, the SH electric field must follow the selection rules that apply to the nonlinear polarization, i.e. the rules induced by the Eqs. (5.8) and (5.9), in order to fulfill the Curie dissymmetry principle. That clearly means that the SH electric field distribution must be described using only symmetric modes, corresponding to the modes for which

$$E_x(\mathbf{r}, 2\omega) = 0, \forall \mathbf{r} = (0, y, z). \quad (5.10)$$

In other words, only the modes for which the normal component of the electric field vanishes in the plane $x = 0$ have to be considered to expand the SH wave. From the eigenmode analysis, it is clear that the two modes with the shortest resonant wavelengths are involved in the SH wave due to their symmetry properties. In order to confirm this hypothesis, the SH intensity scattered in the (O, x, z) plane was calculated as a function of the scattering direction θ , Fig. 5.13(g). Several incident wavelengths, corresponding to the resonant excitation of the eigenmodes at the SH wavelength, were considered in order to determine which modes are active at the SH emission step. Note that the SH intensity vanishes in the forward direction, as expected for a metallic nanostructure with a centrosymmetric shape [407]. The scattered SH intensity is maximal when the symmetric modes are resonantly excited at the SH wavelength, especially the mode corresponding to two parallel dipole moments pointing in the same direction. As discussed by J. I. Dadap in the case of isolated spherical nanoparticles [407],

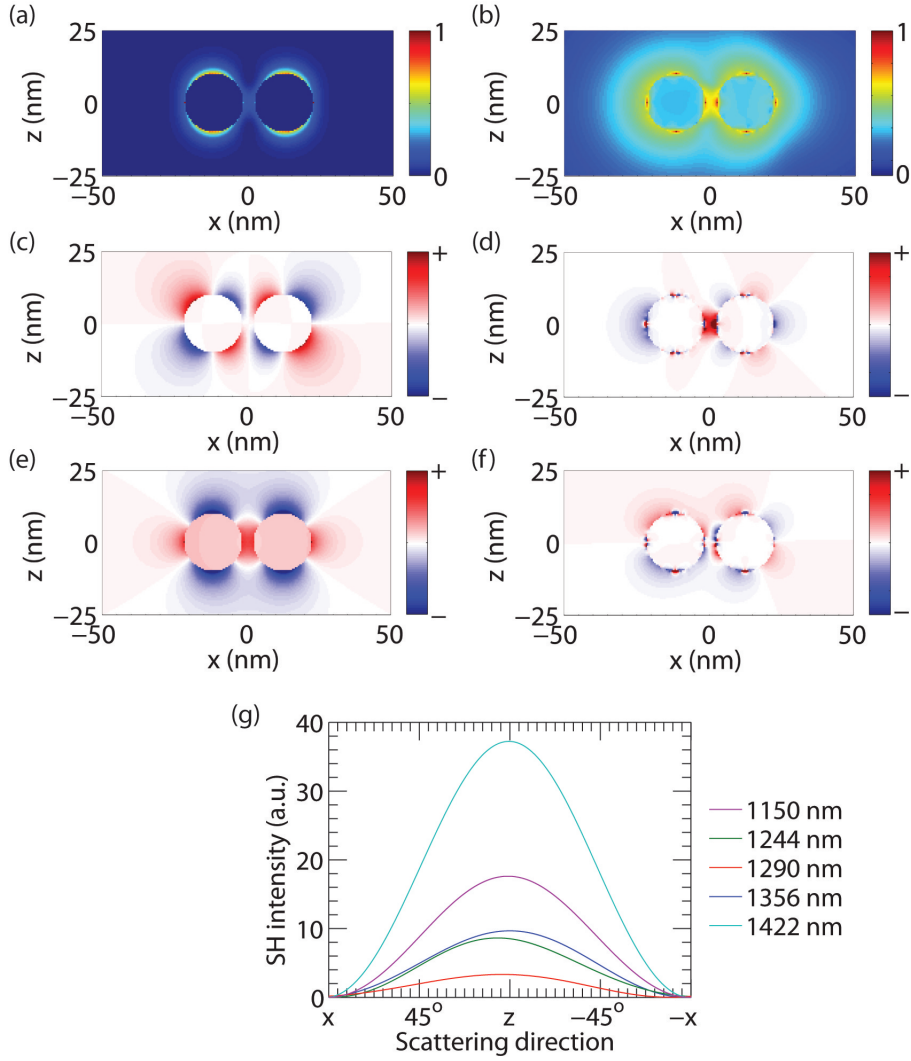


Figure 5.15: SH generation from symmetric nanoparticle dimer: propagation along dimer axis. Near-field distribution of (a) the fundamental and (b) the SH intensities close to a nanodimer composed of two 20 nm gold nanoparticles. The spacing between the two nanoparticles is 4 nm. An incident planewave propagating along the x -axis and polarized along the z -axis is considered. The incident wavelength is $\lambda = 1244$ nm. Real part of the x -component for (c) the fundamental and (d) the SH electric fields, as well as the real part of the z -component for (e) the fundamental and (f) the SH electric fields. (g) Scattered SH intensity as a function of the scattering direction θ (Fig. 5.14) computed for different incident wavelengths increasing from $\lambda = 1244$ nm to 1492 nm.

this mode is excited by the phase variation of the incident wave across the considered nanostructure. This mode is resonant at $\lambda = 645$ nm and is resonant at the SH wavelength for an incident wavelength $\lambda = 1290$ nm (red curve). Indeed, it was shown that localized surface plasmon resonances can increase SHG either at the fundamental or SH wavelength [407]. In this case, the far-field SH intensity is 7 times higher than in the off-resonant case ($\lambda = 1150$

5.5. Correlation between mode symmetry and second harmonic generation from nanoclusters

nm) even though the fundamental intensity is slightly lower. This observation indicates that the symmetric modes are the ones involved in the scattered SH wave, as predicted by the eigenmode analysis. These results indicate that modes with the required symmetry properties effectively contribute to the SHG from coupled plasmonic nanostructures although these modes cannot be directly excited by an incoming planewave in the linear regime.

Influence of the excitation condition

In order to investigate the influence of the excitation condition on the derived selection rules, an incident planewave propagating along the x -axis and polarized along the z -axis is considered (see Fig. 5.14). The first consequence of this excitation configuration is that the plane $x = 0$ is no longer a symmetry/antisymmetry plane. In the present case, the selection rules must be derived relatively to the plane $z = 0$ (Fig. 5.14) and can be written as:

$$P_z(\mathbf{r}_1, 2\omega) = -P_z(\mathbf{r}_2, 2\omega), \quad (5.11)$$

$$P_{x,y}(\mathbf{r}_1, 2\omega) = P_{x,y}(\mathbf{r}_2, 2\omega), \quad (5.12)$$

where $\mathbf{r}_1 = (x, y, z)$ and $\mathbf{r}_2 = (x, y, -z)$ are linked by a mirror symmetry relation, and

$$E_z(\mathbf{r}, 2\omega) = 0, \forall \mathbf{r} = (x, y, 0). \quad (5.13)$$

The plane $z = 0$ is clearly an antisymmetry plane for the fundamental electric field but a symmetry one for the SH electric field (see the near-field distributions in Fig. 5.15) as observed for the plane $x = 0$ when an incident planewave polarized along the x -axis and propagating along the z -axis are considered (see the discussion in section 5.5.1). The mode excited at the fundamental wavelength is the one for which two parallel dipole moments point in the same direction (see Fig. 5.12(e)). The mode excited at the SH wavelength corresponds to the mode for which two aligned dipole moments point in the same direction (see Fig. 5.12(c)). This observation is confirmed by the far-field analysis. Indeed, the far-field SH intensity is maximal when this mode is resonantly excited at the SH wavelength, Fig. 5.15(g), demonstrating that the contribution of this mode to the scattered SH wave is important. It is interesting to note that here the excitation scheme is the reverse of the previous one: the mode excited at the fundamental (SH) wavelength in the previous case is now the mode excited at the SH (fundamental) wavelength. Nevertheless, the far-field SH intensity vanishes along the backward and forward directions in each case. In the following part, asymmetric dimers are considered, reducing the symmetry of the problem under study in order to test the generality

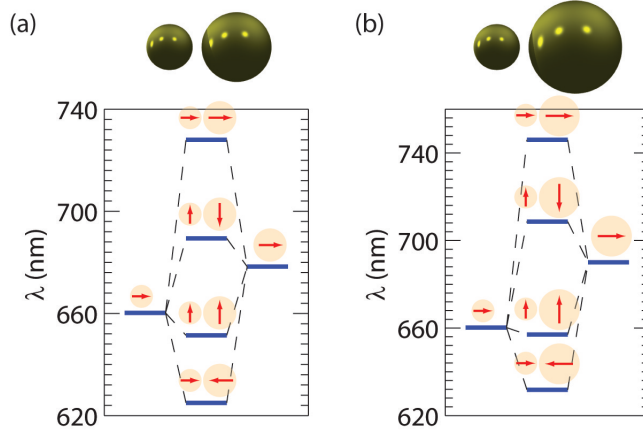


Figure 5.16: **Schematics and modes of asymmetric dimer.** (a) the two asymmetric nanodimers considered in this work. Diagrams describing the resonant wavelength of the eigenmodes arising from the coupling between the dipolar modes of an asymmetric dimer composed of a 20 nm gold nanoparticle with (b) a 30 nm or (c) a 40 nm gold nanoparticles. The spacing between the two nanoparticles is 4 nm.

of the derived selection rules and to address the influence of symmetry breaking on the SH response of nanoparticle clusters.

5.5.2 Asymmetric dimers

Dimers composed of gold nanoparticles with different diameters are investigated. Similar systems were experimentally studied in [454]. The diameter of one nanoparticle is kept constant (20 nm) while two different diameters are considered for the second, larger, nanoparticle: 30 nm and 40 nm. These nanodimers are no longer centrosymmetric, schematically illustrated in Fig. 5.16(a) and (b). The nanogap is 4 nm for all cases. The real part of the eigenwavelength for the 30 nm nanoparticle is $\lambda_m = 678$ nm and that of the 40 nm nanoparticle is $\lambda_m = 700$ nm. Figure 5.16 shows the wavelengths of the eigenmodes arising from the coupling between the dipolar modes of a 20 nm gold nanoparticles with the dipolar modes of a 30 nm, Fig. 5.16(b), or a 40 nm, Fig. 5.16(c), gold nanoparticle. The resonance wavelengths of the hybridized modes, as compared to the symmetric dimer, are different since the resonance wavelengths of the individual dipole modes supported by the nanoparticles vary with the nanoparticle diameter. Nevertheless, the orientations of the dipolar moment for the different hybridized modes are identical to those of the symmetric dimer discussed in the section 5.5.1. For instance, for all the nanodimers studied, the hybridized mode with the longest resonant wavelength corresponds to the coupling between two dipolar moments aligned in the same direction. The near-field distributions of the fundamental and SH intensities, as well as the corresponding distribution of the real part of the x -component of the electric field, were computed using SIE for an incident planewave polarized along the x -axis and propagating along the z -axis (see Figs. 5.17 and 5.18).

5.5. Correlation between mode symmetry and second harmonic generation from nanoclusters

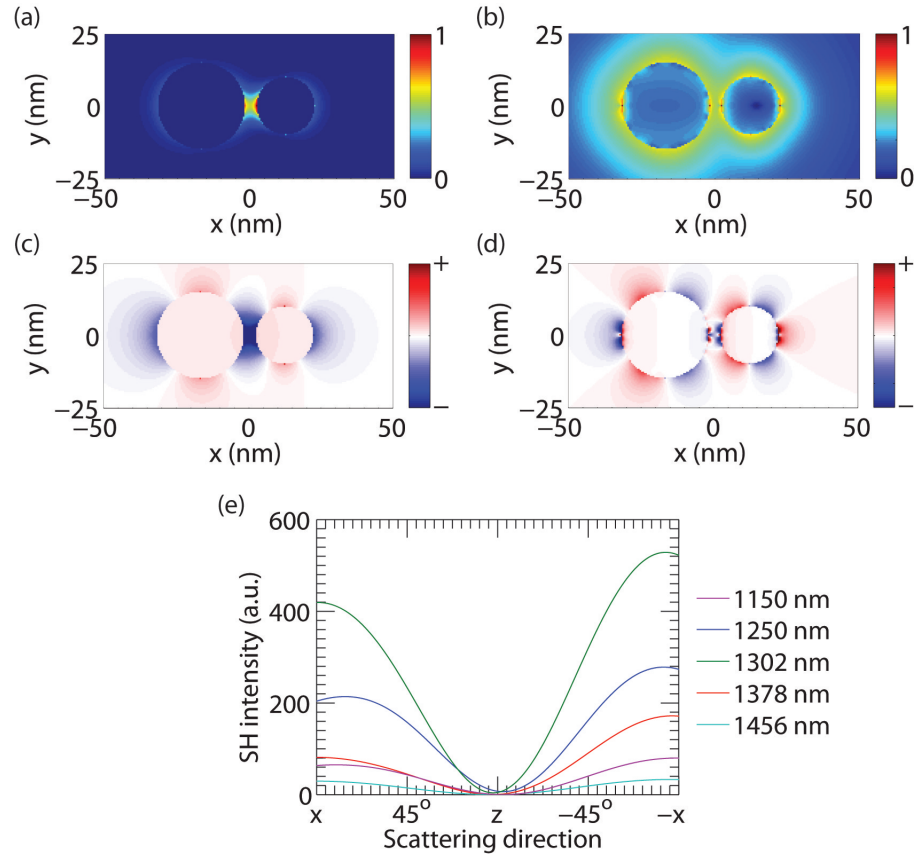


Figure 5.17: **SH generation from asymmetric dimer with 20 and 30 nm particles.** Near-field distribution for (a) the fundamental and (b) the SH intensities close to a nanodimer composed of a 20 nm and a 30 nm gold nanoparticles. The spacing between the two nanoparticles is 4 nm. The incident wavelength is 1456 nm. Real part of the x -component for (c) the fundamental and (d) the SH electric fields. (e) Scattered SH intensity as a function of the scattering direction computed for fundamental wavelengths increasing from $\lambda = 1150$ nm to $\lambda = 1456$ nm.

At the first sight, the general behavior of the near-field distributions is identical to that observed for the symmetric nanodimer. For example, an enhancement of the fundamental electric field is observed in the nanogap, but no particular enhancement of the SH electric field in this region is visible, Fig. 5.17(b) and 5.18(b). This observation indicates that the selection rules derived in the previous section hold qualitatively in the case of asymmetric dimers even though these nanostructures do not possess any symmetry/antisymmetry planes. Note that the nanoparticles considered in the present work are perfectly spherical but the selection rules are broken in the case of realistic metallic nanoparticles with small sizes as was experimentally demonstrated [455]. In order to investigate the influence of the asymmetry on the SHG in the far-field, the SH intensity scattered in the (O, x, z) plane was calculated as a function of the scattering direction for the two asymmetric nanodimers considering several incident wavelengths corresponding to resonant excitation of the eigenmodes at the SH wavelength (see Fig. 5.16). As in the case of the symmetric nanodimer, the scattered SH intensity is maximal

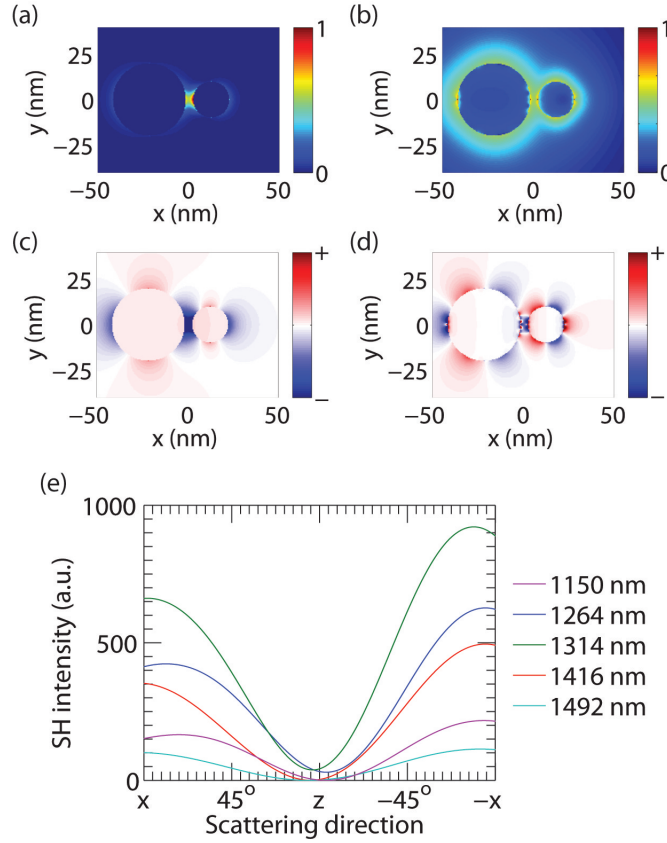


Figure 5.18: SH generation from asymmetric dimer with 20 and 40 nm particles. Near-field distribution for (a) the fundamental and (b) the SH intensities close to a nanodimer composed of a 20 nm and a 40 nm gold nanoparticles. The spacing between the two nanoparticles is 4 nm. The incident wavelength is $\lambda = 1492$ nm. Real part of the x -component for (c) the fundamental and (d) the SH electric fields. (e) Scattered SH intensity as a function of the scattering direction computed for fundamental wavelengths increasing from $\lambda = 1150$ nm to $\lambda = 1492$ nm.

when the symmetric modes (using the same terminology even though the field amplitudes are different in the asymmetric cases, Figs. 5.17 and 5.18) are resonantly excited at the SH wavelength. The asymmetry of the nanodimer is clearly revealed by the SH far-field since the SH intensity scattered along the $-x$ direction differs from that scattered along x direction, Fig. 5.17(e) and 5.18(e) [390]. Even though the centrosymmetry is broken, the SH intensity scattered in the forward direction is not dramatically increased but remains only a small part of the total SH intensity. This observation is consistent with previous experimental results which report lower SHG from asymmetric dimers than from symmetric ones [454]. This point confirms that the selection rules are not completely broken when the diameter of one of the nanoparticles is twice the diameter of the other one.

5.5. Correlation between mode symmetry and second harmonic generation from nanoclusters

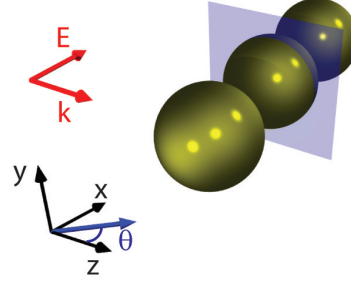


Figure 5.19: **Schematic of linear trimer.** The gold nanotrimers studied in this work. The nanoparticle diameter is 20 nm and the spacing is 4 nm. The blue plane corresponds to the plane discussed in the main text ($x=0$). This plane is alternatively a symmetry or antisymmetry plane for the electromagnetic field (see the discussion in the main text). The scattering angle θ is defined relatively to the z -axis.

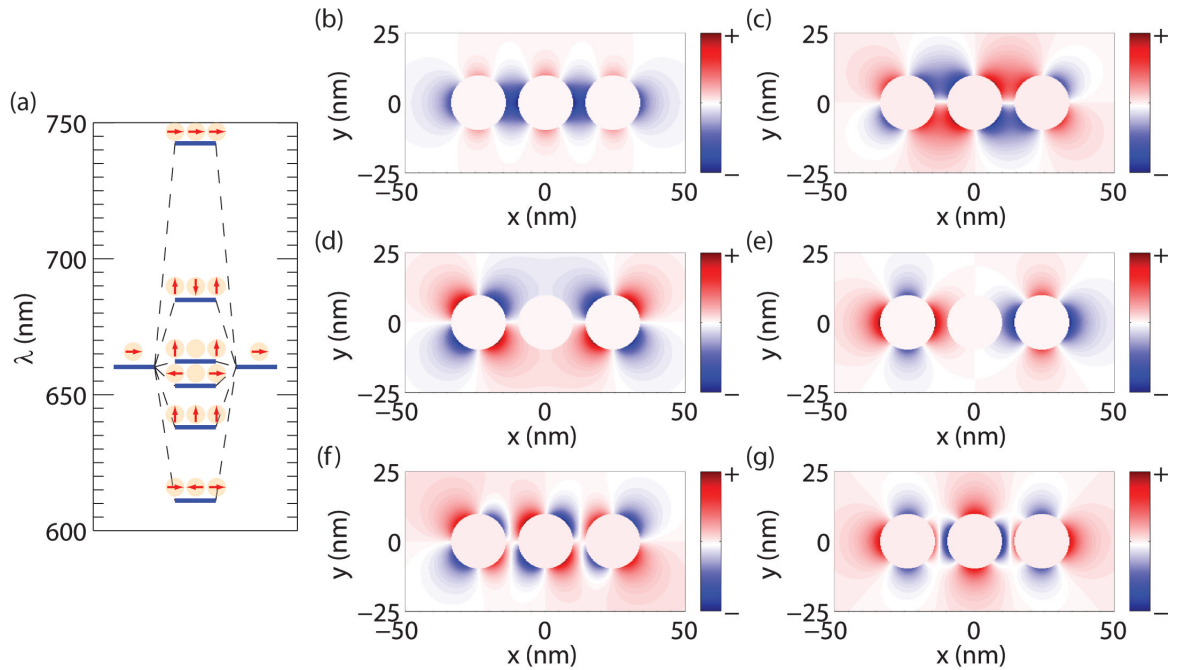


Figure 5.20: **Energy diagram and field distributions of a linear trimer.** (a) Diagram describing the resonant wavelength of the eigenmodes arising from the coupling between the dipolar modes of three 20 nm gold nanoparticles with nanogaps of 4 nm. The three nanoparticles are lined up along the x -axis. The arrows indicate the orientation of the dipolar moments for the corresponding eigenmodes. (b-g) Real part of the x -component of electric field evaluated for the eigenmode with a resonant wavelength of (b) 742.5 nm, (c) 685 nm, (d) 662 nm, (e) 653 nm, (f) 638 nm, and (g) 611 nm.

5.5.3 Linear trimer

Metallic nanostructures with several nanogaps are also promising for applications in non-linear plasmonics. For example, it was recently demonstrated that the SHG from 3-arms multi-resonant plasmonic nanoantennas is higher than SHG from antennas resonant only at the fundamental wavelength [456]. A linear nanotrimer composed of three identical 20 nm nanoparticles lined up with 4 nm separations is considered (Fig. 5.19). The eigenmodes analysis for this cluster is presented in Fig. 5.20. The total number of eigenmodes is 9 corresponding to 6 resonant wavelengths, since modes with resonant wavelengths $\lambda_m = 685$ nm, 662 nm, and 638 nm are degenerated. As observed in the case of the symmetric nanodimer studied in section 5.5.1, both symmetric and antisymmetric modes resulting from the coupling between original dipolar modes are revealed by the eigenmode analysis.

SIE computations were performed considering an incident plane wave polarized along the x -axis and propagating along the z -axis. Due to the specific nanoparticles organization and

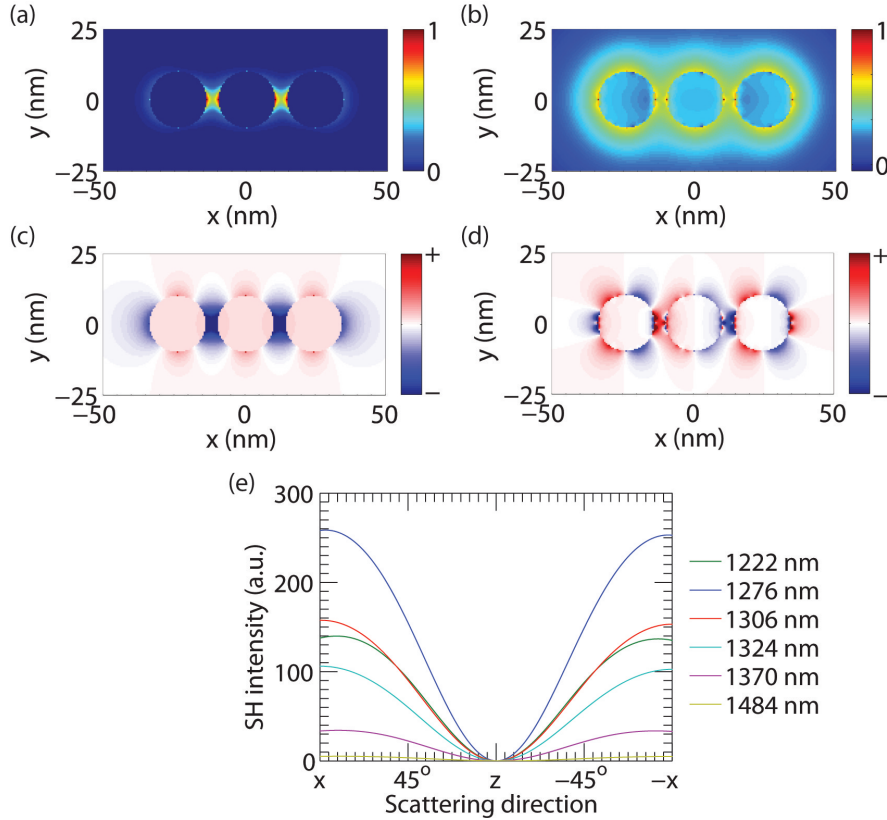


Figure 5.21: **SH generation from a linear trimer.** Near-field distribution of (a) the fundamental and (b) the SH intensities close to a linear nanotrimer composed of three 20 nm gold nanoparticles. The spacing between the nanoparticles is 4 nm. The incident wavelength is $\lambda = 1306$ nm. Real part of the x -component for (c) the fundamental and (d) the SH electric fields. (e) The scattered SH intensity as a function of the scattering direction computed for incident wavelength increasing from $\lambda = 1222$ nm to $\lambda = 1484$ nm.

fundamental near-field distribution symmetry (Fig. 5.21), the selection rules Eq. (5.8) and (5.9) derived for the SHG from symmetric nanodimer also apply to the case of SHG from this linear nanotrimer. Note that the x -component of the SH electric field does not necessarily vanish in the gap center since the nanogaps do not stand in $x = 0$ plane (the symmetry plane shown in Fig. 5.19). Indeed, the fundamental electric field amplitudes computed on each side of a given nanogap are not perfectly identical and the amplitudes of the nonlinear currents are then different, resulting not in total destructive interferences. In order to determine which modes dominate the nonlinear response, the SH intensity scattered in the (O, x, z) plane was calculated as a function of the scattering direction and shown in Fig. 5.21(e). Several incident wavelengths, corresponding to resonant excitation of the available eigenmodes at the SH wavelength, were considered. As observed in the case of the nanodimers, the SH far-field intensity is maximal when the SH wavelength matches the resonant wavelength of the mode for which all the dipolar moments are parallel and pointing in the same direction. This confirms that the derived selection rules are general and can be applied to different kinds of nanoparticle clusters.

5.6 Summary

A method for computing the eigenmodes of a plasmonic system composed of nanoparticles based on the Green's tensor technique was developed. Using examples of monomers, dimers and trimers, I showed that the modes exhibit complex eigenwavelengths. The effect of various geometrical parameters on the complex eigenwavelengths was studied in detail. In the case of a dimer, it was shown that the imaginary part of the dielectric constant of the plasmonic metal at the eigenwavelengths indicates the contribution of radiative and intrinsic damping in a given mode. Next, the effect of symmetry breaking was studied in the case of a nanoparticle trimer by monitoring both the eigenwavelengths and the excitation strengths of the modes by various incident conditions. Finally, a plasmonic quadrumer exhibiting polarization control property was investigated by studying the modal behavior of the system. Comparisons with full wave calculations, have shown that this simple quadrumer captures the entire behavior of the complex original structure.

After studying the linear modes of nanoparticle clusters, I studied the SHG from interacting spherical plasmonic nanoparticles. Several cluster geometries including symmetric / asymmetric dimers, and linear trimers were considered in this work. The fundamental and SH responses of the corresponding clusters were computed and an eigenmode analysis was performed. The role played by the different eigenmodes in the SHG, at both the excitation and reemission steps, was emphasized in relation with the cluster symmetry. It was in particular observed that the SHG can be significantly enhanced when the fundamental field is such that its SH matches modes with suitable symmetry. The results presented in this chapter are not specific to SHG. Our method can be applied to complex assemblies with an arbitrary number of nanoparticles as well as other nonlinear optical processes, such as third harmonic generation.

6 Perfect absorption of light by plasmonic structures

In this chapter, perfect absorption of light using plasmonic structures is studied both theoretically and experimentally. Perfect absorption is achieved by either exploiting the critical coupling (CC) or the coherent perfect absorption (CPA) phenomena and it is shown that nearly all the incident light energy can be used for enhancing the plasmonic near-field. In case of the CPA based perfect absorbers, it is experimentally demonstrated that the absorption in the system can be tuned from 18% to 96% by modifying the illumination condition. Furthermore, this enhanced near field due to perfect absorption is probed by studying the SERS signals of molecules in the plasmonic near field.

6.1 Introduction

Plasmonic structures, supporting both localized and propagating surface plasmons, have been studied in great detail for various applications exploiting their strong near-field enhancement [9, 12, 13, 17–19, 37–39, 41, 47, 51–53, 62, 67, 457]. However, in many of these applications only a part of the incident light is used in exciting the relevant plasmon modes leading to non-optimized near-fields around the structure. For example, consider a system composed of a thin gold film placed in the Kretschman configuration. When this structure is excited using a TM polarized plane wave, the film thickness controls the net reflection by the structure at the plasmon resonance and thereby its near field enhancement (Fig. 6.1). It is clear that there exists an optimal thickness for which the field is maximized and reflectivity is minimized. As one moves away from this optimal coupling condition, the percentage of incident light used for exciting the plasmon resonance reduces. Therefore, it is vital to explore methods by which the excitation efficiency can be enhanced in case of a non-optimized plasmonic system. As mentioned in the previous chapter a significant improvement can be introduced by exploiting the recently reported notion of coherent perfect absorption (CPA) and critical coupling (CC) [164, 165, 335, 458–460] in the plasmonic structure, which is the main theme of this chapter.

Currently, several distinct ways of achieving perfect absorption in plasmonic structures exist,

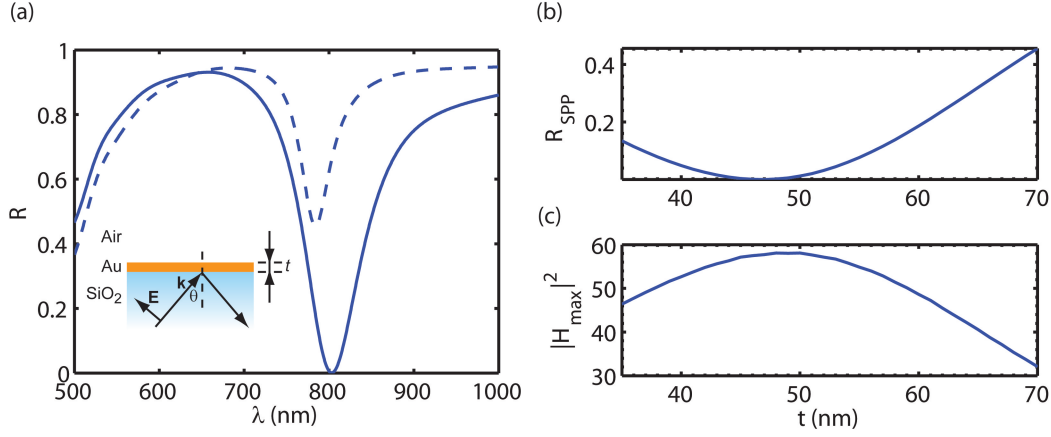


Figure 6.1: **Comparison between reflectivity and field enhancement for a thin gold film.** (a) Reflectivity from a gold film with thickness of 46 nm (solid curve) and 70 nm (dashed curve) as a function of wavelength. (b) Reflectivity and (c) magnetic field intensity as a function of film thickness, t , at the plasmon resonance wavelength. The structure is illuminated with a TM polarized plane wave at an incidence angle of 43° .

which do not use CC or CPA. The dependence of the plasmon resonance on the geometrical parameters has been exploited for tailoring resonances which exhibit low or zero scattering losses and absorb most or all of the incident energy [457, 461–468]. For example, Popov *et al.* considered absorption of light by a grating made in a thick metallic slab [462]. It was shown that an appropriate choice of parameters could trap all the light in the structure. Alternatively, it is possible to design plasmonic structures supporting non-radiative or dark resonances which intrinsically possess low scattering losses [153, 156, 159, 463–465, 467]. Such perfect absorbers based on non-radiative resonances can also be realized by placing a plasmonic structure supporting a bright dipolar mode on top of a metallic film with a very small gap [463–467]. One of the main advantages of perfect absorbers which are created via tailoring the plasmon resonance itself is that they are relatively easy to realize and can lead to the generation of extremely large near fields. However, this approach invariably leads to modification of the underlying plasmonic mode which can some times be undesirable. Svedendahl *et al.* recently demonstrated perfect absorption of light near the critical angle using a structure with random sparse distribution of gold nanodisks [121]. Even though this approach can be used for achieving perfect absorption using weak plasmonic resonances, it is limited to illumination angles close to the critical angle.

In contrast to the above methods relying heavily on structured surfaces for perfect absorption, a relatively easy technique is offered by far-field interference with a single incident beam (CC) [335, 458–460, 469] or dual beams (CPA) [164, 165]. It was shown that destructive and constructive interference in the far field can lead to tuning the absorption of a plasmonic structure. In fact one can tune the system over a broad range from perfect absorption (destructive interference) to superscattering (constructive interference). There have been several theoretical and experimental demonstrations of CC [335, 458–460, 470]. In critical coupling

configuration, the plasmonic structure is placed on top of a perfect mirror with a gap. By controlling the properties of the structure and the thickness of the gap, the nature of interference between the reflected plane waves in the medium of incidence can be tuned. It is thus possible to choose parameters such that perfect destructive interference occurs in the far field and that all the light is absorbed by the structure. CPA was shown only very recently [164, 165]. The group of H. Cao and D. Stone showed complete control over the absorption by a $100\text{ }\mu\text{m}$ Si slab when it was illuminated with two plane waves simultaneously. This effect is also known as anti-lasing or time reversed lasing since it mimics the operation of a time reversed laser near threshold. Note that time reversal would imply the replacement of the amplifying medium by an absorbing medium with outgoing waves replaced by incoming ones. Since then CPA has been realized in various optical systems and used for various applications [465, 471–479]. However, very few experimental studies of CPA-plasmonic structures exist, where the two plane waves are incident from the same side of the structure [480–482].

Often the coupled plasmonic structures can support a multitude of modes. For example the coupling of the two interface plasmons in a thin metal film can lead to the so-called long and short range modes due to normal mode splittings [6]. I probe another interesting feature of CPA to excite one of the preselected modes. In other words I explore the useful property of the CPA-plasmonic systems to absorb all the incident light and channel the energy into a given mode of the structure. Similar efforts are currently ongoing in the context of spherical nanostructures [483] with very useful applications in a multi-modal system. To this end I exploit the coupled modes of a gap plasmon guide [484], which uses the resonant tunneling phenomenon for finite transmission, essential for CPA.

This Chapter is structured as follows. Section 1.2 is devoted to CPA with a gap plasmon waveguide supporting coupled surface plasmons. Section 1.3 deals with CPA using a metal-dielectric composite film supporting localized plasmons. In the last Section, I develop a critical coupling geometry using large scale SERS substrates to control the absorption efficiency of plasmonic structures and evaluate its effect on SERS.

6.2 Coherent perfect absorption mediated selective mode excitation

In this section, I demonstrate selective and near perfect excitation of a plasmonic mode in a multi-modal system. This is achieved using coherent perfect absorption (CPA) where the CPA dip in the frustrated total reflection geometry coincides with the resonance. A standard configuration CPA uses a symmetric structure with symmetric illumination from both sides, so that light reflected from one side can have complete destructive interference with that transmitted from the other side. One can also have the opposite, namely, superscattering (SS) as a consequence of constructive interference.

Note that CPA based on complete destructive interference can ensure perfect absorption, while the resonance coincidence allows for the complete transfer of the incident energy into the chosen guided or the surface mode of the structure. This is possible since the mode

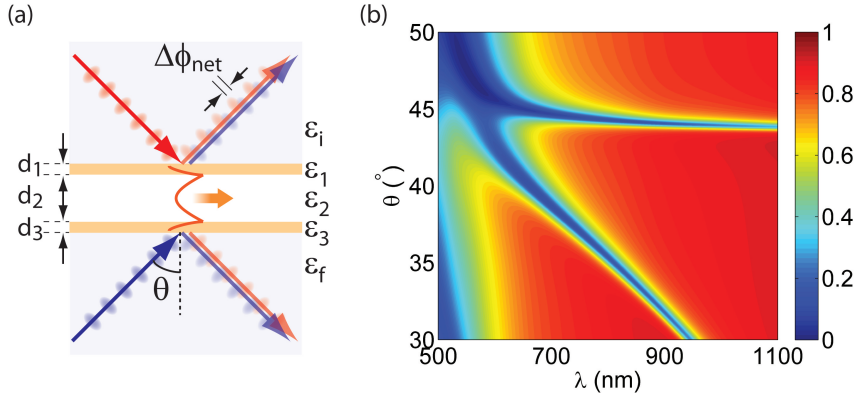


Figure 6.2: **Gap plasmon waveguide structure.** (a) Schematic diagram of the geometry. (b) Simulated dispersion diagram of structure with the following parameters : $d_1 = d_3 = 40$ nm, $d_2 = 600$ nm, $\epsilon_i = \epsilon_f = 2.28$, $\epsilon_1 = \epsilon_3 = \epsilon_{Au}$ and $\epsilon_2 = 1$. Note that a 2 nm chromium layer between each of the gold-glass interfaces is included in the simulations.

frequencies of a system have comparatively smaller dispersion, while the CPA resonance can be moved around by changing the other parameters of the system like absorption (for a composite medium), widths of the layers, angle of incidence, etc... . Using the example of a symmetric gap plasmon waveguide, I show experimentally that at least 96% of the incident energy can be absorbed and channeled into a given plasmon mode. Moreover, the π phase difference between these coupled plasmon modes supported by the gap plasmon structure ensures that the complete absorption (due to destructive interference) in one of these would ensure super scattering (constructive interference) at the other frequency. A variation of relative phase in the incident beam from zero to π is shown to lead to a transition from superscattering to CPA states.

6.2.1 Simulation of gap plasmon waveguide structures

Consider the gap plasmon waveguide structure shown in Fig. 6.2(a). The complex reflection (r) and transmission coefficients (t) for single plane wave incidence are calculated using the transfer matrix method [260]. The total scattering from the structure due to simultaneous incidence of two plane waves on the top and bottom are given by $I_T = |r + te^{i\Delta\phi}|^2$ and $I_B = |re^{i\Delta\phi} + t|^2$, where $\Delta\phi$ is the initial phase difference between the plane wave incident from the top and bottom. Additionally, I define the phase difference between the reflection and transmission coefficients as $\Delta\phi_{r-t} = \phi_r - \phi_t$. Note that the total scattered intensity on either side, I_T and I_B , are identical if $\Delta\phi = 0$ or $\Delta\phi = \pi$. The dielectric function of gold is taken from the work of Johnson and Christy [259].

6.2.2 Fabrication of plasmon waveguide structures

The samples used in this study are fabricated by a collaborator in the lab, B. Abasahl, using the following protocol. Two float glass substrates (10 mm x 10 mm and the thickness of 500 μm) are coated with 2 nm of chromium and 40 nm of gold by electron beam deposition. After partially covering one of the glass substrates with a Kapton tape (10 mm x 2 mm) along the center. On this protected substrate a 2 nm layer of chromium and 560 nm of aluminum are evaporated. Afterwards, the two substrates are exposed to mild oxygen plasma (30 watts, 250 mbar) for 30 seconds and pressed together in a pneumatic press at pressure 1.5 KPa. After 30 minutes, the sample is temporarily released and the corners are bonded with an adhesive. Enough care is taken to ensure that the adhesive did not invade the gap. The sample finally is left overnight in the press.

6.2.3 Optical measurements of gap plasmon waveguide structures

Dispersion measurements

The dispersion diagram (reflectivity, R , as a function of λ and θ) of the plasmonic system is measured using a broadband angle resolved setup. The details of the experimental setup are provided in Arash *et al.* [485]. Briefly, the sample is mounted on a cylindrical glass slab ($\epsilon = 2.13$) such that plasmons can be excited using the Kretschmann configuration. The sample is then illuminated using a single TM polarized plane wave at various angles and the reflected light collected using a fiber is analyzed using a spectrometer (Ocean optics HR4000). The raw reflected intensity is normalized with the intensity of the lamp to extract the reflectivity of the sample.

Dual plane wave experiment

The experimental setup used for simultaneous dual beam incidence is shown in Fig. 6.3. A super-continuum source (Fianium FemtoPower 1060) is used as the light source in these measurements. The output from the laser is split into two individual beams using a beam splitter. On both the paths a thin glass cover slip (thickness 150 μm) is placed and the cover slip on one of the arms is rotated to control the phase difference between the two paths. The two input beams are then incident on the sample through two glass prisms ($\epsilon = 2.28$) at identical angles of incidence. The total scattered light on either sides, D1 and D2, is simultaneously measured using two spectrometers (Ocean optics model H4000; $400 \text{ nm} \leq \lambda \leq 1000 \text{ nm}$). The raw scattered intensity is normalized with the intensity of the supercontinuum to convert the counts into normalized scattered intensity. For measuring the response due to a single plane wave one of the arms of the interferometer is blocked while measuring the outputs, D1 and D2.

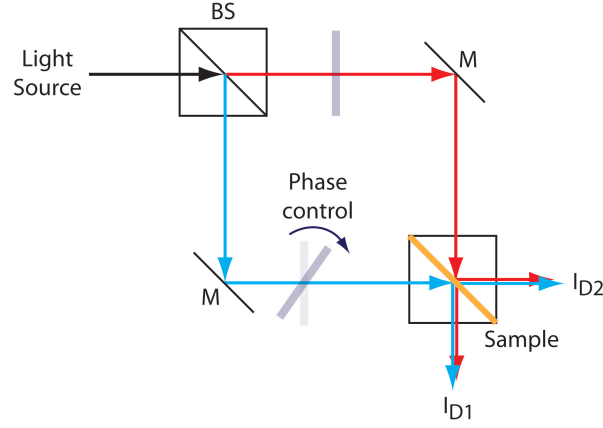


Figure 6.3: Schematic of the setup used for CPA measurements with simultaneous dual plane wave incidence.

6.2.4 Theoretical demonstration of CPA and SS

Resonances of a gap plasmon waveguide

In order to demonstrate CPA assisted perfect energy transfer to a given mode I use a symmetric gap plasmon structure shown in Fig. 6.2(a). Two gold films deposited on glass substrates are separated by a controlled air gap (thickness d_2 nm) which serves the purpose of controlling the coupling between the plasmon at the two gold-air interfaces. Figure 6.2(b) shows the calculated reflected intensity as a functions of angle of incidence (θ) and wavelength (λ), when the structure is illuminated by a single TM polarized plane wave from one side. The two resonance branches observed correspond to the plasmon mode with symmetric (upper branch) and the anti-symmetric (lower branch) magnetic field distributions. Furthermore, note that the structure exhibits a finite transmission because of resonant energy transfer mediated by the coupled plasmon modes.

Conditions required for CPA

When a symmetric structure is illuminated with two plane waves simultaneously, the total scattering from the structure on each side is given by the interference of the reflected light due to plane wave incident from that side with the transmitted light due to a plane wave incident from the opposite side. Consequently CPA occurs only if the conditions for perfect destructive interference are satisfied and total scattering on either side is identically equal to zero, i.e., $I_T = I_B = 0$. Thus, the conditions that must be satisfied for CPA are the following:

$$|r| = |t|,$$

$$\Delta\phi_{net} = \Delta\phi_{r-t} + \Delta\phi = \pi.$$

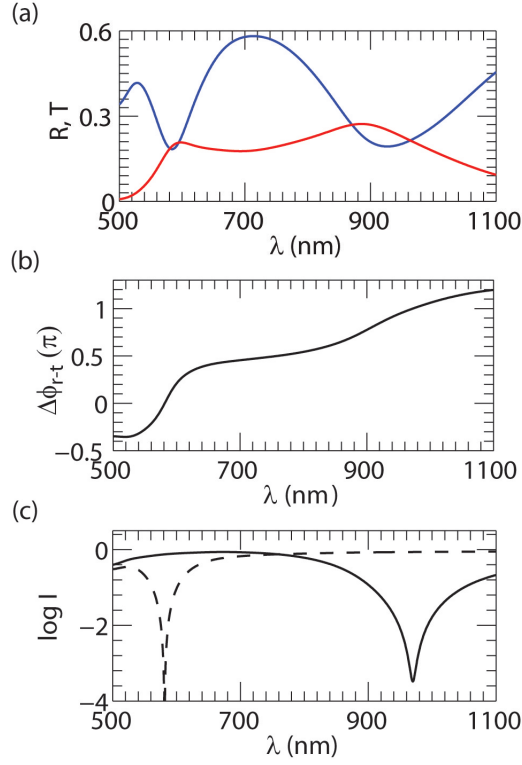


Figure 6.4: **Interchangeable CPA and SS at the long range and short range gap plasmons.** (a) Reflection (blue) and transmission (red) spectra when a single plane wave is incident on the structure. (b) Phase difference between the reflection and transmission coefficients as a function of wavelength. (c) Log of the total scattered intensity ($\log_{10} I$) due to simultaneous incidence of two plane waves for $\Delta\phi = 0$ (solid curve) and $\Delta\phi = \pi$ (dashed curve). The system parameters are: $\theta = 44^\circ$, $d_1 = d_3 = 40$ nm, $d_2 = 600$ nm, $\epsilon_i = \epsilon_f = 2.28$, $\epsilon_1 = \epsilon_3 = \epsilon_{Au}$ and $\epsilon_2 = 1$. Note that a 2 nm chromium layer between each of the gold-glass interfaces is included in the simulations.

Note that $\Delta\phi_{r-t}$ corresponds to the phase difference that occurs due to the resonances of the structure and $\Delta\phi$ is the initial phase difference between the two plane waves.

At the symmetric gap plasmon resonance

The reflection and transmission spectra of a waveguide with $d_2 = 600$ nm and $d_3 = 40$ nm, on illumination with a single plane wave at $\theta = 44^\circ$ is shown in Fig. 6.4(a). The two peaks (dips) in the transmission (reflection) spectra correspond to the anti-symmetric and symmetric surface plasmon resonances.

It is clear that the amplitude condition required for CPA is satisfied at both the plasmon resonances located at 581 and 969 nm. Furthermore, $\Delta\phi_{r-t} = \pi$ at the plasmon at longer wavelength (see Fig. 6.4(b)), implying that both the conditions of phase and amplitude are met at this wavelength for $\Delta\phi = 0$. Therefore, the total scattering due to simultaneous dual

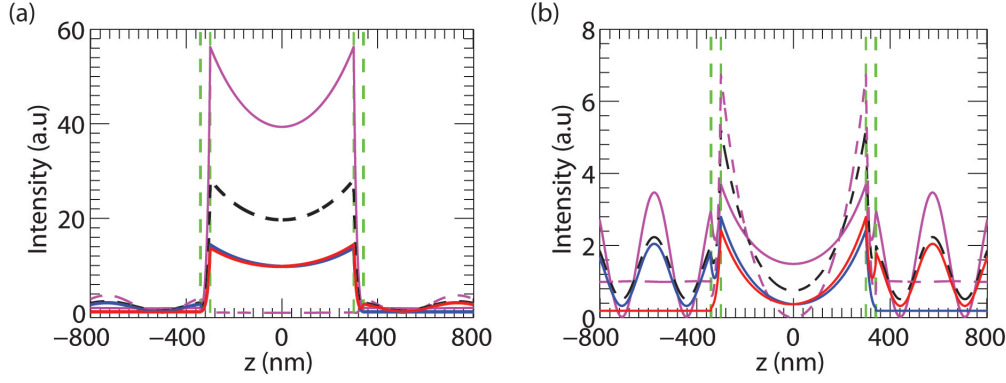


Figure 6.5: **Field enhancement and suppression due to CPA and SS.** Magnetic field intensities at 969 nm (a) and 581 nm (b) due to a single plane wave incidence from top (red), bottom (blue) and simultaneous incidence of two plane waves for $\Delta\phi = 0$ (solid magenta) and $\Delta\phi = \pi$ (dashed magenta). Also, the back dashed curve shows the intensity due to incidence of simultaneous incidence of two incoherent plane waves. Rest of the parameters are the same as in Fig. 6.4

plane wave incidence is expected to be zero at this wavelength and this is evident from Fig. 6.4(c). At 969 nm the total scattering is around 0.01%, thus 99.99% light is absorbed by the structure. On the other hand the plasmon mode at 581 nm shows superscattering due to constructive interference and the resonance is not excited for $\Delta\phi = 0$. However, by introducing an additional phase of π to one of the plane waves, it is seen that the CPA condition is satisfied at 581 nm and again more than 99.9% of the light is absorbed at this resonance. An added effect of introducing an additional phase of π to one of the plane waves is that the plasmon resonance at 969 nm now shows satisfies SS conditions and the resonance is totally killed.

One of the main motivations for developing perfect absorbers is to transfer efficiently the incident energy into the near-field of the structure. Thus, it is crucial to study the near-field profiles at the CPA wavelength for both single and dual plane wave incidence. Fig. 6.5 plots the component of the magnetic field parallel to the interfaces for both single and dual plane wave incidence at the two plasmon resonances. The field distribution at 961 nm due to a single plane wave shows the following features: a standing wave pattern in the domain of incidence, an exponentially decaying functions away from the gold interfaces and a constant intensity on the opposite side. The standing wave pattern in the incidence medium is formed because of the counter propagating incident and reflected plane waves. Comparatively, the field distribution for a simultaneous dual plane wave incidence with $\Delta\phi = 0$, corresponding to CPA at 961 nm, does not show the standing wave pattern outside the structure. The absence of standing wave pattern outside the structure is due negligible scattering when the CPA condition is satisfied. However, the field intensity inside the structure is enhanced from 29 (seen in the case of incidence of two incoherent plane waves given by $|H_T|^2 + |H_B|^2$) to 59 (in the case of CPA as given by $|H_T + H_B|^2$). In contrast, when the SS condition is satisfied ($\Delta\phi = \pi$), the field in the air gap is near zero and a strong standing wave pattern is observed outside the structure.

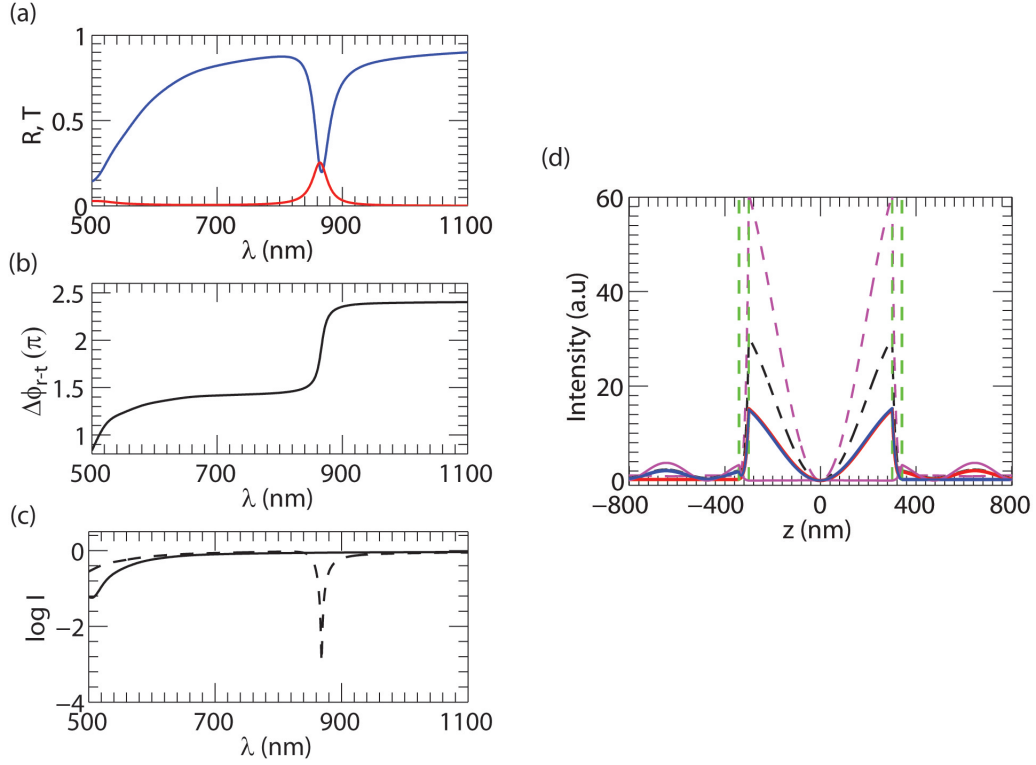


Figure 6.6: **CPA and SS at the short range plasmon resonance.** (a) Reflection (blue) and transmission (red) spectra when a single plane wave is incident on the structure. (b) Phase difference between the reflection and transmission coefficients as a function of wavelength. (c) Log of the total scattered intensity ($\log_{10} I$) due to simultaneous incidence of two plane waves for $\Delta\phi = 0$ (solid curve) and $\Delta\phi = \pi$ (dashed curve). (d) Magnetic field intensity at 868 nm due to a single plane wave incidence from top (red), bottom (blue) and simultaneous incidence of two plane waves for $\Delta\phi = 0$ (solid magenta) and $\Delta\phi = \pi$ (dashed magenta). Also, the back dashed curve shows the intensity due to incidence of simultaneous incidence of two incoherent plane waves. The system parameters are: $\theta = 33^\circ$, $d_1 = d_3 = 40$ nm, $d_2 = 600$ nm, $\epsilon_i = \epsilon_f = 2.28$, $\epsilon_1 = \epsilon_3 = \epsilon_{Au}$ and $\epsilon_2 = 1$. Note that a 2 nm chromium layer between each of the gold-glass interfaces is included in the simulations.

Thus, in this configuration no energy is used for exciting the plasmon resonance. Figure 6.5(b) shows the field distributions at 581 nm for all the different illumination conditions. Note that the plasmon field is enhanced when CPA condition is met ($\Delta\phi = \pi$) and suppressed when SS condition is satisfied ($\Delta\phi = 0$). A comparatively smaller modulation is observed at 581 nm as opposed to 969 nm, due to its shorter wavelength and lower quality factor of gold at this wavelength.

To definitively prove that the field can also be enhanced or suppressed significantly at the lower wavelength plasmon resonance, the angle of incidence is changed from 44° to 33° . The change in the incidence angle red shifts the plasmon resonance from 581 nm to 868 nm. The reflection and transmission spectra along with the phase difference between the reflection

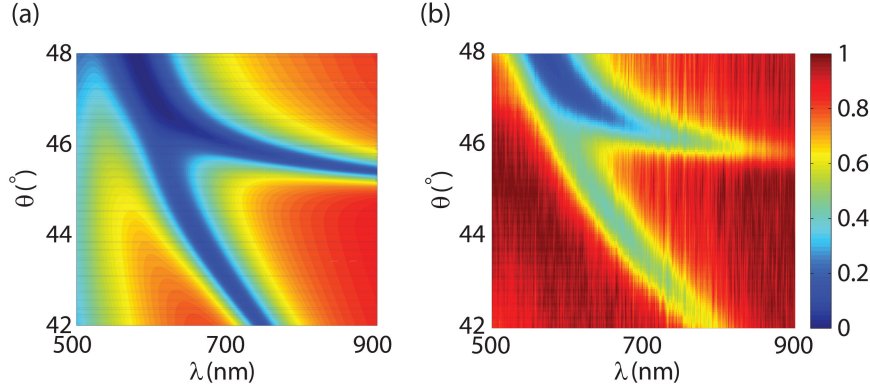


Figure 6.7: **Experimentally measured dispersion of gap plasmon waveguide structure.** (a) and (b) Simulated and measured dispersion diagrams of structure, respectively. The system parameters are: $d_1 = d_3 = 40$ nm, $d_2 = 600$ nm, $\epsilon_i = \epsilon_f = 2.13$, $\epsilon_1 = \epsilon_3 = \epsilon_{Au}$ and $\epsilon_2 = 1$. Note that a 2 nm chromium layer between each of the gold-glass interfaces is included in the simulations.

and transmission coefficients is plotted in Fig. 6.6 (a) and (b). It is clear from Fig. 6.6(c) that for $\Delta\phi = 0$ and $\Delta\phi = \pi$ the structure satisfies SS and CPA condition at 868 nm, respectively. Fig. 6.6 (d) shows the magnetic field intensity distributions for the different illumination conditions. Unlike previously, here when the SS condition is satisfied, i.e. $\Delta\phi = 0$, it is seen that the field is close to zero and the resonance is totally suppressed. Also, when the CPA condition is satisfied at this wavelength, the field is enhanced by a factor of 2 as compared to the case of illumination with two incoherent plane waves.

6.2.5 Experimental demonstration of CPA and SS using gap plasmons

In order to experimentally demonstrate CPA assisted perfect energy transfer to a given mode, a symmetric gap plasmon structure as shown in Fig. 6.2(a) is fabricated. Two gold films deposited on glass substrates are separated by a controlled air gap (thickness d_2 nm) which serves the purpose of controlling the coupling between the plasmon at the two gold-air interfaces. Figure 6.7(a) and (b) show the calculated and measured reflected intensities as a functions of angle of incidence (θ) and wavelength (λ), when the structure is illuminated by a single TM polarized plane wave from one side. Both the symmetric and the anti-symmetric plasmon mode can be clearly observed.

Figure 6.8(a) shows the calculated reflection and transmission spectra when the structure is illuminated by a single TM polarized plane wave incident at 45° . The phase difference between the reflection coefficient (r) and transmission coefficient (t) is also plotted. The two dips in the reflection spectra correspond to the two plasmon modes, the symmetric mode at 567 nm and the anti-symmetric mode at 672 nm. A broad peak is seen in the transmitted spectrum which is due to the excitation of the plasmon modes and corresponds closely with the resonances observed in the reflection spectrum. The measured reflection spectra shows the two plasmon

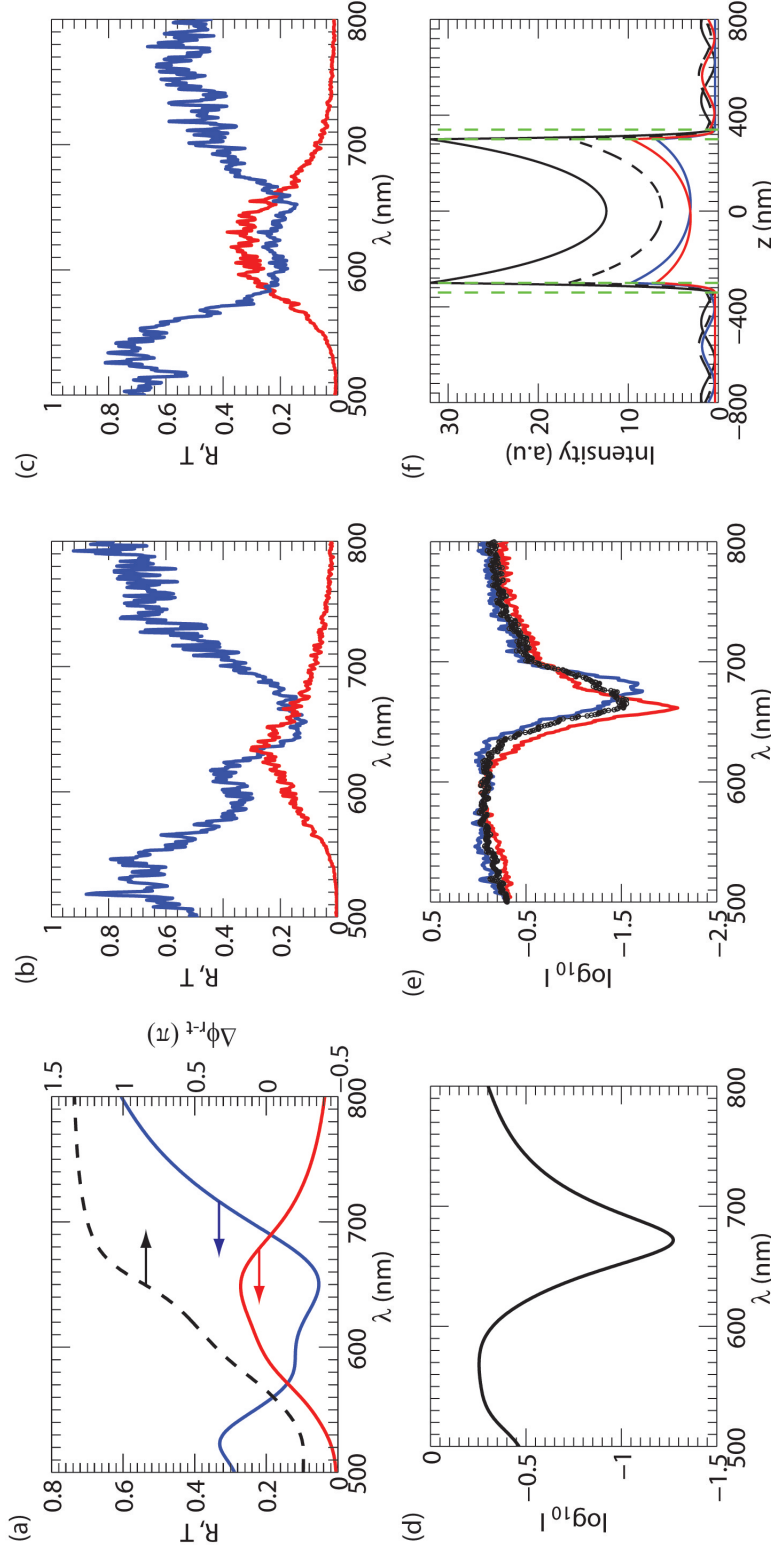


Figure 6.8: **Experimental demonstration of CPA and SS at the short range surface plasmon.** (a) Simulated reflection (blue) and transmission (red) spectra due to single plane wave incidence. Also shown is the phase difference (black dashed) between the complex reflection and the transmission coefficients, $\Delta\phi_{r-t}$, as a function of wavelength. (b) and (c) Experimentally measured reflection (blue) and transmission (red) spectra for a single plane wave incidence at the detectors D1 and D2, respectively. (d) Simulated total scattering from the structure as a function of wavelength due to simultaneous dual beam incidence ($\log_{10} I = \log_{10} I_T = \log_{10} I_B$) for $\Delta\phi = 0$. (e) Measured total scattered intensity ($\log_{10} I$) as a function of wavelength at detector D1 (red) and D2 (blue) for dual plane wave incidence with $\Delta\phi = 0$. The black curve shows the average of the scattered intensity detected at D1 and D2. (f) Magnetic field intensity as a function of distance for single plane wave incident from the top (red), bottom (blue) and for simultaneous dual plane wave illumination (black solid). The sum of the intensities due to two individual plane waves (dashed black) is also shown. The green dashed lines show the various interfaces and $z = 0$ nm corresponds to the center of the structure. The system parameters for the simulations are: $d_1 = d_3 = 40$ nm, $d_2 = 600$ nm, $\epsilon_i = \epsilon_f = 2.28$, $\epsilon_1 = \epsilon_3 = \epsilon_{Au}$, $\epsilon_2 = 1$ and $\theta = 45^\circ$.

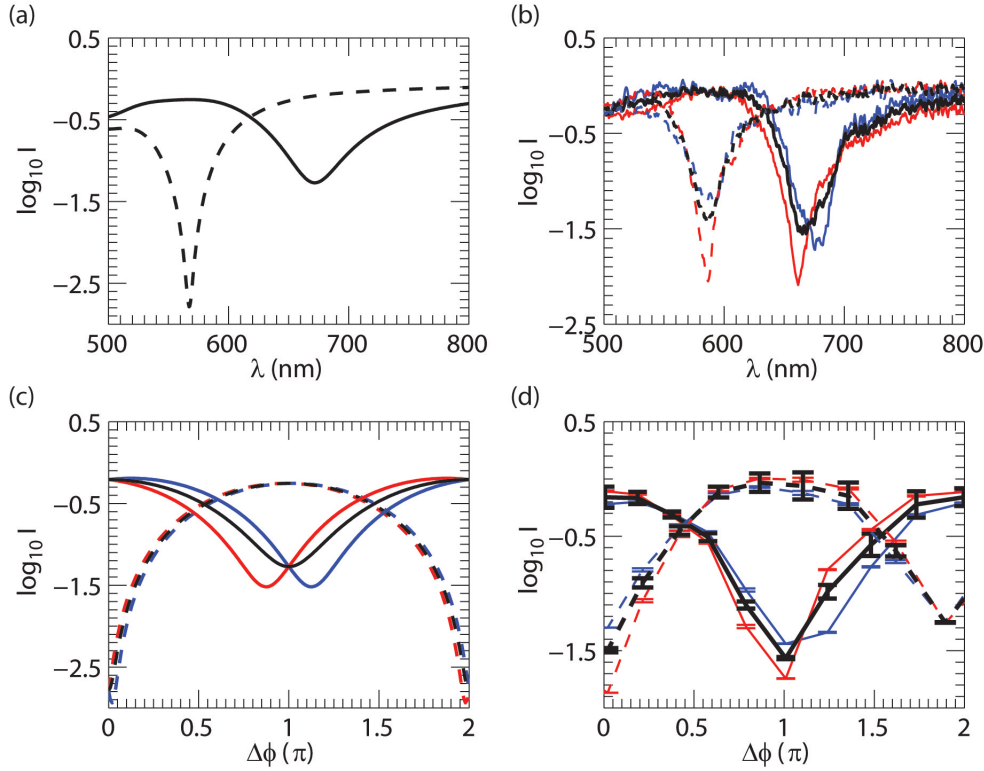


Figure 6.9: **Phase control of CPA and SS.** (a) Simulated total scattering spectra from the structure for $\Delta\phi = 0$ (solid) and π (dashed). (b) Experimentally measured intensities as a function of wavelength at the detectors D1 (red) and D2 (blue) for $\Delta\phi = 0$ (solid) and $\Delta\phi = \pi$ (dashed), respectively. The black curves show the average total scattering intensity at D1 and D2. (c) Simulated intensities at the two plasmon resonances, 672 nm (solid) and 567 nm (dashed) as a function of initial phase difference, $\Delta\phi$. Red, blue and black curves correspond to $\log_{10} I_T$, $\log_{10} I_B$ and $\log_{10}((I_T + I_B)/2)$, respectively. (d) Measured total scattered intensities at the two plasmon resonances, 668 nm (solid) and 586 nm (dashed), as a function of initial phase difference, $\Delta\phi$. Red, blue and black curves correspond to the intensity measured at D1, at D2 and the average of D1 and D2.

dips at 586 nm and 668 nm and the transmitted spectra shows the broadened resonance as observed in the simulations. Recall that, the conditions required for CPA at a given wavelength are $|r|^2 = |t|^2$ and $\Delta\phi_{net} = \Delta\phi_{r-t} + \Delta\phi = \pi$. In this context note that for the plasmon mode around 670 nm, the reflection and transmission intensities are close in magnitude and there exists a phase difference of π between the reflection and transmission coefficients (Fig. 6.8(a)). Thus, the CPA requirements are nearly satisfied at this plasmon resonance when $\Delta\phi = 0$. The calculated and measured response due to simultaneous incidence of two plane waves clearly demonstrates CPA occurring near 670 nm, as shown in Fig. 6.8(d) and (e). The total scattered intensity on either side ($\log_{10} I$) is minimized and more than 96% is absorbed by the structure. Furthermore, since the CPA dip occurs exactly at the plasmon resonance, all the energy is channeled into the plasmon mode. Thus through this approach it is possible to increase the excitation efficiency of the anti-symmetric plasmon mode from 75% for a single plane

6.2. Coherent perfect absorption mediated selective mode excitation

wave incidence to 96% for CPA configuration. Because of near π phase difference between the symmetric and anti-symmetric plasmon mode, the plasmon mode at 586 nm, on the other hand satisfies the condition for superscattering. Therefore, the symmetric mode can be completely killed. The magnetic field distribution at 671 nm for the dual and single plane wave incidence is shown in 6.8(f), which clearly shows the enhancement of the field due to satisfaction of the CPA condition. This enhancement is two times larger than the sum of intensities due to two individual plane waves.

In situations where the intensity condition for CPA or SS are satisfied, it is the phase that dictates which of the two will occur. Thus, in principle, it should be possible to have transition from a CPA state to a SS state by providing an additional phase of π to one of the incident plane waves, i.e., by varying $\Delta\phi$. Calculations and experiments indeed show such a switching behavior (between CPA and SS states or vice versa) as shown in Fig. 6.9(a)-(b). The CPA (SS) state is initially located around 668 nm (586 nm) and it switches to 580 nm (668 nm) when one of the plane waves is delayed by a phase of π . When the CPA state occurs at 586 nm, more than 96% of the incident light is absorbed by the structure and channeled into the symmetric plasmon mode. It is therefore possible to use the phase delay between the two incident plane waves as a handle over the amount of energy being channeled into each plasmon mode. A gradual variation of the phase delay as shown in Fig. 6.9(c) and (d) clearly illustrates that the excitation efficiency for a given mode can be tuned from around 18% to 96% (12% to 96%) for the plasmon resonance at 668 nm (586 nm).

6.3 Perfect absorption of light by a metal-dielectric composite slab

In the previous section, CPA mediated near perfect energy transfer to propagating surface plasmons is demonstrated. In this section, I show that CPA can also be realized in metal-dielectric composites systems supporting localized plasmon resonances. Such metal–dielectric nano-composites have found interesting applications in optics, especially since the eighties, when researchers appreciated that the effective medium properties of the composite can be better than those of its individual constituents [486–488]. Here, I present a detailed study of CPA in a slab of composite medium with illumination by coherent waves at identical angle of incidence from both sides. I present results which are indicative of a critical minimum of absorption below which CPA is not possible. This clearly demonstrates the necessity of absorption for CPA. I further demonstrate the controllability of the frequency over a broad range (from visible to near-IR) at which null-scattering can take place. Unlike CPA demonstrated using gap plasmon structures where CPA could only be realized at a single wavelength, I show that CPA can be realized at two distinct wavelengths simultaneously even in presence of dispersion.

6.3.1 Simulating the optical response of metal-dielectric films

Consider the geometry shown in Fig. 6.10, where a metal–dielectric composite layer of thickness d is excited by two coherent monochromatic waves with unit amplitude from both sides. All the media in Fig. 6.10 are assumed nonmagnetic and the angle of incidence θ is the same for both waves. For future reference I label the forward (backward) propagating wave incident from left (right) and resulting reflected and transmitted waves with subscript f (b). The structure is symmetric, since the medium of incidence and emergence are the same. Symmetry ensures that the total scattered amplitudes in the medium of incidence and emergence are the same since the reflected and transmitted coefficients individually are the same ($r = r_f = r_b$, $t = t_f = t_b$). The nature of scattering in both directions is governed by the interference between, say, r_f and t_b . As mentioned previously, it will be destructive and leading to CPA if the magnitudes of these waves are the same with a phase difference of π , i.e., $|r_f| = |t_b|$ and $|\Delta\phi_{r-t}| = |\phi_r - \phi_t| = \pi$, where ϕ_r and ϕ_t refer to the phases of r and t , respectively. Note that in all the simulations presented in this section the two incident plane waves have a zero initial phase difference $\Delta\phi = 0$. Again the inherent symmetry implies that $r + t = r_f + t_b = r_b + t_f$, leading to the same scattered amplitudes on both sides. Thus destructive cancellation in the incidence medium would imply the same in the emergence medium, leading to CPA.

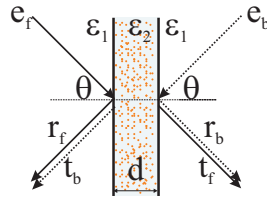


Figure 6.10: Schematics of the CPA geometry using metal-dielectric composite film.

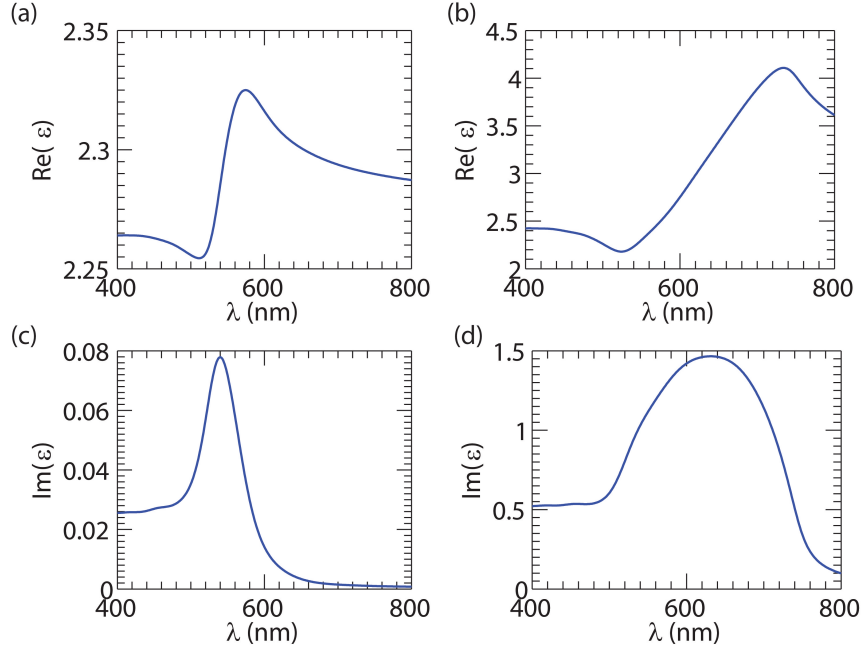


Figure 6.11: **Dielectric function of metal-dielectric composite films.** (a), (b) Real and (c), (d) imaginary parts of the dielectric constant for a gold-silica composite at two different volume fractions: (a), (c) $f_m = 0.004$ and (b), (d) $f_m = 0.08$. Here $\epsilon_d = 2.25$ and ϵ_m is taken from the work of Johnson and Christy [259].

The complex reflection and transmission amplitudes for any given polarization for the structure shown in Fig. 6.10 can be easily calculated using the standard characteristic matrix approach [260]. As mentioned earlier, localized plasmon resonances of the composite play a key role in determining the nature of scattering. The optical properties of this metal-dielectric medium are obtained from the Bruggeman formula, where both constituents in the two-component medium are treated on the same footing [489]. The permittivity of the composite is thus given by

$$\epsilon_2 = \frac{1}{4} \left\{ (3f_m - 1)\epsilon_m + (3f_d - 1)\epsilon_d \pm \sqrt{[(3f_m - 1)\epsilon_m + (3f_d - 1)\epsilon_d]^2 + 8\epsilon_m\epsilon_d} \right\}, \quad (6.1)$$

where f_m and ϵ_m (f_d and ϵ_d) are the volume fraction and the permittivity of the metal (dielectric), respectively. Since the composite has only two components, $f_d = 1 - f_m$. The square root is taken such that the imaginary part of the permittivity is positive to ensure causality [260, 489].

The flexibility offered by the structure in Fig. 6.10 in the context of CPA can easily be assessed, even before any calculations. There are now several parameters controlling the nature of the scattered light, namely, the width d , the angle of incidence θ ; both controlling the optical path and hence the single-pass or roundtrip phase and attenuation for a given frequency. Most importantly, the volume fraction of both constituents of the metal-dielectric composite provide a very efficient control of its absorption and dispersion. In the next section I demonstrate

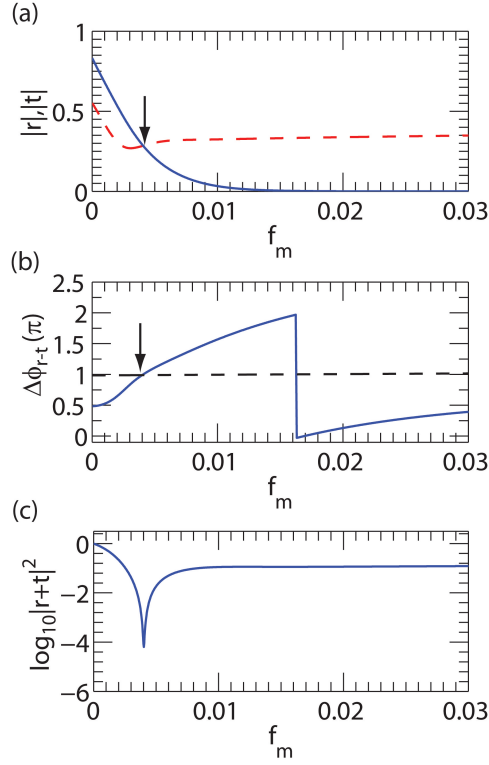


Figure 6.12: **Dependence of CPA frequency on the volume fraction of metal in a composite film.** (a) Absolute values of reflected (dashed line) and transmitted (solid line) amplitudes $|r|$ and $|t|$ (arrow shows the point where conditions for CPA are satisfied), (b) phase difference $\Delta\phi$ between the forward reflected and backward transmitted plane waves and (c) $\log_{10}|r+t|^2$ as a function of f_m for $d=5 \mu\text{m}$ and $\lambda = 562 \text{ nm}$.

this freedom of choice of optical parameters for a gold–silica composite. I consider very low volume fraction for the metal, leading to a localized plasmon resonance around $\lambda = 540 \text{ nm}$ and producing CPA dips near $\lambda = 560 \text{ nm}$. Figure 6.11 shows the dependence of the real and imaginary parts of the permittivity for a gold–silica composite as functions of the wavelength λ for two different values of the metal volume fraction: $f_m = 0.004$ and $f_m = 0.08$. The dramatic changes of the absorption and localized plasmon resonance wavelength are clearly visible. An increased value of f_m , say $f_m = 0.08$, red-shifts the localized plasmon modes to about $\lambda = 630 \text{ nm}$, bringing the CPA effect within the reach of laser diodes in the $\lambda = 750\text{--}790 \text{ nm}$ spectral range.

6.3.2 CPA using a metal-dielectric composite film

All the calculations are performed for a gold–silica composite layer illuminated by a transverse electric (TE) polarized plane waves incident at an angle $\theta = 45^\circ$. The dielectric function of gold ϵ_m is obtained by interpolating the experimental data of Johnson and Christy [259]. Other parameters are taken as follows: $\epsilon_1 = 1.0$, $\epsilon_d = 2.25$. In order to study the influence of the

6.3. Perfect absorption of light by a metal-dielectric composite slab

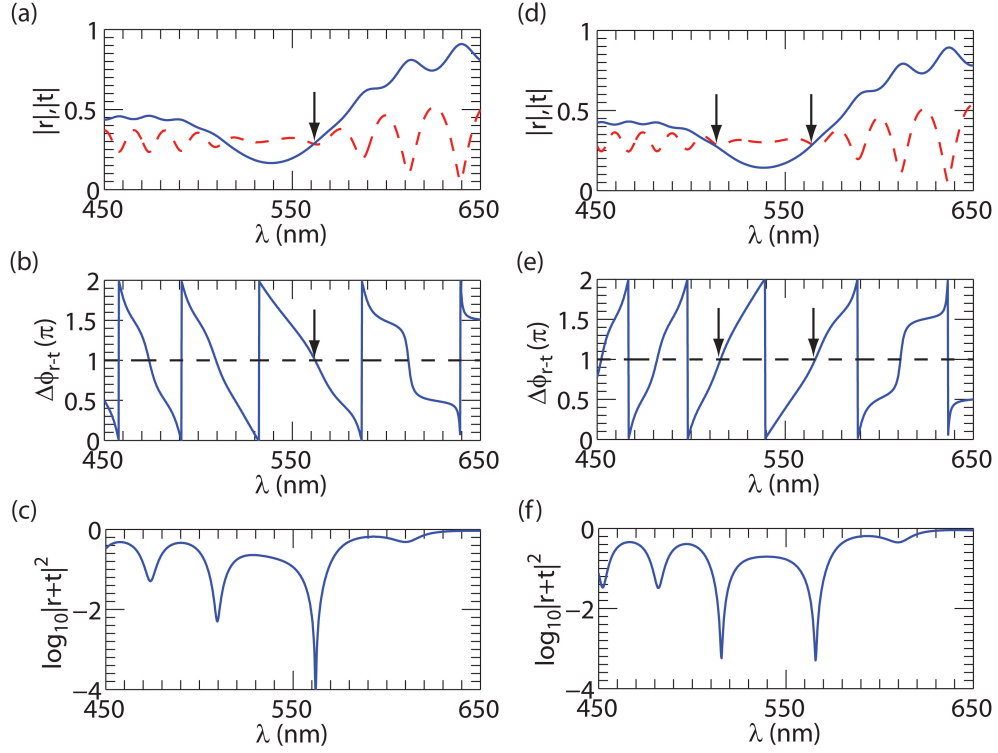


Figure 6.13: **Realization of CPA at multiple wavelengths using a composite film.** (a) and (d) Reflection and transmission amplitudes, (b) and (e) phase difference $\Delta\phi$ between the forward reflected and backward transmitted plane waves and, (c) and (f) $\log_{10}|r+t|^2$ as a function of λ for $d = 5\mu\text{m}$ ((a), (b) and (c)) and $d = 5.45\mu\text{m}$ ((d), (e) and (f)). The volume fraction is fixed at 0.004. The arrows show the points at which the CPA conditions are satisfied.

geometrical and material parameters, I have computed the modulus of the reflected and transmitted amplitudes, $|r|$, $|t|$, their phase difference $\Delta\phi$ and the intensity of the scattered light $|r+t|^2$ as functions of d , f_m or λ .

As previously mentioned, the CPA results from an extremely delicate balance where the interfering waves have the same modulus and differ by a phase of π . This is investigated in Fig. 6.12, where the amplitude of the reflected and transmitted waves are shown as a function of f_m for $\lambda = 562\text{ nm}$ and $d = 5\mu\text{m}$. A logarithmic scale is used in Fig. 6.12(c) to highlight the depth of the dip where CPA occurs at $f_m = 0.004$, where the required conditions are fulfilled, i.e., $|r| = |t|$ and $|\Delta\phi| = \pi$.

The dependence of $|r|$, $|t|$, $|\Delta\phi|$ and $\log_{10}|r+t|^2$ as a function of λ for a composite layer with $f_m = 0.004$ and $d = 5\mu\text{m}$ is shown in Fig. 6.13(a)-(c). These data confirm the necessary conditions for CPA, i.e., destructive interference between r and t . They also indicate new possibilities, such as having CPA at two distinct frequencies for the same structure under illumination at the same angle of incidence. Note in Fig. 6.13(a) the multiple crossing of the $|r|$ and $|t|$ curves, implying amplitude matching at more than one wavelength. While the

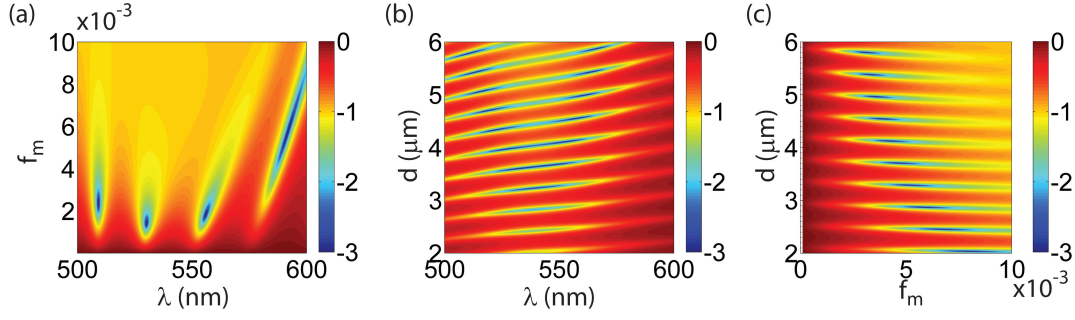


Figure 6.14: **Parametric study of CPA in a composite film.** Color map of $\log_{10}|r + t|^2$ as functions of (a) f_m and λ for $d = 10 \mu\text{m}$, (b) d and λ for $f_m = 0.004$, and (c) d and f_m for $\lambda = 562 \text{ nm}$.

phase difference vanishes at one of these crossing (at $\lambda = 562 \text{ nm}$), it is slightly off for the other wavelengths. It is thus expected that in the parameter space a nearby point can be found, where the matching is complete at least at two distinct frequencies. This is indeed possible and the results are shown in Fig. 6.13(d)-(f) for $f_m = 0.004$ and $d = 5.45 \mu\text{m}$. It is not ruled out that a judicious choice of parameters, possibly with periodic variations of the refractive index, could lead to CPA at more than two frequencies.

In order to further explore the influence of the different parameters on the CPA condition, I study in Fig. 6.14 the scattered intensity $\log_{10}|r + t|^2$ as a functions of two of the parameters (keeping the third one constant) in a three-parameter space (comprising of f_m , λ and d). The results for the log of the scattered intensity on one side are shown as color plots as a function of f_m and λ for $d = 10 \mu\text{m}$ in Fig. 6.14(a), as a function of d and λ for $f_m = 0.004$ in Fig. 6.14(b), and as a function of d and f_m for $\lambda = 562 \text{ nm}$ in Fig. 6.14(c), respectively. The islands and stripes in Fig. 6.14 indicate that it is nontrivial to meet the CPA condition, which results from a very delicate balance ensuring destructive interference. As can be seen from Fig. 6.14(b) and (c), the stripes contain the islands and the CPA condition is met at a point near the middle of the island. The occurrence of several islands with sharp dips suggests that CPA is possible for several pairs of parameter values, when the third parameter is kept fixed. The dependence shown in Figs. 6.14(a) and (b) is also indicative of another important fact, namely, absorption is essential for CPA. Fig. 6.14(a) clearly points to a limiting volume fraction of metal, below which CPA is ruled out. Note that in our model the metallic inclusions are the only source of losses and hence existence of a minimum critical value of metal volume fraction implies a similar minimum absorption for the realization of CPA. Both Figs. 6.14(a) and (b) suggest that a possible adjustment of d and f_m , respectively, can lead to two ‘point dips’ on the same horizontal line, thereby leading to CPA at two frequencies for the same structure. Finally, Fig. 6.14(c) implies that an increase of d , resulting in an overall absorption increase, can lead to CPA at a lower volume fraction f_m .

6.4 Probing near-field enhancement in single beam CPA structures

In the previous sections, phase-amplitude controlled perfect absorption of light due to dual plane wave incidence is demonstrated. However, in many practical applications such a illumination geometry may not be suitable. This can be circumvented by exploiting a critical coupling configuration, single plane wave analogue of CPA, where a dielectric spacer with a reflective layer is used as the underlying substrate of a given plasmonic structure [335, 458–460, 470]. Such critical coupling structures have been used for making perfectly absorbing substrates with just a 5 nm thick absorbing layer [460]. In our critical coupling configuration, the reflective layer ensures null transmission of light and the spacer with an appropriate thickness enables complete destructive interference in the medium of incidence amongst the different reflected plane waves from the various interfaces. Thus, when the reflection and the transmission are simultaneously zero, all the incident light must be absorbed by the structure. It should be mentioned that enhanced or perfect absorption via critical coupling in realistic situations is strongly warranted because it allows the coupling of the total incident light into the near-field of a given plasmonic structure. In this section, I use the SERS signals of molecules to probe the near field of the critically coupled structures [490]. Consequently, the compound plasmonic structures presented here can be used as high efficiency SERS substrates. I show that the interference in these plasmonic crescent arrays can be controlled using either the gap of the array, which modifies the complex transmission and reflection coefficients [343], and/or the spacer thickness, which controls the phase difference between the plane waves propagating back and forth in the cavity. I also study the dependence of SERS signals on the planewave reflectivity at the laser excitation and Raman shifted wavelengths for the various structures investigated. The dispersive character of the resonance of the composite structure is further exploited to demonstrate angle dependent tuning of SERS signals.

6.4.1 Numerical simulation of the critical coupling structure

The far-field spectra and the near-field amplitudes are calculated with a full-field numerical method based on the solution of surface integrals [372]. The crescent arrays and the layered substrate are simulated in a 3D unit cell with periodic boundary conditions along and across the gap plane. A triangular mesh with a maximum side length of 10 nm is used to discretize one crescent. The polarization of the electric field is set across the gap. The reflecting layer is made of gold and the spacing layer is glass. The refractive index of the glass and the HSQ photoresist is estimated with 1.5 and 1.39, respectively. The dielectric function of gold used in the simulations is taken from Johnson and Christy [259]. The refractive index of the surrounding medium is taken to be 1.0 (air).

6.4.2 Fabrication of the crescent array structures

The structures used in this current study are fabricated by a collaborator, T. Siegfried, at the Paul Scherrer Institute (PSI) using the following protocol. Line array patterns with a period

of 250 nm are obtained by extreme ultraviolet interference (EUV) lithography in an 80 nm thick hydrogen silsesquioxane (HSQ) film and over an area of $0.6 \times 1.8 \text{ mm}^2$. HSQ is developed in 25% tetra methyl ammonium hydroxide (TMAH) for 60 s. Gold (Balzers, 99.99 % purity) is thermally evaporated on HSQ at a glancing angle of 60° from the surface normal. The substrate is aligned at an azimuthal orientation of the line array perpendicular to the gap expansion. The substrate is repeatedly tilted to the opposite direction ($\pm 60^\circ$) after every 2 nm of evaporated metal. The crescent spacing is set by the resist duty cycle, which is controlled by the EUV exposure time.

6.4.3 Optical measurements

Reflection measurement

The normal incidence reflection measurements are performed using an inverted optical microscope (Olympus IX-71) coupled to a spectrometer (Jobin Yvon Horiba Triax 550). The sample is illuminated using a halogen light source focused onto the sample using a 20x objective (NA 0.2). The illumination is such that the angle of incidence is below 2° . The reflected light is collected using the same objective and analyzed using a spectrometer. The reflected intensity is normalized to the reflection from a silver mirror. Reflectivity as a function of wavelength and incidence angle is measured using a home-made prism-based setup as described by Farhang *et al.* [485]. Again, the spectrally resolved reflected intensity is normalized with the reflectivity of a silver film (thickness 100 nm).

Raman measurement

Surface enhanced Raman scattering (SERS) measurements are performed by a collaborator, T. Seigfried, at PSI using the following methodology. SERS is measured using an excitation wavelength of 633 nm on samples coated with a self assembled benzene-ethane-thiol (BET) monolayer, formed during 12 h immersion in a 1 mM solution. The reported SERS intensities relate to the Raman peak intensity at the 1008 cm^{-1} vibrational mode of BET. Raman peak intensities from alternative modes are noted in the text. A Horiba LabRam HR instrument with a spectral resolution of 1 cm^{-1} is used. An incident power of 2 mW is focused (50x, numerical aperture NA 0.5) and deflected within an area of $10 \times 10 \text{ }\mu\text{m}^2$ to minimize photobleaching. Sixteen spectra are taken over an area of $300 \times 800 \text{ }\mu\text{m}^2$ for signal averaging and the calculation of signal deviation.

6.4.4 Critical coupling mediated SERS enhancement

A schematic illustration and a representative SEM image of the fabricated structure used to demonstrate perfect absorption of light for SERS substrates is shown in Fig. 6.15. The structure consists of a periodic crescent array (period 250 nm thickness 30 nm and gap size $g=10 - 70 \text{ nm}$) placed on top of a spacer (thickness $d=100 - 700 \text{ nm}$) and a reflective gold layer

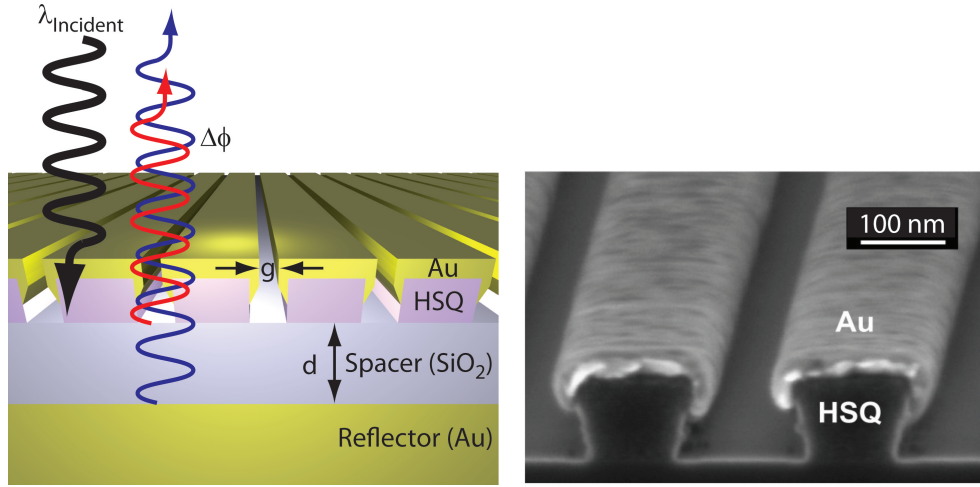


Figure 6.15: **Critical coupling geometry.** Schematic of the layered geometry used in the study. The structure is defined by a spacer layer with thickness d , and a crescent layer with a gap g . The inset shows a SEM image of an isolated crescent array.

(thickness 70 nm). The crescent array is fabricated using EUV lithography followed by angular evaporation, with details given in Sec. 6.4.2 and published elsewhere [491, 492]. A chromium adhesion layer is applied between all layers to ensure the structure's stability. Near-field damping by the chromium is suppressed by a minimal layer thickness of 1 nm evaporated at normal incidence to avoid direct contact with the plasmonic near-field hot spot [493]. When the structure is illuminated with a planewave at normal incidence, the 70 nm thick reflective layer ensures near zero transmission over the here employed spectral range. The reflectivity from the layered structure, as is known for a multilayer Fabry Perot (FP) cavity, is governed by constructive or destructive interference between the various plane waves reflected from the different interfaces. As compared to a standard FP cavity, our system is complicated due to the presence of the resonant plasmonic crescent layer, which adds a phase modifying the spectral position of destructive interference. This additional phase shift can take values between 0 and π depending on the spectral overlap of the standard FP cavity mode and the plasmon resonance. The interference is thus controlled by the thickness of the spacer, and the gap and the thickness of the crescent array. In this manner it is possible to choose a set of system parameters that achieve perfect destructive interference of the reflected plane waves at a given wavelength. At this wavelength all the incident energy is absorbed by the plasmonic pattern and the continuous layer underneath as dictated by energy conservation, i.e. $A=1-R-T$. If such a reflection minimum coincides with the plasmon resonance, the energy of the incident wave will be absorbed largely by the plasmonic structure yielding strong near field enhancement at its hotspot. In the following I refer to the resonance of the complete structure, formed by the coupling of the FP cavity and the plasmonic crescent resonance, unless otherwise mentioned.

Figures 6.16 (a) and (b) show the numerically calculated and experimentally measured reflection spectra from crescent arrays without the underlying reflecting layer (dashed lines)

and from arrays with varying spacer thicknesses from $d = 100$ nm to 700 nm. The structures are illuminated by a planewave at normal incidence which is polarized across the gap of the crescent array. We only chose spacer thicknesses larger than 100 nm, thus preventing the formation of new hybridized plasmon modes by coupling to image charges in the subjacent gold layer [494]. The reflection spectra of the crescent array without the reflecting layer shows a broad reflection minimum which is associated with the fundamental plasmon mode of the crescents. The minimum originates from the destructive interference between the directly reflected light and the light scattered by this resonant mode, as demonstrated by Gallinet et al. [343]. The half-width at half-maximum of the crescent plasmon mode is found to be about 150 nm which provides a significant wavelength window, in which critical coupling of light to the structure can be applied. In contrast to the rather broad plasmon resonance observed for the pattern without a cavity, the FP reflection minima are steep and easily tunable by the spacer thickness, as shown in Fig. 6.16(a) and (b). Under appropriate conditions, the reflectivity at resonance can be reduced below 5%, such that more than 95% of the light is absorbed by the structure with a 60 nm gap. Without the spacer and the reflecting layers, only about 70% of the incident light is absorbed by the otherwise identical structure with a 60 nm

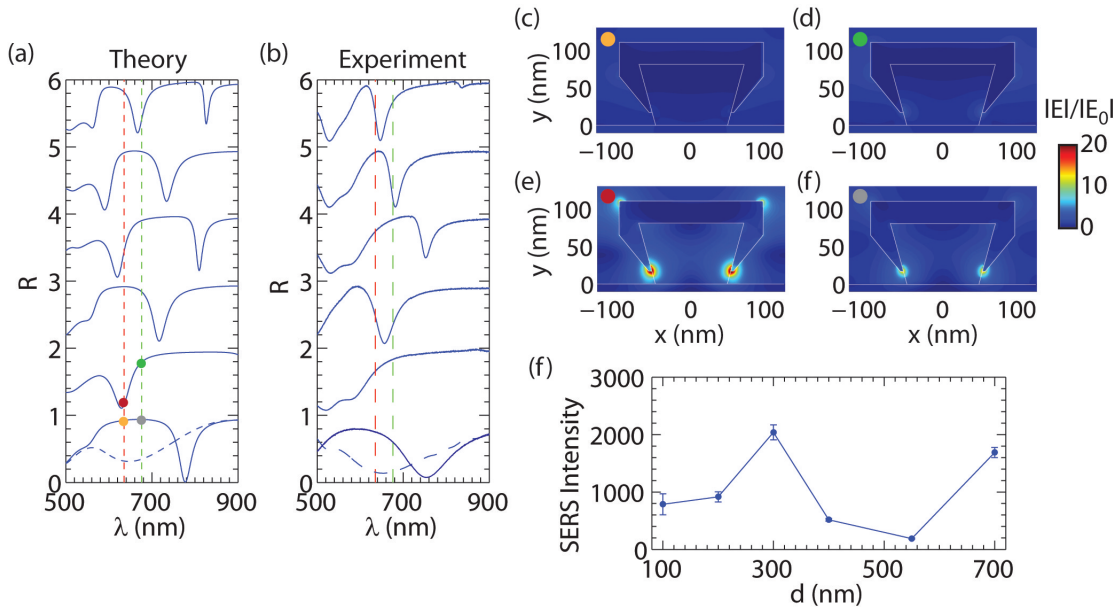


Figure 6.16: **Effect of spacer thickness on critical coupling wavelength.** (a) Simulated and (b) experimentally measured reflection spectra for normal incidence for a crescent gap size of $g = 62$ nm and various spacer thicknesses d (from bottom to top: 100 nm, 200 nm, 300 nm, 400 nm, 550 nm and 700 nm). The blue dashed line shows the response of crescent arrays placed on top of a glass substrate without a reflecting layer underneath. The red and green dashed lines indicate $\lambda = 633$ nm and $\lambda = 676$ nm. (c) - (f) Near-field amplitude enhancement plotted in the xy -plane for a structure with $g = 62$ nm at $\lambda_{ex} = 633$ nm and $\lambda_{em} = 676$ nm. Spacer thickness is $d = 100$ nm ((c) and (d)), and $d = 200$ nm ((e) and (f)), respectively. (g) SERS intensity variation as a function of the spacer thickness d for a structure with $g = 62$ nm.

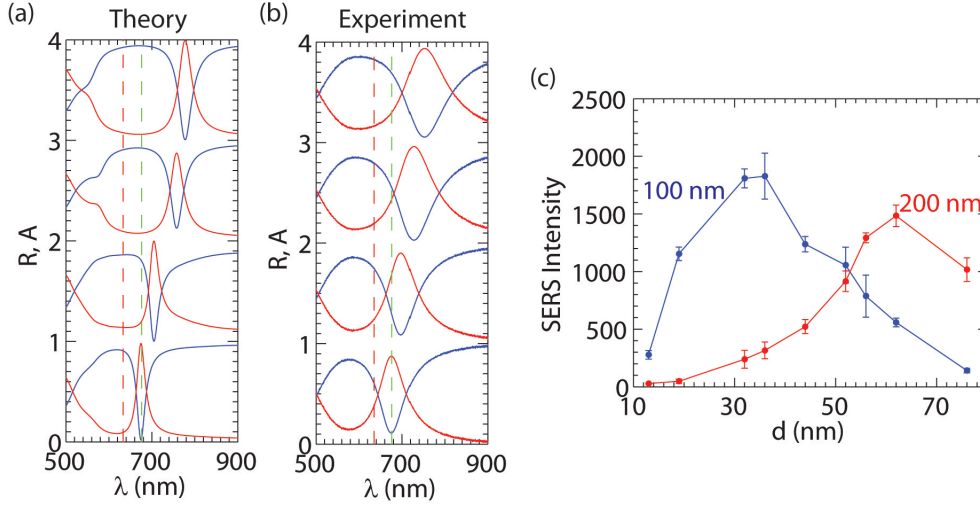


Figure 6.17: **Effect of nano-crescent gap on critical coupling.** (a) Simulated and (b) experimentally measured reflection (blue) and absorption (red) spectra under normal incidence for $g = 36$ nm, 42 nm, 48 nm and 62 nm (from bottom to top) and a fixed $d = 100$ nm. The red and green dashed lines indicate 633 nm and 676 nm, respectively. (c) SERS intensity as a function of gap size for $d = 100$ nm (blue) and $d = 200$ nm (red).

gap shown by the modelling. To experimentally validate that near perfect absorption leads to an enhanced near-field, SERS measurements originating from a self-assembled analyte monolayer of benzene-ethane-thiol is carried out. The two wavelengths of primary interest for our experiments are 633 nm and 676 nm, corresponding to the excitation and the Stokes shifted Raman line of the analyte at 1008 cm^{-1} . Enhancing the near-field at either or both the excitation/observation wavelength is achieved by controlling the resonance position via the spacer thickness. Figures 6.16(c) - (f) show the simulated electric field plots at the two different wavelengths (633 nm and 676 nm) for two different spacer thicknesses (100 and 200 nm). We observe that the crescent array with the underlying spacer of 100 nm is off-resonance, while the array with the 200 nm spacer is near-resonance at both wavelengths of interest. Correspondingly, the near-field of the 100 nm spacer, c.f. Fig. 6.16(c) and (d), is significantly lower as compared to the 200 nm spacer, with a maximum near-field enhancement of $\times 25$ at the hotspot of the plasmon mode. The experimental validation of this observation by SERS reveals a modulated signal when varying the spacer thickness, see Fig. 6.16(g). The modulation contrast exceeds 95% (ratio between the minimum and maximum > 20), which conclusively proves that the near field is strongly enhanced when the critical coupling condition is satisfied.

In the following we show that the gap of the crescent array enables us to adjust the complex amplitude of the reflected planewave, thereby providing a second handle for controlling the absorption of light and thus the coupling strength. Figure 6.17 (a) and (b) show the simulated and the experimentally measured reflection spectra for crescents placed on the substrate with the 100 nm spacer for gaps between $g = 36$ nm and $g = 62$ nm. A significant red shift of the reflection resonance is observed on increasing the gap. As the gap is modified for a given

spacer thickness, alike the change of the spacer thickness for constant gap size, results in a shift of the reflection dip. Figure 6.17(c) compares the SERS intensity dependence on the gap sizes g in the range between 10 and 80 nm for two spacer thicknesses d of 100 nm and 200 nm. The optimal gap size with maximal SERS signal is found for $g = 36$ nm in case of the 100 nm spacer and for $g = 62$ nm in case of the 200 nm spacer. This shift from $g = 36$ nm to $g = 62$ nm thus assists to recover the optimal resonance matching with the SERS excitation and emission wavelengths. In reverse, by changing the underlying spacer thickness similar optimal SERS enhancement are obtained for various gaps. Such a handle on the gap size for optimal SERS signals opens up numerous possibilities in the sensing of complex biological samples. For example, most biological samples contain significant contaminants, which require a purification step prior to the use of an analytical measurement tool. However, the structure proposed here intrinsically provides a route for size-based exclusion of unwanted contaminants depending on the nanogap employed. Only molecules that can diffuse through the gap of the crescent array are detected by SERS, since the near-field hot spot is located on the rear side at the sharp crescent tip [493].

In most reported cases, the SERS signal is correlated to the extinction at the mean wavelength of the excitation and emission [495]. However, in our nearly perfectly absorbing structure such a scheme breaks down, due to the resonance width being comparable to the wavelength difference between the excitation and emission wavelengths. Under conditions where the excitation (or emission) wavelength is in resonance while the emission (or excitation) at the Stoke shifted wavelength is off resonance, the SERS intensity may be weakened. Instead, I correlate the SERS to the reflectivity at both the excitation and the emission wavelength and thus, the connection of the SERS intensity to both the emission and excitation enhancement becomes evident. The 2D map shown in Fig. 6.18(a) summarizes the normalized SERS intensity for all spacers d (between 100 and 700 nm) and all crescent gap sizes g (between 10 and 80 nm) plotted against the reflectivity at the excitation (x -axis) and emission wavelength (y -axis). The plot is generated using three Raman lines (800 cm^{-1} , 1000 cm^{-1} and 1600 cm^{-1}) corresponding to the emission wavelength at 667 nm, 676 nm and 705 nm, respectively. The intensities are normalized to the maximal intensity for each of the lines. We observe that the regions of high SERS intensities - colored yellow and white in Fig. 6.18(a) - are surrounded by regions of low SERS intensities (black regions, Fig. 6.18(a)). Low SERS intensities are found when either the excitation or the emission is off resonance defined by $R_{em} > 0.8$ or $R_{ex} > 0.8$. When the reflectivity at the excitation (λ_{ex}) and emission (λ_{em}) wavelengths is in the range between 0.2 and 0.75, the detected SERS signal is high irrespective of the actual gap or spacer. Since the reflectivity is only low when a resonance is near λ_{ex} and λ_{em} , the occurrence of strong SERS exclusively supports our here proposed mechanism that the near field is enhanced due to the near total absorption. From theory the calculated SERS enhancement ($|E_{ex}|^2|E_{em}|^2$) as a function of the reflectivity at the excitation and emission wavelengths indeed matters. In Figure 6.18(b), the calculated near field enhancement at both wavelengths is plotted in a 2D map for simulated arrays with different spacer thicknesses ($d = 100\text{ nm} - 700\text{ nm}$) and gaps ($g = 50\text{ nm}$ and 60 nm). A good agreement is observed between the numerically calculated and

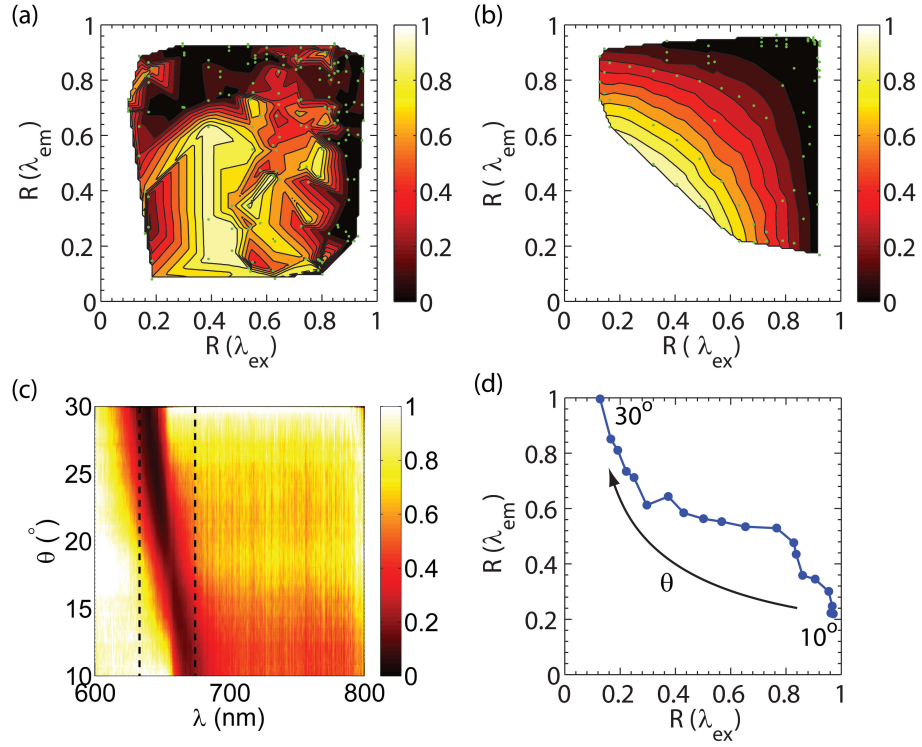


Figure 6.18: SERS intensity as a function of reflectivity and dynamic tunability of critical coupling. (a) and (b) Measured and simulated normalized SERS signal as a function of reflectivity at excitation and emission wavelengths. Three different Raman lines (800 cm^{-1} , 1008 cm^{-1} and 1600 cm^{-1}) are used for computing this map. The SERS signal is normalized to the maximum signal for each Raman line. Green dots indicate the measured signals. (c) Reflectivity measured as a function of the angle of incidence θ and λ for a spacer thickness $d = 700\text{ nm}$ and a crescent gap size $g = 62\text{ nm}$. The dashed black lines indicate our typical incident and emitted Raman wavelength of 633 nm and 676 nm . (d) Trace of the reflectivity at excitation ($\lambda_{ex}=633\text{ nm}$) and emission ($\lambda_{em}=676\text{ nm}$) wavelengths for a 62 nm gap when changing the angle of incidence from 10° to 30° in steps of 1° . The arrow indicates the direction of increasing angle of incidence. The spacer thickness is 700 nm .

the experimentally measured SERS maps. Knowing that the resonance condition is governed by the FP cavity, the angle of incidence - analogous to the spacer thickness discussed before - provides a control of the phase difference between the reflected plane waves. This behavior is unique for our cavity based structure because crescent arrays, or antennas in general, without a reflecting layer support only non-dispersive localized modes. Figure 6.18(c) shows a dispersion curve, with the experimental reflectivity plotted against the angle of incidence and wavelength, for a crescent array with gap $g = 62\text{ nm}$ and a spacer of $d = 700\text{ nm}$. We observe a 60 nm blue shift upon changing the angle of incidence from 10° to 30° . The trajectory of the reflectivity at the here applied excitation and emission wavelengths is shown in Fig. 6.18(d). For a 10° angle of incidence, the structure is off-resonance because R_{ex} exceeds 0.8 , which, according to Fig. 6.18(a) is when the SERS signals are low. Changing the angle of incidence

from 10° to 20° , the resonance crosses the excitation wavelength, and again from the analogy with Fig. 6.18(a), a high SERS intensity is expected. This case thus represents a ‘*SERS on*’ state. Further increase in the angle of incidence would generate again a ‘*SERS off*’ state. We expect that this simple angular control will give an additional degree of freedom for optimizing plasmonic structures for SERS measurements, e.g. by changing the incidence angle in situ under the microscope.

6.5 Summary

In the first part of this Chapter, I have demonstrated that CPA can be used for transferring nearly all the incident light energy into a given plasmonic resonance of a gap plasmon waveguide. I showed that nearly 96% of the light can be channeled into either of the two coupled surface plasmon modes. Thus light can be perfectly absorbed by a plasmonic structure supporting propagating plasmon resonances. Furthermore, I showed that it is possible to switch the state of the system from perfectly absorbing (CPA) to a perfectly scattering (SS) states, with an experimentally measured modulation of more than 70%.

In the second part of this Chapter, I studied CPA in a two-component metal–dielectric heterogeneous medium symmetrically illuminated from both sides at arbitrary angle of incidence. The flexibility in the dielectric response of the composite medium due to the localized plasmon resonance (controlled by the volume fraction of metal) allows the tuning of the CPA wavelength over large ranges of frequencies. This flexibility is further exploited to obtain CPA at two different frequencies for the same structure retaining material dispersion. The presented analysis clearly shows that a minimum absorption is a necessary prerequisite for CPA.

In the final part of this Chapter, I have exploited critical coupling of light to realize a plasmonic perfect absorber based on large scale SERS substrates. The spacing between the reflecting and the plasmonic layer controls the phase relations leading to perfect destructive interference and near total absorption. This technique does not modify the character of the near-field distribution of the plasmonic layer but alters the field enhancement at a given wavelength, and adds control over the plasmon resonance without having to modify the plasmonic pattern. Spacer–thickness-dependent SERS signal variations in excess of 20 times are demonstrated. Moreover, the optimal SERS operating regime is identified, when the reflectivity at both the excitation and emission wavelengths is in the range between 0.2 and 0.75. Finally, the dispersive nature of the modes allows for angle of incidence controlled tuning of the SERS enhancement. These results can lead to a unified SERS substrate for the optimal use at multiple excitation and emission wavelengths.

7 Conclusions and future outlook

In this thesis, plasmonic nanostructures for various applications have been studied. This chapter presents the main conclusions of this thesis along with some of the potential future routes of research.

Chapter 2:

In chapter 2, the interaction of absorbing molecules with plasmonic resonances was investigated for enhancing the sensing capabilities of the nanostructures towards small molecules. In the first part of this chapter, it was shown that strong coupling between propagating plasmons and the absorption bands of Hemoglobin can be used to enhance the sensitivity of the system for the detection of oxygen. Both the angle and wavelength modes of interrogation were studied. In contrast, the second part of this chapter studied the effect of weak coupling between gold nanoparticles and Cytochrome *c* molecules. It was shown that an enhancement in the absorption of Cytochrome *c* was seen when it was placed in the vicinity of the gold nanoparticle. The effect of the gold core size as well as the thickness of the Cytochrome *c* layer on the absorption enhancement was studied using generalized Mie theory. A single step synthesis of Cytochrome *c* coated gold nanoparticles was presented. The presence of the Cytochrome *c* molecules on the gold nanoparticles was confirmed using SERS signals from nanoparticle aggregates as well as from a single trapped gold nanoparticle. Two small modulations were observed in the extinction spectrum of Cytochrome *c* coated gold nanoparticles treated with ascorbic acid. However, the peaks observed from the extinction measurements differed significantly from the native absorption peaks of Cytochrome *c*. The origin of the peaks observed in the extinction spectrum is not clear and could be explored in future. Furthermore, the absorption enhancement observed in case of isolated gold nanoparticles was small and would have to be enhanced significantly for any practical applications. In this regard, I believe that core-satellite structure, schematically shown in Fig. 7.1(a), can help significantly improving the absorption enhancement of the Cytochrome *c* molecules.

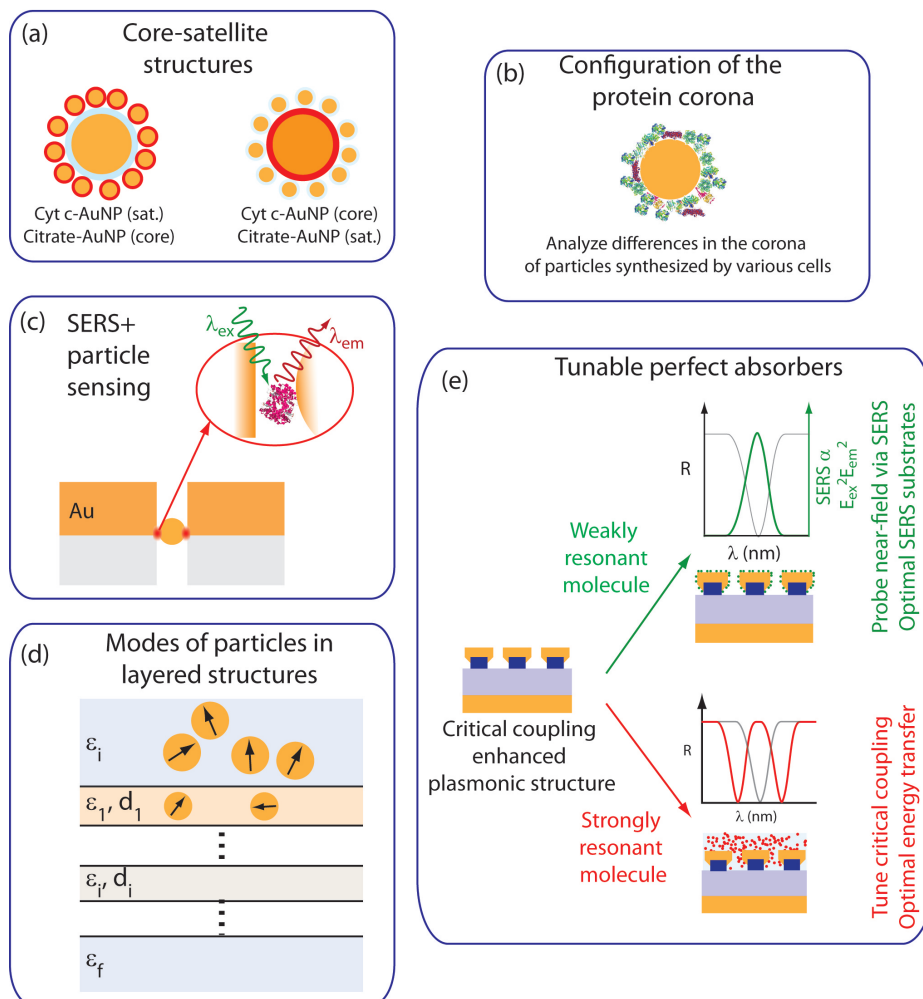


Figure 7.1: (a) Potential routes for enhancing the absorption of Cyt *c* molecules further using core-satellite structures. (b) Understanding the configuration and the arrangements of the various proteins in the corona of the particles synthesized by human cells. (c) Combining SERS and coupling based nanoparticle tracking for simultaneous detection of surface coating and particle dimensions. (d) Development of a technique for computing the modes of a nanoparticle cluster placed in a layered structure. (e) Using strongly resonant molecules for controlling the critical coupling condition and for efficient transfer of energy into the hybrid modes.

Chapter 3:

Human cell assisted synthesis of gold nanoparticles was addressed in Chapter 3. In particular, human cerebral endothelial cells were used for synthesizing gold nanoparticles. Initially, the optimal conditions for particle synthesis were determined. Subsequently, two photon and electron microscopy were used to confirm the presence of nanoparticles in the intracellular region of all the cells. It was shown that the intracellular and the extracellular particles

exhibit different sizes. Additionally, proteomic analysis of the corona of the intracellular and extracellular particles illustrated significant differences between the two. However, cell viability studies clearly showed that the cells were not viable after the synthesis process. The effect of cell membrane permeability on the synthesized nanoparticle size was also studied, which provided a handle for controlling the particle size. I also showed that the intracellular redox state of the cell prior to the addition of HAuCl_4 can also be used to control the size of the synthesized nanoparticles. Preliminary experiments performed on uptake of human cell synthesized gold nanoparticles by other human cells show preferential behavior. This is especially interesting with respect to cancer metastasis.

The results on the human cell synthesized gold nanoparticles presented here can be used as a stepping stone for other research in future. Understanding the configuration and arrangement of proteins in the corona of both the intracellular as well as extracellular particles or particles synthesized by various cells will be of significant interest (Fig. 7.1(b)). This would allow us to understand the interaction of such particles with cells better. The uptake of the human cell synthesized nanoparticles by other human cells needs to be studied further using alternative techniques. Transmission electron microscopy is one of the tools that can provide significant amount of information in this regard. Finally, real time monitoring of nanoparticle uptake by human cells will also be an interesting avenue to pursue and could shed light on the dynamics of the process.

Chapter 4:

A significant portion of this thesis dealt with plasmonic nanoparticles with sizes in the range of 10 to 60 nm. In chapter 4, I developed a technique for the detection of nanoparticles exploiting the hybridization of plasmon resonances. Nanohole arrays with different hole sizes were realized on free standing Si_3N_4 membranes with micro- and nano-fabrication techniques, which served as a template for nanoparticle detection. Using simulations, I demonstrated that it is possible to infer the size of the nanoparticles as it traverses the nanoholes. Gold nanoparticles with a size of 30 nm were successfully detected in the experiments. Finally, it is shown that the developed technique can also be used for analyzing the core size of gold nanoshells. However, the temporal resolution as well as the signal to noise ratio of the optical setup have to be improved for the detection of particles smaller than 20 nm. Additionally, the detection system could be integrated with a microfluidic system for efficient delivery of nanoparticles to the nanohole array, increasing the efficiency of the method. Furthermore, this technique could also be used for acquiring the SERS signal of molecules on the surface of the gold nanoparticles, Fig. 7.1(c), thanks to the large electric field intensities generated in the gap between the nanoparticle and the wall of the nanohole.

Chapter 5:

In chapter 5, I developed a method for computing the eigenmodes of a cluster of plasmonic nanoparticles based on the Green's tensor approach. This technique was initially validated by studying the modes of a single nanoparticle, for which an analytical solution exists in

the small particle limit. Next, I studied the effect of various geometrical parameters and of symmetry breaking in a nanoparticle dimer and trimer. A special case of a nanoparticle quadramer was studied, which exhibited polarization control properties. The generation of circular polarization from nanoparticle quadramer was explained in terms of spectral separation of the modes. In the final part of this chapter, the determined modes were used to study the symmetry effect on second harmonic generation. It was shown that the mode symmetry strongly affects the generated second harmonic signal.

Most plasmonic structures are fabricated on substrates that can sometimes be quite complex or exhibit a resonant behavior, Fig. 7.1(d). In such structures, an extension of the method presented here using the Green's tensor method could provide an insight into the underlying physics of such systems. The developed technique could also be used for studying systems with a large number of particles for understanding their modal structure.

Chapter 6:

An important facet of any application involving plasmonic structures is understanding the interaction of light with the nanostructure itself. In this context, it is often beneficial to engineer either the structure or the illumination condition such that all the incident energy can be used for the corresponding application. In chapter 6, I have studied some of the ways of performing perfect absorption of light by plasmonic structures. In the first part, coherent perfect absorption (CPA) of light by a gap plasmon waveguide exhibiting coupled plasmons was studied. Using both experiments and simulations I showed that nearly 97% of the incident light can be coupled into a given plasmonic mode. Additionally, the phase of one of the incident planewaves can be used to modulate the absorption by nearly 80%. In the second part of the chapter, a single beam analogue of CPA was demonstrated using nanocrescent arrays. SERS was used for probing the enhanced near-field due to perfect absorption of light and consequently improving the capabilities of the nanocrescent arrays as SERS substrates.

CPA in coupled plasmonic gap plasmon waveguides can be extended in future for realization of low-threshold plasmonic lasers. Another attractive prospect lies in the incorporation of active materials in such CPA systems which provide added tunability feature to the perfect absorption dip. One approach could be based on the principle of strong coupling explored in Chapter 1, where instead of a weakly resonant molecule which probes the electromagnetic field, strongly resonant molecules would allow the strong coupling and control over the critical coupling point via control of molecule density (Fig. 7.1(e)).

A Abbreviations

Abbreviation	Full name
STEM	Scanning transmission electron microscope
AuNP	Gold nanoparticle
TEM	Transmission electron microscope
SERS	Surface enhanced Raman scattering
DOP	Degree of polarization
SH	Second harmonic
SHG	Second harmonic generation
CPA	Coherent perfect absorption
SS	Super-scattering
CC	Critical coupling

Table A.1: Table of frequently used abbreviations.

Appendix A. Abbreviations

Abbreviation	Full name
Cyt <i>c</i>	Cytochrome <i>c</i>
H ₂ O ₂	Hydrogen peroxide
HEPES	4-(2-hydroxyethyl)-1-piperazineethanesulfonic acid
AA	Ascorbic acid
PBS	Phosphate buffered saline
MPA	Mercapto propanoic acid
EDC	1-Ethyl-3-(3-dimethylaminopropyl)carbodiimide
NHS	N-Hydroxysuccinimide
ROS	Reactive oxygen species
GSH	Reduced glutathione
NAC	N-Acetyl cysteine
BSO	Buthionine-(S,R)-Sulfoxime
Hb	Hemoglobin
DMEM	Dulbecco's modified Eagle's medium
RPMI-1640	Roswell Park Memorial Institute medium
FBS	Fetal bovine serum
HBSS	Hanks' Balanced Salt solution
BET	Benzene-ethane-thiol

Table A.2: Table of frequently used chemicals and their abbreviations.

B Plasmon modified absorption of molecules: Additional data

B.1 Hemoglobin

The parameters used for computation of the dielectric function of Hemoglobin in the oxygenated and deoxygenated states are presented in Table B.1 and Table B.2, respectively.

C (mM)	ν_{p1} (THz)	ν_{p2} (THz)	ν_{p3} (THz)	γ_{01} (THz)	γ_{02} (THz)	γ_{03} (THz)
5	10.5	7	39	32.5	15	39
7.5	12.9	8.5	47.5	32.5	15	39
10	14.8	9.8	54.2	32.5	15	39
15	18	12.25	67.5	32.5	15	39
50	33	22	125	32.5	15	39

Table B.1: Parameters for the dielectric function of oxygenated Hemoglobin

C (mM)	ν_{p1} (THz)	ν_{p2} (THz)	ν_{p3} (THz)	γ_{01} (THz)	γ_{02} (THz)	γ_{03} (THz)
5	16	1.5	28.5	66	10	20
7.5	19.5	2	35	66	10	20
10	22.5	2	40	66	10	20
15	27.5	2.75	49.5	66	10	20
50	50.5	4	95	66	10	20

Table B.2: Parameters for the dielectric function of deoxygenated Hemoglobin

B.2 Cytochrome *c*

The parameters used for computation of the dielectric function of Cytochrome *c* in the reduced and oxidized states are presented in Table B.3 and Table B.4, respectively. Figure. B.1 shows the real and imaginary parts of the dielectric function of reduced and oxidized 50 mM Cyt *c* solution.

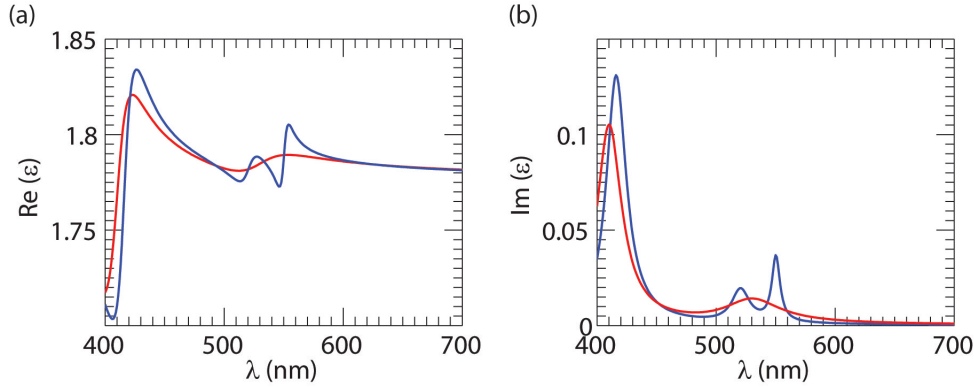


Figure B.1: (a) Real and (b) imaginary parts of the dielectric constant of 50 mM reduced (blue) and oxidized (red) Cyt *c*.

C (mM)	ν_{p1} (THz)	ν_{p2} (THz)	ν_{p3} (THz)	γ_{01} (THz)	γ_{02} (THz)	γ_{03} (THz)
0.001	0.054	0.0625	0.2535	8	20	35
0.005	0.0122	0.14	0.567	8	20	35
0.01	0.172	0.2	0.8	8	20	35
0.025	0.27	0.32	1.27	8	20	35
0.05	0.38	0.45	1.79	8	20	35
0.1	0.54	0.625	2.53	8	20	35
0.25	0.855	1	4	8	20	35
0.5	1.21	1.41	5.67	8	20	35
1	1.725	2	8	8	20	35
2	2.4	2.8	11.3	8	20	35
10	5.45	6.275	25.35	8	20	35
25	8.6	10	40.25	8	20	35
50	12.2	14.1	57.5	8	20	35

Table B.3: Parameters for the dielectric function of reduced Cytochrome *c*.

B.3 Variation of differential absorption and scattering signals from a gold core-Cyt *c* particle as a function of the core size

In Chapter 2, I studied the effect of modifying the gold core size on the differential signal arising from the redox state change of Cyt *c* molecule. Figure B.2 shows similar spectra but for larger values of the core size. Furthermore, it is seen that multiple optimal size can be determined, each corresponding to the best match between the absorption bands of Cyt *c* and one of the plasmon resonances. For example, the first maximum in the differential signal arises because of optimal match of the dipole resonance with the absorption band of Cyt *c*. The second maximum occurs due to the best match with the quadrupolar mode and the absorption bands of Cyt *c*.

B.3. Variation of differential absorption and scattering signals from a gold core-Cyt *c* particle as a function of the core size

C (mM)	ν_{p1} (THz)	ν_{p2} (THz)	ν_{p3} (THz)	γ_{01} (THz)	γ_{02} (THz)	γ_{03} (THz)
0.001	0.09	-	0.26	60	-	45
0.005	0.205	-	0.58	60	-	45
0.01	0.29	-	0.8225	60	-	45
0.025	0.455	-	1.3	60	-	45
0.05	0.645	-	1.84	60	-	45
0.1	0.91	-	2.6	60	-	45
0.25	1.45	-	4.1	60	-	45
0.5	2.05	-	5.8	60	-	45
1	2.9	-	8.22	60	-	45
2	4.1	-	11.65	60	-	45
10	9.25	-	26.1	60	-	45
25	14.5	-	41.4	60	-	45
50	20.5	-	58.75	60	-	45

Table B.4: Parameters for the dielectric function of oxidized Cytochrome *c*.

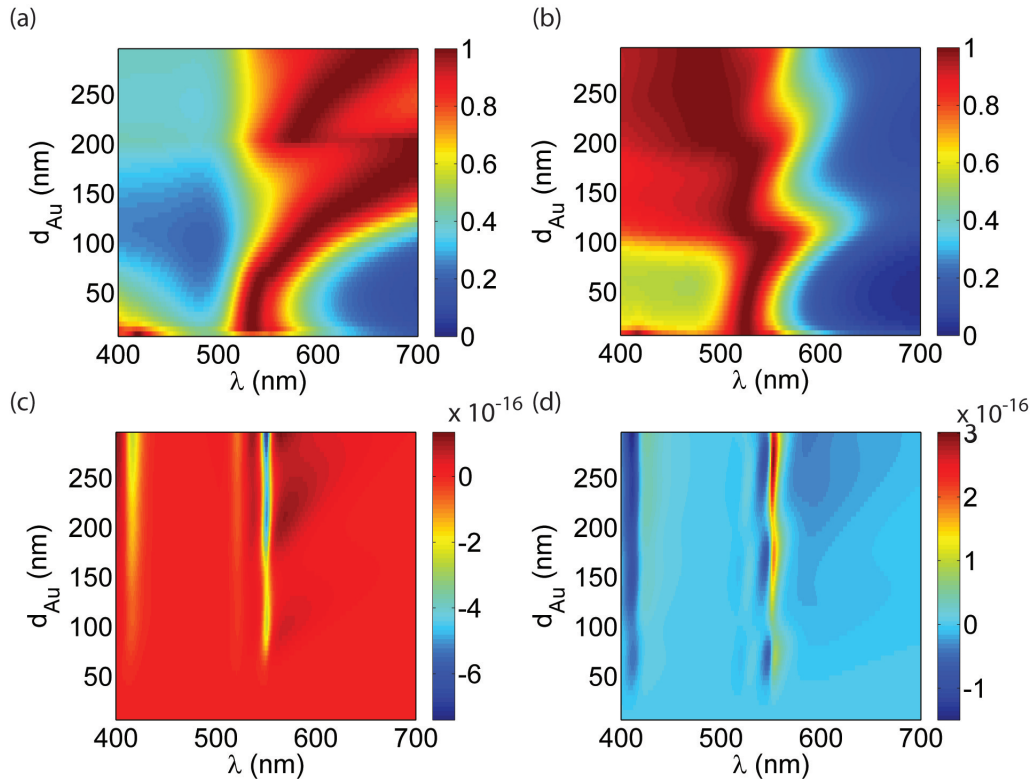


Figure B.2: **Gold core size for optimal differential signals.** (a) Normalized scattering, (b) normalized absorption, (c) differential scattering and (d) differential absorption spectra of Cyt *c* coated gold nanoparticle for different values of the gold core size. For calculating the normalized scattering and absorption spectra, the Cyt *c* layer is taken to be in a fully reduced state. The thickness of the Cyt *c* layer is fixed at 3.4 nm.

C Biological system assisted gold nanoparticle synthesis

C.1 Gold nanoparticle synthesis by cell culture media

In Chapter 3 the biosynthesis of gold nanoparticles by human cells and their properties is studied. However, prior to synthesis of gold nanoparticles using human cells, it is necessary to screen the various cell culture media to check whether they facilitate nanoparticle synthesis. For this purpose the following common cell culture media and buffer solutions are studied: DMEM (with glucose), RPMI-1640 (with glucose), 10%FBS, HBSS (with glucose), DMEM (with glucose)+10%FBS and RPMI-1640 (with glucose)+10%FBS.

The protocol used for checking nanoparticle synthesis is outlined here. A specified volume of a given medium is added to PBS or HBSS to a final volume of 375 μL . I also define a dilution ratio (r) as the ratio between the volume of media to the diluting solution (PBS or HBSS). Then HAuCl_4 is added to a final concentration of 0.5 mM. The solution is gently mixed and incubated at 37°C for 24 h. All the experiments are performed in triplicates and repeated twice. Figure C.1 shows color of the samples 24 h after the addition of HAuCl_4 . Recall that the color is a distinctive indicator of the presence or absence of gold nanoparticles.

Gold salt added to PBS (without glucose) did not lead to particle synthesis at any dilution ratio (not shown here). However HBSS, a buffer used frequently for cell culture, did synthesize particles for high dilution ratio values ($r=1$ and 0.86). The addition of 10% FBS (the concentration used during standard cell culture protocol) to PBS and HBSS resulted in the inhibition of the particle synthesis and no visible color change is observed. This is probably due to the interaction of serum proteins with the gold salt and effective lowering of gold salt concentration in solution. DMEM diluted in PBS (for $r=0.4$ -0.06) leads to the synthesis of aggregated nanoparticles, as evidenced by the grayish black color of the solution. Note that no particle synthesis is observed for pure DMEM solutions ($r=1$). The dilution of DMEM supplemented with 10% FBS in either PBS or HBSS leads to the synthesis of unaggregated particles for low dilution ratio ($r=0.13$ -0.02). Analogous results are obtained in the case of RPMI, another common cell culture medium. The results presented here show that the proteins present in the FBS can act as stable capping agents and assist in synthesis of unaggregated particles. In

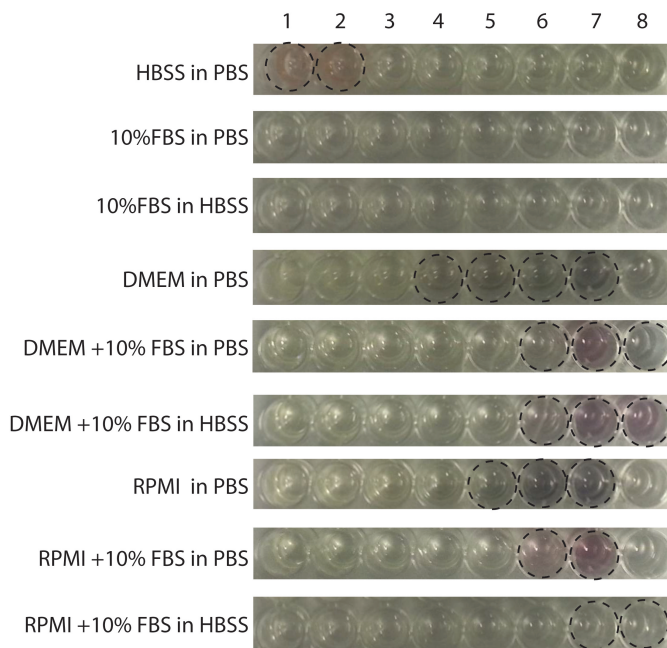


Figure C.1: **Biosynthesis control experiments.** Synthesis of gold nanoparticles from HAuCl_4 by different cell culture media. The numbers 1-8 represent different dilutions of the media in either PBS or HBSS as indicated. The dilution ratio (volume ratio of media to diluting solution) in the different cases are : (1) $r=1$, (2) $r=0.86$, (3) $r=0.53$, (4) $r=0.4$, (5) $r=0.26$, (6) $r=0.13$, (7) $r=0.06$ and (8) $r=0.02$. The total volume of the diluted media was fixed at $375 \mu\text{L}$. The concentration of gold salt was kept fixed at 0.5 mM . The dilutions that showed the synthesis of gold nanoparticles as observed by the change of color of the solution are indicated by dashed circles.

addition to the results shown here, identical experiments performed with DMEM and RPMI (without glucose) did not result in the synthesis of any gold nanoparticles. This indicates that the glucose in the cell culture medium is the reducing agent responsible for conversion of Au^{3+} to Au^0 .

C.2 Gold nanoparticle synthesis by human cells: Additional data

Biosynthesis of gold nanoparticles by human cerebral endothelial cells is investigated in Chapter 3. Figure C.2 shows the size histograms computed using the nanoparticle sizes measured from the STEM images for the three cases (particles generated by live cells, ethanol

treated cells and formaldehyde treated cells).

C.3 Time dependent modification of cell morphology on incubation in PBS

In this section, I study the cell morphological changes when they are incubated in PBS. The experimental procedure is as follows: The cells are cultured for 24 h in DMEM supplemented with 10% FBS post the seeding step. Next, the cells are washed twice with PBS and then left to incubate for the required time in PBS. Figure C.3 shows that the cellular morphology gets modified drastically for incubation times longer than 30 min. Furthermore, longer incubation times lead to the cells assuming a spherical shape and detaching from the surface on washing the culture well. This morphological change is probably due to the absence of glucose and other minerals in the PBS solution. This is further evidenced by the fact that such morphological changes are not observed when the cells are incubated in HBSS supplemented with glucose.

C.4 Complete list of proteins

The complete list of proteins determined via the proteomic analysis for the human cell synthesized gold nanoparticles can be downloaded from [**http://goo.gl/lc1uET**](http://goo.gl/lc1uET).

The complete list of proteins determined from proteomic analysis for gold nanoparticles synthesized in the presence of medium supplemented with HEPES can be downloaded from [**http://goo.gl/Hw3P0z**](http://goo.gl/Hw3P0z).

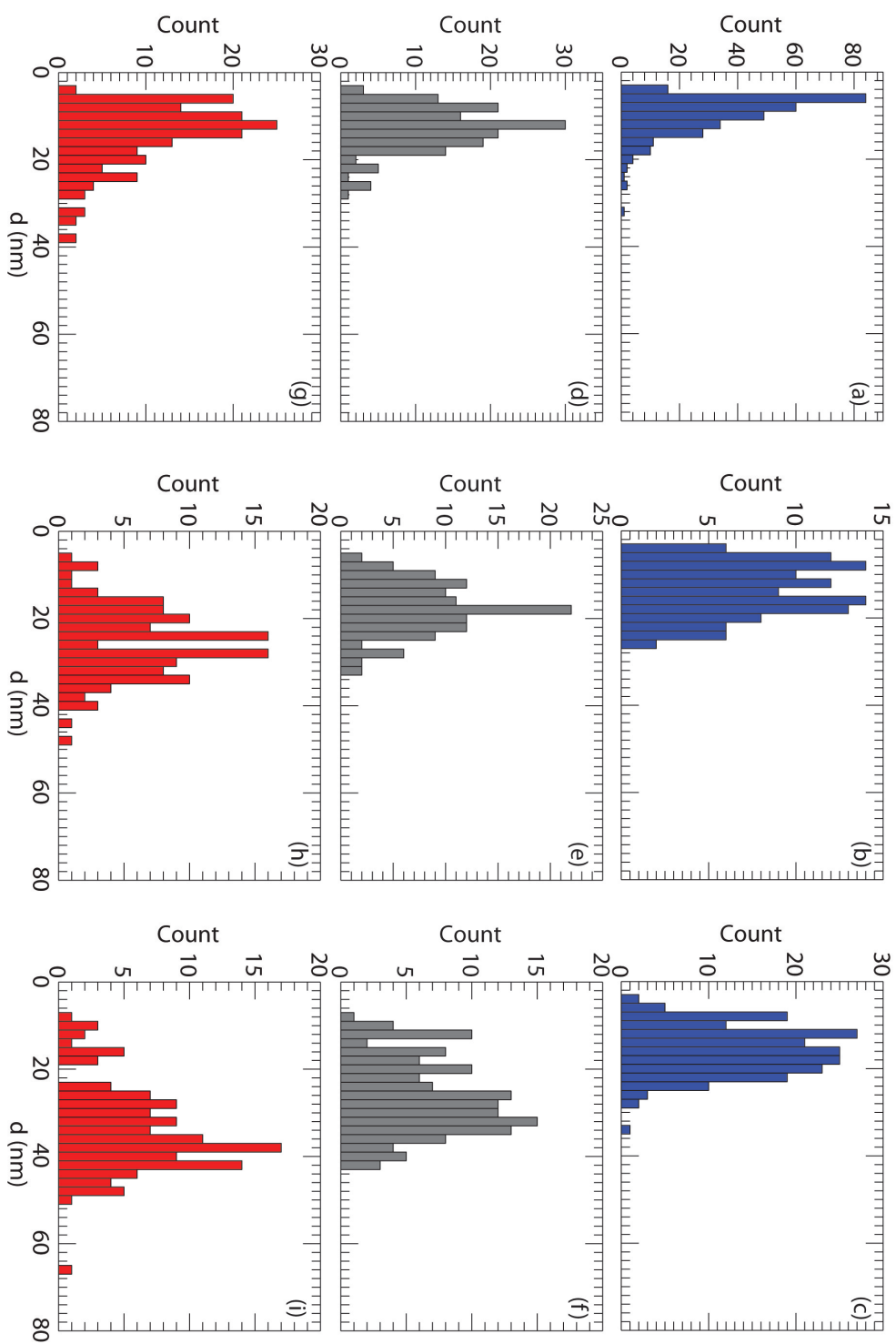


Figure C.2: **Particle size histograms.** Extracellular particle size histograms extracted from the STEM images when synthesized using live cells (red), cells fixed with 4% formaldehyde (blue) and cells fixed with 50% ethanol (black). (a), (d) and (g) are particles generated with 0.2 mM HAuCl₄, (b), (e) and (h) are particles generated with 0.4 mM HAuCl₄ and (c), (f) and (i) are particles generated with 0.5 mM HAuCl₄.

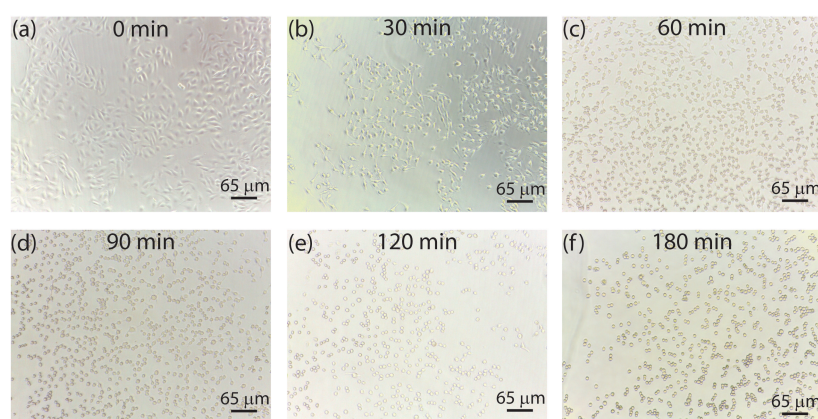


Figure C.3: **PBS induced cell morphology modification.** Modification in the cellular morphology after incubation in PBS (pH 7.2) for (a) 0 min, (b) 30 min, (c) 60 min, (d) 90 min, (e) 120 min and (f) 180 min.

D Nanoparticle sensing using metallic hole arrays

In Chapter 5 we studied particle sensing using a nanohole array in a metal film.

D.1 Spectral dependence on pairs of hole-particle size

For completeness, the reflection and transmission spectra of various hole-particle size pairs are shown in Fig. D.1.

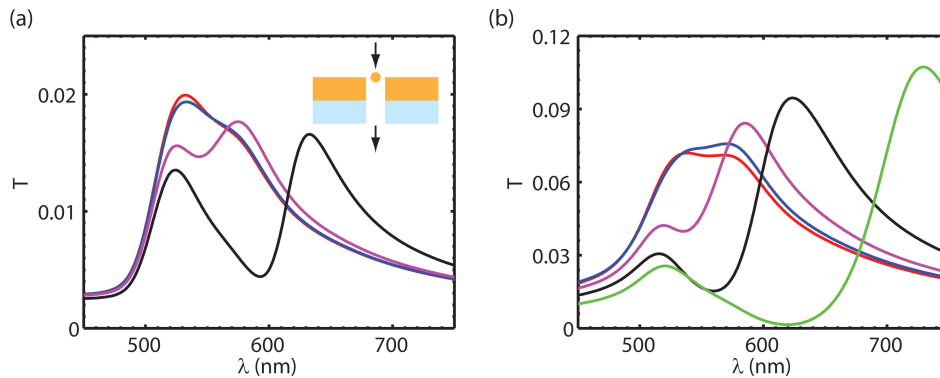


Figure D.1: **Transmission spectra for hole-particle pairs.** (a) Transmission spectra of a 40 nm hole array with no particles (red), 10 nm particle (blue), 20 nm particle (magenta) and 30 nm particle (black). The inset depicts the position of the particle in addition to illumination and collection directions. (b) Transmission spectra of a 60 nm hole array with no particles (red), 20 nm particle (blue), 30 nm particle (magenta), 40 nm particle (black) and 50 nm particle (green).

D.2 Proof of hybridization of plasmon modes of particle and hole

In Chapter 5, the hybridization of the mode of the nanoparticle and the hole is used for developing a method for probing the nanoparticle size. However, in all the data shown, only the low energy mode with lower net dipole moment was observed. In this section, I clearly

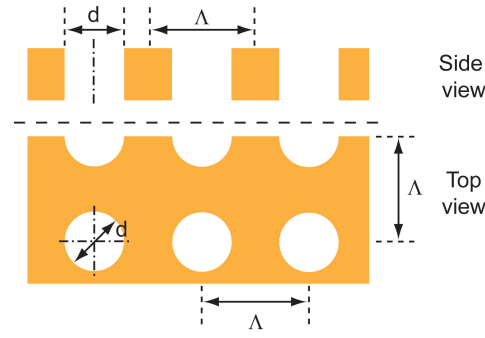


Figure D.2: **Schematic of the system.** Geometry used for studying hybridization in a particle-hole system.

illustrate that both the modes can be visualized if the parameters of the system are slightly modified. As mentioned in Chapter 5, the main reason of non visualization of the high energy hybridized mode is the presence of the interband transition of gold below 500 nm. Here I use an analogous system, shown in Fig. D.2, in which the background dielectric constant is taken to be equal to 4, i.e., equal to Si_3N_4 . Figure D.3 shows that the native resonance of the hole array is red shifted to around 620 nm when compared to the hole array placed in water on increasing the refractive index of the background. The additional peak observed in the spectrum close to 540 nm arises from the interband transitions of gold. On filling each of the holes with particles, I observe that the single peak at 620 nm splits into two new resonances (in total 3 resonances are observed). The field distributions close to these resonances are plotted in in Fig. D.3. Note that norm component of the electric field is taken close to 560 nm in order to visualize the high energy mode, which otherwise is obscured by the distribution of the low energy mode. It is clear from the charge distributions that in case of the high energy (low wavelength) mode the dipole moment of the particle and the hole are in the same direction. Whereas in case of the low energy mode the dipole moments of the particle and the hole orient in an anti-parallel fashion. The field distributions correspond exactly with those drawn schematically using the plasmon hybridization model.

D.3 Modulation of transmission and reflection intensities due to a gold nanoparticle in a symmetric hole array structure

In this section, I study the effect of the nanoparticle position on transmission and reflection spectra from the symmetric structure shown in Fig. D.2 where the hole is filled with a 30 nm gold nanoparticle. Note that this structure exhibits a mirror symmetry about the plane $z = -50$ nm in the absence of the particle. Figure D.4 (a) and (b) shows the transmission and reflection spectra when the structure is illuminated from the top with a plane wave propagating in $-z$ direction and polarized along x axis. In case of the transmission spectra, as the particle approaches the hole ($z \geq 0$ nm) there is an increase in the coupling between the modes of the particle and that of the hole (Fig. D.4(c) and (d)). This is followed by a region of maximal

D.3. Modulation of transmission and reflection intensities due to a gold nanoparticle in a symmetric hole array structure

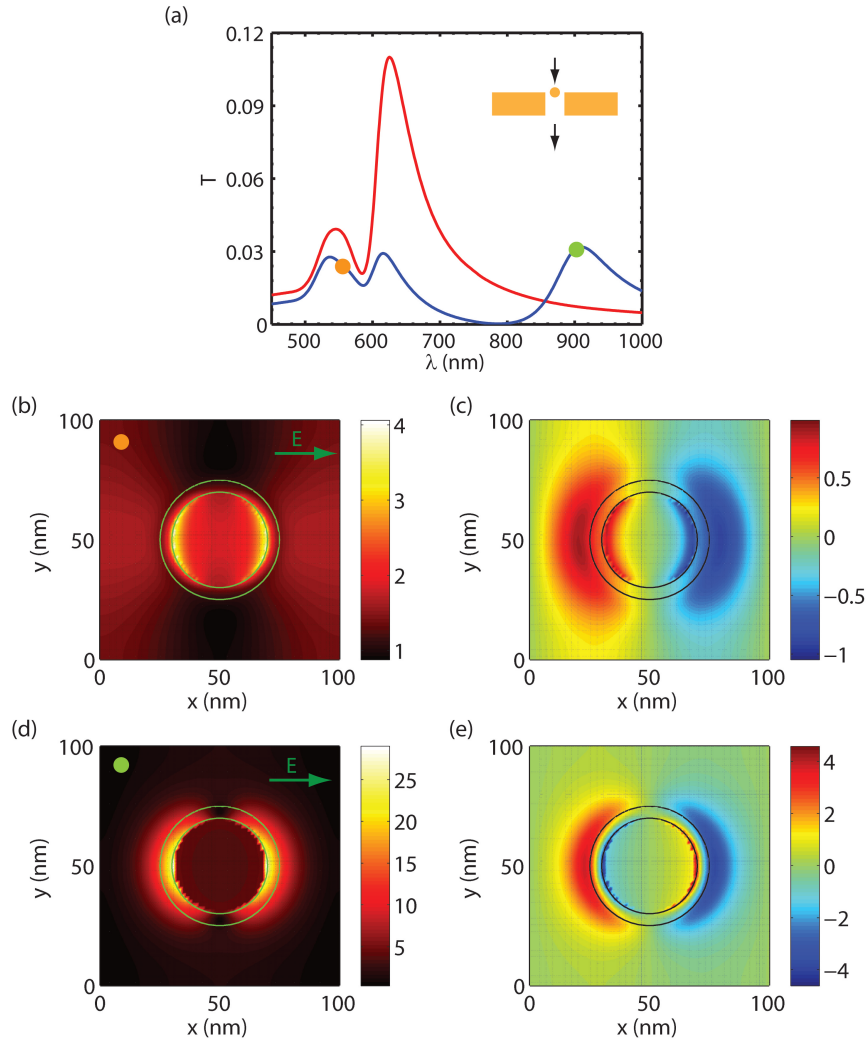


Figure D.3: **Demonstration of hybridized modes in particle-hole system.** (a) Transmission spectrum of the hole array without (red) and with (blue) a 40 nm gold particles. The dielectric constant of the background is taken as 4. The inset shows the vertical position of the particle with respect to the hole and the illumination and collection direction. (b) and (d) Total field intensities at $\lambda = 540$ nm and $\lambda = 900$ nm on a XY plane with $z = 5$ nm. The respective wavelengths are also marked in the transmission spectrum using orange ($\lambda = 540$ nm) and green ($\lambda = 900$ nm) circles. The polarization of incident field is shown using a green arrow. (c) and (e) Real part of E_z at $\lambda = 540$ nm and $\lambda = 900$ nm on a XY plane with $z = 5$ nm.

coupling (at around $z = -10$ nm) and then a reduction in the coupling due to decrease in the spatial overlap of the fields of the particle and resonance of the hole. However, the coupling is increased once again when the particle approaches the lower Au-water interface. Note that the transmission spectra are nearly identical (less than 2% variation) for the particle located at $z = 0$ nm and $z = -100$ nm. On the other hand, in case of reflection spectra, the maximum modification is observed when the particle is located at the top Au-water interface and the coupling decreases as the particle traverses the hole (Fig. D.4 (b) and (e)). Furthermore, both

the transmission intensity at any wavelength and the resonance wavelength are symmetric about the plane $z = -50$ nm for various positions of the particle.

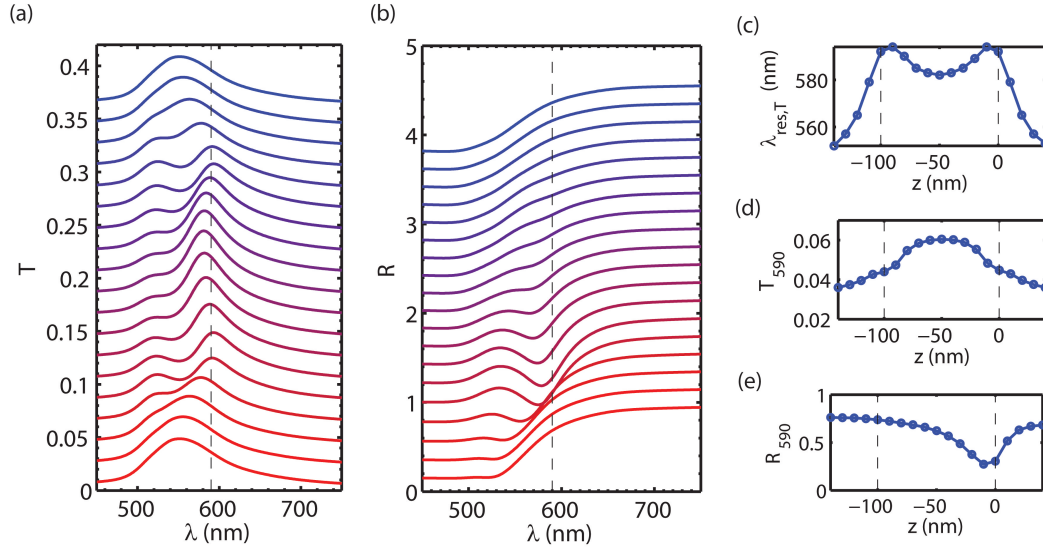


Figure D.4: Transmission and reflection spectra from various nanoparticle positions a symmetric hole array. (a) Transmission and (b) reflection spectra of the hole array with 30 nm gold particle placed at different z positions ($-140 \text{ nm} \leq z \leq 40 \text{ nm}$, $\Delta z = 10 \text{ nm}$). The dielectric constant of the background is taken as 1.7689. Each successive transmission and reflection spectra are shifted by 0.02 and 0.2 units, respectively, for clarity. (c) Peak position of the plasmon resonance in the transmission spectra as a function of z position. (d) Transmission and (e) reflection intensity at $\lambda = 590 \text{ nm}$ as a function of the z position of the particle. $z = 0$ corresponds to the top Au-water interface and $z = -100 \text{ nm}$ corresponds to the bottom Au-water interface. Note that in these simulations the Si_3N_4 substrate is absent.

E Eigenmode analysis of plasmonic clusters: Additional data

In Chapter 5, the eigenmode analysis is performed using wavelength as the eigenvalue. However, in many other modal analysis methods frequency is used as the eigenvalue [422]. Here, I briefly show that the same results are obtained when performing the eigenmode analysis using the frequency as eigenvalue, instead of the wavelength, as done in the main text.

Figure E.1 shows the variation of $\log_{10}|\xi - 1|$ as a function of $\text{Re}(\omega/\omega_p)$ and $\text{Im}(\omega/\omega_p)$ for a 20 nm gold nanoparticle suspended in a medium with $\epsilon_B = 6.145$. As explained previously, the equation $\xi(\omega) = 1$ is satisfied for $\omega = (0.2091 - 0.0045i)\omega_p$, which is the eigenfrequency of the single particle. Correspondingly, $\lambda = 662 + 14i$ which is exactly the same eigenwavelength as computed in Chapter 5. Thus, eigenmode analysis with frequency as the eigenvalue is identical with the analysis performed using wavelength as the eigenvalue.

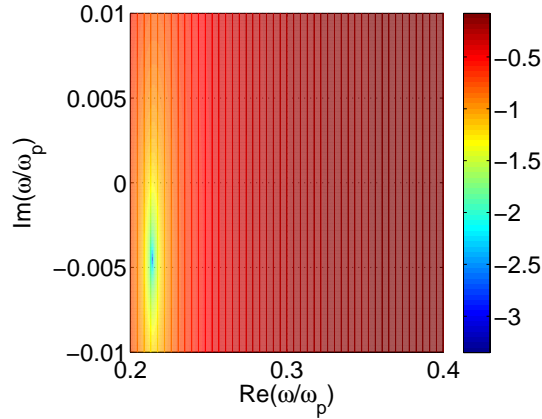


Figure E.1: **Eigenmode computation using frequency as the eigenvalue.** $\log_{10}|\xi - 1|$ plotted as a function of the real and imaginary parts of the normalized frequency ω/ω_p .

F Perfect absorption of light mediated by plasmon resonances

F.1 CPA mediated anomalous reflection from a corrugated metallic film

In chapter 6, I studied coherent perfect absorption of light in structures supporting both propagating plasmons excited using the prism coupling geometry. In addition to the prism coupling method, it is also possible to excite the gap plasmons using gratings. In this section, I show that CPA and SS can be achieved with a free standing corrugated metal film supporting coupled surface plasmons (see Fig. F.1(a)) illuminated from both sides at the same angles of incidence. The illumination geometry is analogous to the one used in chapter 6 and the specular zeroth order light (both reflected and transmitted) can be suppressed for suitable system parameters. For gratings with $K = k_{SP}$ ($K = 2\pi/\Lambda$ is the grating vector and k_{SP} is the surface plasmon (SP) wavevector), one can excite the SP's using the ± 1 diffraction orders for normal incidence (see Fig. F.1(b)). CPA with bi-directional incidence can then suppress the specular order and thus all the incident energy will be converted into the surface plasmons in the $\pm x$ directions with half of the incident plane wave energy in each direction. In the calculations I use the geometry shown in Fig. F.1(c), where one of the surface waves (in the $-x$ direction) is changed to a propagating mode, while the $+1$ order can excite the SP satisfying the momentum matching condition $k_0 \sin(\theta) + K = k_{SP}$ (k_0 is the vacuum wave vector, θ is the angle of incidence). Coupled with the CPA assisted suppression of the specular zeroth order, this manifests itself as counterintuitive scattering of light on the same side of the normal.

Free standing metal films have been studied both theoretically and experimentally [496, 497]. It was shown that for shallow gratings perturbative method like Rayleigh expansion is well suited and can lead to excellent agreements with the experimental results. For sufficiently thin films the coupling was shown to lead to the long range (LR) and short range (SR) modes, which can be excited at different angles of incidence. In this section I use the same technique albeit with illumination by plane waves from both sides (see Fig. F.1(a)).

Consider a corrugated metal film of dielectric constant ϵ_m suspended in air (dielectric constant

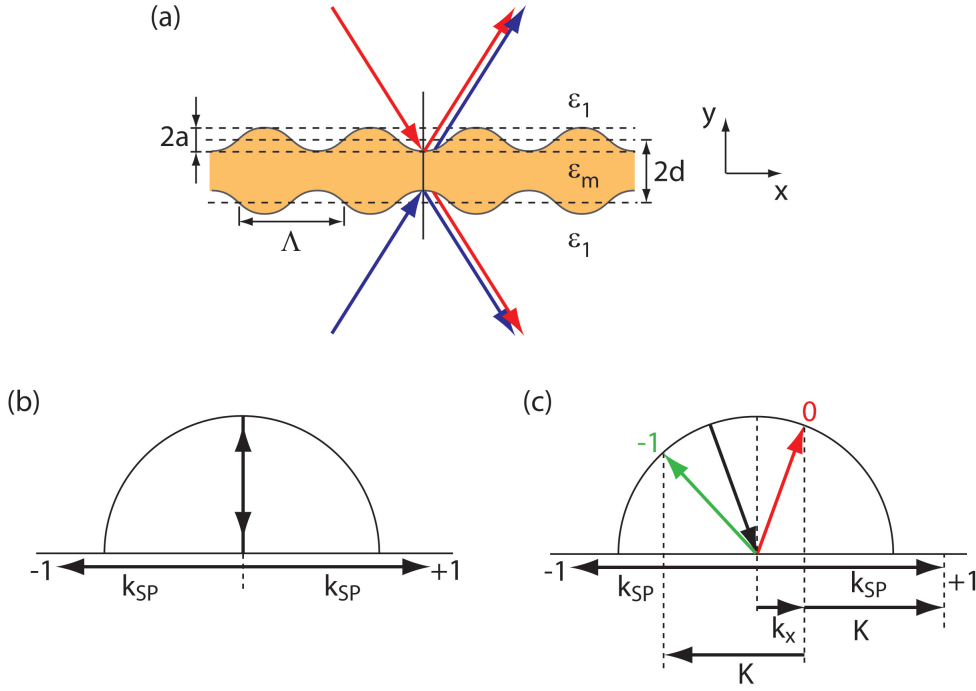


Figure F.1: **Schematic of the geometry.** (a) Schematics of the corrugated metal film and the illumination geometry (only the specular diffracted orders are shown). (b) Excitation of SP's under normal incidence of light in reciprocal space. (c) Excitation of 0 (red) and -1 (green) harmonics as propagating modes for small angle incidence. Figures are not drawn to scale.

ϵ_1) as shown in Fig. F.1(a). The surface profiles are given by the following equations

$$y_{\pm} = \pm d \pm a \sin Kx, \quad (\text{F.1})$$

where the $+$ ($-$) sign refers to the top (bottom) interface and $2d$ and a give the width and the corrugation amplitude, respectively. Calculations were performed retaining 13 spatial harmonics and convergence is satisfactory for the grating parameters used in calculations. The following system parameters are chosen for most of the calculations: incident wavelength $\lambda = 780$ nm, $d = 27$ nm, $\epsilon_1 = 1.0$. I used silver as the film material with ϵ_m taken from the experimental work of Johnson and Christie [259]. Calculations are performed for two values of grating period Λ so as to lead to two near-normal angles of incidence, satisfying plasmon resonance conditions with the $+1$ diffraction order. The choice of parameters is not arbitrary, and they needed to be adjusted such that CPA condition is met for the zeroth specular order. Thus I used different values of the modulation depth a for the same grating period Λ in order to meet the CPA condition at the LR and SR modes. Moreover, in order to demonstrate the phase sensitivity a delay in one of the incident beams is introduced. The delay will be assumed to be zero unless otherwise stated. It will be shown below how a change in this delay from zero to π can change the character of scattering from SS to CPA.

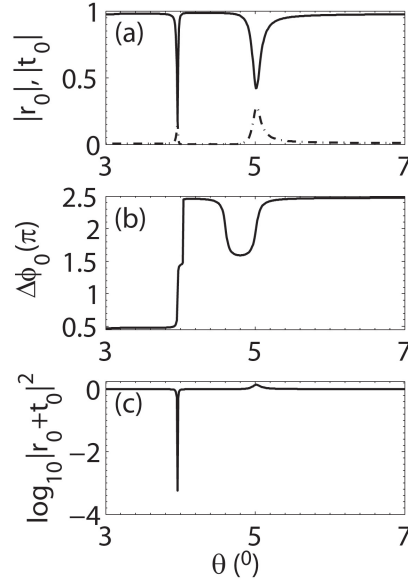


Figure F.2: **CPA at the long range surface plasmon.** (a) Absolute values of zeroth order reflected (solid line) and transmitted (dash-dotted line) amplitudes $|r_0|$ and $|t_0|$, (b) phase difference $\Delta\phi_0$ and (c) total scattered intensity on each side $\log_{10}|r_0 + t_0|^2$ as functions of angle of incidence for $\lambda = 780$ nm, $\Lambda = 826$ nm, $a = 7.2$ nm, $d = 27$ nm and $\epsilon_1 = 1.0$. The incident plane waves have a null phase delay.

Let r_m and t_m represent the m -th amplitude reflection and transmission diffraction orders for unit amplitude p-polarized plane wave incidence. Let $\Delta\phi_m$ represent the phase difference (normalized to π) between r_m and t_m . In the context of the zeroth order, the role of these quantities in CPA was discussed in detail in chapter 6 highlighting the importance of destructive interference, when $|r_0| = |t_0|$ and $\Delta\phi_0 = \pm 1$. The results for CPA with the LR mode are shown in Fig. F.2, where we have plotted $|r_0|$ and $|t_0|$ (Fig. F.2(a)), $\Delta\phi_0$ (Fig. F.2(b)) and total scattered intensity on either side $\log_{10}|r_0 + t_0|^2$ (Fig. F.2(c)) for $\Lambda = 826$ nm and $a = 7.2$ nm. One can easily see that at $\theta \sim 4^\circ$ the CPA condition is met along with simultaneous excitation of the LRSP and one has near-null scattering at that angle.

It may be noted that for a thin planar metal film the LR and SR modes differ by a phase difference of π , though perturbation of the surface in a corrugated film slightly offsets this value (1.08π for parameters of Fig. F.2). Otherwise, same system parameters yielding CPA for the LR mode would lead to the SS at the SR mode. Because of the offset I had to pick slightly different system parameter, namely, $a = 8.9$ nm for the same grating period $\Lambda = 826$ nm as in Fig. F.2 for demonstrating both SS and CPA with the SR mode. In particular the short range mode was picked for demonstrating CPA, since without interference it can never lead to null reflection. The results for $|r_m|$ and $|t_m|$, $\Delta\phi_m$ (normalized to π), and the log of the total scattered intensity $\log_{10}|r_m + t_m|^2$ for two different orders, namely, $m = 0$ and $m = -1$ are shown in Fig. F.3. The results for $m = +1$ (not shown) confirms the SP-mediated local field

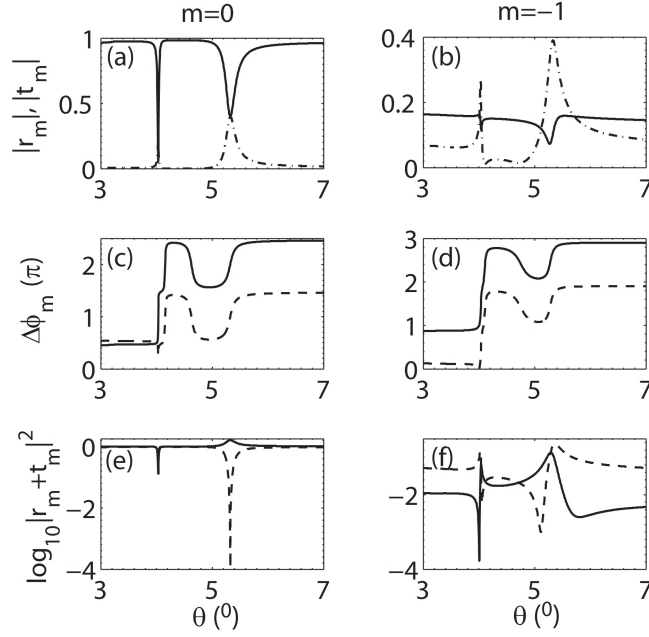


Figure E3: **CPA at short range surface plasmon.** Absolute values of reflected (solid line) and transmitted (dash-dotted line) amplitudes $|r_m|$ and $|t_m|$ (top row: (a) and (b)), phase difference $\Delta\phi_m$ (middle row: (c) and (d)) and total scattered intensity on one side $\log_{10}|r_m + t_m|^2$ (bottom row: (e) and (f)), as functions of angle of incidence θ for the 0 order (left column) and -1 order (right column). The solid and dashed lines in (c)-(f) are for null and π phase delay, respectively, between the incident waves. The other parameters are as in Fig. E2, except that now $a = 8.9$ nm.

enhancement. All other harmonics (not shown) are evanescent and their excitation efficiency is low due to shallow corrugation. As can be seen from Fig. E3(a) that $|t_0| = |r_0|$ for an incident angle of 5.3° implying that both CPA and SS can be realized provided that the phase difference is adjusted accordingly. It can be seen from Fig. E3(c) that for a phase delay of π between the incident plane waves (dashed curve) the necessary conditions for CPA are met at the short range plasmon resonance since $\Delta\phi_0 = \pi$ ensuring destructive interference. In contrast, incident waves with the same phase result in $\Delta\phi_0 \sim 2\pi$ yielding constructive interference leading to SS (solid curve for $m = 0$ in Fig. E3). Both these features can be read from Fig. E3(e) where I used a log plot to stress the null of scattering for CPA. The right column in Fig. E3 shows the results for the $m = -1$ diffraction order, which displays a dramatic change when the LR and SR modes are excited. In fact, for a phase delay of π between the input beams at $\theta = 5.3^\circ$ (CPA for zeroth order) there can be significant scattering in the -1 order (see right peak in Fig. E3(f)) at the SR resonance.

I now show that the closer it is to normal incidence, the larger will be the anomalous scattering in the -1 diffraction order. The bottom panel of Fig. E3 is reproduced for two different values of grating period, namely, $\Lambda = 826$ nm (top row in Fig. E4) and 787 nm (bottom row) with

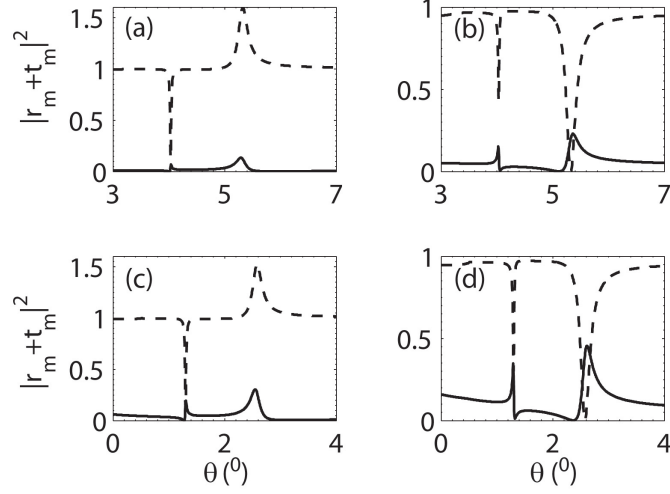


Figure E4: **Anomalous scattering of light.** Total scattered intensity as a function of angle of incidence, for an initial phase delay of 0 (left column) and π (right column). The top and bottom rows are for $\Lambda = 826$ nm and $\Lambda = 787$ nm, respectively. Dashed and solid lines in each panel are for 0 and -1 harmonics, respectively. The other parameters are as in Fig. E3.

parameters meeting the CPA/SS conditions for the SRSP. Note that Λ closer to λ corresponds to smaller angles for the excitation of the SRSP. Dashed (solid) lines show the results for $m = 0$ ($m = -1$) order. Left and right columns in Fig. E4 correspond to phase delays 0 and π , respectively, between the incident waves. For the zeroth order, null phase delay corresponds to SS (dashed curve peak in Fig. E4(a) and (c)), while a delay of π results in CPA at the SR mode resonance (dashed curve, right dip in Fig. E4(b) and (d)). It is thus clear that the character of interference plays a very important role. A comparison of Figs. E4(b) and (d) clearly reveals that for the shorter grating period one has larger total scattering in the $m = -1$ order and it can be as high as 45%. Thus near the SR resonance zeroth order gets suppressed due to CPA, while there is enhanced scattering in the only other propagating order, namely the $m = -1$ order. In other words light bends in the ‘wrong’ direction on the same side of the normal.

In conclusion, I have exploited CPA in a free standing corrugated metal film for near normal illumination from both sides to show apparent bending of light on the same side of the normal.

Bibliography

- [1] B. Abasahl, S. Dutta-Gupta, C. Santschi, and O. J. F. Martin, "Coupling strength can control the polarization twist of a plasmonic antenna," *Nano Letters*, vol. 13, no. 9, pp. 4575–4579, 2013.
- [2] U. Leonhardt, "Optical metamaterials: Invisibility cup," *Nature Photonics*, vol. 1, no. 4, pp. 207–208, 2007.
- [3] J. J. Kunicki-Goldfinger, I. C. Freestone, I. McDonald, J. A. Hobot, H. Gilderdale-Scott, and T. Ayers, "Technology, production and chronology of red window glass in the medieval period – rediscovery of a lost technology," *Journal of Archaeological Science*, vol. 41, no. 0, pp. 89–105, 2014.
- [4] M. Faraday, "The bakerian lecture: Experimental relations of gold (and other metals) to light," *Philosophical Transactions of the Royal Society of London*, vol. 147, pp. 145–181, 1857.
- [5] G. Mie, "Beitrage zur optik truber medien, speziell kolloidaler metallosungen," *Annalen der Physik*, vol. 330, no. 3, pp. 377–445, 1908.
- [6] H. Raether, *Surface Plasmons on Smooth and Rough Surfaces and on Gratings*. Springer, 1988.
- [7] I. Abdulhalim, M. Zourob, and A. Lakhtakia, "Surface plasmon reosnance for biosensing: A mini-review," *Electromagnetics*, vol. 28, pp. 214–242, 2008.
- [8] W. L. Barnes, A. Dereux, and T. W. Ebbesen, "Surface plasmon subwavelength optics," *Nature*, vol. 424, p. 824, 2003.
- [9] J. Homola, *Surface plasmon resonance based sensors*. Springer series on chemical sensors and biosensors., Springer, 2006.
- [10] J. Homola, S. S. Yee, and G. Gauglitz, "Surface plasmon resonance sensors: review," *Sensors and Actuators B*, vol. 54, pp. 3–15, 1999.
- [11] M. Kauranen and A. V. Zayats, "Nonlinear plasmonics," *Nature Photonics*, vol. 6, no. 11, pp. 737–748, 2012.

Bibliography

- [12] A. V. Zayats and I. I. Smolyaninov, "Near-field photonics: surface plasmon polaritons and localized surface plasmons," *Journal of Optics A: Pure and Applied Optics*, no. 4, p. S16, 2003.
- [13] J. N. Anker, W. P. Hall, O. Lyandres, N. C. Shah, J. Zhao, and R. P. Van Duyne, "Biosensing with plasmonic nanosensors," *Nature Materials*, vol. 7, no. 6, pp. 442–453, 2008.
- [14] F. J. Garcia-Vidal, J. Sanchez-Dehesa, A. Dechelette, E. Bustarret, T. Lopez-Rios, T. Fournier, and B. Pannetier, "Localized surface plasmons in lamellar metallic gratings," *Lightwave Technology, Journal of*, vol. 17, no. 11, pp. 2191–2195, 1999.
- [15] A. Haes and R. Duyne, "A unified view of propagating and localized surface plasmon resonance biosensors," *Analytical and Bioanalytical Chemistry*, vol. 379, no. 7-8, pp. 920–930, 2004.
- [16] K. M. Mayer and J. H. Hafner, "Localized surface plasmon resonance sensors," *Chemical Reviews*, vol. 111, no. 6, pp. 3828–3857, 2011.
- [17] S. G. Penn, L. He, and M. J. Natan, "Nanoparticles for bioanalysis," *Current Opinion in Chemical Biology*, vol. 7, no. 5, pp. 609–615, 2003.
- [18] E. Petryayeva and U. J. Krull, "Localized surface plasmon resonance: Nanostructures, bioassays and biosensing– a review," *Analytica Chimica Acta*, vol. 706, no. 1, pp. 8–24, 2011.
- [19] B. Sepulveda, P. C. Angelome, L. M. Lechuga, and L. M. Liz-Marzan, "LSPR-based nanobiosensors," *Nano Today*, vol. 4, no. 3, pp. 244–251, 2009.
- [20] A. Serra, E. Filippo, M. Re, M. Palmisano, M. Vittori-Antisari, A. Buccolieri, and D. Manno, "Non-functionalized silver nanoparticles for a localized surface plasmon resonance-based glucose sensor," *Nanotechnology*, vol. 20, no. 16, 2009.
- [21] L. J. Sherry, S.-H. Chang, G. C. Schatz, R. P. Van Duyne, B. J. Wiley, and Y. Xia, "Localized surface plasmon resonance spectroscopy of single silver nanocubes," *Nano Letters*, vol. 5, no. 10, pp. 2034–2038, 2005.
- [22] L. J. Sherry, R. Jin, C. A. Mirkin, G. C. Schatz, and R. P. Van Duyne, "Localized surface plasmon resonance spectroscopy of single silver triangular nanoprisms," *Nano Letters*, vol. 6, no. 9, pp. 2060–2065, 2006.
- [23] P. West, S. Ishii, G. Naik, N. Emani, V. Shalaev, and A. Boltasseva, "Searching for better plasmonic materials," *Laser & Photonics Reviews*, vol. 4, no. 6, pp. 795–808, 2010.
- [24] W. A. Murray and W. L. Barnes, "Plasmonic materials," *Advanced Materials*, vol. 19, no. 22, pp. 3771–3782, 2007.

-
- [25] K. Diest, V. Liberman, D. M. Lennon, P. B. Welander, and M. Rothschild, "Aluminum plasmonics: Optimization of plasmonic properties using liquid-prism-coupled ellipsometry," *Optics Express*, vol. 21, no. 23, pp. 28638–28650, 2013.
- [26] M. W. Knight, N. S. King, L. Liu, H. O. Everitt, P. Nordlander, and N. J. Halas, "Aluminum for plasmonics," *ACS Nano*, vol. 8, no. 1, pp. 834–840, 2014.
- [27] M. W. Knight, L. Liu, Y. Wang, L. Brown, S. Mukherjee, N. S. King, H. O. Everitt, P. Nordlander, and N. J. Halas, "Aluminum plasmonic nanoantennas," *Nano Letters*, vol. 12, no. 11, pp. 6000–6004, 2012.
- [28] G. V. Naik, V. M. Shalaev, and A. Boltasseva, "Alternative plasmonic materials: Beyond gold and silver," *Advanced Materials*, vol. 25, no. 24, pp. 3264–3294, 2013.
- [29] F. D. Stefani, K. Vasilev, N. Bocchio, N. Stoyanova, and M. Kreiter, "Surface-plasmon-mediated single-molecule fluorescence through a thin metallic film," *Physical Review Letters*, vol. 94, p. 023005, 2005.
- [30] M. Achermann, "Exciton-plasmon interactions in metal-semiconductor nanostructures," *The Journal of Physical Chemistry Letters*, vol. 1, no. 19, pp. 2837–2843, 2010.
- [31] K. Aslan, M. Wu, J. R. Lakowicz, and C. D. Geddes, "Fluorescent core-shell Ag@SiO₂ Nanocomposites for metal-enhanced fluorescence and single nanoparticle sensing platforms," *Journal of the American Chemical Society*, vol. 129, no. 6, pp. 1524–1525, 2007.
- [32] R. Beams, D. Smith, T. W. Johnson, S.-H. Oh, L. Novotny, and A. N. Vamivakas, "Nanoscale fluorescence lifetime imaging of an optical antenna with a single diamond nv center," *Nano Letters*, vol. 13, no. 8, pp. 3807–3811, 2013.
- [33] Y. Fu, J. Zhang, and J. R. Lakowicz, "Plasmon-enhanced fluorescence from single fluorophores end-linked to gold nanorods," *Journal of the American Chemical Society*, vol. 132, no. 16, pp. 5540–5541, 2010.
- [34] C. M. Galloway, M. P. Kreuzer, S. S. Acimovic, G. Volpe, M. Correia, S. B. Petersen, M. T. Neves-Petersen, and R. Quidant, "Plasmon-assisted delivery of single nano-objects in an optical hot spot," *Nano Letters*, vol. 13, no. 9, pp. 4299–4304, 2013.
- [35] M. Geiselmann, R. Marty, J. Renger, F. J. García de Abajo, and R. Quidant, "Deterministic optical-near-field-assisted positioning of nitrogen-vacancy centers," *Nano Letters*, vol. 14, no. 3, pp. 1520–1525, 2014.
- [36] A. M. Kern and O. J. F. Martin, "Excitation and reemission of molecules near realistic plasmonic nanostructures," *Nano Letters*, vol. 11, no. 2, pp. 482–487, 2011.
- [37] S. Kuhn, U. Hakanson, L. Rogobete, and V. Sandoghdar, "Enhancement of single-molecule fluorescence using a gold nanoparticle as an optical nanoantenna," *Physical Review Letters*, vol. 97, p. 017402, 2006.

- [38] J. Lakowicz and Y. Fu, "Modification of single molecule fluorescence near metallic nanostructures," *Laser & Photonics Reviews*, vol. 3, no. 1-2, pp. 221–232, 2009.
- [39] J. R. Lakowicz, K. Ray, M. Chowdhury, H. Szmazinski, Y. Fu, J. Zhang, and K. Nowaczyk, "Plasmon-controlled fluorescence: A new paradigm in fluorescence spectroscopy," *Analyst*, vol. 133, pp. 1308–1346, 2008.
- [40] E. C. Le Ru, P. G. Etchegoin, J. Grand, N. Felidj, J. Aubard, and G. Levi, "Mechanisms of spectral profile modification in surface-enhanced fluorescence," *The Journal of Physical Chemistry C*, vol. 111, no. 44, pp. 16076–16079, 2007.
- [41] T. Ming, H. Chen, R. Jiang, Q. Li, and J. Wang, "Plasmon-controlled fluorescence: Beyond the intensity enhancement," *The Journal of Physical Chemistry Letters*, vol. 3, no. 2, pp. 191–202, 2012.
- [42] T. Ming, L. Zhao, Z. Yang, H. Chen, L. Sun, J. Wang, and C. Yan, "Strong polarization dependence of plasmon-enhanced fluorescence on single gold nanorods," *Nano Letters*, vol. 9, no. 11, pp. 3896–3903, 2009.
- [43] O. L. Muskens, V. Giannini, J. A. Sanchez-Gil, and J. Gomez Rivas, "Strong enhancement of the radiative decay rate of emitters by single plasmonic nanoantennas," *Nano Letters*, vol. 7, no. 9, pp. 2871–2875, 2007.
- [44] M. Ringler, A. Schwemer, M. Wunderlich, A. Nichtl, K. Kurzinger, T. A. Klar, and J. Feldmann, "Shaping emission spectra of fluorescent molecules with single plasmonic nanoresonators," *Physical Review Letters*, vol. 100, p. 203002, 2008.
- [45] S. Schietinger, M. Barth, T. Aichele, and O. Benson, "Plasmon-enhanced single photon emission from a nanoassembled metal-diamond hybrid structure at room temperature," *Nano Letters*, vol. 9, no. 4, pp. 1694–1698, 2009.
- [46] J. Seelig, K. Leslie, A. Renn, S. Kuhn, V. Jacobsen, M. van de Corput, C. Wyman, and V. Sandoghdar, "Nanoparticle-induced fluorescence lifetime modification as nanoscopic ruler: A demonstration at the single molecule level," *Nano Letters*, vol. 7, no. 3, pp. 685–689, 2007.
- [47] F. Tam, G. P. Goodrich, B. R. Johnson, and N. J. Halas, "Plasmonic enhancement of molecular fluorescence," *Nano Letters*, vol. 7, no. 2, pp. 496–501, 2007.
- [48] J. Ando, K. Fujita, N. I. Smith, and S. Kawata, "Dynamic SERS imaging of cellular transport pathways with endocytosed gold nanoparticles," *Nano Letters*, vol. 11, no. 12, pp. 5344–5348, 2011.
- [49] G. Chen, Y. Wang, M. Yang, J. Xu, S. J. Goh, M. Pan, and H. Chen, "Measuring ensemble-averaged surface-enhanced Raman scattering in the hotspots of colloidal nanoparticle dimers and trimers," *Journal of the American Chemical Society*, vol. 132, no. 11, pp. 3644–3645, 2010.

-
- [50] W. E. Doering and S. Nie, "Single-molecule and single-nanoparticle SERS: Examining the roles of surface active sites and chemical enhancement," *The Journal of Physical Chemistry B*, vol. 106, no. 2, pp. 311–317, 2002.
- [51] P. G. Etchegoin and E. C. Le Ru, "A perspective on single molecule SERS: current status and future challenges," *Physical Chemistry Chemical Physics*, vol. 10, pp. 6079–6089, 2008.
- [52] D. Graham and R. Goodacre, "Chemical and bioanalytical applications of surface enhanced Raman scattering spectroscopy," *Chemical Society Reviews*, vol. 37, pp. 883–884, 2008.
- [53] J. Kneipp, H. Kneipp, and K. Kneipp, "SERS a single-molecule and nanoscale tool for bioanalytics," *Chemical Society Reviews*, vol. 37, pp. 1052–1060, 2008.
- [54] J. Kneipp, H. Kneipp, B. Wittig, and K. Kneipp, "Following the dynamics of pH in endosomes of live cells with SERS nanosensors," *The Journal of Physical Chemistry C*, vol. 114, no. 16, pp. 7421–7426, 2010.
- [55] K. Kneipp, H. Kneipp, V. B. Kartha, R. Manoharan, G. Deinum, I. Itzkan, R. R. Dasari, and M. S. Feld, "Detection and identification of a single DNA base molecule using surface-enhanced Raman scattering (SERS)," *Phys. Rev. E*, vol. 57, pp. R6281–R6284, 1998.
- [56] K. Kneipp, Y. Wang, H. Kneipp, L. T. Perelman, I. Itzkan, R. R. Dasari, and M. S. Feld, "Single molecule detection using surface-enhanced Raman scattering (SERS)," *Physical Review Letters*, vol. 78, pp. 1667–1670, 1997.
- [57] E. C. Le Ru, M. Meyer, and P. G. Etchegoin, "Proof of single-molecule sensitivity in surface enhanced Raman scattering (SERS) by means of a two-analyte technique," *The Journal of Physical Chemistry B*, vol. 110, no. 4, pp. 1944–1948, 2006.
- [58] X. Lu, M. Rycenga, S. E. Skrabalak, B. Wiley, and Y. Xia, "Chemical synthesis of novel plasmonic nanoparticles," *Annual Review of Physical Chemistry*, vol. 60, no. 1, pp. 167–192, 2009.
- [59] G. McNay, D. Eustace, W. E. Smith, K. Faulds, and D. Graham, "Surface-enhanced raman scattering (SERS) and surface-enhanced resonance raman scattering (SERRS): A review of applications," *Applied Spectroscopy*, vol. 65, no. 8, pp. 825–837, 2011.
- [60] M. J. Mulvihill, X. Y. Ling, J. Henzie, and P. Yang, "Anisotropic etching of silver nanoparticles for plasmonic structures capable of single-particle SERS," *Journal of the American Chemical Society*, vol. 132, no. 1, pp. 268–274, 2010.
- [61] S. Nie and S. R. Emory, "Probing single molecules and single nanoparticles by surface-enhanced Raman scattering," *Science*, vol. 275, no. 5303, pp. 1102–1106, 1997.

Bibliography

- [62] A. Otto, "What is observed in single molecule SERS, and why?," *Journal of Raman Spectroscopy*, vol. 33, no. 8, pp. 593–598, 2002.
- [63] X. Qian, J. Li, and S. Nie, "Stimuli-responsive sers nanoparticles: Conformational control of plasmonic coupling and surface raman enhancement," *Journal of the American Chemical Society*, vol. 131, no. 22, pp. 7540–7541, 2009.
- [64] X. Qian, X. Zhou, and S. Nie, "Surface-enhanced Raman nanoparticle beacons based on bioconjugated gold nanocrystals and long range plasmonic coupling," *Journal of the American Chemical Society*, vol. 130, no. 45, pp. 14934–14935, 2008.
- [65] X.-M. Qian and S. M. Nie, "Single-molecule and single-nanoparticle sers: from fundamental mechanisms to biomedical applications," *Chemical Society Reviews*, vol. 37, pp. 912–920, 2008.
- [66] L. Rodriguez-Lorenzo, R. A. Alvarez-Puebla, I. Pastoriza-Santos, S. Mazzucco, O. Staphan, M. Kociak, L. M. Liz-Marzan, and F. J. Garcia de Abajo, "Zeptomol detection through controlled ultrasensitive surface-enhanced Raman scattering," *Journal of the American Chemical Society*, vol. 131, no. 13, pp. 4616–4618, 2009.
- [67] S. Schlucker, "SERS microscopy: Nanoparticle probes and biomedical applications," *ChemPhysChem*, vol. 10, no. 9-10, pp. 1344–1354, 2009.
- [68] S. M. Stranahan and K. A. Willets, "Super-resolution optical imaging of single-molecule SERS hot spots," *Nano Letters*, vol. 10, no. 9, pp. 3777–3784, 2010.
- [69] F. Svedberg, Z. Li, H. Xu, and M. Käll, "Creating hot nanoparticle pairs for surface-enhanced Raman spectroscopy through optical manipulation," *Nano Letters*, vol. 6, no. 12, pp. 2639–2641, 2006.
- [70] X. Wang, X. Qian, J. J. Beitler, Z. G. Chen, F. R. Khuri, M. M. Lewis, H. J. C. Shin, S. Nie, and D. M. Shin, "Detection of circulating tumor cells in human peripheral blood using surface-enhanced Raman scattering nanoparticles," *Cancer Research*, vol. 71, no. 5, pp. 1526–1532, 2011.
- [71] H. Xu, E. J. Bjerneld, M. Käll, and L. Borjesson, "Spectroscopy of single Hemoglobin molecules by surface enhanced Raman scattering," *Physical Review Letters*, vol. 83, pp. 4357–4360, 1999.
- [72] W. Ahn, Y. Qiu, and B. M. Reinhard, "Generation of scalable quasi-3d metallo-dielectric SERS substrates through orthogonal reactive ion etching," *J. Mater. Chem. C*, vol. 1, pp. 3110–3118, 2013.
- [73] B. Yan, Y. Hong, T. Chen, and B. M. Reinhard, "Monitoring enzymatic degradation of pericellular matrices through SERS stamping," *Nanoscale*, vol. 4, pp. 3917–3925, 2012.

- [74] E. B. Dickerson, E. C. Dreaden, X. Huang, I. H. El-Sayed, H. Chu, S. Pushpanketh, J. F. McDonald, and M. A. El-Sayed, "Gold nanorod assisted near-infrared plasmonic photothermal therapy (PPTT) of squamous cell carcinoma in mice," *Cancer Letters*, vol. 269, no. 1, pp. 57–66, 2008.
- [75] L. R. Hirsch, R. J. Stafford, J. A. Bankson, S. R. Sershen, B. Rivera, R. E. Price, J. D. Hazle, N. J. Halas, and J. L. West, "Nanoshell-mediated near-infrared thermal therapy of tumors under magnetic resonance guidance," *Proceedings of the National Academy of Sciences*, vol. 100, no. 23, pp. 13549–13554, 2003.
- [76] X. Huang, P. Jain, I. El-Sayed, and M. El-Sayed, "Plasmonic photothermal therapy (PPTT) using gold nanoparticles," *Lasers in Medical Science*, vol. 23, no. 3, pp. 217–228, 2008.
- [77] S. Lal, S. E. Clare, and N. J. Halas, "Nanoshell-enabled photothermal cancer therapy: Impending clinical impact," *Accounts of Chemical Research*, vol. 41, no. 12, pp. 1842–1851, 2008.
- [78] D. Pissuwan, S. M. Valenzuela, and M. B. Cortie, "Therapeutic possibilities of plasmonically heated gold nanoparticles," *Trends in Biotechnology*, vol. 24, no. 2, pp. 62–67, 2006.
- [79] J. L. West and N. J. Halas, "Engineered nanomaterials for biophotonics applications: Improving sensing, imaging, and therapeutics," *Annual Review of Biomedical Engineering*, vol. 5, no. 1, pp. 285–292, 2003.
- [80] E. A. Smith, W. D. Thomas, L. L. Kiessling, and R. M. Corn, "Surface plasmon resonance imaging studies of protein-carbohydrate interactions," *Journal of the American Chemical Society*, vol. 125, no. 20, pp. 6140–6148, 2003.
- [81] J. M. Brockman, B. P. Nelson, and R. M. Corn, "Surface plasmon resonance imaging measurements of ultrathin ORganic films," *Annual Review of Physical Chemistry*, vol. 51, no. 1, pp. 41–63, 2000.
- [82] X. Yu, J. Wang, A. Feizpour, and B. M. Reinhard, "Illuminating the lateral organization of cell-surface CD24 and CD44 through plasmon coupling between Au nanoparticle immunolabels," *Analytical Chemistry*, vol. 85, no. 3, pp. 1290–1294, 2013.
- [83] G. Rong and B. M. Reinhard, "Monitoring the size and lateral dynamics of erbb1 enriched membrane domains through live cell plasmon coupling microscopy," *PLoS ONE*, vol. 7, no. 3, p. e34175, 2012.
- [84] J. Wang, S. V. Boriskina, H. Wang, and B. M. Reinhard, "Illuminating epidermal growth factor receptor densities on filopodia through plasmon coupling," *ACS Nano*, vol. 5, no. 8, pp. 6619–6628, 2011.
- [85] H. Wang, G. Rong, B. Yan, L. Yang, and B. M. Reinhard, "Optical sizing of immunolabel clusters through multispectral plasmon coupling microscopy," *Nano Letters*, vol. 11, no. 2, pp. 498–504, 2011.

Bibliography

- [86] X. Yu, A. Feizpour, N.-G. P. Ramirez, L. Wu, H. Akiyama, F. Xu, S. Gummuluru, and B. M. Reinhard, "Glycosphingolipid-functionalized nanoparticles recapitulate CD169-dependent HIV-1 uptake and trafficking in dendritic cells," *Nature Communications*, vol. 5, pp. 1–12, 2014.
- [87] L. Huang, S. J. Maerkl, and O. J. Martin, "Integration of plasmonic trapping in a microfluidic environment," *Optics Express*, vol. 17, no. 8, pp. 6018–6024, 2009.
- [88] A. Lovera and O. J. F. Martin, "Plasmonic trapping with realistic dipole nanoantennas: Analysis of the detection limit," *Applied Physics Letters*, vol. 99, no. 15, pp. –, 2011.
- [89] A. A. E. Saleh and J. A. Dionne, "Toward efficient optical trapping of sub-10-nm particles with coaxial plasmonic apertures," *Nano Letters*, vol. 12, no. 11, pp. 5581–5586, 2012.
- [90] K. C. Toussaint, M. Liu, M. Pelton, J. Pesic, M. J. Guffey, P. Guyot-Sionnest, and N. F. Scherer, "Plasmon resonance-based optical trapping of single and multiple Au nanoparticles," *Optics Express*, vol. 15, no. 19, pp. 12017–12029, 2007.
- [91] K. Wang, E. Schonbrun, P. Steinvurzel, and K. B. Crozier, "Scannable plasmonic trapping using a gold stripe," *Nano Letters*, vol. 10, no. 9, pp. 3506–3511, 2010.
- [92] W. Zhang, L. Huang, C. Santschi, and O. J. F. Martin, "Trapping and sensing 10 nm metal nanoparticles using plasmonic dipole antennas," *Nano Letters*, vol. 10, no. 3, pp. 1006–1011, 2010.
- [93] M. Besenicar, P. Macek, J. H. Lakey, and G. Anderluh, "Surface plasmon resonance in protein-membrane interactions," *Chemical and Physics of Lipids*, vol. 141, pp. 169–178, 2006.
- [94] S. Boussaad, J. Pean, and N. J. Tao, "High-resolution multiwavelength surface plasmon resonance spectroscopy for probing conformational and electronic changes in redox proteins," *Analytical Chemistry*, vol. 72, pp. 222–226, 2000.
- [95] E. Descrovi, V. Paeder, L. Vaccaro, and H. P. Herzig, "A virtual optical probe based on localized surface plasmon polaritons," *Optics Express*, vol. 13, no. 18, p. 7017, 2005.
- [96] R. J. Green, R. A. Frazier, K. M. Shakesheff, M. C. Davies, C. J. Roberts, and S. J. B. Tendler, "Surface plasmon resonance analysis of dynamic biological interactions with biomaterials," *Biomaterials*, vol. 21, pp. 1823–1835, 2000.
- [97] A. Hanning, J. Roeraade, J. J. Delrow, and R. Jorgenson, "Enhanced sensitivity of wavelength modulated surface plasmon resonance devices using dispersion from a die solution," *Sensors and Actuators B*, vol. 54, pp. 25–36, 1999.
- [98] H. Kano and S. Kawata, "Surface-plasmon sensor for absorption-sensitivity enhancement," *Applied Optics*, vol. 33, no. 22, pp. 5166–5170, 1994.

-
- [99] K. Kurihara and K. Suzuki, "Theoretical understanding of an absorption-based surface plasmon resonance sensor based on kretschmann's configuration," *Analytical Chemistry*, vol. 74, pp. 696–701, 2002.
- [100] X. Liu, D. Song, Q. Zhang, Y. Tian, L. Ding, and H. Zhang, "Wavelength-modulation surface plasmon sensor," *Trends in Analytical Chemistry*, vol. 24, no. 10, pp. 887–893, 2005.
- [101] M. Nakkach, P. Lecaruyer, F. Bardin, J. Sakly, Z. B. Lakhdar, and M. Canva, "Absorption and related optical dispersion effects on the spectral response of a surface plasmon resonance sensor," *Applied Optics*, vol. 47, no. 33, pp. 6177–6182, 2008.
- [102] S. Scarano, M. Mascini, A. P. Turner, and M. Minunni, "Surface plasmon resonance imaging for affinity-based biosensors," *Biosensors & Bioelectronics*, vol. 25, pp. 957–966, 2010.
- [103] M. Vala, K. Chadt, M. Pilarik, and J. Homola, "High-performance compact SPR sensor for multi-analyte sensing," *Sensors and Actuators B: Chemical*, vol. 148, pp. 544–549, 2010.
- [104] S. Wang, S. Boussaad, and N. J. Tao, "Surface plasmon resonance enhanced optical absorption spectroscopy for studying molecular adsorbates," *Review of Scientific Instruments*, vol. 72, no. 7, pp. 3055–3060, 2001.
- [105] Y. Yanase, T. Hiragun, S. Kaneko, H. J. Gould, M. W. Greaves, and M. Hide, "Detection of refractive index changes in individual living cells by means of surface plasmon resonance imaging," *Biosensors & Bioelectronics*, vol. 26, pp. 674–681, 2010.
- [106] E. M. Larsson, C. Langhammer, I. Zoric, and B. Kasemo, "Nanoplasmonic probes of catalytic reactions," *Science*, vol. 326, no. 5956, pp. 1091–1094, 2009.
- [107] N. Liu, M. L. Tang, M. Hentschel, H. Giessen, and A. P. Alivisatos, "Nanoantenna-enhanced gas sensing in a single tailored nanofocus," *Nature Materials*, vol. 10, no. 8, pp. 631–636, 2011.
- [108] J. Yu, H. Tao, and B. Cheng, "In situ monitoring of heterogeneous catalytic reactions," *ChemPhysChem*, vol. 11, no. 8, pp. 1617–1618, 2010.
- [109] E. M. Larsson, J. Alegret, M. Käll, and D. S. Sutherland, "Sensing characteristics of NIR localized surface plasmon resonances in gold nanorings for application as ultrasensitive biosensors," *Nano Letters*, vol. 7, no. 5, pp. 1256–1263, 2007.
- [110] T. Rindzevicius, Y. Alaverdyan, A. Dahlin, F. Hook, D. S. Sutherland, and M. Käll, "Plasmonic sensing characteristics of single nanometric holes," *Nano Letters*, vol. 5, no. 11, pp. 2335–2339, 2005.

Bibliography

- [111] M. Wersall, R. Verre, M. Svedendahl, P. Johansson, M. Käll, and T. Shegai, "Directional nanoplasmonic antennas for self-referenced refractometric molecular analysis," *The Journal of Physical Chemistry C*, vol. 118, no. 36, pp. 21075–21080, 2014.
- [112] S. Chen, M. Svedendahl, T. J. Antosiewicz, and M. Käll, "Plasmon-enhanced enzyme-linked immunosorbent assay on large arrays of individual particles made by electron beam lithography," *ACS Nano*, vol. 7, no. 10, pp. 8824–8832, 2013.
- [113] L. Wu and B. M. Reinhard, "Probing subdiffraction limit separations with plasmon coupling microscopy: Concepts and applications," *Chem. Soc. Rev.*, vol. 43, pp. 3884–3897, 2014.
- [114] J. Wang, X. Yu, S. V. Boriskina, and B. M. Reinhard, "Quantification of differential ErbB1 and ErbB2: Cell surface expression and spatial nanoclustering through plasmon coupling," *Nano Letters*, vol. 12, no. 6, pp. 3231–3237, 2012.
- [115] B. Yan, S. V. Boriskina, and B. M. Reinhard, "Design and implementation of noble metal nanoparticle cluster arrays for plasmon enhanced biosensing," *The Journal of Physical Chemistry C*, vol. 115, no. 50, pp. 24437–24453, 2011.
- [116] W. Zhang, H. Fischer, T. Schmid, R. Zenobi, and O. J. F. Martin, "Mode-selective surface-enhanced Raman spectroscopy using nanofabricated plasmonic dipole antennas," *Journal of Physical Chemistry C*, vol. 113, no. 33, pp. 14672–14675, 2009.
- [117] H.-D. Yu, M. D. Regulacio, E. Ye, and M.-Y. Han, "Chemical routes to top-down nanofabrication," *Chemical Society Reviews*, vol. 42, pp. 6006–6018, 2013.
- [118] F. Watt, A. A. Bettiol, J. A. V. Kan, E. J. Teo, and M. B. H. Breese, "Ion beam lithography and nanofabrication: A review," *International Journal of Nanoscience*, vol. 04, no. 03, pp. 269–286, 2005.
- [119] J. Henzie, J. Lee, M. H. Lee, W. Hasan, and T. W. Odom, "Nanofabrication of plasmonic structures," *Annual Review of Physical Chemistry*, vol. 60, no. 1, pp. 147–165, 2009.
- [120] E. M. Hicks, S. Zou, G. C. Schatz, K. G. Spears, R. P. Van Duyne, L. Gunnarson, T. Rindzevicius, B. Kasemo, and M. Käll, "Controlling plasmon line shapes through diffractive coupling in linear arrays of cylindrical nanoparticles fabricated by electron beam lithography," *Nano Letters*, vol. 5, no. 6, pp. 1065–1070, 2005.
- [121] M. Svedendahl, P. Johansson, and M. Käll, "Complete light annihilation in an ultrathin layer of gold nanoparticles," *Nano Letters*, vol. 13, no. 7, pp. 3053–3058, 2013.
- [122] R. Verre, T. J. Antosiewicz, M. Svedendahl, K. Lodewijks, T. Shegai, and M. Käll, "Quasi-isotropic surface plasmon polariton generation through near-field coupling to a penrose pattern of silver nanoparticles," *ACS Nano*, vol. 8, no. 9, pp. 9286–9294, 2014.

- [123] T. Chen, M. Pourmand, A. Feizpour, B. Cushman, and B. M. Reinhard, "Tailoring plasmon coupling in self-assembled one-dimensional au nanoparticle chains through simultaneous control of size and gap separation," *The Journal of Physical Chemistry Letters*, vol. 4, no. 13, pp. 2147–2152, 2013.
- [124] Y. Hong, M. Pourmand, S. V. Boriskina, and B. M. Reinhard, "Enhanced light focusing in self-assembled optoplasmonic clusters with subwavelength dimensions," *Advanced Materials*, vol. 25, no. 1, pp. 115–119, 2013.
- [125] A. J. Pasquale, B. M. Reinhard, and L. Dal Negro, "Concentric necklace nanolenses for optical near-field focusing and enhancement," *ACS Nano*, vol. 6, no. 5, pp. 4341–4348, 2012.
- [126] C. Forestiere, A. J. Pasquale, A. Capretti, G. Miano, A. Tamburrino, S. Y. Lee, B. M. Reinhard, and L. Dal Negro, "Genetically engineered plasmonic nanoarrays," *Nano Letters*, vol. 12, no. 4, pp. 2037–2044, 2012.
- [127] A. J. Pasquale, B. M. Reinhard, and L. Dal Negro, "Engineering photonic-plasmonic coupling in metal nanoparticle necklaces," *ACS Nano*, vol. 5, no. 8, pp. 6578–6585, 2011.
- [128] E. Prodan, C. Radloff, N. J. Halas, and P. Nordlander, "A hybridization model for the plasmon response of complex nanostructures," *Science*, vol. 302, no. 5644, pp. 419–422, 2003.
- [129] J. A. Fan, C. Wu, K. Bao, J. Bao, R. Bardhan, N. J. Halas, V. N. Manoharan, P. Nordlander, G. Shvets, and F. Capasso, "Self-assembled plasmonic nanoparticle clusters," *Science*, vol. 328, no. 5982, pp. 1135–1138, 2010.
- [130] D. P. Fromm, A. Sundaramurthy, P. J. Schuck, G. Kino, and W. E. Moerner, "Gap-dependent optical coupling of single "bowtie" nanoantennas resonant in the visible," *Nano Letters*, vol. 4, no. 5, pp. 957–961, 2004.
- [131] A. M. Funston, C. Novo, T. J. Davis, and P. Mulvaney, "Plasmon coupling of gold nanorods at short distances and in different geometries," *Nano Letters*, vol. 9, no. 4, pp. 1651–1658, 2009.
- [132] N. Grillet, D. Manchon, F. Bertorelle, C. Bonnet, M. Broyer, E. Cottancin, J. Lerme, M. Hiltenkamp, and M. Pellarin, "Plasmon coupling in silver nanocube dimers: Resonance splitting induced by edge rounding," *ACS Nano*, vol. 5, no. 12, pp. 9450–9462, 2011.
- [133] N. J. Halas, S. Lal, W.-S. Chang, S. Link, and P. Nordlander, "Plasmons in strongly coupled metallic nanostructures," *Chemical Reviews*, vol. 111, no. 6, pp. 3913–3961, 2011.
- [134] M.-D. He, Z.-Q. Gong, S. Li, Y.-F. Luo, J.-Q. Liu, X. Chen, and W. Lu, "Coupling of localized surface plasmon modes in compound structure with metallic nanoparticle and nanohole arrays," *Journal of Applied Physics*, vol. 108, no. 9, p. 093520, 2010.

Bibliography

- [135] P. K. Jain and M. A. El-Sayed, "Surface plasmon coupling and its universal size scaling in metal nanostructures of complex geometry: Elongated particle pairs and nanosphere trimers," *Journal of Physical Chemistry C*, vol. 112, no. 13, pp. 4954–4960, 2008.
- [136] P. K. Jain and M. A. El-Sayed, "Universal scaling of plasmon coupling in metal nanostructures: Extension from particle pairs to nanoshells," *Nano Letters*, vol. 7, no. 9, pp. 2854–2858, 2007.
- [137] P. K. Jain, S. Eustis, and M. A. El-Sayed, "Plasmon coupling in nanorod assemblies: Optical absorption, discrete dipole approximation simulation, and exciton-coupling model," *Journal of Physical Chemistry B*, vol. 110, no. 37, pp. 18243–18253, 2006.
- [138] P. K. Jain, W. Huang, and M. A. El-Sayed, "On the universal scaling behavior of the distance decay of plasmon coupling in metal nanoparticle pairs: A plasmon ruler equation," *Nano Letters*, vol. 7, no. 7, pp. 2080–2088, 2007.
- [139] S. Kim, K. L. Shuford, H.-M. Bok, S. K. Kim, and S. Park, "Intraparticle surface plasmon coupling in quasi-one-dimensional nanostructures," *Nano Letters*, vol. 8, no. 3, pp. 800–804, 2008.
- [140] N. S. King, M. W. Knight, N. Large, A. M. Goodman, P. Nordlander, and N. J. Halas, "Orienting nanoantennas in three dimensions to control light scattering across a dielectric interface," *Nano Letters*, vol. 13, no. 12, pp. 5997–6001, 2013.
- [141] A. O. Pinchuk and G. C. Schatz, "Nanoparticle optical properties: Far- and near-field electrodynamic coupling in a chain of silver spherical nanoparticles," *Materials Science and Engineering: B*, vol. 149, no. 3, pp. 251–258, 2007.
- [142] P. Pramod and K. G. Thomas, "Plasmon coupling in dimers of Au nanorods," *Advanced Materials*, vol. 20, no. 22, pp. 4300–4305, 2008.
- [143] E. Prodan, P. Nordlander, and N. J. Halas, "Electronic structure and optical properties of gold nanoshells," *Nano Letters*, vol. 3, no. 10, pp. 1411–1415, 2003.
- [144] C. Sonnichsen, B. M. Reinhard, J. Liphardt, and A. P. Alvisatos, "A molecular ruler based on plasmon coupling of single gold and silver nanoparticles," *Nature Biotechnology*, vol. 23, no. 6, pp. 741–745, 2005.
- [145] A. S. Urban, X. Shen, Y. Wang, N. Large, H. Wang, M. W. Knight, P. Nordlander, H. Chen, and N. J. Halas, "Three-dimensional plasmonic nanoclusters," *Nano Letters*, vol. 13, no. 9, pp. 4399–4403, 2013.
- [146] K.-Y. Wu, X.-L. Cheng, and L. P. Lee, "Intra-particle coupling and plasmon tuning of multilayer Au/dielectric/Au nanocrescents adhered to a dielectric cylinder," *Nanotechnology*, vol. 23, no. 5, p. 055201, 2012.
- [147] A. Artar, A. A. Yanik, and H. Altug, "Directional double Fano resonances in plasmonic hetero-oligomers," *Nano Letters*, vol. 11, pp. 3694–3700, 2011.

-
- [148] H. Chen, L. Shao, Y. C. Man, C. Zhao, J. Wang, and B. Yang, "Fano resonance in (gold core) - (dielectric shell) nanostructures without symmetry breaking," *Small*, vol. 8, no. 10, pp. 1503–1509, 2012.
- [149] D. Dregely, M. Hentschel, and H. Giessen, "Excitation and tuning of higher-order fano resonances in plasmonic oligomer clusters," *ACS Nano*, vol. 5, no. 10, pp. 8202–8211, 2011.
- [150] Y. H. Fu, J. B. Zhang, Y. F. Yu, and B. Luk'yanchuk, "Generating and manipulating higher order fano resonances in dual-disk ring plasmonic nanostructures," *ACS Nano*, vol. 6, no. 6, pp. 5130–5137, 2012.
- [151] F. Hao, Y. Sonnefraud, P. V. Dorpe, S. A. Maier, N. J. Halas, and P. Nordlander, "Symmetry breaking in plasmonic nanocavities: Subradiant LSPR sensing and a tunable fano resonance," *Nano Letters*, vol. 8, no. 11, pp. 3983–3988, 2008.
- [152] M. Hentschel, M. Saliba, R. Vogelgesang, H. Giessen, A. P. Alivisatos, and N. Liu, "Transition from isolated to collective modes in plasmonic oligomers," *Nano Letters*, vol. 10, no. 7, pp. 2721–2726, 2010.
- [153] S.-D. Liu, Z. Yang, R.-P. Liu, and X.-Y. Li, "Multiple Fano resonances in plasmonic heptamer clusters composed of split nanorings," *ACS Nano*, vol. 6, no. 7, pp. 6260–6271, 2012.
- [154] F. Lopez-Tejeira, R. Paniagua-Dominguez, and J. A. Sanchez-Gil, "High-performance nanosensors based on plasmonic Fano-like interference: Probing refractive index with individual nanorice and nanobelts," *ACS Nano*, vol. 6, no. 10, pp. 8989–8996, 2012.
- [155] A. Lovera, B. Gallinet, P. Nordlander, and O. J. F. Martin, "Mechanisms of Fano resonances in coupled plasmonic systems," *ACS Nano*, vol. 7, no. 5, pp. 4527–4536, 2013.
- [156] A. E. Miroshnichenko, S. Flach, and Y. S. Kivshar, "Fano resonances in nanoscale structures," *Reviews of Modern Physics*, vol. 82, no. 3, pp. 2257–2298, 2010.
- [157] T. Pakizeh, C. Langhammer, I. Zoric, P. Apell, and M. Käll, "Intrinsic Fano interference of localized plasmons in pd nanoparticles," *Nano Letters*, vol. 9, no. 2, pp. 882–886, 2009.
- [158] M. Rahmani, B. Luk'yanchuk, and M. Hong, "Fano resonance in novel plasmonic nanostructures," *Laser & Photonics Reviews*, vol. 7, no. 3, pp. 329–349, 2012.
- [159] B. Luk'yanchuk, N. I. Zheludev, S. A. Maier, N. J. Halas, P. Nordlander, H. Giessen, and C. T. Chong, "The Fano resonance in plasmonic nanostructures and metamaterials," *Nature Materials*, vol. 9, no. 9, pp. 707–715, 2010.
- [160] A. Ridolfo, R. Saija, S. Savasta, P. H. Jones, M. A. Iati, and O. M. Marago, "Fano-Doppler laser cooling of hybrid nanostructures," *ACS Nano*, vol. 5, no. 9, pp. 7354–7361, 2011.

- [161] Y. Sonnefraud, N. Verellen, H. Sobhani, G. A. E. Vandenbosch, V. V. Moshchalkov, P. Van Dorpe, P. Nordlander, and S. A. Maier, "Experimental realization of subradiant, superradiant, and Fano resonances in ring/disk plasmonic nanocavities," *ACS Nano*, vol. 4, no. 3, p. 7, 2010.
- [162] K. Thyagarajan, J. Butet, and O. J. F. Martin, "Augmenting second harmonic generation using Fano resonances in plasmonic systems," *Nano Letters*, vol. 13, no. 4, pp. 1847–1851, 2013.
- [163] N. Verellen, Y. Sonnefraud, H. Sobhani, F. Hao, V. V. Moshchalkov, P. Van Dorpe, P. Nordlander, and S. A. Maier, "Fano resonances in individual coherent plasmonic nanocavities," *Nano Letters*, vol. 9, no. 4, pp. 1663–1667, 2009.
- [164] Y. D. Chong, L. Ge, H. Cao, and A. D. Stone, "Coherent perfect absorbers: Time-reversed lasers," *Physical Review Letters*, vol. 105, p. 053901, 2010.
- [165] W. Wan, Y. Chong, L. Ge, H. Noh, A. D. Stone, and H. Cao, "Time-reversed lasing and interferometric control of absorption," *Science*, vol. 331, no. 6019, pp. 889–892, 2011.
- [166] T. Ambjörnsson, G. Mukhopadhyay, S. P. Apell, and M. Käll, "Resonant coupling between localized plasmons and anisotropic molecular coatings in ellipsoidal metal nanoparticles," *Physical Review B*, vol. 73, 2006.
- [167] N. T. Fofang, T.-H. Park, O. Neumann, N. A. Mirin, P. Nordlander, and N. J. Halas, "Plexitonic nanoparticles: Plasmon-exciton coupling in nanoshell-J-aggregate complexes," *Nano Letters*, vol. 8, no. 10, pp. 3481–3487, 2008.
- [168] T. Ming, L. Zhao, M. Xiao, and J. Wang, "Resonance-coupling-based plasmonic switches," *Small*, vol. 6, no. 22, pp. 2514–2519, 2010.
- [169] W. Ni, T. Ambjörnsson, S. P. Apell, H. Chen, and J. Wang, "Observing plasmonic-molecular resonance coupling on single gold nanorods," *Nano Letters*, vol. 10, pp. 77–84, 2010.
- [170] D. Melnikau, D. Savateeva, A. Susa, A. L. Rogach, and Y. P. Rakovich, "Strong plasmon-exciton coupling in a hybrid system of gold nanostars and J-aggregates," *Nanoscale Research Letters*, vol. 8, no. 1, pp. 1–6, 2013.
- [171] P. Vasa, W. Wang, R. Pomraenke, M. Lammers, M. Maiuri, C. Manzoni, G. Cerullo, and C. Lienau, "Real-time observation of ultrafast rabi oscillations between excitons and plasmons in metal nanostructures with J-aggregates," *Nature Photonics*, vol. 7, pp. 128–132, 2013.
- [172] G. P. Wiederrecht, G. A. Wurtz, and J. Hranisavljevic, "Coherent coupling of molecular excitons to electronic polarizations of noble metal nanoparticles," *Nano Letters*, vol. 4, no. 11, pp. 2121–2125, 2004.

- [173] F. H. L. Koppens, D. E. Chang, and F. J. Garcia de Abajo, "Graphene plasmonics: A platform for strong light-matter interactions," *Nano Letters*, vol. 11, no. 8, pp. 3370–3377, 2011.
- [174] A. Trugler and U. Hohenester, "Strong coupling between a metallic nanoparticle and a single molecule," *Physical Review B*, vol. 77, p. 115403, 2008.
- [175] G. A. Wurtz, P. R. Evans, W. Hendren, R. Atkinson, W. Dickson, R. J. Pollard, A. V. Zayats, W. Harrison, and C. Bower, "Molecular plasmonics with tunable exciton-plasmon coupling strength in J-aggregate hybridized au nanorod assemblies," *Nano Letters*, vol. 7, no. 5, pp. 1297–1303, 2007.
- [176] W. Ni, Z. Yang, H. Chen, L. Li, and J. Wang, "Coupling between molecular and plasmonic resonances in freestanding dye-rod nanorod hybrid nanostructures," *Journal of the American Chemical Society*, vol. 130, no. 21, pp. 6692–6693, 2008.
- [177] J. Lee, P. Hernandez, J. Lee, A. O. Govorov, and N. A. Kotov, "Exciton-plasmon interactions in molecular spring assemblies of nanowires and wavelength-based protein detection," *Nature Materials*, vol. 6, no. 4, pp. 291–295, 2007.
- [178] N. T. Fofang, N. K. Grady, Z. Fan, A. O. Govorov, and N. J. Halas, "Plexciton dynamics: Exciton-plasmon coupling in a J-aggregate-au nanoshell complex provides a mechanism for nonlinearity," *Nano Letters*, vol. 11, no. 4, pp. 1556–1560, 2011.
- [179] Y. B. Zheng, B. K. Juluri, L. Lin Jensen, D. Ahmed, M. Lu, L. Jensen, and T. J. Huang, "Dynamic tuning of plasmon-exciton coupling in arrays of nanodis-J-aggregate complexes," *Advanced Materials*, vol. 22, no. 32, pp. 3603–3607, 2010.
- [180] N. I. Cade, T. Ritman-Meer, and D. Richards, "Strong coupling of localized plasmons and molecular excitons in nanostructured silver films," *Physical Review B*, vol. 79, 2009.
- [181] J. Dintinger, S. Klein, F. Bustos, W. L. Barnes, and T. W. Ebbesen, "Strong coupling between surface plasmon polaritons and organic molecules in subwavelength hole arrays," *Physical Review B*, vol. 71, 2005.
- [182] C. Bonnand, J. Bellessa, and J.-C. Plenet, "Study of strong coupling between surface plasmon and exciton in an organic semiconductor," *Journal of Non-Crystalline Solids*, vol. 353, pp. 1683–1685, 2006.
- [183] T. Schwartz, J. A. Hutchison, C. Genet, and T. W. Ebbesen, "Reversible switching of ultrastrong light-molecule coupling," *Physical Review Letters*, vol. 106, no. 19, p. 196405, 2011.
- [184] Y. Sugawara, T. A. Kelf, J. J. Baumberg, M. E. Abdelsalam, and P. N. Bartlett, "Strong coupling between localized plasmons and organic excitons in metal nanovoids," *Physical Review Letters*, vol. 97, p. 266808, 2006.

Bibliography

- [185] J. Bellessa, C. Bonnand, J. C. Plenet, and J. Mugnier, "Strong coupling between surface plasmons and excitons in an organic semiconductor," *Physical Review Letters*, vol. 93, p. 036404, 2004.
- [186] C. Bonnand, J. Bellessa, and J. C. Plenet, "Properties of surface plasmons strongly coupled to excitons in an organic semiconductor near a metallic surface," *Physical Review B*, vol. 73, p. 245330, 2006.
- [187] A. Salomon, R. J. Gordon, Y. Prior, T. Seideman, and M. Sukharev, "Strong coupling between molecular excited states and surface plasmon modes of a slit array in a thin metal film," *Physical Review Letters*, vol. 109, p. 073002, 2012.
- [188] C. Symonds, C. Bonnand, J. C. Plenet, A. Brahier, R. Parashkov, J. S. Lauret, E. Deleporte, and J. Bellessa, "Particularities of surface plasmon-exciton strong coupling with large Rabi splitting," *New Journal of Physics*, vol. 10, no. 6, p. 065017, 2008.
- [189] S. Aberra Guebrou, C. Symonds, E. Homeyer, J. C. Plenet, Y. N. Gartstein, V. M. Agronovich, and J. Bellessa, "Coherent emission from a disordered organic semiconductor induced by strong coupling with surface plasmons," *Physical Review Letters*, vol. 108, p. 066401, 2012.
- [190] A. Berrier, R. Cools, C. Arnold, P. Offermans, M. Crego-Calama, S. H. Brongersma, and J. Gómez-Rivas, "Active control of the strong coupling regime between porphyrin excitons and surface plasmon polaritons," *ACS Nano*, vol. 5, no. 8, pp. 6226–6232, 2011.
- [191] G. S. Agarwal, "Vacuum-field Rabi oscillations of atoms in a cavity," *Journal of Optical Society of America B*, vol. 2, no. 3, pp. 480–485, 1985.
- [192] S. D. Gupta and G. S. Agarwal, "Strong coupling cavity physics in microspheres with whispering gallery modes," *Optics Communications*, vol. 115, pp. 597–605, 1995.
- [193] D. G. Lidzey, D. D. C. Bradley, M. S. Skolnick, T. Virgili, S. Walker, and D. M. Whittaker, "Strong-exciton coupling in an organic semiconductor microcavity," *Nature*, vol. 395, pp. 53–55, 1998.
- [194] M. G. Raizen, R. J. Thompson, R. J. Brecha, H. J. Kimble, and H. J. Carmichael, "Normal-mode splitting and linewidth averaging for two-state atoms in an optical cavity," *Physical Review Letters*, vol. 63, no. 3, pp. 240–243, 1989.
- [195] J. R. Tischler, M. S. Bradley, Q. Zhang, T. Atay, A. Nurmikko, and V. Bulovic, "Solid state cavity QED: strong coupling in organic thin films," *Organic Electronics*, vol. 8, pp. 94–113, 2007.
- [196] A. Salomon, C. Genet, and T. W. Ebbesen, "Molecule-light complex: Dynamics of hybrid molecule-surface plasmon states," *Angewandte Chemie*, vol. 121, no. 46, pp. 8904–8907, 2009.

- [197] J. A. Hutchison, T. Schwartz, C. Genet, E. Devaux, and T. W. Ebbesen, "Modifying chemical landscapes by coupling to vacuum fields," *Angewandte Chemie International Edition*, vol. 51, no. 7, pp. 1592–1596, 2012.
- [198] S. Dutta-Gupta and O. J. F. Martin, "Strongly coupled bio-plasmonic system: Application to oxygen sensing," *Journal of Applied Physics*, vol. 110, no. 4, pp. 1–6, 2011.
- [199] A. A. Yanik, A. E. Cetin, M. Huang, A. Artar, S. H. Mousavi, A. Khanikaev, J. H. Connor, G. Shvets, and H. Altug, "Seeing protein monolayers with naked eye through plasmonic Fano resonances," *Proceedings of the National Academy of Sciences*, vol. 108, no. 29, pp. 11784–11789, 2011.
- [200] Y. Kim, R. C. Johnson, and J. T. Hupp, "Gold nanoparticle-based sensing of spectroscopically silent heavy metal ions," *Nano Letters*, vol. 1, no. 4, pp. 165–167, 2001.
- [201] O. Kedem, A. Vaskevich, and I. Rubinstein, "Critical issues in localized plasmon sensing," *The Journal of Physical Chemistry C*, vol. 118, no. 16, pp. 8227–8244, 2014.
- [202] R. Elghanian, J. J. Storhoff, R. C. Mucic, R. L. Letsinger, and C. A. Mirkin, "Selective colorimetric detection of polynucleotides based on the distance-dependent optical properties of gold nanoparticles," *Science*, vol. 277, no. 5329, pp. 1078–1081, 1997.
- [203] J. J. Storhoff, A. D. Lucas, V. Garimella, Y. P. Bao, and U. R. Muller, "Homogeneous detection of unamplified genomic DNA sequences based on colorimetric scatter of gold nanoparticle probes," *Nature Biotechnology*, vol. 22, no. 4, pp. 553–558, 2004.
- [204] J. Liu and Y. Lu, "Fast colorimetric sensing of adenosine and cocaine based on a general sensor design involving aptamers and nanoparticles," *Angewandte Chemie*, vol. 118, no. 1, pp. 96–100, 2006.
- [205] N. T. K. Thanh and Z. Rosenzweig, "Development of an aggregation-based immunoassay for anti-protein A using gold nanoparticles," *Analytical Chemistry*, vol. 74, no. 7, pp. 1624–1628, 2002.
- [206] S. O. Obare, R. E. Hollowell, and C. J. Murphy, "Sensing strategy for lithium ion based on gold nanoparticles," *Langmuir*, vol. 18, no. 26, pp. 10407–10410, 2002.
- [207] C.-C. Huang and H.-T. Chang, "Selective gold-nanoparticle-based "turn-on" fluorescent sensors for detection of mercury(II) in aqueous solution," *Analytical Chemistry*, vol. 78, no. 24, pp. 8332–8338, 2006.
- [208] W. Zhao, W. Chiuman, M. A. Brook, and Y. Li, "Simple and rapid colorimetric biosensors based on DNA aptamer and noncrosslinking gold nanoparticle aggregation," *ChemBioChem*, vol. 8, no. 7, pp. 727–731, 2007.
- [209] W. Zhao, M. A. Brook, and Y. Li, "Design of gold nanoparticle-based colorimetric biosensing assays," *ChemBioChem*, vol. 9, no. 15, pp. 2363–2371, 2008.

Bibliography

- [210] W. Zhao, M. M. Ali, S. D. Aguirre, M. A. Brook, and Y. Li, "Paper-based bioassays using gold nanoparticle colorimetric probes," *Analytical Chemistry*, vol. 80, no. 22, pp. 8431–8437, 2008.
- [211] K. Sato, K. Hosokawa, and M. Maeda, "Rapid aggregation of gold nanoparticles induced by non-cross-linking DNA hybridization," *Journal of the American Chemical Society*, vol. 125, no. 27, pp. 8102–8103, 2003.
- [212] R. Mout, D. F. Moyano, S. Rana, and V. M. Rotello, "Surface functionalization of nanoparticles for nanomedicine," *Chemical Society Reviews*, vol. 41, no. 7, pp. 2539–2544, 2012.
- [213] T. Finkel and N. J. Holbrook, "Oxidants, oxidative stress and the biology of ageing," *Nature*, vol. 408, no. 6809, pp. 239–47, 2000.
- [214] M. Valko, D. Leibfritz, J. Moncol, M. T. Cronin, M. Mazur, and J. Telser, "Free radicals and antioxidants in normal physiological functions and human disease," *The International Journal of Biochemistry & Cell Biology*, vol. 39, no. 1, pp. 44–84, 2007.
- [215] M. Valko, C. Rhodes, J. Moncol, M. Izakovic, and M. Mazur, "Free radicals, metals and antioxidants in oxidative stress-induced cancer," *Chemico-Biological Interactions*, vol. 160, no. 1, pp. 1–40, 2006.
- [216] P. Storz, "Reactive oxygen species-mediated mitochondria-to-nucleus signaling: A key to aging and radical-caused diseases," *Science Signaling*, vol. 2006, no. 332, 2006.
- [217] C. J. Murphy, A. M. Gole, J. W. Stone, P. N. Sisco, A. M. Alkilany, E. C. Goldsmith, and S. C. Baxter, "Gold nanoparticles in biology: Beyond toxicity to cellular imaging," *Accounts of Chemical Research*, 2008.
- [218] A. M. Alkilany, L. B. Thompson, S. P. Boulos, P. N. Sisco, and C. J. Murphy, "Gold nanorods: Their potential for photothermal therapeutics and drug delivery, tempered by the complexity of their biological interactions," *Advanced Drug Delivery Reviews*, vol. 64, no. 2, pp. 190–199, 2012.
- [219] M.-C. Daniel and D. Astruc, "Gold nanoparticles: Assembly, supramolecular chemistry, quantum-size-related properties, and applications toward biology, catalysis, and nanotechnology," *Chemical Reviews*, vol. 104, no. 1, pp. 293–346, 2004.
- [220] E. C. Dreaden, A. M. Alkilany, X. Huang, C. J. Murphy, and M. A. El-Sayed, "The golden age: Gold nanoparticles for biomedicine," *Chemical Society Reviews*, vol. 41, no. 7, pp. 2740–2779, 2012.
- [221] R. Huang, R. P. Carney, F. Stellacci, and B. L. T. Lau, "Colloidal stability of self-assembled mono layer-coated gold nanoparticles: The effects of surface compositional and structural heterogeneity," *Langmuir*, vol. 29, no. 37, pp. 11560–11566, 2013.

- [222] A. M. Jackson, J. W. Myerson, and F. Stellacci, "Spontaneous assembly of subnanometre-ordered domains in the ligand shell of monolayer-protected nanoparticles," *Nature Materials*, vol. 3, no. 5, pp. 330–336, 2004.
- [223] H. Kim, R. P. Carney, J. Reguera, Q. K. Ong, X. Liu, and F. Stellacci, "Synthesis and characterization of Janus gold nanoparticles," *Advanced Materials*, vol. 24, pp. 3857–3863, 2012.
- [224] J. Y. Kim, J.-B. Chang, C. A. Ross, and F. Stellacci, "Seeded solution growth of nanoparticles into ordered three-dimensional supracrystals," *RSC Advances*, vol. 3, no. 27, pp. 10628–10631, 2013.
- [225] J. Reguera, H. Kim, and F. Stellacci, "Advances in Janus Nanoparticles," *Chimia*, vol. 67, no. 11, pp. 811–818, 2013.
- [226] P. d. Pino, B. Pelaz, Q. Zhang, P. Maffre, G. U. Nienhaus, and W. J. Parak, "Protein corona formation around nanoparticles - from the past to the future," *Mater. Horiz.*, pp. –, 2014.
- [227] C. D. Walkey, J. B. Olsen, F. Song, R. Liu, H. Guo, D. W. H. Olsen, Y. Cohen, A. Emili, and W. C. W. Chan, "Protein corona fingerprinting predicts the cellular interaction of gold and silver nanoparticles," *ACS Nano*, vol. 8, no. 3, pp. 2439–2455, 2014.
- [228] S. Tenzer, D. Docter, S. Rosfa, A. Wlodarski, J. Kuharev, A. Rekik, S. K. Knauer, C. Bantz, T. Nawroth, C. Bier, J. Sirirattanapan, W. Mann, L. Treuel, R. Zellner, M. Maskos, H. Schild, and R. H. Stauber, "Nanoparticle size is a critical physicochemical determinant of the human blood plasma corona: A comprehensive quantitative proteomic analysis," *ACS Nano*, vol. 5, no. 9, pp. 7155–7167, 2011.
- [229] S. Tenzer, D. Docter, J. Kuharev, A. Musyanovych, V. Fetz, R. Hecht, F. Schlenk, D. Fischer, K. Kiouptsi, C. Reinhardt, K. Landfester, H. Schild, M. Maskos, S. K. Knauer, and R. H. Stauber, "Rapid formation of plasma protein corona critically affects nanoparticle pathophysiology," *Nature Nanotechnology*, vol. 8, no. 10, pp. 772–781, 2013.
- [230] M. Lundqvist, "Nanoparticles: Tracking protein corona over time," *Nature Nanotechnology*, vol. 8, no. 10, pp. 701–702, 2013.
- [231] G. U. Nienhaus, P. Maffre, and K. Nienhaus, "Chapter four - studying the protein corona on nanoparticles by {FCS}," in *Fluorescence Fluctuation Spectroscopy (FFS), Part B* (S. Y. Tetin, ed.), vol. 519 of *Methods in Enzymology*, pp. 115–137, Academic Press, 2013.
- [232] T. Cedervall, I. Lynch, S. Lindman, T. Berggard, E. Thulin, H. Nilsson, K. A. Dawson, and S. Linse, "Understanding the nanoparticle-protein corona using methods to quantify exchange rates and affinities of proteins for nanoparticles," *Proceedings of the National Academy of Sciences*, vol. 104, no. 7, pp. 2050–2055, 2007.
- [233] A. Cifuentes-Rius, H. de Puig, J. C. Y. Kah, S. Borros, and K. Hamad-Schifferli, "Optimizing the properties of the protein corona surrounding nanoparticles for tuning payload release," *ACS Nano*, vol. 7, no. 11, pp. 10066–10074, 2013.

Bibliography

- [234] M. Lundqvist, J. Stigler, G. Elia, I. Lynch, T. Cedervall, and K. A. Dawson, "Nanoparticle size and surface properties determine the protein corona with possible implications for biological impacts," *Proceedings of the National Academy of Sciences*, vol. 105, no. 38, pp. 14265–14270, 2008.
- [235] E. Casals, T. Pfaller, A. Duschl, G. J. Oostingh, and V. Puentes, "Time evolution of the nanoparticle protein corona," *ACS Nano*, vol. 4, no. 7, pp. 3623–3632, 2010.
- [236] M. P. Monopoli, D. Walczyk, A. Campbell, G. Elia, I. Lynch, F. Baldelli Bombelli, and K. A. Dawson, "Physical-chemical aspects of protein corona: Relevance to in vitro and in vivo biological impacts of nanoparticles," *Journal of the American Chemical Society*, vol. 133, no. 8, pp. 2525–2534, 2011.
- [237] R. Gref, M. Luck, P. Quellec, M. M Marchand, E. Dellacherie, S. Harnisch, and T. Blunk, "'stealth' corona-core nanoparticles surface modified by polyethylene glycol (PEG): influences of the corona (PEG chain length and surface density) and of the core composition on phagocytic uptake and plasma protein adsorption," *Colloids and Surfaces B: Biointerfaces*, vol. 18, no. 3-4, pp. 301–313, 2000.
- [238] M. Lundqvist, J. Stigler, T. Cedervall, T. Berggard, M. B. Flanagan, I. Lynch, G. Elia, and K. Dawson, "The evolution of the protein corona around nanoparticles: A test study," *ACS Nano*, vol. 5, no. 9, pp. 7503–7509, 2011.
- [239] A. Lesniak, A. Campbell, M. P. Monopoli, I. Lynch, A. Salvati, and K. A. Dawson, "Serum heat inactivation affects protein corona composition and nanoparticle uptake," *Biomaterials*, vol. 31, no. 36, pp. 9511–9518, 2010.
- [240] I. Lynch and K. A. Dawson, "Protein-nanoparticle interactions," *Nano Today*, vol. 3, no. 1-2, pp. 40–47, 2008.
- [241] J. S. Gebauer, M. Malissek, S. Simon, S. K. Knauer, M. Maskos, R. H. Stauber, W. Peukert, and L. Treuel, "Impact of the nanoparticle-protein corona on colloidal stability and protein structure," *Langmuir*, vol. 28, no. 25, pp. 9673–9679, 2012.
- [242] A. Lesniak, F. Fenaroli, M. P. Monopoli, C. Aberg, K. A. Dawson, and A. Salvati, "Effects of the presence or absence of a protein corona on silica nanoparticle uptake and impact on cells," *ACS Nano*, vol. 6, no. 7, pp. 5845–5857, 2012.
- [243] M. Safi, J. Courtois, M. Seigneuret, H. Conjeaud, and J.-F. Berret, "The effects of aggregation and protein corona on the cellular internalization of iron oxide nanoparticles," *Biomaterials*, vol. 32, no. 35, pp. 9353–9363, 2011.
- [244] E. Casals, T. Pfaller, A. Duschl, G. J. Oostingh, and V. F. Puentes, "Hardening of the nanoparticle-protein corona in metal (Au, Ag) and oxide (Fe₃O₄, CoO, and CeO₂) nanoparticles," *Small*, vol. 7, no. 24, pp. 3479–3486, 2011.

- [245] J. Klein, "Probing the interactions of proteins and nanoparticles," *Proceedings of the National Academy of Sciences*, vol. 104, no. 7, pp. 2029–2030, 2007.
- [246] R. Huang, R. P. Carney, F. Stellacci, and B. L. T. Lau, "Protein-nanoparticle interactions: the effects of surface compositional and structural heterogeneity are scale dependent," *Nanoscale*, vol. 5, no. 15, pp. 6928–6935, 2013.
- [247] R. Huang, R. R. Carney, K. Ikuma, F. Stellacci, and B. L. T. Lau, "Effects of surface compositional and structural heterogeneity on nanoparticle-protein interactions: Different protein configurations," *ACS Nano*, vol. 8, no. 6, pp. 5402–5412, 2014.
- [248] V. L. S. Lapointe, A. T. Fernandes, N. C. Bell, F. Stellacci, and M. M. Stevens, "Nanoscale topography and chemistry affect embryonic stem cell self-renewal and early differentiation," *Advanced Healthcare Materials*, vol. 2, no. 12, pp. 1644–1650, 2013.
- [249] L. Du, H. Jiang, X. Liu, and E. Wang, "Biosynthesis of gold nanoparticles assisted by *Escherichia coli* DH5a and its application on direct electrochemistry of hemoglobin," *Electrochemistry Communications*, vol. 9, pp. 1165–1170, 2007.
- [250] P. Schabes-Retchkiman, G. Canizal, R. Herrera-Becerra, C. Zorrilla, H. Liu, and J. Ascencio, "Biosynthesis and characterization of Ti/Ni bimetallic nanoparticles," *Optical Materials*, vol. 29, pp. 95–99, 2006.
- [251] A. K. Jha, K. Prasad, and A. Kulkarni, "Synthesis of TiO₂ nanoparticles using microorganisms," *Colloids and Surfaces B: Biointerfaces*, vol. 71, pp. 226–229, 2009.
- [252] R. R. Naik, S. J. Stringer, G. Agarwal, S. E. Jones, and M. O. Stone, "Biomimetic synthesis and patterning of silver nanoparticles," *Nature Materials*, vol. 1, pp. 169–172, 2002.
- [253] K. N. Thakkar, S. S. Mhatre, and R. Y. Parikh, "Biological synthesis of metallic nanoparticles," *Nanomedicine: Nanotechnology, Biology, and Medicine*, vol. 6, pp. 257–262, 2010.
- [254] Anshup, J. S. Venkataraman, C. Subramaniam, R. R. Kumar, S. Priya, T. R. S. Kumar, R. V. Omkumar, A. John, and T. Pradeep, "Growth of gold nanoparticles in human cells," *Langmuir*, vol. 21, pp. 11562–11567, 2005.
- [255] S. Prahl, "Optical absorption of hemoglobin (<http://omlc.ogi.edu/spectra/hemoglobin/index.html>)," 1999.
- [256] G. L. Liu, Y. T. Long, Y. Choi, T. Kang, and L. P. Lee, "Quantized plasmon quenching dips nanospectroscopy via plasmon resonance energy transfer," *Nature Methods*, vol. 4, no. 12, pp. 1015–1017, 2007.
- [257] Y. Choi, T. Kang, and L. P. Lee, "Plasmon resonance energy transfer (PRET)-based molecular imaging of cytochrome c in living cells," *Nano Letters*, vol. 9, no. 1, pp. 85–90, 2009.

Bibliography

- [258] G. Suarez, C. Santschi, V. I. Slaveykova, and O. J. F. Martin, "Sensing the dynamics of oxidative stress using enhanced absorption in protein-loaded random media," *Scientific Reports*, vol. 3, 2013.
- [259] P. B. Johnson and R. W. Christy, "Optical constants of the noble metals," *Physical Review B*, vol. 6, no. 12, pp. 4370–4379, 1972.
- [260] M. Born and E. Wolf, *Principles of Optics: Electromagnetic Theory of Propagation*. Cambridge: Cambridge University Press, 2001.
- [261] W. A. Eaton, E. R. Henry, J. Hofrichter, and A. Mozzarelli, "Is cooperative oxygen binding by hemoglobin really understood?," *Nature Structural Biology*, vol. 6, pp. 351 – 358, 1999.
- [262] C.-H. Lee, J. Lang, C.-W. Yen, P.-C. Shih, T.-S. Lin, and C.-Y. Mou, "Enhancing stability and oxidation activity of cytochrome c by immobilization in the nanochannels of mesoporous aluminosilicates," *The Journal of Physical Chemistry B*, vol. 109, no. 25, pp. 12277–12286, 2005.
- [263] W. D. Butt and D. Keilin, "Absorption spectra and some other properties of cytochrome c and of its compounds with ligands," *Proceedings of the Royal Society of London. Series B, Biological Sciences*, vol. 156, no. 965, pp. 429–458, 1962.
- [264] Y.-L. P. Ow, D. R. Green, Z. Hao, and T. W. Mak, "Cytochrome c: functions beyond respiration," *Nature Reviews Molecular Cell Biology*, vol. 9, pp. 532–542, 2008.
- [265] N. Gochman and J. M. Schmitz, "Application of a new peroxide indicator reaction to the specific, automated determination of glucose with glucose oxidase," *Clinical Chemistry*, vol. 18, no. 9, pp. 943–950, 1972.
- [266] O. J. F. Martin and N. B. Piller, "Electromagnetic scattering in polarizable backgrounds," *Phys. Rev. E*, vol. 58, pp. 3909–3915, 1998.
- [267] A. M. Kern and O. J. F. Martin, "Pitfalls in the determination of optical cross sections from surface integral equation simulations," *IEEE Trans. Antennas. Propag.*, vol. 58, no. 6, pp. 2158–2161, 2010.
- [268] C. F. Bohren and D. R. Huffman, *Absorption and Scattering of Light by Small Particles*. WILEY-VCH Verlag GmbH & Co. KGaA, 1998.
- [269] J. Xie, J. Y. Lee, and D. I. C. Wang, "Seedless, surfactantless, high-yield synthesis of branched gold nanocrystals in hepes buffer solution," *Chemistry of Materials*, vol. 19, no. 11, pp. 2823–2830, 2007.
- [270] J. M. Slocik, M. O. Stone, and R. R. Naik, "Synthesis of gold nanoparticles using multi-functional peptides," *Small*, vol. 1, no. 11, pp. 1048–1052, 2005.
- [271] A. Lovera, *Optical Nanoantennas: New Directions and Applications*. PhD thesis, STI, Lausanne, 2014.

- [272] W. Haiss, N. T. K. Thanh, J. Aveyard, and D. G. Fernig, "Determination of size and concentration of gold nanoparticles from UV-vis spectra," *Analytical Chemistry*, vol. 79, no. 11, pp. 4215–4221, 2007.
- [273] P. Alonso-González, P. Albella, F. Neubrech, C. Huck, J. Chen, F. Golmar, F. Casanova, L. Hueso, A. Pucci, J. Aizpurua, and R. Hillenbrand, "Experimental verification of the spectral shift between near- and far-field peak intensities of plasmonic infrared nanoantennas," *Physical Review Letters*, vol. 110, p. 203902, 2013.
- [274] J. Zuloaga and P. Nordlander, "On the energy shift between near-field and far-field peak intensities in localized plasmon systems," *Nano Letters*, vol. 11, no. 3, pp. 1280–1283, 2011.
- [275] T. Aoki, B. Dayan, E. Wilcut, W. P. Bowen, A. S. Parkins, T. J. Kippenberg, K. J. Vahala, and H. J. Kimble, "Observation of strong coupling between one atom and a monolithic microresonator," *Nature*, vol. 443, pp. 671–674, 2006.
- [276] L. Stryer and R. P. Haugland, "Energy transfer: a spectroscopic ruler," *Proceedings of the National Academy of Sciences*, vol. 58, no. 2, pp. 719–726, 1967.
- [277] J. Griffin, A. K. Singh, D. Senapati, P. Rhodes, K. Mitchell, B. Robinson, E. Yu, and P. C. Ray, "Size- and distance-dependent nanoparticle surface-energy transfer (NSET) method for selective sensing of hepatitis c virus rna," *Chemistry: A European Journal*, vol. 15, no. 2, pp. 342–351, 2009.
- [278] C. S. Yun, A. Javier, T. Jennings, M. Fisher, S. Hira, S. Peterson, B. Hopkins, N. O. Reich, and G. F. Strouse, "Nanometal surface energy transfer in optical rulers, breaking the fret barrier," *Journal of the American Chemical Society*, vol. 127, no. 9, pp. 3115–3119, 2005.
- [279] R. F. Aroca, G. Y. Teo, H. Mohan, A. R. Guerrero, P. Albella, and F. Moreno, "Plasmon-enhanced fluorescence and spectral modification in SHINEF," *The Journal of Physical Chemistry C*, vol. 115, no. 42, pp. 20419–20424, 2011.
- [280] A. M. Kern, A. J. Meixner, and O. J. F. Martin, "Molecule-dependent plasmonic enhancement of fluorescence and Raman scattering near realistic nanostructures," *ACS Nano*, vol. 6, no. 11, pp. 9828–9836, 2012.
- [281] G. Zengin, G. Johansson, P. Johansson, T. J. Antosiewicz, M. Käll, and T. Shegai, "Approaching the strong coupling limit in single plasmonic nanorods interacting with j-aggregates," *Scientific Reports*, vol. 3, pp. 1–6, 2013.
- [282] F. Neubrech, A. Pucci, T. Cornelius, S. Karim, A. Garcia-Etxarri, and J. Aizpurua, "Resonant plasmonic and vibrational coupling in a tailored nanoantenna for infrared detection," *Physical Review Letters*, vol. 101, p. 157403, 2008.
- [283] N. A. Mirin, K. Bao, and P. Nordlander, "Fano resonances in plasmonic nanoparticle aggregates," *Journal of Physical Chemistry A*, vol. 113, no. 16, pp. 4028–4034, 2009.

Bibliography

- [284] J. Margueritat, A. Bouhelier, L. Markey, G. Colas des Francs, A. Dereux, S. Lau-Truong, J. Grand, G. Lévi, N. Félidj, J. Aubard, and E. Finot, "Discerning the origins of the amplitude fluctuations in dynamic Raman nanospectroscopy," *The Journal of Physical Chemistry C*, vol. 116, no. 51, pp. 26919–26923, 2012.
- [285] T. G. Spiro and T. C. Strekas, "Resonance Raman spectra of Hemoglobin and Cytochrome c: Inverse polarization and vibronic scattering," *Proceedings of the National Academy of Sciences*, vol. 69, no. 9, pp. 2622–2626, 1972.
- [286] S. Hu, I. K. Morris, J. P. Singh, K. M. Smith, and T. G. Spiro, "Complete assignment of Cytochrome c resonance Raman spectra via enzymic reconstitution with isotopically labeled hemes," *Journal of the American Chemical Society*, vol. 115, no. 26, pp. 12446–12458, 1993.
- [287] M. Gouterman, "Spectra of porphyrins," *Journal of Molecular Spectroscopy*, vol. 6, no. 0, pp. 138–163, 1961.
- [288] J. Liu and Y. Lu, "Preparation of aptamer-linked gold nanoparticle purple aggregates for colorimetric sensing of analytes," *Nature Protocols*, vol. 1, no. 1, pp. 246–252, 2006.
- [289] K. M. Mayer, S. Lee, H. Liao, B. C. Rostro, A. Fuentes, P. T. Scully, C. L. Nehl, and J. H. Hafner, "A label-free immunoassay based upon localized surface plasmon resonance of gold nanorods," *ACS Nano*, vol. 2, no. 4, pp. 687–692, 2008.
- [290] E. S. Cho, J. Kim, B. Tejerina, T. M. Hermans, H. Jiang, H. Nakanishi, M. Yu, A. Z. Patashinski, S. C. Glotzer, F. Stellacci, and B. A. Grzybowski, "Ultrasensitive detection of toxic cations through changes in the tunnelling current across films of striped nanoparticles," *Nature Materials*, vol. 11, no. 11, pp. 978–985, 2012.
- [291] C. M. Cobley, J. Chen, E. C. Cho, L. V. Wang, and Y. Xia, "Gold nanostructures: A class of multifunctional materials for biomedical applications," *Chemical Society Reviews*, vol. 40, no. 1, pp. 44–56, 2011.
- [292] P. K. Jain, X. Huang, I. H. El-Sayed, and M. A. El-Sayed, "Noble metals on the nanoscale: Optical and photothermal properties and some applications in imaging, sensing, biology, and medicine," *Accounts of Chemical Research*, 2008.
- [293] S. J. Tan, M. J. Campolongo, D. Luo, and W. Cheng, "Building plasmonic nanostructures with DNA," *Nat Nano*, vol. 6, no. 5, pp. 268–276, 2011.
- [294] X. Liu, M. Yu, H. Kim, M. Mameli, and F. Stellacci, "Determination of monolayer-protected gold nanoparticle ligand-shell morphology using NMR," *Nature Communications*, vol. 3, 2012.
- [295] Q. Ong Khac, J. Reguera, P. J. Silva, M. Moglianetti, K. Harkness, M. Longobardi, K. S. Mali, C. Renner, S. De Feyter, and F. Stellacci, "High-resolution scanning tunneling microscopy: Characterization of mixed monolayer protected gold nanoparticles," *ACS Nano*, vol. 7, no. 10, pp. 8529–8539, 2013.

- [296] M. Brust, M. Walker, D. Bethell, D. J. Schiffrin, and R. Whyman, "Synthesis of thiol-derivatised gold nanoparticles in a two-phase liquid-liquid system," *Journal of the Chemical Society, Chemical Communications*, no. 7, pp. 801–802, 1994.
- [297] M. Grzelczak, J. Perez-Juste, P. Mulvaney, and L. M. Liz-Marzan, "Shape control in gold nanoparticle synthesis," *Chemical Society Reviews*, vol. 37, no. 9, pp. 1783–1791, 2008.
- [298] X. Jiang, A. Brioude, and M. Pileni, "Gold nanorods: Limitations on their synthesis and optical properties," *Colloids and Surfaces A: Physicochemical and Engineering Aspects*, vol. 277, no. 1-3, pp. 201–206, 2006.
- [299] J. Kimling, M. Maier, B. Okenve, V. Kotaidis, H. Ballot, and A. Plech, "Turkevich method for gold nanoparticle synthesis revisited," *The Journal of Physical Chemistry B*, vol. 110, no. 32, pp. 15700–15707, 2006.
- [300] D. T. Nguyen, D.-J. Kim, and K.-S. Kim, "Controlled synthesis and biomolecular probe application of gold nanoparticles," *Micron*, vol. 42, no. 3, pp. 207–227, 2011.
- [301] J. Perez-Juste, I. Pastoriza-Santos, L. M. Liz-Marzan, and P. Mulvaney, "Gold nanorods: Synthesis, characterization and applications," *Coordination Chemistry Reviews*, vol. 249, no. 17-18, pp. 1870–1901, 2005.
- [302] K.-T. Yong, M. Swihart, H. Ding, and P. Prasad, "Preparation of gold nanoparticles and their applications in anisotropic nanoparticle synthesis and bioimaging," *Plasmonics*, vol. 4, no. 2, pp. 79–93, 2009.
- [303] S. Ghosh, S. Patil, M. Ahire, R. Kitture, S. Kale, K. Pardesi, S. S. Cameotra, J. Bellare, D. D. Dhavale, A. Jabgunde, and B. A. Chopade, "Synthesis of silver nanoparticles using dioscorea bulbifera tuber extract and evaluation of its synergistic potential in combination with antimicrobial agents," *International journal of nanomedicine*, vol. 7, pp. 483–496, 2012.
- [304] A. Shamsaie, M. Jonczyk, J. Sturgis, J. P. Robinson, and J. Irudayaraj, "Intracellularly grown gold nanoparticles as potential surface-enhanced Raman scattering probes," *Journal of Biomedical Optics*, vol. 12, no. 2, p. 020502, 2007.
- [305] P. Zijlstra, J. W. M. Chon, and M. Gu, "Five-dimensional optical recording mediated by surface plasmons in gold nanorods," *Nature*, vol. 459, pp. 410–413, 2009.
- [306] S. Milani, F. Baldelli Bombelli, A. S. Pitek, K. A. Dawson, and J. Radler, "Reversible versus irreversible binding of transferrin to polystyrene nanoparticles: Soft and hard corona," *ACS Nano*, vol. 6, no. 3, pp. 2532–2541, 2012.
- [307] R. P. Carney, Y. Astier, T. M. Carney, K. Voitchovsky, P. H. J. Silva, and F. Stellacci, "Electrical method to quantify nanoparticle interaction with lipid bilayers," *ACS Nano*, vol. 7, no. 2, pp. 932–942, 2013.

Bibliography

- [308] E. Campos, C. E. Mcvey, R. P. Carney, F. Stellacci, Y. Astier, and J. Yates, "Sensing single mixed-monolayer protected gold nanoparticles by the alpha-Hemolysin nanopore," *Analytical Chemistry*, vol. 85, no. 21, pp. 10149–10158, 2013.
- [309] Y.-S. Yang, R. Carney, y P., F. Stellacci, and D. J. Irvine, "Enhancing radiotherapy by lipid nanocapsule-mediated delivery of amphiphilic gold nanoparticles to intracellular membranes," *ACS Nano*, vol. 8, no. 9, pp. 8992–9002, 2014.
- [310] A. Verma, O. Uzun, Y. Hu, Y. Hu, H.-S. Han, N. Watson, S. Chen, D. J. Irvine, and F. Stellacci, "Surface-structure-regulated cell-membrane penetration by monolayer-protected nanoparticles," *Nature Materials*, vol. 7, no. 7, pp. 588–595, 2008.
- [311] A. B. Roberts, L. C. Lamb, D. L. Newton, M. B. Sporn, J. E. De Larco, and G. J. Todaro, "Transforming growth factors: Isolation of polypeptides from virally and chemically transformed cells by acid/ethanol extraction," *Proceedings of the National Academy of Sciences*, vol. 77, no. 6, pp. 3494–3498, 1980.
- [312] M. Moloney, L. McDonnell, and H. OShea, "Atomic force microscopy of BHK-21 cells: an investigation of cell fixation techniques," *Ultramicroscopy*, vol. 100, no. 3–4, pp. 153–161, 2004.
- [313] B. Halamoda Kenzaoui, C. Chapuis Bernasconi, H. Hofmann, and L. Juillerat-Jeanneret, "Evaluation of uptake and transport of ultrasmall superparamagnetic iron oxide nanoparticles by human brain-derived endothelial cells," *Nanomedicine*, vol. 7, no. 1, pp. 39–53, 2011.
- [314] B. Halamoda Kenzaoui, C. Chapuis Bernasconi, S. Guney Ayra, and L. Juillerat-Jeanneret, "Induction of oxidative stress, lysosome activation and autophagy by nanoparticles in human brain-derived endothelial cells," *Biochemical Journal*, vol. 441, pp. 813–821, 2012.
- [315] H. P. Broquist, "Buthionine sulfoximine, an experimental tool to induce glutathione deficiency: Elucidation of glutathione and ascorbate in their role as antioxidants," *Nutrition Reviews*, vol. 50, no. 4, pp. 110–111, 1992.
- [316] I. A. Cotgreave, M. S. Sandy, M. Berggren, R. W. Moldeus, and M. T. Smith, "N-acetyl cysteine and glutathione-dependent protective effect of PZ51 (ebselen) against diquat-induced cytotoxicity in isolated hepatocytes," *Biochemical Pharmacology*, vol. 36, no. 18, pp. 2899–2904, 1987.
- [317] D. A. Dickinson and H. J. Forman, "Cellular glutathione and thiol metabolism," *Biochemical Pharmacology*, vol. 64, pp. 1919–1026, 2002.
- [318] H. J. Forman, H. Zhang, and A. Rinna, "Glutathione: Overview of its protective roles, measurement, and biosynthesis," *Molecular Aspects of Medicine*, vol. 30, pp. 1–12, 2009.

- [319] R. Hong, G. Han, J. M. Fernandez, B.-j. Kim, N. S. Forbes, and V. M. Rotello, "Glutathione-mediated delivery and release using monolayer protected nanoparticle carriers," *Journal of the American Chemical Society*, vol. 128, no. 4, pp. 1078–1079, 2006.
- [320] D. M. Townsend, K. D. Tew, and H. Tapiero, "The importance of glutathione in human disease," *Biomedicine & Pharmacotherapy*, vol. 57, pp. 145–155, 2003.
- [321] C. Gorrini, I. S. Harris, and T. W. Mak, "Modulation of oxidative stress as an anticancer strategy," *Nature Reviews Drug Discovery*, vol. 12, pp. 931–947, 2013.
- [322] A. Gole and C. J. Murphy, "Seed-mediated synthesis of gold nanorods: Role of the size and nature of the seed," *Chemistry of Materials*, vol. 16, no. 19, pp. 3633–3640, 2004.
- [323] E. E. Connor, J. Mwamuka, A. Gole, C. J. Murphy, and M. D. Wyatt, "Gold nanoparticles are taken up by human cells but do not cause acute cytotoxicity," *Small*, vol. 1, no. 3, pp. 325–327, 2005.
- [324] B. D. Chithrani, A. A. Ghazani, and W. C. W. Chan, "Determining the size and shape dependence of gold nanoparticle uptake into mammalian cells," *Nano Letters*, vol. 6, no. 4, pp. 662–668, 2006.
- [325] Y. Liu, M. K. Shipton, J. Ryan, E. D. Kaufman, S. Franzen, and D. L. Feldheim, "Synthesis, stability, and cellular internalization of gold nanoparticles containing mixed peptide-poly(ethylene glycol) monolayers," *Analytical Chemistry*, vol. 79, pp. 2221–2229, 2007.
- [326] R. Levy, U. Shaheen, Y. Cesbron, and V. See, "Gold nanoparticles delivery in mammalian live cells: a critical review," *Nano Reviews*, vol. 1, pp. 1–18, 2010.
- [327] W. Jiang, B. Y. S. Kim, J. T. Rutka, and W. C. W. Chan, "Nanoparticle-mediated cellular response is size-dependent," *Nature Nanotechnology*, vol. 3, pp. 145–150, 2008.
- [328] B. D. Chithrani and W. C. W. Chan, "Elucidating the mechanism of cellular uptake and removal of protein-coated gold nanoparticles of different sizes and shapes," *Nano Letters*, vol. 7, no. 6, pp. 1542–1550, 2007.
- [329] A. C. Guyton and J. E. Hall, *Textbook of medical physiology*. Elsevier, 2011.
- [330] W. S. Chang, J. B. Lassiter, P. Swanglap, H. Sobhani, S. Khatua, P. Nordlander, N. J. Halas, and S. Link, "A plasmonic fano switch," *Nano Letters*, vol. 12, no. 9, pp. 4977–4982, 2012.
- [331] T. J. Davis, D. E. Gomez, and K. C. Vernon, "Simple model for the hybridization of surface plasmon resonances in metallic nanoparticles," *Nano Letters*, vol. 10, no. 7, pp. 2618–2625, 2010.
- [332] N. J. Halas, S. Lal, S. Link, W.-S. Chang, D. Natelson, J. H. Hafner, and P. Nordlander, "A plethora of plasmonics from the laboratory for nanophotonics at rice university," *Advanced Materials*, vol. 24, no. 36, pp. 4842–4877, 2012.

Bibliography

- [333] P. Nordlander, C. Oubre, E. Prodan, K. Li, and M. I. Stockman, "Plasmon hybridization in nanoparticle dimers," *Nano Letters*, vol. 4, no. 5, pp. 899–903, 2004.
- [334] H. Wang, Y. Wu, B. Lassiter, C. L. Nehl, J. H. Hafner, P. Nordlander, and N. J. Halas, "Symmetry breaking in individual plasmonic nanoparticles," *Proceedings of the National Academy of Sciences of the United States of America*, vol. 103, no. 29, pp. 10856–10860, 2006.
- [335] R. Ameling, L. Langguth, M. Hentschel, M. Mesch, P. V. Braun, and H. Giessen, "Cavity-enhanced localized plasmon resonance sensing," *Applied Physics Letters*, vol. 97, no. 25, pp. –, 2010.
- [336] J. Butet, B. Gallinet, K. Thyagarajan, and O. J. F. Martin, "Second-harmonic generation from periodic arrays of arbitrary shape plasmonic nanostructures: A surface integral approach," *Journal of the Optical Society of America B: Optical Physics*, vol. 30, no. 11, pp. 2970–2979, 2013.
- [337] J. Butet and O. J. F. Martin, "Nonlinear plasmonic nanorulers," *ACS Nano*, vol. 8, no. 5, pp. 4931–4939, 2014.
- [338] A. Christ, Y. Ekinici, H. H. Solak, N. A. Gippius, S. G. Tikhodeev, and O. J. F. Martin, "Controlling the Fano interference in a plasmonic lattice," *Physical Review B*, vol. 76, 2007.
- [339] A. Christ, G. Leveque, O. J. F. Martin, T. Zentgraf, J. Kuhl, C. Bauer, H. Giessen, and S. G. Tikhodeev, "Near-field induced tunability of surface plasmon polaritons in composite metallic nanostructures," *Journal of Microscopy*, vol. 229 Pt 2, pp. 344–353, 2008.
- [340] A. Christ, T. Zentgraf, S. G. Tikhodeev, N. A. Gippius, O. J. F. Martin, J. Kuhl, and H. Giessen, "Interaction between localized and delocalized surface plasmon polariton modes in a metallic photonic crystal," *Physica status solidi b*, vol. 243, no. 10, pp. 2344–2348, 2006.
- [341] A. Farhang, T. Siegfried, Y. Ekinici, H. Sigg, and O. J. F. Martin, "Large-scale sub-100 nm compound plasmonic grating arrays to control the interaction between localized and propagating plasmons," *Journal of Nanophotonics*, vol. 8, no. 1, pp. 083897–083897, 2014.
- [342] N. Liu, M. Hentschel, T. Weiss, A. P. Alivisatos, and H. Giessen, "Three-dimensional plasmon rulers," *Science*, vol. 332, no. 6036, pp. 1407–1410, 2011.
- [343] B. Gallinet, T. Siegfried, H. Sigg, P. Nordlander, and O. J. F. Martin, "Plasmonic radiance: Probing structure at the angstrom scale with visible light," *Nano Letters*, vol. 13, no. 2, pp. 497–503, 2012.
- [344] J. Wang, X. Yu, S. V. Boriskina, and B. M. Reinhard, "Quantification of differential ErbB1 and ErbB2 Cell surface expression and spatial nanoclustering through plasmon coupling," *Nano Letters*, vol. 12, no. 6, pp. 3231–3237, 2012.

-
- [345] H. Wang, L. Wu, and B. M. Reinhard, "Scavenger receptor mediated endocytosis of silver nanoparticles into J774A.1 macrophages is heterogeneous," *ACS Nano*, vol. 6, no. 8, pp. 7122–7132, 2012.
- [346] M. L. Juan, M. Righini, and R. Quidant, "Plasmon nano-optical tweezers," *Nat Photon*, vol. 5, no. 6, pp. 349–356, 2011.
- [347] Y. Pang and R. Gordon, "Optical trapping of a single protein," *Nano Letters*, vol. 12, no. 1, pp. 402–406, 2012.
- [348] A. Zehtabi-Oskuie, H. Jiang, B. R. Cyr, D. W. Rennehan, A. A. Al-Balushi, and R. Gordon, "Double nanohole optical trapping: dynamics and protein-antibody co-trapping," *Lab on a Chip*, vol. 13, pp. 2563–2568, 2013.
- [349] T. W. Ebbesen, H. J. Lezec, H. F. Ghaemi, T. Thio, and P. A. Wolff, "Extraordinary optical transmission through sub-wavelength hole arrays," *Nature*, vol. 391, no. 12, pp. 667–669, 1998.
- [350] L. Martin-Moreno, F. J. Garcia-Vidal, H. J. Lezec, K. M. Pellerin, T. Thio, J. B. Pendry, and T. Ebbesen, "Theory of extraordinary optical transmission through subwavelength hole arrays," *Physical Review Letters*, vol. 86, no. 6, pp. 1114–1117, 2001.
- [351] K. L. van der Molen, K. J. Klein Koerkamp, S. Enoch, F. B. Segerink, N. F. van Hulst, and L. Kuipers, "Role of shape and localized resonances in extraordinary transmission through periodic arrays of subwavelength holes: Experiment and theory," *Physical Review B*, vol. 72, p. 045421, 2005.
- [352] K. J. K. Koerkamp, S. Enoch, F. B. Segerink, N. F. van Hulst, and L. Kuipers, "Strong influence of hole shape on extraordinary transmission through periodic arrays of sub-wavelength holes," *Physical Review Letters*, vol. 92, p. 183901, 2004.
- [353] H. T. Liu and P. Lalanne, "Microscopic theory of the extraordinary optical transmission," *Nature*, vol. 452, no. 7188, pp. 728–731, 2008.
- [354] M. Mrejen, A. Israel, H. Taha, M. Palchan, and A. Lewis, "Near-field characterization of extraordinary optical transmission in sub-wavelength aperture arrays," *Optics Express*, vol. 15, no. 15, pp. 9129–9138, 2007.
- [355] M. B. Duhring and O. Sigmund, "Optimization of extraordinary optical absorption in plasmonic and dielectric structures," *Journal of the Optical Society of America B: Optical Physics*, vol. 30, no. 5, pp. 1154–1160, 2013.
- [356] L. Y. Wu, B. M. Ross, and L. P. Lee, "Optical properties of the crescent-shaped nanohole antenna," *Nano Letters*, vol. 9, no. 5, pp. 1956–1961, 2009.
- [357] Z. L. Zhang, H. R. Zheng, J. Dong, X. Q. Yan, Y. Sun, and H. X. Xu, "Surface enhanced fluorescence by porous alumina with nanohole arrays," *Science China Physics Mechanics and Astronomy*, 2012.

Bibliography

- [358] X. Cui, K. Tawa, K. Kintaka, and J. Nishii, “Enhanced fluorescence microscopic imaging by plasmonic nanostructures: From a 1D grating to a 2D nanohole array,” *Advanced Functional Materials*, p. NA, 2010.
- [359] Z. L. Cao, S. L. Wong, S. Y. Wu, H. P. Ho, and H. C. Ong, “High performing phase-based surface plasmon resonance sensing from metallic nanohole arrays,” *Applied Physics Letters*, vol. 104, no. 17, pp. 1–5, 2014.
- [360] F. Eftekhari, C. Escobedo, J. Ferreira, X. B. Duan, E. M. Girotto, A. G. Brolo, R. Gordon, and D. Sinton, “Nanoholes as nanochannels: Flow-through plasmonic sensing,” *Analytical Chemistry*, vol. 81, no. 11, pp. 4308–4311, 2009.
- [361] R. Gordon, A. G. Brolo, A. McKinnon, A. Rajora, B. Leathem, and K. L. Kavanagh, “Strong polarization in the optical transmission through elliptical nanohole arrays,” *Physical Review Letters*, vol. 92, no. Copyright (C) 2009 The American Physical Society, p. 037401, 2004.
- [362] F. M. Huang, T. S. Kao, V. A. Fedotov, Y. Chen, and N. I. Zheludev, “Nanohole array as a lens,” *Nano Letters*, vol. 8, no. 8, pp. 2469–2472, 2008.
- [363] G. M. Hwang, P. Lin, E. H. Mullen, and Y. Fainman, “Plasmonic sensing of biological analytes through nanoholes,” *Sensors Journal, IEEE*, vol. 8, no. 12, pp. 2074–2079, 2008.
- [364] H. Im, A. Lesuffleur, N. C. Lindquist, and S. H. Oh, “Plasmonic nanoholes in a multichannel microarray format for parallel kinetic assays and differential sensing,” *Analytical Chemistry*, vol. 81, no. 8, pp. 2854–2859, 2009.
- [365] H. Leong and J. Guo, “A surface plasmon resonance spectrometer using a super-period metal nanohole array,” *Optics Express*, vol. 20, no. 19, pp. 21318–21323, 2012.
- [366] R. Zhou, H. Lu, X. Liu, Y. Gong, and D. Mao, “Second-harmonic generation from a periodic array of noncentrosymmetric nanoholes,” *Journal of the Optical Society of America B: Optical Physics*, vol. 27, no. 11, pp. 2405–2409, 2010.
- [367] C. Genet and T. W. Ebbesen, “Light in tiny holes,” *Nature*, vol. 445, pp. 39–46, 2007.
- [368] M. Virk, K. Xiong, M. Svedendahl, M. Käll, and A. B. Dahlin, “A thermal plasmonic sensor platform: Resistive heating of nanohole arrays,” *Nano Letters*, vol. 14, no. 6, pp. 3544–3549, 2014.
- [369] J. Lim, S. P. Yeap, H. X. Che, and S. C. Low, “Characterization of magnetic nanoparticle by dynamic light scattering,” *Nanoscale Research Letters*, vol. 8, no. 381, pp. 1–14, 2013.
- [370] R. P. Carney, J. Y. Kim, H. Qian, R. Jin, H. Mehenni, F. Stellacci, and O. M. Bakr, “Determination of nanoparticle size distribution together with density or molecular weight by 2D analytical ultracentrifugation,” *Nature Communications*, vol. 2, no. 335, 2011.

-
- [371] R. F. Domingos, M. A. Baalousha, Y. Ju-Nam, M. M. Reid, N. Tufenkji, J. R. Lead, G. G. Leppard, and K. J. Wilkinson, "Characterizing manufactured nanoparticles in the environment: Multimethod determination of particle sizes," *Environmental Science & Technology*, vol. 43, no. 19, pp. 7277–7284, 2009.
- [372] B. Gallinet, A. M. Kern, and O. J. F. Martin, "Accurate and versatile modeling of electromagnetic scattering on periodic nanostructures with a surface integral approach," *Journal of the Optical Society of America A: Optics and Image Science*, vol. 27, no. 10, pp. 2261–2271, 2010.
- [373] C. Yan and O. J. F. Martin, "Periodicity-induced symmetry breaking in a Fano lattice: Hybridization and tight-binding regimes," *ACS Nano*, vol. 8, no. 11, pp. 11860–11868, 2014.
- [374] R. Bardhan, S. Lal, A. Joshi, and N. J. Halas, "Theranostic nanoshells: From probe design to imaging and treatment of cancer," *Accounts of Chemical Research*, vol. 44, no. 10, pp. 936–946, 2011.
- [375] N. Grady, N. Halas, and P. Nordlander, "Influence of dielectric function properties on the optical response of plasmon resonant metallic nanoparticles," *Chemical Physics Letters*, vol. 399, no. 1–3, pp. 167–171, 2004.
- [376] S. Mukherjee, H. Sobhani, J. B. Lassiter, R. Bardhan, P. Nordlander, and N. J. Halas, "Fano shells: Nanoparticles with built-in fano resonances," *Nano Letters*, vol. 10, no. 7, pp. 2694–2701, 2010.
- [377] A. M. Kern and O. J. F. Martin, "Strong enhancement of forbidden atomic transitions using plasmonic nanostructures," *Physical Review A*, vol. 85, p. 022501, 2012.
- [378] B. Gallinet and O. J. F. Martin, "Refractive index sensing with subradiant modes: A framework to reduce losses in plasmonic nanostructures," *ACS Nano*, vol. 7, no. 8, pp. 6978–6987, 2013.
- [379] G. Colas des Francs, A. Bouhelier, E. Finot, J. C. Weeber, A. Dereux, C. Girard, and E. Dujardin, "Fluorescence relaxation in the near-field of a mesoscopic metallic particle: distance dependence and role of plasmon modes," *Optics Express*, vol. 16, no. 22, pp. 17654–17666, 2008.
- [380] G. Baffou, C. Girard, E. Dujardin, G. Colas des Francs, and O. J. F. Martin, "Molecular quenching and relaxation in a plasmonic tunable system," *Physical Review B*, vol. 77, p. 121101, 2008.
- [381] P. Mandal, A. Singh, S. Kasture, A. V. Gopal, and A. Vengurlekar, "Plasmon assisted intense blue-green emission from ZnO/ZnS nanocrystallites," *Optical Materials*, vol. 33, no. 11, pp. 1786–1791, 2011.

Bibliography

- [382] M. R. Beversluis, A. Bouhelier, and L. Novotny, "Continuum generation from single gold nanostructures through near-field mediated intraband transitions," *Physical Review B*, vol. 68, no. 11, p. 115433, 2003.
- [383] J. Butet, J. Duboisset, G. Bachelier, I. Russier-Antoine, E. Benichou, C. Jonin, and P.-F. Brevet, "Optical second harmonic generation of single metallic nanoparticles embedded in a homogeneous medium," *Nano Letters*, vol. 10, no. 5, pp. 1717–1721, 2010.
- [384] B. K. Canfield, H. Husu, J. Laukkanen, B. Bai, M. Kuittinen, J. Turunen, and M. Kauranen, "Local field asymmetry drives second-harmonic generation in noncentrosymmetric nanodimers," *Nano Letters*, vol. 7, no. 5, pp. 1251–1255, 2007.
- [385] Y. Zhang, N. K. Grady, C. Ayala-Orozco, and N. J. Halas, "Three-dimensional nanostructures as highly efficient generators of second harmonic light," *Nano Letters*, vol. 11, no. 12, pp. 5519–5523, 2011.
- [386] M. Hentschel, T. Utikal, H. Giessen, and M. Lippitz, "Quantitative modeling of the third harmonic emission spectrum of plasmonic nanoantennas," *Nano Letters*, vol. 12, no. 7, pp. 3778–3782, 2012.
- [387] M. Lippitz, M. A. van Dijk, and M. Orrit, "Third-harmonic generation from single gold nanoparticles," *Nano Letters*, vol. 5, no. 4, pp. 799–802, 2005.
- [388] H. Harutyunyan, G. Volpe, R. Quidant, and L. Novotny, "Enhancing the nonlinear optical response using multifrequency gold-nanowire antennas," *Physical Review Letters*, vol. 108, p. 217403, 2012.
- [389] J. Butet, I. Russier-Antoine, C. Jonin, N. Lascoux, E. Benichou, and P.-F. Brevet, "Sensing with multipolar second harmonic generation from spherical metallic nanoparticles," *Nano Letters*, vol. 12, no. 3, pp. 1697–1701, 2012.
- [390] J. Butet, K. Thyagarajan, and O. J. F. Martin, "Ultrasensitive optical shape characterization of gold nanoantennas using second harmonic generation," *Nano Letters*, vol. 13, no. 4, pp. 1787–1792, 2013.
- [391] C. Sauerbeck, M. Haderlein, B. Schurer, B. Braunschweig, W. Peukert, and R. N. Klupp Taylor, "Shedding light on the growth of gold nanoshells," *ACS Nano*, vol. 8, no. 3, pp. 3088–3096, 2014.
- [392] G. Bautista, M. J. Huttunen, J. Makitalo, J. M. Kontio, J. Simonen, and M. Kauranen, "Second-harmonic generation imaging of metal nano-objects with cylindrical vector beams," *Nano Letters*, vol. 12, no. 6, pp. 3207–3212, 2012.
- [393] V. K. Valev, "Characterization of nanostructured plasmonic surfaces with second harmonic generation," *Langmuir*, vol. 28, no. 44, pp. 15454–15471, 2012.
- [394] H. Harutyunyan, S. Palomba, J. Renger, R. Quidant, and L. Novotny, "Nonlinear dark-field microscopy," *Nano Letters*, vol. 10, no. 12, pp. 5076–5079, 2010.

-
- [395] Y. Tsuji, "Finite element method using port truncation by perfectly matching layer boundary conditions for optical waveguide discontinuity problems.," *Journal of Lightwave Technology*, vol. 20, no. 3, p. 463, 2002.
- [396] A. Downes, D. Salter, and A. Elfick, "Finite element simulations of tip-enhanced Raman and fluorescence spectroscopy," *Journal of Physical Chemistry B*, vol. 110, no. 13, pp. 6692–6698, 2006.
- [397] J. M. McMahon, A. I. Henry, K. L. Wustholz, M. J. Natan, R. G. Freeman, R. P. Van Duyne, and G. C. Schatz, "Gold nanoparticle dimer plasmonics: finite element method calculations of the electromagnetic enhancement to surface-enhanced Raman spectroscopy," *Analytical and Bioanalytical Chemistry*, vol. 394, no. 7, pp. 1819–1825, 2009.
- [398] P. Gay-Balmaz and O. J. Martin, "Validity domain and limitation of non-retarded Green's tensor for electromagnetic scattering at surfaces," *Optics Communications*, vol. 184, no. 1–4, pp. 37–47, 2000.
- [399] M. Paulus and O. J. F. Martin, "Green's tensor technique for scattering in two-dimensional stratified media," *Phys. Rev. E*, vol. 63, p. 066615, 2001.
- [400] B. T. Draine and P. J. Flatau, "Discrete-dipole approximation for scattering calculations," *Journal of the Optical Society of America A: Optics, Image Science, and Vision*, vol. 11, no. 4, pp. 1491–1499, 1994.
- [401] B. T. Draine and P. J. Flatau, "Discrete-dipole approximation for periodic targets: theory and tests," *Journal of the Optical Society of America A: Optics, Image Science, and Vision*, vol. 25, no. 11, pp. 2693–2703, 2008.
- [402] F. J. Garcia de Abajo, "Optical excitations in electron microscopy," *Rev. Mod. Phys.*, vol. 82, no. 1, pp. 209–275, 2010.
- [403] F. J. Garcia de Abajo and A. Howie, "Retarded field calculation of electron energy loss in inhomogeneous dielectrics," *Physical Review B*, vol. 65, p. 115418, 2002.
- [404] U. Hohenester and A. Trugler, "MNPBEM - a matlab toolbox for the simulation of plasmonic nanoparticles," *Computer Physics Communications*, vol. 183, no. 2, pp. 370–381, 2012.
- [405] J. Makitalo, S. Suuriniemi, and M. Kauranen, "Boundary element method for surface nonlinear optics of nanoparticles," *Optics Express*, vol. 19, no. 23, pp. 23386–23399, 2011.
- [406] A. M. Kern and O. J. F. Martin, "Surface integral formulation for 3D simulations of plasmonic and high permittivity nanostructures," *Journal of the Optical Society of America A: Optics, Image Science, and Vision*, vol. 26, no. 4, pp. 732–740, 2009.
- [407] J. I. Dadap, J. Shan, and T. F. Heinz, "Theory of optical second-harmonic generation from a sphere of centrosymmetric material: small-particle limit," *Journal of the Optical Society of America B: Optical Physics*, vol. 21, no. 7, pp. 1328–1347, 2004.

Bibliography

- [408] M. Finazzi, P. Biagioni, M. Celebrano, and L. Duò, “Selection rules for second-harmonic generation in nanoparticles,” *Physical Review B*, vol. 76, p. 125414, 2007.
- [409] P. Ginzburg, A. Krasavin, Y. Sonnefraud, A. Murphy, R. J. Pollard, S. A. Maier, and A. V. Zayats, “Nonlinearly coupled localized plasmon resonances: Resonant second-harmonic generation,” *Physical Review B*, vol. 86, p. 085422, 2012.
- [410] Y. Zeng, D. A. R. Dalvit, J. O’Hara, and S. A. Trugman, “Modal analysis method to describe weak nonlinear effects in metamaterials,” *Physical Review B*, vol. 85, p. 125107, 2012.
- [411] J. Xu and X. Zhang, “Second harmonic generation in three-dimensional structures based on homogeneous centrosymmetric metallic spheres,” *Optics Express*, vol. 20, no. 2, pp. 1668–1684, 2012.
- [412] Y. Liu and X. Zhang, “Spin-based second-harmonic generation by metal nanoparticles,” *Physical Review A*, vol. 88, p. 063810, 2013.
- [413] A. Rose, D. Huang, and D. R. Smith, “Nonlinear interference and unidirectional wave mixing in metamaterials,” *Physical Review Letters*, vol. 110, p. 063901, 2013.
- [414] O. J. F. Martin, A. Dereux, and C. Girard, “Iterative scheme for computing exactly the total field propagating in dielectric structures of arbitrary shape,” *Journal of the Optical Society of America A Optics and Image Science*, vol. 11, no. 3, pp. 1073–80, 1994.
- [415] J. Grandidier, S. Massenot, G. C. des Francs, A. Bouhelier, J.-C. Weeber, L. Markey, A. Dereux, J. Renger, M. U. González, and R. Quidant, “Dielectric-loaded surface plasmon polariton waveguides: Figures of merit and mode characterization by image and Fourier plane leakage microscopy,” *Physical Review B*, vol. 78, p. 245419, 2008.
- [416] G. Colas des Francs, J. Grandidier, S. Massenot, A. Bouhelier, J.-C. Weeber, and A. Dereux, “Integrated plasmonic waveguides: A mode solver based on density of states formulation,” *Physical Review B*, vol. 80, p. 115419, 2009.
- [417] M. Iwanaga, “Electromagnetic eigenmodes in a stacked complementary plasmonic crystal slab,” *Physical Review B*, vol. 82, no. 15, p. 155402, 2010.
- [418] I. A. Ibrahim, M. Mivelle, T. Grosjean, J. T. Allegre, G. W. Burr, and F. I. Baida, “Bowtie-shaped nanoaperture: a modal study,” *Optics Letters*, vol. 35, no. 14, pp. 2448–2450, 2010.
- [419] C.-Y. Tai, W.-H. Yu, and S. H. Chang, “Giant angular dispersion mediated by plasmonic modal competition,” *Optics Express*, vol. 18, no. 24, pp. 24510–24515, 2010.
- [420] W. Zhang, B. Gallinet, and O. J. F. Martin, “Symmetry and selection rules for localized surface plasmon resonances in nanostructures,” *Physical Review B*, vol. 81, no. 23, p. 233407, 2010.

-
- [421] H. Guo, B. Oswald, and P. Arbenz, “3-dimensional eigenmodal analysis of plasmonic nanostructures,” *Optics Express*, vol. 20, no. 5, pp. 5481–5500, 2012.
- [422] T. Sandu, “Eigenmode decomposition of the near-field enhancement in localized surface plasmon resonances of metallic nanoparticles,” *Plasmonics*, vol. 8, no. 2, pp. 391–402, 2013.
- [423] G. Volpe, G. Molina-Terriza, and R. Quidant, “Deterministic subwavelength control of light confinement in nanostructures,” *Physical Review Letters*, vol. 105, p. 216802, 2010.
- [424] S.-O. Guillaume, F. J. G.-a. de Abajo, and L. Henrard, “Efficient modal-expansion discrete-dipole approximation: Application to the simulation of optical extinction and electron energy-loss spectroscopies,” *Physical Review B*, vol. 88, no. 24, p. 245439, 2013.
- [425] R. Fuchs, “Theory of the optical properties of small cubes,” *Physics Letters A*, vol. 48, no. 5, pp. 353–354, 1974.
- [426] R. Fuchs, “Theory of the optical properties of ionic crystal cubes,” *Physical Review B*, vol. 11, no. 4, p. 1732, 1975.
- [427] M. Scalora, M. A. Vincenti, D. de Ceglia, V. Roppo, M. Centini, N. Akozbek, and M. J. Bloemer, “Second- and third-harmonic generation in metal-based structures,” *Physical Review A*, vol. 82, p. 043828, 2010.
- [428] Y. Zeng, W. Hoyer, J. Liu, S. W. Koch, and J. V. Moloney, “Classical theory for second-harmonic generation from metallic nanoparticles,” *Physical Review B*, vol. 79, p. 235109, 2009.
- [429] G. Bachelier, I. Russier-Antoine, E. Benichou, C. Jonin, and P.-F. Brevet, “Multipolar second-harmonic generation in noble metal nanoparticles,” *Journal of the Optical Society of America B: Optical Physics*, vol. 25, no. 6, pp. 955–960, 2008.
- [430] J. Butet, I. Russier-Antoine, C. Jonin, N. Lascoux, E. Benichou, O. J. F. Martin, and P.-F. m. c. Brevet, “Universal scaling of plasmon coupling in metal nanostructures: Checking the validity for higher plasmonic modes using second harmonic generation,” *Physical Review B*, vol. 87, p. 235437, 2013.
- [431] Y. Zhang, F. Wen, Y.-R. Zhen, P. Nordlander, and N. J. Halas, “Coherent fano resonances in a plasmonic nanocluster enhance optical four-wave mixing,” *Proceedings of the National Academy of Sciences*, vol. 110, no. 23, pp. 9215–9219, 2013.
- [432] P. G. Etchegoin, E. C. Le Ru, and M. Meyer, “An analytic model for the optical properties of gold,” *The Journal of Chemical Physics*, vol. 125, no. 16, pp. –, 2006.
- [433] H. Goldstein, C. H. J. Poole, and J. L. Safko, *Classical Mechanics*. Addison Wesley, 3 ed., 2000.

Bibliography

- [434] M. Tooley and M. Tooley, *Electronic Circuits: Fundamentals and Applications*. Elsevier, 3 ed., 2006.
- [435] S. Rao, D. Wilton, and A. Glisson, "Electromagnetic scattering by surfaces of arbitrary shape," *Antennas and Propagation, IEEE Transactions on*, vol. 30, no. 3, pp. 409–418, 1982.
- [436] G. Bachelier, J. Butet, I. Russier-Antoine, C. Jonin, E. Benichou, and P.-F. Brevet, "Origin of optical second-harmonic generation in spherical gold nanoparticles: Local surface and nonlocal bulk contributions," *Physical Review B*, vol. 82, p. 235403, 2010.
- [437] F. X. Wang, F. J. Rodriguez, W. M. Albers, R. Ahorinta, J. E. Sipe, and M. Kauranen, "Surface and bulk contributions to the second-order nonlinear optical response of a gold film," *Physical Review B*, vol. 80, p. 233402, 2009.
- [438] T. F. Heinz, *Nonlinear Surface Electromagnetic Phenomena*. Elsevier, Amsterdam, 1991, 1991.
- [439] M. Zhang, G. Lin, C. Dong, and L. Wen, "Amorphous TiO₂ films with high refractive index deposited by pulsed bias arc ion plating," *Surface and Coatings Technology*, vol. 201, no. 16–17, pp. 7252 – 7258, 2007.
- [440] I. Romero, J. Aizpurua, G. W. Bryant, and F. J. G. D. Abajo, "Plasmons in nearly touching metallic nanoparticles: singular response in the limit of touching dimers," *Optics Express*, vol. 14, no. 21, pp. 9988–9999, 2006.
- [441] D. W. Brandl, N. A. Mirin, and P. Nordlander, "Plasmon modes of nanosphere trimers and quadrumers," *Journal of Physical Chemistry B*, vol. 110, no. 25, pp. 12302–12310, 2006.
- [442] A. Papakostas, A. Potts, D. M. Bagnall, S. L. Prosvirnin, H. J. Coles, and N. I. Zheludev, "Optical manifestations of planar chirality," *Physical Review Letters*, vol. 90, p. 107404, 2003.
- [443] A. Drezet, C. Genet, J.-Y. Laluet, and T. W. Ebbesen, "Optical chirality without optical activity: how surface plasmons give a twist to light," *Optics Express*, vol. 16, no. 17, pp. 12559–12570, 2008.
- [444] L. Huang, X. Chen, B. Bai, Q. Tan, G. Jin, T. Zentgraf, and S. Zhang, "Helicity dependent directional surface plasmon polariton excitation using a metasurface with interfacial phase discontinuity," *Light: Science & Applications*, vol. 2, no. 70, pp. 1–7, 2013.
- [445] N. Yu, F. Aieta, P. Genevet, M. A. Kats, Z. Gaburro, and F. Capasso, "A broadband, background-free quarter-wave plate based on plasmonic metasurfaces," *Nano Letters*, vol. 12, no. 12, pp. 6328–6333, 2012.

-
- [446] M. Kuwata-Gonokami, N. Saito, Y. Ino, M. Kauranen, K. Jefimovs, T. Vallius, J. Turunen, and Y. Svirko, "Giant optical activity in quasi-two-dimensional planar nanostructures," *Physical Review Letters*, vol. 95, p. 227401, 2005.
- [447] A. Drezet, C. Genet, and T. W. Ebbesen, "Miniature plasmonic wave plates," *Physical Review Letters*, vol. 101, p. 043902, 2008.
- [448] T. Li, H. Liu, S.-M. Wang, X.-G. Yin, F.-M. Wang, S.-N. Zhu, and X. Zhang, "Manipulating optical rotation in extraordinary transmission by hybrid plasmonic excitations," *Applied Physics Letters*, vol. 93, no. 2, pp. –, 2008.
- [449] K. A. Bachman, J. J. Peltzer, P. D. Flammer, T. E. Furtak, R. T. Collins, and R. E. Hollingsworth, "Spiral plasmonic nanoantennas as circular polarization transmission filters," *Optics Express*, vol. 20, no. 2, pp. 1308–1319, 2012.
- [450] O. Erdem and K. Sendur, "Circularly and elliptically polarized near-field radiation from nanoscale subwavelength apertures," *Applied Physics Letters*, vol. 96, no. 14, pp. –, 2010.
- [451] A. Taflov and S. C. Hagness, *Computational Electrodynamics: The Finite-Difference Time-Domain Method*. Artech House, Boston, 2 ed., 2000.
- [452] P. Muhlschlegel, H.-J. Eisler, O. J. F. Martin, B. Hecht, and D. W. Pohl, "Resonant optical antennas," *Science*, vol. 308, no. 5728, pp. 1607–1609, 2005.
- [453] J. Berthelot, G. Bachelier, M. Song, P. Rai, G. C. des Francs, A. Dereux, and A. Bouhelier, "Silencing and enhancement of second-harmonic generation in optical gap antennas," *Optics Express*, vol. 20, no. 10, pp. 10498–10508, 2012.
- [454] A. Slablab, L. L. Xuan, M. Zielinski, Y. de Wilde, V. Jacques, D. Chauvat, and J.-F. Roch, "Second-harmonic generation from coupled plasmon modes in a single dimer of gold nanospheres," *Optics Express*, vol. 20, no. 1, pp. 220–227, 2012.
- [455] J. Nappa, G. Revillod, I. Russier-Antoine, E. Benichou, C. Jonin, and P. F. Brevet, "Electric dipole origin of the second harmonic generation of small metallic particles," *Physical Review B*, vol. 71, p. 165407, 2005.
- [456] K. Thyagarajan, S. Rivier, A. Lovera, and O. J. Martin, "Enhanced second-harmonic generation from double resonant plasmonic antennae," *Optics Express*, vol. 20, no. 12, pp. 12860–12865, 2012.
- [457] K. Aydin, V. E. Ferry, R. M. Briggs, and H. A. Atwater, "Broadband polarization-independent resonant light absorption using ultrathin plasmonic super absorbers," *Nat Commun*, vol. 2, p. 517, 2011.
- [458] S. Dutta Gupta, "Strong-interaction mediated critical coupling at two distinct frequencies," *Optics Letters*, vol. 32, no. 11, pp. 1483–1485, 2007.

Bibliography

- [459] M. K. Hedayati, M. Javaherirahim, B. Mozooni, R. Abdelaziz, A. Tavassolizadeh, V. S. K. Chakravadhanula, V. Zaporotchenko, T. Strunkus, F. Faupel, and M. Elbahri, "Perfect plasmonic absorber: Design of a perfect black absorber at visible frequencies using plasmonic metamaterials," *Advanced Materials*, vol. 23, no. 45, pp. 5409–5409, 2011.
- [460] J. R. Tischler, M. S. Bradley, and V. Bulovi, "Critically coupled resonators in vertical geometry using a planar mirror and a 5 nm thick absorbing film," *Optics Letters*, vol. 31, no. 13, pp. 2045–2047, 2006.
- [461] N. Bonod, G. Tayeb, D. Maystre, S. Enoch, and E. Popov, "Total absorption of light by lamellar metallic gratings," *Optics Express*, vol. 16, no. 20, pp. 15431–15438, 2008.
- [462] E. Popov, L. Tsonev, and D. Maystre, "Losses of plasmon surface waves on metallic grating," *Journal of Modern Optics*, vol. 37, no. 3, pp. 379–387, 1990.
- [463] K. Chen, R. Adato, and H. Altug, "Dual-band perfect absorber for multispectral plasmon-enhanced infrared spectroscopy," *ACS Nano*, vol. 6, no. 9, pp. 7998–8006, 2012.
- [464] Z. Fang, Y.-R. Zhen, L. Fan, X. Zhu, and P. Nordlander, "Tunable wide-angle plasmonic perfect absorber at visible frequencies," *Physical Review B*, vol. 85, p. 245401, 2012.
- [465] R. Bruck and O. L. Muskens, "Plasmonic nanoantennas as integrated coherent perfect absorbers on SOI waveguides for modulators and all-optical switches," *Optics Express*, vol. 21, no. 23, pp. 27652–27661, 2013.
- [466] N. Liu, M. Mesch, T. Weiss, M. Hentschel, and H. Giessen, "Infrared perfect absorber and its application as plasmonic sensor," *Nano Letters*, vol. 10, no. 7, pp. 2342–2348, 2010.
- [467] B. Zhang, Y. Zhao, Q. Hao, B. Kiraly, I.-C. Khoo, S. Chen, and T. J. Huang, "Polarization-independent dual-band infrared perfect absorber based on a metal-dielectric-metal elliptical nanodisk array," *Optics Express*, vol. 19, no. 16, pp. 15221–15228, 2011.
- [468] A. Moreau, C. Ciraci, J. J. Mock, R. T. Hill, Q. Wang, B. J. Wiley, A. Chilkoti, and D. R. Smith, "Controlled-reflectance surfaces with film-coupled colloidal nanoantennas," *NATURE*, vol. 492, no. 7427, pp. 86+, 2012.
- [469] S. Spillane, T. Kippenberg, O. Painter, and K. Vahala, "Ideality in a fiber-taper-coupled microresonator system for application to cavity quantum electrodynamics," *Physical Review Letters*, vol. 91, p. 043902, 2003.
- [470] D. Subimal, G. Shourya Dutta, J. Banerji, and S. D. Gupta, "Critical coupling at oblique incidence," *Journal of Optics A: Pure and Applied Optics*, vol. 9, no. 7, p. 555, 2007.
- [471] S. Longhi, "Coherent perfect absorption in a homogeneously broadened two-level medium," *Physical Review A*, vol. 83, no. 5, 2011.

-
- [472] M. Pu, Q. Feng, M. Wang, C. Hu, C. Huang, X. Ma, Z. Zhao, C. Wang, and X. Luo, "Ultrathin broadband nearly perfect absorber with symmetrical coherent illumination," *Optics Express*, vol. 20, no. 3, pp. 2246–2254, 2012.
- [473] S. Longhi and G. Della Valle, "Coherent perfect absorbers for transient, periodic, or chaotic optical fields: Time-reversed lasers beyond threshold," *Physical Review A*, vol. 85, no. 5, 2012.
- [474] M. Crescimanno, N. J. Dawson, and J. H. Andrews, "Coherent perfect rotation," *Physical Review A*, vol. 86, no. 3, 2012.
- [475] M. Pu, Q. Feng, C. Hu, and X. Luo, "Perfect Absorption of Light by Coherently Induced Plasmon Hybridization in Ultrathin Metamaterial Film," *PLASMONICS*, vol. 7, no. 4, pp. 733–738, 2012.
- [476] Y. D. Chong, H. Cao, and A. D. Stone, "Noise properties of coherent perfect absorbers and critically coupled resonators," *Physical Review A*, vol. 87, no. 1, 2013.
- [477] N. Gutman, A. A. Sukhorukov, Y. D. Chong, and C. M. de Sterke, "Coherent perfect absorption and reflection in slow-light waveguides," *Optics Letters*, vol. 38, no. 23, pp. 4970–4973, 2013.
- [478] K. N. Reddy and S. D. Gupta, "Light-controlled perfect absorption of light," *Optics Letters*, vol. 38, no. 24, pp. 5252–5255, 2013.
- [479] S. D. Gupta and G. S. Agarwal, "Two-photon quantum interference in plasmonics: Theory and applications," *Optics Letters*, vol. 39, no. 2, pp. 390–393, 2014.
- [480] F. C. Evering, "Artificial diffraction anomalies for gratings of rectangular profile," *Applied Optics*, vol. 5, no. 8, pp. 1313–1317, 1966.
- [481] J. W. Yoon, G. M. Koh, S. H. Song, and R. Magnusson, "Measurement and modeling of a complete optical absorption and scattering by coherent surface plasmon-polariton excitation using a silver thin-film grating," *Physical Review Letters*, vol. 109, p. 257402, 2012.
- [482] J. Zhang, K. F. MacDonald, and N. I. Zheludev, "Controlling light-with-light without nonlinearity," *Light Science and Application*, vol. 1, p. e18, 2012.
- [483] H. Noh, Y. Chong, A. D. Stone, and H. Cao, "Perfect coupling of light to surface plasmons by coherent absorption," *Physical Review Letters*, vol. 108, p. 186805, 2012.
- [484] K. Welford and J. Sambles, "Coupled surface plasmons in a symmetric system," *Journal of Modern Optics*, vol. 35, no. 9, pp. 1467–1483, 1988.
- [485] A. Farhang, B. Abasahl, S. Dutta-Gupta, A. Lovera, P. Mandracci, E. Descrovi, and O. J. F. Martin, "Broadband wide-angle dispersion measurements: Instrumental setup, alignment, and pitfalls," *Review of Scientific Instruments*, vol. 84, no. 3, pp. –, 2013.

Bibliography

- [486] G. S. Agarwal and S. Dutta Gupta, "T-matrix approach to the nonlinear susceptibilities of heterogeneous media," *Physical Review A*, vol. 38, pp. 5678–5687, 1988.
- [487] S. D. Gupta, *Progress in Optics (Nonlinear Optics of Stratified Media)*, vol. 38. Amsterdam: North Holland, 1998.
- [488] G. L. Fischer, R. W. Boyd, R. J. Gehr, S. A. Jenekhe, J. A. Osaheni, J. E. Sipe, and L. A. Weller-Brophy, "Enhanced nonlinear optical response of composite materials," *Physical Review Letters*, vol. 74, pp. 1871–1874, 1995.
- [489] W. Cai and V. Shalaev, *Optical Metamaterials: Fundamentals and Applications*. Springer, New York, 2010.
- [490] T. Siegfried, Y. Ekinici, O. J. Martin, and H. Sigg, "Gap plasmons and near-field enhancement in closely packed sub-10 nm gap resonators," *Nano Letters*, vol. 13, no. 11, pp. 5449–53, 2013.
- [491] T. Siegfried, Y. Ekinici, H. H. Solak, O. J. F. Martin, and H. Sigg, "Fabrication of sub-10 nm gap arrays over large areas for plasmonic sensors," *Applied Physics Letters*, vol. 99, no. 26, p. 263302, 2011.
- [492] T. Siegfried, M. Kind, A. Terfort, O. J. F. Martin, M. Zharnikov, N. Ballav, and H. Sigg, "Reusable plasmonic substrates fabricated by interference lithography: a platform for systematic sensing studies," *Journal of Raman Spectroscopy*, vol. 44, no. 2, pp. 170–175, 2012.
- [493] T. Siegfried, Y. Ekinici, O. J. F. Martin, and H. Sigg, "Engineering metal adhesion layers that do not deteriorate plasmon resonances," *ACS Nano*, vol. 7, no. 3, pp. 2751–2757, 2013.
- [494] G. Leveque and O. J. F. Martin, "Optical interactions in a plasmonic particle coupled to a metallic film," *Optics Express*, vol. 14, no. 21, pp. 9971–9981, 2006.
- [495] S. L. Kleinman, B. Sharma, M. G. Blaber, A.-I. Henry, N. Valley, R. G. Freeman, M. J. Natan, G. C. Schatz, and R. P. Van Duyne, "Structure enhancement factor relationships in single gold nanoantennas by surface-enhanced Raman excitation spectroscopy," *Journal of the American Chemical Society*, vol. 135, no. 1, pp. 301–308, 2012.
- [496] T. Inagaki, M. Motosuga, E. Arakawa, and J. Goudonnet, "Coupled surface plasmons excited by photons in a free-standing thin silver film," *Physical Review B*, vol. 31, pp. 2548–2550, 1985.
- [497] S. D. Gupta, G. Varada, and G. S. Agarwal, "Surface plasmons in two-sided corrugated thin films," *Physical Review B*, vol. 36, pp. 6331–6335, 1987.

Shourya Dutta Gupta

Nanophotonics and Metrology Laboratory (NAM),
Swiss Federal Institute of Technology Lausanne (EPFL),
Switzerland
shourya.duttagupta@epfl.ch;shouryad@gmail.com
(+41) 21-693-7864

ADDRESS ELG 232, EPFL-STI-IMT-NAM (Station 11),
EPFL, Lausanne, CH – 1015,
Switzerland

EDUCATION *Ph. D.* , Nanophotonics and Metrology Laboratory (NAM),
Swiss Federal Institute of Technology Lausanne (EPFL),
Ongoing (July 2010 – till date)

Bachelor of Technology, Materials and Metallurgical Engineering,
Indian Institute of Technology Kanpur (IIT), June 2006 – May 2010

SELECTED SKILLS

- Familiar with human cell culture and standard biochemical assays
- Nanoparticle synthesis and functionalization
- Single particle dark field spectroscopy
- Nanofabrication and characterization
- Numerical simulations with transfer matrix method, surface integral equation (SIE) and COMSOL.

WORK EXPERIENCE

- Reviewer for Optics Letters, Optics Express and Journal of Nanophotonics
- Teaching assistant for the course Ingénierie optique, a bachelor level course in the Microtechnology (2010 – 2013)
- Teaching assistant for the course Advanced Optics, a master level course in the Microtechnology (2010 – 2013)
- Summer internship at Nanophotonics and Metrology Laboratory (NAM), EPFL, Switzerland (May 2009 – July 2009).
- Summer internship at Biomaterials Laboratory, IIT Kanpur, India (May 2008 – July 2008).
- Summer internship at Central Glass and Ceramic Research Institute (CGCRI), Kolkata, India (May 2007 – July 2007).

PUBLICATIONS

Under preparation

22. Mohsen Bahramipanah, **Shourya Dutta-Gupta**, Toralf Scharf, and Olivier J. F. Martin, *Active control of Liquid Crystal molecules orientation in the vicinity of plasmonic nanostructures* (Manuscript under preparation, 2014)
21. Mohsen Bahramipanah, **Shourya Dutta-Gupta**, Banafsheh Abasahl, and Olivier J. F. Martin, *Observation of the fano resonance in imperfect gold nanodisk array* (Manuscript under preparation, 2014)

20. Mohsen Bahramipanah, **Shourya Dutta-Gupta**, and Olivier J. F. Martin, *Detection and trapping of protein molecules with dc voltage in cavity-coupled plasmonic structure* (Manuscript under preparation, 2014)
 19. Banafsheh Abasahl , Mohsen Bahramipanah, **Shourya Dutta-Gupta**, Christian Santschi, and Olivier J. F. Martin, *Transmission enhancement in plasmonic horn nanoantennas*, (Manuscript under preparation, 2014)
 18. Mohsen Bahramipanah, **Shourya Dutta-Gupta**, Banafsheh Abasahl, and Olivier J. F. Martin, *Realization of Cavity-Coupled Plasmonic Device with Enhanced Sensitivity and Figure-of-Merit*, (Manuscript under preparation, 2014)
 17. Andrea Lovera, **Shourya Dutta-Gupta**, P. Mandracci, Emiliano Descrovi and Olivier J.F. Martin, *Full control of strong coupling in a plasmonic antenna lattice on a resonant substrate*, (Manuscript under preparation, 2014).
 16. **Shourya Dutta-Gupta**, Davide Staedler, Christian Santschi, Sandrine Gerber, L. Juillerat and Olivier J.F. Martin, *Cell state dependent biosynthesis of gold nanoparticles by human cells*, (Manuscript under preparation, 2014).
 15. **Shourya Dutta-Gupta**, Krishnan Thyagarajan and Olivier J.F. Martin, *Dispersion controlled shift of plasmonic spectra*, (Manuscript under preparation, 2014).
 14. **Shourya Dutta-Gupta**, Thomas Siegfried, Yasin Ekinici, Hans Sigg and Olivier J.F. Martin, *Cavity-controlled perfect absorption in plasmonic crescent arrays can command the Raman enhancement*, (Manuscript under preparation, 2014).
 13. **Shourya Dutta-Gupta**, Banafsheh Abasahl, S. Dutta Gupta and Olivier J. F. Martin , *Interchangeable coherent perfect absorption and super-scattering with the long and short range surface plasmons*, (Manuscript under preparation 2014).
- 2014**
12. **Shourya Dutta-Gupta** and Olivier J.F. Martin, *An insight into the eigenmodes of plasmonic nanoclusters based on Green's tensor method*, JOSA B, (in press 2014).
 11. Jeremy Butet, **Shourya Dutta-Gupta** and Olivier J.F. Martin, *Surface second-harmonic generation from coupled spherical plasmonic nanoparticles: Eigenmode analysis and symmetry properties*, Physical Review B, 89, pp 245449 (2014). doi:10.1103/PhysRevB.89.245449.
- 2013**
10. B. Abasahl, **S. Dutta-Gupta**, C. Santschi and O. J. F. Martin, *Coupling strength can control the polarization twist of a plasmonic antenna*, Nano Lett., 13 (9), pp 45754579 (2013). doi:10.1021/nl4029363
 9. A. Farhang, B. Abasahl, **S. Dutta-Gupta**, A. Lovera, P. Mandracci, E. Descrovi, O. J. F. Martin, *Broadband wide-angle dispersion measurements: Instrumental setup, alignment, and pitfalls*, Review of Scientific Instruments, 84, p. 033107 (2013). doi:10.1063/1.4795455
 8. V. Auzelyte, V. Flauraud, Ch. Santschi, B. Gallinet, **S. Dutta-Gupta**, Olivier J.F. Marin and J. Brugger, *Direct nanoimprint of gold plasmonic nanostructures using gold-parylene bilayer*, Advanced Optical Materials, 1 (1), p. 5054 (2013). doi:10.1002/adom.201200017
- 2012**
7. **Shourya Dutta-Gupta**, R. Deshmukh, A. V. Gopal, Olivier J.F. Martin and S. Dutta Gupta, *Coherent perfect absorption of light using a grating: Anomalous reflection and refraction*, Optics Letters, 37 (21) p. 4452-4454 (2012). doi: 10.1364/OL.37.004452

6. **Shourya Dutta-Gupta**, Olivier J.F. Martin, S. Dutta Gupta and G. S. Agarwal, *Controllable coherent perfect absorption in a composite film*, Optics Express, 20 (2) p. 13301336 (2012). doi: 10.1364/OE.20.001330
- 2011**
5. **Shourya Dutta-Gupta** and Olivier J.F. Martin, *Strongly coupled bio-plasmonic system: application to oxygen sensing*, Journal of Applied Physics, 110, p. 044701 (2011). doi:10.1063/1.3626786
 4. Ashutosh Kumar Dubey, **Shourya Dutta-Gupta** and Bikramjit Basu, *Optimization of electrical stimulation parameters for enhanced cell proliferation on biomaterial surfaces*, Journal of Biomedical Research B, Vol. 98B, Issue 1, p. 1829 (July, 2011). doi: 10.1002/jbm.b.31827
- 2010**
3. **Shourya Dutta-Gupta**, Subimal Deb and S. Dutta Gupta, *Signature of strong atom-cavity interaction on critical coupling*, Journal of Optics, Vol. 12, No 7 (2010). doi: 10.1088/2040-8978/12/7/075103
- 2009**
2. Ashutosh Kumar Dubey, **Shourya Dutta-Gupta**, Ravi Kumar, Abhishek Tewari and Bikramjit Basu, *Time constant determination for electrical equivalent of a biological cell*, J. Appl. Phys., 105 (2009) 084705. doi:10.1063/1.3086627
- 2007**
1. Subimal Deb, **Shourya Dutta-Gupta**, J. Banerji and S. Dutta Gupta, *Critical coupling at oblique incidence*, J. Opt. A: Pure Appl. Opt., 9 (2007) 1-5. doi: 10.1088/1464-4258/9/7/001

PROCEEDINGS

- 2012**
3. **Shourya Dutta-Gupta**, G. Suarez, C. Santschi and Olivier J.F. Martin, *Ultra-sensitive system for the real time detection of H_2O_2 based on strong coupling in a bio-plasmonic system*, Proc. SPIE 8234, Plasmonics in Biology and Medicine IX, 82340K (February 9, 2012). doi: 10.1117/12.910292
 2. **Shourya Dutta-Gupta**, Olivier J.F. Martin and S. Dutta Gupta, *Novel biosensor for detecting Hemoglobin and its oxygenation state based on nonreciprocity in a coupled waveguide system*, Proc. SPIE 8234, Plasmonics in Biology and Medicine IX, 82341C (February 9, 2012). doi: 10.1117/12.907859
 1. G. Suarez, C. Santschi, **Shourya Dutta-Gupta** and Olivier J.F. Martin, *Biophotonic tool for sensing the dynamics of H_2O_2 extracellular release in stressed cells*, Proc. SPIE 8229, Optical Diagnostics and Sensing XII: Toward Point-of-Care Diagnostics; and Design and Performance Validation of Phantoms Used in Conjunction with Optical Measurement of Tissue IV, 822908 (February 1, 2012). doi: 10.1117/12.910318

CONFERENCES

- 2014**
10. **S. Dutta-Gupta**, C. Santschi, Davide Stadler, Sandrine Gerber, L. Juillerat-Jenneret and O. J. F. Martin, *Biosynthesis of gold nanostructures using human cells*, META 2014 - The 5th international conference on metamaterials, photonic crystals and plasmonics, Singapore (2014) (Oral presentation).

2012

9. G. Suarez, C. Santschi, **S. Dutta-Gupta**, L. Juillerat-Jenneret and O. J. F. Martin, *Biophotonic sensor for real-time and non-invasive detection of extracellular H_2O_2 released by stimulated cells*, Eurosensors 2012, Krakow, Poland (September 2012) (Oral presentation).
8. **S. Dutta-Gupta**, G. Suarez, C. Santschi, A. Lovera, L. Juillerat-Jenneret and O. J. F. Martin, *Biosynthesis of gold nanoparticles in human cells*, ICNP 2012- Sixth International Conference on Nanophotonics, Beijing, China (2012) (Oral presentation).
7. **S. Dutta-Gupta**, G. Surez, C. Santschi, L. Juillerat-Jenneret and O. J. F. Martin, *Detecting oxidative stress in cells based on biosynthesis of gold nanoparticles*, Gordon research conference on Nobel Metal Nanoparticles, USA (17-22 June 2012) (Poster presentation).
6. **Shourya Dutta-Gupta**, O.J.F. Martin and S. Dutta Gupta, *Tunable coherent perfect absorption using a composite film*, META 2012, Paris, France (19-22 April 2012) (Oral presentation).
5. **S. Dutta-Gupta**, G. Surez, C. Santschi, L. Juillerat-Jenneret and O. J. F. Martin, *Biosynthesis of Gold Nanoparticles: Towards a Rapid Oxidative Stress Assay*, USBBE, Lausanne, Switzerland (6-7 February 2012) (Poster presentation).
4. G. Surez, C. Santschi, **S. Dutta-Gupta**, L. Juillerat-Jenneret and O. J. F. Martin, *Biophotonic Tool for Sensing the Dynamics of Oxidative Stress in Living Cells*, USBBE, Lausanne, Switzerland (6-7 February 2012) (Poster presentation).

2011

3. **Shourya Dutta-Gupta**, G. Suarez, C. Santschi, L. Juillerat-Jenneret and O.J.F. Martin, *Biosensor based on plasmon resonance energy transfer for real time H_2O_2 detection*, Oral presentation at Frontiers in optics and photonics, IIT Delhi, Delhi, India (2 - 5 December 2011) (Oral presentation).
2. **Shourya Dutta-Gupta**, G. Suarez and Olivier J.F. Martin, *Strong coupling between surface plasmon polaritons and Hemoglobin: Application to oxygen sensing*, 5th International conference on surface plasmon photonics (SPP 5), Busan, Korea (15 - 20 May 2011) (Poster presentation).
1. **Shourya Dutta-Gupta**, Guillaume Suarez, Christian Santschi, Olivier J. F. Martin, *Biosensing based on plasmon resonance energy transfer (PRET)*, SPIE, Sandiego, USA (August 2011).

LANGUAGES

- English (Bilingual proficiency)
- Hindi (Fluent)
- Bengali (Mother tongue)
- Telugu (Spoken)